Springer Theses
Recognizing Outstanding Ph.D. Research

Michael Taylor

Quantum Microscopy of Biological Systems

Springer

Springer Theses

Recognizing Outstanding Ph.D. Research

Aims and Scope

The series "Springer Theses" brings together a selection of the very best Ph.D. theses from around the world and across the physical sciences. Nominated and endorsed by two recognized specialists, each published volume has been selected for its scientific excellence and the high impact of its contents for the pertinent field of research. For greater accessibility to non-specialists, the published versions include an extended introduction, as well as a foreword by the student's supervisor explaining the special relevance of the work for the field. As a whole, the series will provide a valuable resource both for newcomers to the research fields described, and for other scientists seeking detailed background information on special questions. Finally, it provides an accredited documentation of the valuable contributions made by today's younger generation of scientists.

Theses are accepted into the series by invited nomination only and must fulfill all of the following criteria

- They must be written in good English.
- The topic should fall within the confines of Chemistry, Physics, Earth Sciences, Engineering and related interdisciplinary fields such as Materials, Nanoscience, Chemical Engineering, Complex Systems and Biophysics.
- The work reported in the thesis must represent a significant scientific advance.
- If the thesis includes previously published material, permission to reproduce this must be gained from the respective copyright holder.
- They must have been examined and passed during the 12 months prior to nomination.
- Each thesis should include a foreword by the supervisor outlining the significance of its content.
- The theses should have a clearly defined structure including an introduction accessible to scientists not expert in that particular field.

More information about this series at http://www.springer.com/series/8790

Michael Taylor

Quantum Microscopy of Biological Systems

Doctoral Thesis accepted by
the University of Queensland, Australia

Springer

Author
Dr. Michael Taylor
School of Mathematics and Physics
The University of Queensland
Brisbane
Australia

Supervisor
Assoc. Prof. Warwick Bowen
Australian Centre for Engineered Quantum Systems
The University of Queensland
Brisbane
Australia

ISSN 2190-5053 ISSN 2190-5061 (electronic)
Springer Theses
ISBN 978-3-319-18937-6 ISBN 978-3-319-18938-3 (eBook)
DOI 10.1007/978-3-319-18938-3

Library of Congress Control Number: 2015939827

Springer Cham Heidelberg New York Dordrecht London

Printed on acid-free paper

Springer International Publishing AG Switzerland is part of Springer Science+Business Media (www.springer.com)

To my delightful wife Pamela, and our adorable children Jasmine and Annabelle.

Supervisor's Foreword

The prospects of quantum optics for biological measurements and imaging have been recognized since the birth of the field in the 1980s. They arise from the capacity quantum measurements offer to extract more information per photon than is allowed classically. In biological measurements, and especially measurements at the nanoscale, the weak interaction between light and matter demands the use of bright tightly focused laser fields for many important imaging applications. However, biological systems are often highly sensitive to light, with optical fields both intruding on photochemical processes and ultimately terminating biological function. Quantum optics techniques circumvent this otherwise unavoidable compromise between specimen damage and measurement performance.

While applications in biology have long been recognized as a milestone for quantum measurement, progress has been limited due to the complexities of integrating fragile quantum states with the nonideal environments typically associated with biological specimens. Indeed, the most substantial contribution in this thesis was to demonstrate for the first time that quantum-enhanced microscopy of living biological systems is possible. A range of technical developments were required to achieve this outcome, including the development of new quantum measurement techniques capable of resolving low frequency signals relevant to biological systems, but immune to low frequency noise sources; the development of a microscope capable of imaging microscale biological structure and tracking nanoscale biological motion and compatible with the quantum correlated photons necessary for quantum enhanced measurements; theoretical understanding of the quantum limits to measurements of nanoscale motion; and the development of new modalities for optical nanoparticle tracking.

Ultimately, in this thesis Michael Taylor demonstrates for the first time that it is possible to track the motion of nanoparticles with a precision beyond the quantum shot noise limit imposed when using classical light. This technique is then applied to track lipid particles within living cells, allowing the viscoelasticity of the cellular medium in the vicinity of the particles to be monitored with enhanced precision and bandwidth. As the lipid particles diffuse around the cell, spatial structure could be

probed with sub-diffraction limited resolution via a form of quantum-enhanced photonic force microscopy. This first one-dimensional demonstration of quantum-enhanced sub-diffraction-limited imaging achieved resolution comparable to state-of-the-art classical systems and is significant since most subcellular structures have length scales far below the diffraction limit.

This thesis sets the stage for future applications of quantum microscopy in biological imaging. Combined with three-dimensional particle tracking and an improved source of quantum-correlated light, full sub-diffraction-limited images with Angstrom-scale resolution may be possible. This would provide access to some of the smallest features within a cell, many of which have so far evaded observation.

Brisbane, Australia
March 2015

Assoc. Prof. Warwick Bowen

Abstract

This thesis reports the development of a quantum enhanced microparticle tracking technique, which applied to measurements within living cells, allowed the first demonstrations of both biological measurements beyond the quantum noise limit and quantum enhanced spatial resolution within biology.

The sensitivity of any optical measurement is limited by noise which follows from quantization of the electromagnetic field. This thesis theoretically characterizes the resulting quantum limit on particle tracking precision, both in the limit of perfect measurements and for the measurements used in real experiments, and theoretically establishes an experimental strategy which could allow the quantum limit to be surpassed via the application of nonclassical light. Further, a computational tool is developed which allows rapid characterization of particle tracking experiments, thus providing researchers the benefit of rigorous theoretical predictions without requiring detailed calculations.

Following this, classical technologies are developed which can improve microparticle tracking sensitivity and which are enabling steps toward integration of nonclassical light. An interferometric strategy is described whereby signal-to-noise is improved by removing unwanted light from the detector. An optical lock-in technique is developed which eliminates low-frequency noise, thus allowing quantum noise limited performance at low frequencies. This is a crucial requirement for quantum enhanced measurements, and can also improve precision in classical experiments. Dark-field illumination is also explored as a method to remove unwanted background light, and the optimal illumination angle is calculated for our intended experiments.

These advances are then applied in the development of the first quantum enhanced particle tracking apparatus. Squeezed states of light are used to improve particle tracking precision by 2.7 dB, demonstrating quantum enhanced microscopy for the first time. This was applied to perform the first measurements of living systems with quantum enhanced precision. Naturally occurring lipid particles were tracked within the cytoplasm of *Saccharomyces cerevisiae* yeast cells, with squeezed light enhancing precision by 2.4 dB. The thermal motion of these particles could then be analyzed to infer the viscosity and elasticity of the local environment, with squeezed light allowing 64 % faster observations, thus improving the

sensitivity to dynamic biological changes. This experiment was then extended to spatially resolved quantum imaging, with lipid particles used as scanning probes in a technique called photonic force microscopy. The particles sample variations in the local environment with resolution limited by measurement precision rather than the diffraction limit. The use of squeezed light was found to enhance spatial resolution by 14 % at an absolute resolution level of 10 nm, comparable to leading classical experiments. This was the first demonstration of both sub-diffraction limited resolution and quantum enhanced resolution in biology, and places practical applications of quantum imaging within reach. Finally, the future challenges and prospects of quantum enhanced particle tracking are outlined.

Acknowledgments

I would like to first thank my supervisor, Assoc. Prof. Warwick Bowen, for consistently contributing his hard work, enthusiasm, and outstanding knowledge to my project. He has been a true driving force in the work presented here. Without him, we would all have given up while the experiments were still impossible.

Joachim Knittel was also a great help in these experiments, and his contributions to both the experiments and writing made life much easier.

The key experiments in this thesis were only possible with the help of our collaborators at the Australian National University, so I would also thank Hans Bachor, Jiri Janousek, Vincent Daria, and Boris Hage for their contributions.

Both Alex Stilgoe and Timo Nieminen provided advice on optical trapping theory which improved my understanding and proved to be invaluable to my own numerical calculations.

I was fortunate to be a part of a group of brilliant people, and truly appreciated the time shared with Eoin Sheridan, Glen Harris, James Bennett, Alex Szorkovszky, Jon Swaim, George Brawley, David McAuslan, Michael Vanner, Stefan Forstner, Kiran Khosla, Lars Madsen, and Robin Cole.

Finally, I would like to thank my wife Pamela. She has been very supportive and has helped to keep my spirits high. Together, we have made a wonderful home for us and our sweet little children Jasmine and Annabelle.

Contents

Symbols, Abbreviations and Terminology

ψ	A normalized mode shape of a field
α	A parameter which characterizes the diffusive regime
G^*	Complex shear modulus, combining loss, and storage moduli
G'	Loss modulus, which defines the viscosity
G''	Storage modulus, which defines elasticity
ω_c	Corner frequency in the mechanical spectra of trapped Brownian motion
i	Detected photocurrent
η	Detection efficiency
D	Diffusion constant
k_{opt}	Effective spring constant of the optical trap
δA	Fluctuations of an arbitrary variable A
μ	Fluid viscosity
γ	Friction coefficient
$U(X)$	Gain function of the detector
$\hat{X}^+$	Amplitude quadrature of the field
$\hat{X}^-$	Phase quadrature of the field
λ	The optical wavelength
F_T	Thermal force
$\hat{a}_n$ and $\hat{a}_n^\dagger$	Annihilation and creation operators of the optical field
$\langle A \rangle$	The expectation value of an arbitrary variable A
X, Y	Position coordinates of fields on the detector
x, y, z	Particle position coordinates within the optical trap
3D	Three dimensional
AM	Amplitude modulator; a device which modulates the amplitude of light
AR	Anti-reflection coating
CCD	Charge-coupled device; a camera

Coherent state	The state of light produced by a laser, with amplitude and phase noise at the level of the vacuum fluctuations
Cytoplasm	Contents of a cell, including both cytosol (watery fluid) and organelles
Diffusive motion	The random thermal movement of a particle in a purely viscous fluid; also called Brownian motion
DM	Dichroic mirror
DNA	Deoxyribonucleic acid
EOM	Electro-optical modulator; a device which modulates the phase of light
Homodyne	A measurement method whereby a signal field is measured by interfering it with a bright local oscillator
Lipid granules	Small spherical fat particles used to store energy in yeast cells
LO	Local oscillator
Microrheology	Rheology at microscale
Mie scattering	The scattering profile of homogeneous spherical particles of any size
Nd:YAG	Neodymium-doped yttrium aluminium garnet; the lasing medium of our laser
NV	Nitrogen vacancy; a defect in diamond with a triplet energy state
OCT	Optical coherence tomography; a medical imaging technique
OPA	Optical parametric amplifier; the squeezed light source
Organelle	Internal sub-structures of a cell, usually bounded by a membrane. Examples include mitochondria and the nucleus
Paraxial optics	The approximate regime in which the Gaussian modes are defined. This is not applicable for tightly focused beams
PBS	Polarising beam splitter
PDH	Pound-Drever-Hall; a technique to lock phase and frequency
PFM	Photonic Force Microscope; a technique where trapped particles act as scanning probes, analogous to Atomic Force Microscopy (AFM)
PID	Proportional-Integral-Differential controller used for locking
QNL	Quantum noise limit; the limit to sensitivity which is set by quantum noise, also known as shot noise
Rayleigh scattering	The scattering profile of point dipoles
RF	Radio frequency
Rheology	The field in which viscoelastic properties of a fluid are measured
RNA	Ribonucleic acid

S. cerevisiae	Saccharomyces cerevisiae; a species of yeast
SNR	Signal-to-noise ratio
SQL	Standard quantum limit; the absolute quantum limit to the achievable sensitivity given the number of photons used
Squeezed state	A state of light for which the fluctuations along one quadrature are smaller than the vacuum fluctuations
Subdiffusion	Thermal motion which spreads slower than diffusive motion
Vacuum fluctuations	The zero-point fluctuations of electromagnetic fields
VIS	Visibility of an interferometer
Viscoelasticity	The combined viscous and elastic properties of a material

Chapter 1
Introduction

1.1 Thesis Aims

1.1.1 Overview

The quantum nature of light fundamentally constrains the sensitivity of any optical measurement [96]. This constraint is an important consequence of quantum mechanics which is highly relevant to practical measurement applications. When a detection apparatus is limited by quantum noise, commonly known as shot noise, its sensitivity can only be improved by increasing the optical power. Quantum metrology offers an alternative approach in which non-classical correlations between photons are engineered to suppress the quantum noise, thus allowing more information to be extracted per photon [66]. For experiments where optical power must be constrained, this approach offers sensitivity which can outperform any classical competitor. In most experiments, however, power can simply be increased when improved precision is required. So far the only practical application of quantum metrology is in gravitational wave observatories, which already operate with sensitivity that exceeds the classical limits of existing technology [1, 2].

Another frontier where quantum metrology is anticipated to have important applications is in biological measurements [27, 44, 172], where photochemical interactions often disturb biological processes and can damage the specimen [122, 131]. Despite over a century of intense study, the mechanics of a living cell still holds immense mystery. The answers to many basic questions remain incomplete, such as how DNA is packed into a chromosome [174], whether or not motor proteins exist in the cytoskeleton of bacteria [18], and how cells respond to changing temperatures [99]. Biological measurements have improved with the development of modern technology, which has enabled observation of a vast collection of previously unobservable phenomena, with further technological advances expected to allow similar advances in understanding. For instance, the advent of optical tweezers based particle tracking microscopy provided a window to the microscopic world which allows the dynamics and response of single molecules to be studied. Since this was first developed by

M. Taylor, *Quantum Microscopy of Biological Systems*, Springer Theses,
DOI 10.1007/978-3-319-18938-3_1

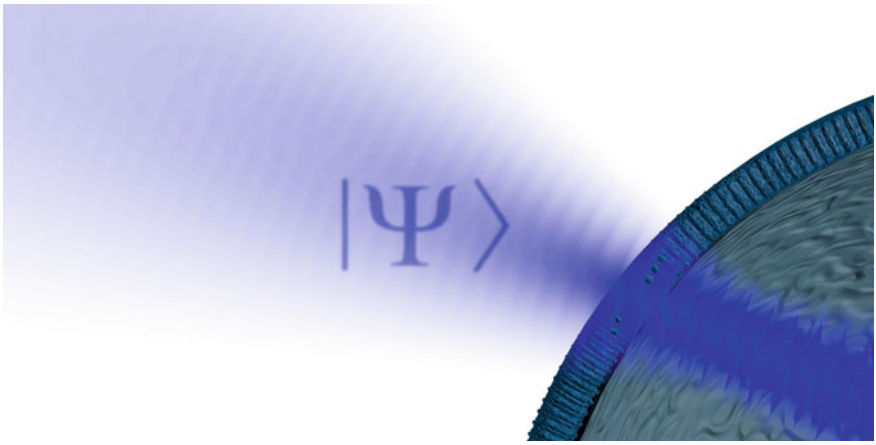

Fig. 1.1 The aim of this thesis is to apply quantum correlated light to enhance biological measurements. In this representation, a living cell is probed with light in the quantum state $|\Psi\rangle$

Ashkin in 1986 [10], it has become one of the most widely used and versatile tools of biophysics, and has enabled a vast array of discoveries. These include both the dynamics and magnitude of the forces applied by biological motors [35, 60, 158], the stretching and folding properties of DNA and RNA [33, 35, 71], the dynamics of virus-host coupling [102], and the mechanical properties of cellular cytoplasm [148, 170, 187].

Although in principle quantum metrology offers a route to improved observation of such biological properties, so far it has lacked the appropriate technology, and all attempts to apply quantum metrology to biology have relied on instruments incapable of biologically relevant measurements [44, 121]. The broad aim of this thesis was to introduce the techniques of quantum metrology to practical biological experiments. The specific goals of this thesis was to develop quantum enhanced particle tracking in optical tweezers, and then to apply it in biological measurements. This technology would make quantum metrology capable of improving observations of a vast range of practical biophysical phenomena. As such, developing this tool and using it to demonstrate a practical improvement in biological measurements is an important step towards establishing the field of biological quantum metrology (Fig. 1.1).

1.1.2 Thesis Structure

This thesis describes the development and application of quantum enhanced particle tracking. It is separated into three main parts, which respectively address the following goals:

- Theoretically determine the quantum noise limit to particle tracking precision.

- Establish experimental strategies to provide the best sensitivity classically possible.
- Introduce non-classical light to overcome the quantum noise limit, and apply this in biological applications.

Part I describes theoretical tools to characterize the quantum limit to sensitivity. These can help to characterize an experimental setup, and provide theoretical insight to the problem of building a classically optimized experiment. Part II then describes strategies which can classically improve the measurement sensitivity, and which can also make optical tweezers compatible with quantum metrology. Although these strategies are developed with quantum enhanced particle tracking in mind, they are also important for classical experiments which require high precision. Finally, in Part III the first quantum enhanced particle tracking apparatus is built, characterized, and applied in biological experiments.

1.2 Quantum Measurements

The over-arching goal of this thesis is to enhance biological measurements by using non-classical states of light. More specifically, we aim to apply squeezed light to enhance the sensitivity of optical tweezers based particle tracking, and to use this device to perform biophysical experiments. This section provides an overview of the broader field of quantum metrology, which this quantum technology will belong to, and describes the status and outlook for real-world biological applications of quantum metrology. This section includes material from the following review paper [164].

1.2.1 Overview

Biological measurements are influenced in a number of important ways by quantum physics. This is usually limiting, with quantum noise placing fundamental constraints on the measurement precision. However, quantum effects can also be harnessed to enable non-classical measurement technologies. For instance, magnetic resonance imaging (MRI) is a particularly well established technique that is based on populating and manipulating spin states of the Hydrogen nuclei within water [81]. Positron emission tomography (PET) relies upon detection of entangled photon pairs to image cancerous tumors and to observe brain function [133]. Superconducting quantum interference devices (SQUIDs) are also used clinically to measure biomagnetic fields for medical diagnosis [41]. Early advances in quantum theory and control have revolutionized biological imaging by enabling such technologies. However, PET is the only such technology to utilize truly non-classical states, as quantum coherence can be understood entirely with classical wave theory.

Although entangled photon pairs have been utilized in PET since the 1960s [101, 135], these are generated uncontrollably via β^+ decay. Recent advances now allow quantum correlated states to be engineered. Control of these states provides access to a new range of non-classical phenomena and opens fundamentally new capabilities in diverse fields such as computing [19], data encryption [68], and measurements [66, 67]. The emerging field of quantum metrology can be broadly defined as the use of quantum correlations to improve measurements [67].

This section aims to summarize both the advances already achieved and the future potential for quantum metrology in biological systems. Prior to the work reported in this thesis, only two proof-of-principle experiments had demonstrated the use of engineered quantum correlations in biological measurements [44, 121]. Both of these applied entangled photon pairs, which allowed some improvement in tissue imaging [121] and in refractive index sensing of a protein solution [44]. Although these experiments have demonstrated that quantum correlated states can improve biological measurements, the sensitivity achieved was not comparable to existing classical technology, and they do not provide a clear route to practical quantum measurements in biology. In principle, however, quantum metrology can enable unrivalled precision in practical biological measurements. Numerous technologies have already been demonstrated in non-biological measurements which could soon have important applications in biology. These near-future applications include cellular imaging with both multi-photon microscopy [168, 175] and super-resolution of fluorescent markers [45, 146], and measurement of biomagnetic fields [184]. An even more promising application is the use of squeezed states of light in optical measurements of biology, as squeezed light is the only quantum state which has been used to outcompete state-of-the-art classical technology. However, prior to the advances reported in this thesis, no method to integrate squeezed light into biological sensing had been demonstrated.

1.2.2 Concepts of Quantum Metrology

Although quantum physics ultimately underlies all forms of measurement, most measurements can be modeled semi-classically. For instance, a classical wave treatment can reproduce almost all optical interactions. However, there are some phenomena which exhibit classically forbidden behavior, such as two-photon interference in a Hong-Ou-Mandel (HOM) interferometer [83] (see Fig. 1.2). Such non-classical phenomena rely on quantum correlations. With recent advances, quantum correlations have been engineered in a range of systems, and are expected to enable numerous technological advances. In quantum metrology, these correlations are applied in measurements, either to improve a classical system or to enable fundamentally new capabilities.

One particularly common class of quantum metrology experiments aim to improve the precision of optical measurements by using non-classical photon correlations. The measurement process generally involves preparing a probe, interacting it with

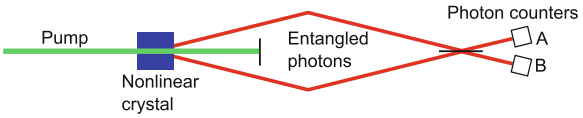

Fig. 1.2 Layout of a Hong-Ou-Mandel interferometer [83]. A nonlinear crystal is pumped to produce entangled photon pairs by parametric down-conversion. These photons are then recombined with a beamsplitter and detected. A classical treatment would predict that the relative phase would dictate the detection events, and would determine whether the photons are more likely to arrive at detector *A* or detector *B*. In reality, non-classical interference ensures that both photons arrive at one detector, with equal probabilities that the photon pair arrives at detector *A* and *B*. This violates the classical wave treatment of light, and can only be predicted with quantum theory

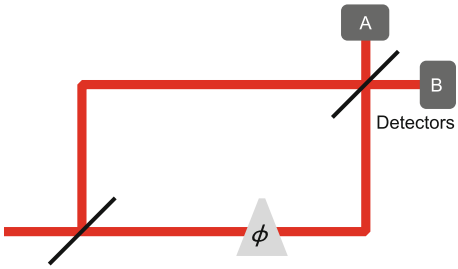

Fig. 1.3 The layout of a phase sensing experiment based on a Mach-Zehnder interferometer. Interference between the fields modulates the intensity at the two detectors, and therefore allows the relative phase shift ϕ to be estimated

a system of interest, and then reading out the probe. In practice, this might involve generating an optical field, propagating it though a Mach-Zehnder interferometer and measuring the power in the two output ports to estimate a phase shift ϕ applied within one arm of the interferometer (see Fig. 1.3). Even if all sources of technical noise are eliminated, the quantization of the optical field introduces noise which sets a lower limit on the achievable precision. Here we provide a qualitative introduction to quantum limits; for a more detailed discussion see Ref. [164].

1.2.2.1 The Quantum Noise Limit

Quantum noise can be understood in an intuitive way by considering photon statistics; for a more rigorous treatment, see Chap. 3. An ideal measurement of optical intensity reveals the total photon flux n which arrives at the detector within a certain timeframe. For coherent laser light, all photons arrive independently so that the measured photon number fluctuates with the random photon spacing. Photon arrivals are then described by Poissonian statistics, which states that the measured photon variance Δn^2 will be given by $\langle n \rangle$. This number fluctuation is commonly known as shot noise, and constrains the precision of any optical measurement that does not utilize quantum correlations [66]. This can be seen for the specific example of interferometric phase

sensing, as shown in Fig. 1.3. For an ideal interferometer, the photon numbers to reach the two detectors are given by

$$\langle n_A \rangle = \langle n \rangle \cos^2(\phi/2) \tag{1.1}$$
$$\langle n_B \rangle = \langle n \rangle \sin^2(\phi/2), \tag{1.2}$$

for the total photon flux n and relative phase shift ϕ. Consequently, the phase can be estimated from measurements of n_A and n_B, with sensitivity maximized when $\phi = \pi/2$. For small displacements about this point, the phase is estimated as

$$\phi_{\text{estimate}} = \frac{\pi}{2} + \frac{n_B - n_A}{\langle n \rangle}. \tag{1.3}$$

The statistical fluctuations on the photon numbers then introduces statistical uncertainty in the phase estimate of

$$\Delta\phi^2 = \frac{\langle \delta n_A^2 \rangle + \langle \delta n_B^2 \rangle - 2\langle \delta n_A \, \delta n_B \rangle}{\langle n \rangle^2}, \tag{1.4}$$

where $\delta n_A = n_A - \langle n_A \rangle$ and $\delta n_B = n_B - \langle n_B \rangle$. If the light is in a coherent state, the photon statistics are completely uncorrelated so that $\langle \delta n_A \, \delta n_B \rangle = 0$, and the number fluctuations at each detector are given by $\langle \delta n_A^2 \rangle = \langle \delta n_B^2 \rangle = \frac{1}{2}\langle n \rangle$. Consequently, the achievable phase precision is given by

$$\Delta\phi = \langle n \rangle^{-1/2}. \tag{1.5}$$

Examination of Eq. 1.4 suggests that precision can be improved if the detection events are correlated, such that $\langle \delta n_A \, \delta n_B \rangle > 0$. Fluctuations in the intensity can provide such correlations, though this also increases the photon number variance $\langle \delta n_A^2 \rangle$ so that precision is not improved. In fact, the sensitivity achieved with a coherent state corresponds to the best precision achievable without quantum correlations; a result which holds for any experiment, not just phase estimation [66]. Consequently, the sensitivity achievable using coherent light of a given power is typically used as a benchmark in quantum metrology experiments. For any given measurement procedure and optical efficiency, the precision limit set by quantum shot noise is referred to as the *quantum noise limit*,[1] while the more stringent *standard quantum limit* defines the precision which would be achievable with no loss and a perfect measurement.[2] As such, Eq. 1.5 corresponds to the quantum noise limit if n is the photon number

[1] Although this limit is widely used, there is no clear consensus as to its name. It is most often referred to as either the quantum noise limit [156, 165, 171] or the shot noise limit [27, 72, 184], often interchangeably [1], though other names are also used [84, 172].

[2] Note that the phrase "standard quantum limit" carries two distinct meanings in different communities. While much of the quantum metrology community uses the definition here, the optomechanics community defines it as the best sensitivity possible with arbitrary optical power, which occurs when quantum back-action from the measurement is equal to the measurement imprecision [66].

at the detector, while it corresponds to the standard quantum limit if n is the incident photon number. These differing limits are generally used in different contexts, with continuous measurements on bright fields often compared to the quantum noise limit and photon counting measurements typically compared to the standard quantum limit.

In many cases, the quantum noise limit is described as the best precision which can be achieved classically [48, 163]. Coherent light, which saturates the quantum noise limit, is sometimes even referred to as "classical light" [66, 165, 171]. This can be confusing, as a classical field can be perfectly noiseless. However, one can derive the limit of Eq. 1.5 without assuming the optical field to be quantized. The measurement procedure requires an electronic record of the light intensity; typically a photocurrent produced in a photodiode. This photocurrent consists of discrete electrons which are themselves subject to electronic shot noise. If a perfectly noiseless optical field were to probabilistically excite photoelectrons, the electron statistics would maintain the quantum noise limit derived above [61]. Violation of the quantum noise limit requires electron correlations in the detected photocurrents which can not follow from probabilistic detection.

1.2.2.2 Squeezed Light

For interferometric phase sensing, the quantum noise limit can be surpassed by injecting a squeezed vacuum state into the unused input port of the interferometer [37]. This entangles the detected fields, and can allow the variance in the difference signal $n_B - n_A$ to be suppressed. A squeezed vacuum state can be visually represented with a phase space diagram, as shown in Fig. 1.4. It is related to the vacuum fluctuations of the electromagnetic field, though its variance along one quadrature is reduced at expense of the other. More generally, any field with fluctuations squeezed below the level of vacuum fluctuations is called a squeezed state. Squeezed light is an important resource in quantum metrology, and can be applied to enhance the precision of any optical measurement. If the amplitude is squeezed, for instance, the photons tend to arrive more evenly spaced than in a coherent field, which is a phenomena known as photon antibunching. This can be used to reduce the variance in amplitude or intensity measurements, and thus enable precision which surpasses the quantum noise limit.

1.2.2.3 Heisenberg Limit

As described above, non-classical correlations can be used to enhance precision. Taken to its extreme, perfect entanglement may allow elimination of all statistical noise in Eq. 1.3; in this case, the phase precision would only be limited by the requirement that n_A and n_B be integers. A phase shift can only be resolved if it changes the difference signal $n_B - n_A$ by at least one photon, which limits the possible precision to

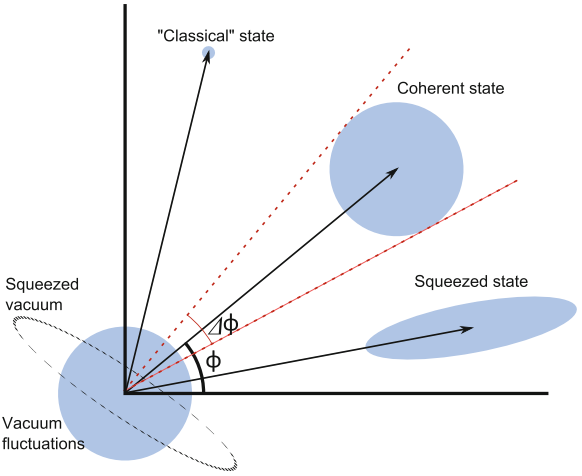

Fig. 1.4 A phase space diagram, illustrating a noiseless classical optical state, and a coherent, squeezed, and vacuum quantum states. The X and Y axes can be interpreted as real and imaginary components of the optical field. An uncertainty relation enforces a minimum phase space area for any quantum state of light (see Chap. 3); in the absence of illumination, this results in the vacuum fluctuations of electromagnetic fields. A coherent field is reached by adding this vacuum noise to a classical field, which is one reason that it is often described as "classical light". These fluctuations establish the minimum resolvable phase ($\Delta\phi$). Squeezed states have reduced variance along one quadrature at the expense of the other. The example shown here is phase squeezed, and can be used to enhance phase precision

$$\Delta\phi \geq \langle n \rangle^{-1}. \tag{1.6}$$

Once again, this qualitative derivation reproduces an important and fundamental result; Eq. 1.6 represents the Heisenberg limit on precision, which sets a lower limit on precision for any quantum state. Heisenberg limited sensitivity is achieved by the NOON state, in which the constituent photons are in a superposition of all occupying one arm of the interferometer, with the other unoccupied [48]. Each mode is therefore occupied by a superposition of 0 and n photons, also known as a cat state. In contrast to the qualitative derivation here, NOON states do not enhance phase precision by reducing measurement noise, but instead amplify the relative phase shift by a factor of n [48].

1.2.2.4 Application to Measurements

While squeezed light and photonic NOON states can both be applied in similar phase sensing applications, they have markedly different characteristics. In principle the NOON state allows measurement at the fundamental Heisenberg limit, while in most implementations, squeezed light does not [66]. Furthermore, a NOON state

contains a definite number of photons, which can allow measurement statistics to be characterized extremely accurately [185]. However, applications of NOON states to precision sensing are constrained because it is technically challenging to generate NOON states with large photon numbers, and such states are generated probabilistically with extremely low flux. The largest NOON state generated to date contained 5 photons, with an average photon flux of order 1 s^{-1} [3]. This co-propagated with well over 1000 s^{-1} photons in other states, such that the optical field was dominated by unwanted light. Squeezed states, by comparison, have been generated with an optical power of 40 kW, or a flux of 10^{23} s^{-1} [1]. Since precision improves with the photon flux, NOON states only offer a practical benefit in those measurements for which the optical power must be constrained to the photon counting regime. The low photon numbers in photonic NOON states also constrains the maximum enhancement which is achievable, such that even a perfect measurement using 5-photon NOON states is limited to 7 dB of quantum enhancement, with real experiments achieving far less. By contrast, 12.7 dB of enhancement has been experimentally demonstrated using squeezed light [50]. Squeezed states also have superior tolerance to inefficiencies, and in the limit of high photon flux and non-negligible losses, can offer the best possible sensitivity [47]. However, squeezed light has a finite frequency band of enhancement, and low frequency signals often fall outside of this squeezing band. Although state-of-the-art squeezed light sources reach down to 10 Hz [115, 156], such sources are extremely challenging to construct, and many sources only provide squeezing in the MHz regime [82, 189]. This can seriously constrain practical applications, as most biological processes studied to date occur in the Hz–kHz regime.

In addition to enhancing sensitivity, non-classical states are also used in quantum metrology to enable new approaches to measurement for which there is no immediate classical analogue. Often such measurements utilize photon pairs produced by parametric down-conversion [19]. These are entangled since detection of one photon always indicates that a second photon was generated. Entangled photon pairs can enable such phenomena as entanglement mediated two-photon absorption [168], or two-photon interference in a Hong-Ou-Mandel (HOM) interferometer [83].

In the field of quantum metrology, quantum correlated states are applied to enhance or enable measurements. This is broadly motivated by two distinct goals. One aim is to establish the fundamental consequences of quantum mechanics for a measurement. Toward this end, the quantum limits and the strategies required to overcome them are both studied. These experiments often aim to breach the standard quantum limit, as this establishes that the measurement procedure is in a classically inaccessible regime. However, this is typically achieved at an extremely low photon flux and with sensitivity far worse than any classical competitor. They can also include post-selection, in which individual measurements are discarded if the light is prepared in the wrong state or disrupted by loss [118]. Overall this degrades sensitivity by discarding information, but improves the comparison between quantum and classical strategies. Such approaches are incompatible with the other aim of quantum metrology, which is to build highly precise sensors for practical applications. The primary motivation for these experiments is to out-compete their classical counterparts in some manner, rather than to overcome a fundamental limit. The best example

of this is in gravitational wave observatories, where squeezed light is used to achieve sensitivity below the quantum noise limit [1, 2]. This is now routinely employed because it has proven to improve performance in absolute terms [72].

From the earliest stage of quantum metrology, the two primary applications discussed were gravitational wave detection and biological measurements [144, 153, 154, 167, 180], since both are fields in which quantum noise can constrain observations and prevent important new discoveries. In the past few years, quantum metrology has seen spectacular progress toward both of these key goals. While quantum measurements in biology do not yet outperform state-of-the-art classical technology, the groundwork has been laid for future quantum sensors with capabilities beyond that which is classically achievable. This section now turns to those technologies, and the practical biological applications which are likely to follow.

1.2.3 Biological Measurements with Entangled Photons

1.2.3.1 Quantum Optical Coherence Tomography

The first application of quantum metrology in biology was in a demonstration of optical coherence tomography (OCT) with entangled photons [121]. Classical OCT is a technique that is widely used for medical diagnosis [85, 143], where it is employed to generate high-resolution 3D images of such structures as the eye and the retina [57], and for dermatology [182] and cardiology [64]. OCT is based on a Michelson interferometer, with interference measured between a reference arm and backscattered light from a specimen. Axial resolution is typically provided by using white light with a short coherence length, such that interference only occurs for light which has backscattered at a specific depth in the sample. Since this relies on broadband white light to provide ultrashort coherence lengths, dispersion within the sample can substantially broaden the axial sectioning resolution.

In quantum OCT entangled photon pairs produced in parametric down-conversion are used instead [119, 120, 169]. Axial resolution is provided by HOM two-photon interference [83], which occurs when the back-scattered and reference arms are of equal length. Scanning of the reference arm therefore scans the depth of the measured image (see Fig. 1.5). When compared to the use of low coherence light, this can provide both superior axial resolution and immunity to dispersion [119, 120]. This quantum approach to OCT was applied to imaging of onion skin cells in Ref. [121]. However, shortly afterwards Ref. [106] demonstrated that the improved resolution and immunity to dispersion demonstrated in quantum OCT could also be achieved with uncorrelated light. The use of classical illumination could also allow a much higher photon flux and corresponding improvement in sensitivity. On a per photon basis, however, the classical technique falls short of quantum OCT. As such, quantum OCT may see revived interest once the technologies required to produce and measure a high flux of entangled photons are developed. In its current form, it has

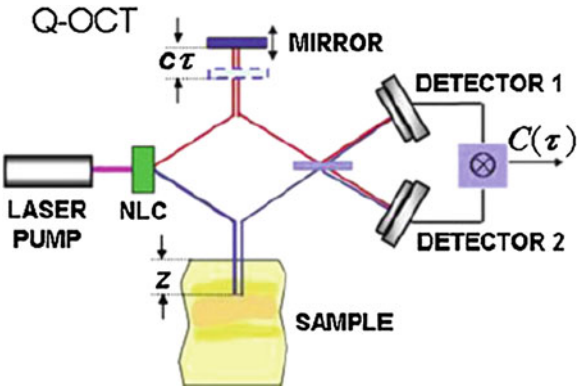

Fig. 1.5 Layout of quantum OCT. The nonlinear crystal (NLC) generates entangled photon pairs, with one photon passing through a reference arm while the other illuminates the scattering sample. When the photons are recombined, two-photon interference only occurs for photons which follow a similar optical path length. Measurement of this interference thus allows an image to be constructed only using photons which have scattered from a specific depth in the sample. Conventional OCT applies short coherence length light to achieve a similar depth resolution. Reproduced with permission from Ref. [169]

primarily been useful for the innovations it brought to both quantum measurements and OCT [169].

1.2.3.2 Sensing Proteins with NOON States via Refractive Index Measurement

Following this application in OCT, entangled photons were applied to measurements of protein concentration in a microfluidic device [44]. A 2-photon NOON state was passed through a Mach-Zehnder interferometer with a microfluidic channel passing through one arm. A standard interferometric phase measurement was then used to infer the refractive index of the fluid within the channel. Proteins within solution were measured via the increase in the fluid refractive index.

In this case, the use of entangled photons increases the phase sensitivity, in principle allowing measurement precision which would classically require increased photon flux. Biological samples are generally photosensitive, and in some cases increasing the photon flux could damage the specimen. While entanglement was shown to improve the interferometer visibility beyond the threshold for supersensitivity, the experiment suffered from low detection efficiency and was unable to overcome the standard quantum limit. More importantly, the flux of measured photon pairs ($0.1\ s^{-1}$) was far below any known damage threshold in biology. Consequently, even with improved technology, similar experiments are not likely to out-compete classical sensors which use high flux coherent light. This demonstration helped to show that quantum correlated light can benefit biological sensing, though it does

not establish a clear route toward practical applications of quantum measurement in biology.

With these demonstrations, quantum measurements of biology are not a future perspective but are a current reality. From a practical point of view, the primary weakness of both quantum OCT and the protein measurement discussed above is the use of low flux sources of entangled photons. Quantum OCT might see widespread applications if it could be performed with the high flux used in classical experiments. Likewise, with a higher photon flux the refractive index measurements could be competitive with classical measurements, which would make it useful in chip-based microfluidic sensing. However, given that neither the light sources or detectors for such measurements are currently available, this thesis adopts a more practical approach which is to use squeezed states of light, which can be applied and detected with arbitrary optical power. In addition to such a squeezed light based measurement, there are a range of other quantum measurements which could also soon hold important applications in biology. This introduction now turns to these future applications.

1.2.4 Entangled Two-Photon Microscopy

Two-photon microscopy is an area in which entangled photons could provide a substantial practical advantage [55, 168]. In two-photon microscopy, two-photon absorption within a sample is studied via its specific fluorescent signature. Since this is a third-order nonlinear optical process, two-photon absorption will typically occur only near the central focus of the illumination. When compared to one-photon absorption, this both sharpens the spatial resolution and suppresses fluorescence away from the focal plane. However, classical two-photon absorption is an extremely inefficient process requiring a very high input flux of photons. The peak power is typically maximized by use of high-peak-intensity pulsed lasers, which can damage the specimen [80].

If highly correlated photon pairs are used instead of classical light, the two-photon absorption rate can be vastly enhanced, with the absorption process depending linearly rather than quadratically on the photon-flux density [129]. This allows multiphoton fluorescence microscopy to proceed with intensities more suited to biological samples (Fig. 1.6). For instance, recent demonstrations in non-biological organic chemistry have found that two-photon absorption and two-photon fluorescence measured with an entangled photon flux of 10^7 s^{-1} is comparable to similar measurements with 10^{17} s^{-1} coherent photons, allowing a 10 order of magnitude reduction in power from tens of mW to a few pW [75, 107].

Furthermore, entangled photons reveal information about the nonlinear absorption mechanism which is inaccessible to classical light sources. Two-photon absorption can occur either via a permanent dipole transition or via a virtual state transition [89]. While these transitions are classically indistinguishable, the different mechanisms have a markedly different response to entangled photons; dipole transitions are not en-

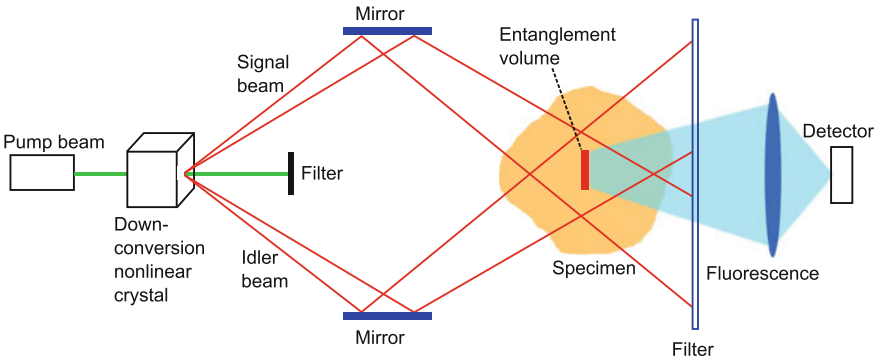

Fig. 1.6 An entangled two photon microscope. A pair of entangled optical fields are generated with a nonlinear crystal, and recombined at the specimen. The entanglement enhances two-photon absorption where the fields recombine, as can be observed by measuring the resulting fluorescence. Adapted from Ref. [168]

hanced by the entanglement [175], while entangled photons that are phase-matched to virtual states are absorbed at a vastly enhanced rate [129, 139]. Even among transitions mediated by virtual states, the entangled photon absorption cross section is not proportional to the classical absorption cross section, as the enhancement depends on the detuning and linewidth of the virtual state [137]. The two-photon transition amplitudes contributed by the entangled photons can also interfere, producing "entanglement-induced transparency", analogous to electromagnetically induced transparency [55]. An entangled two-photon microscope may prove the only tool capable of probing the properties of virtual states.

Although this has not yet been applied in biological measurements, these preliminary results suggest that entanglement could be extremely promising in future two-photon microscopy applications. It could both enhance the visibility in two-photon fluorescent microscopy, and reveal classically inaccessible information.

1.2.5 Quantum Super-Resolution in Fluorescence Microscopy

While the non-classical states used in most quantum metrology experiments require sophisticated state preparation, systems such as fluorescent particles naturally emit non-classically correlated light. These quantum correlations are ignored in classical experiments, though recent results have shown that measurement of the correlations provides additional information that can be used to enhance spatial resolution [145]. In classical fluorescent microscopy, the optical diffraction limit restricts the resolution with which fluorescent particles can be distinguished to approximately half the wavelength of light. This limits the use of fluorescent imaging in living cells. To overcome this limit, a number of fluorescent super-resolution techniques were devel-

oped for photo-switchable particles, including stimulated emission depletion (STED) microscopy [142, 183], photoactivated localization microscopy (PALM) [152], and stochastic optical reconstruction microscopy (STORM) [138]. These have enabled great progress in biological research by allowing cellular structure to be characterized at the nanometer level. In some applications, however, photo-switchable markers cannot be used. In this case, structured illumination has instead been used to sample the fluorescent emission over a wider range of spatial frequencies. In this approach, the fluorescent emission is spatially modulated with a high spatial frequency via structure in the illumination field. This down-shifts some of the high spatial frequency information which would not usually be measured. By capturing information from the fluorescent field which is typically neglected, this approach allows the resolution to be approximately halved [105].

In a similar manner, photon statistics can also be measured to capture more of the information from the fluorescent emission. In fluorescence microscopy, a fluorescent particle absorbs energy as it is excited to a higher state, and is then imaged as it decays back to the ground state by re-radiating at another wavelength. This mechanism generally only allows emission of one photon at a time, which results in photon antibunching and associated non-classical photon correlations. As such, coincident photons must originate from separate fluorescent centers.

This concept has been applied in two separate approaches to resolve fluorescent particles below the diffraction limit. In Ref. [45] the photon statistics were measured in a scanning confocal microscope to provide an additional channel of information, which thus improved the statistical estimation of the positions of the fluorescent particles. Such an estimation procedure is a class of image deconvolution [128], with the measurement of photon coincidences improving resolution by providing information that is not available in classical deconvolution methods.

A related approach was also demonstrated in Ref. [146]. In that work, however, a large collection of fluorescent particles were excited with pulsed light and simultaneously measured in wide-field imaging (Fig. 1.7). With this configuration, the fluorescent particles could only emit one photon each per excitation pulse. By measuring the N photon coincidences at each pixel and analyzing the correlations, an image of the fluorescent particles can be constructed with the resolution enhanced by a factor of $N^{1/2}$ [145]. The experimental demonstration measured photon coincidences up to $N = 3$, and allowed the spatial resolution to be enhanced from 272 to 181 nm [146]. This enhancement could hold practical significance, just as structured illumination is already used in important biological applications. Furthermore, applying this method in conjunction with structured illumination could potentially combine the resolution enhancements, which would allow this technique to resolve smaller features than any directly comparable classical technique.

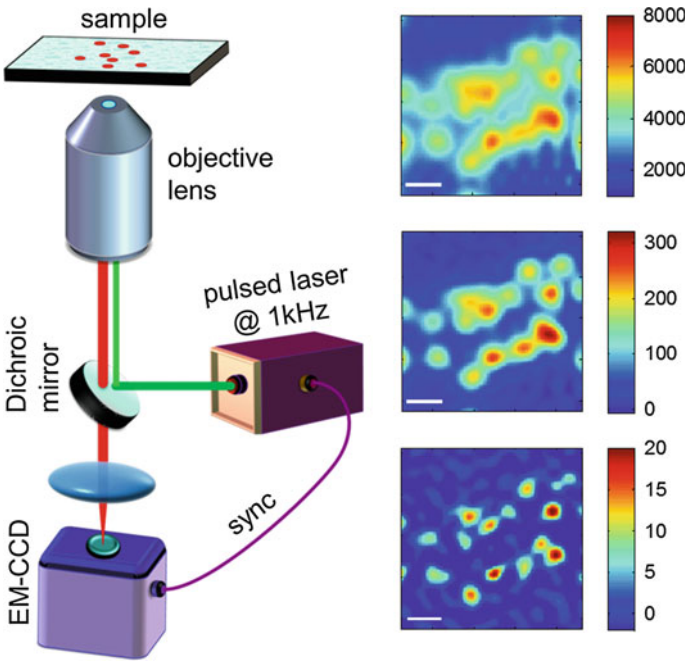

Fig. 1.7 Super-resolution via measurement of photon coincidence statistics. Fluorescent particles are illuminated with short pulses of laser light, and the resulting fluorescence is measured on a high efficiency camera. Each pulse is sufficiently fast that a particle can only be excited once per pulse, and each coincident photon must originate from a different fluorescent particle. An analysis of the N photon coincidences then allows a $N^{1/2}$ enhancement in resolution, with example data shown at the right. This shows the $N = 1$, which is simply the intensity profile, the $N = 2$ and the $N = 3$ data. As N increases the resolution is visibly improved, though the contrast is degraded. Reproduced with permission from Ref. [146]

1.2.6 Phase Contrast Microscopy

Quantum metrology could also provide enhanced sensitivity in phase contrast microscopy, which is another technique that is widely used for biological imaging. In such measurements, a light beam is split and focused through two slightly different sections of a sample. The phase difference between the paths is then measured to determine differences in the refractive index along differing paths. This can then be used to reconstruct the spatial profile of the refractive index within the sample [92].

Phase measurements have been enhanced with quantum correlated light for some time, which suggests that phase contrast microscopy can also be enhanced with quantum correlated light. The feasibility of this was demonstrated in Ref. [125], where

two photon NOON states were used to allow sub-shot noise imaging.[3] This demonstration did not achieve either sensitivity or spatial resolution which was comparable to classical techniques, partly because ultra-low photon flux was used and partly because the specimen could not be imaged at the focus of the imaging optics. However, an extension of this technique which applies high flux quantum correlated light with diffraction limited spatial resolution would provide an extremely useful tool for biological research.

1.2.7 Atomic Magnetometers

The development of high sensitivity magnetometers capable of measuring biomagnetic fields has both advanced biological research and enabled new methods in medical diagnosis. In particular, such studies have provided rich information about the function of the heart [56] and brain [76], which both produce a relatively large biomagnetic field. Initially the SQUID was the only magnetometer capable of useful biomedical applications, but with recent advances atom based magnetometers can now provide the sensitivity of a SQUID while operating at room temperature [32, 46, 98]. As such, atomic magnetometers are used in the above mentioned biological applications, measuring both the dynamics and spatial profile of the biomagnetic field generated by a beating heart [21–23], and the field generated from neural activity in the brain in response to stimuli [186]. Atomic magnetometers are also used in applications beyond those investigated with SQUIDs, including multichannel measurements of neural activity in a brain [91], cryogen-free low-field MRI [141], and in attempts to measure biomagnetic fields in plants [43].

1.2.7.1 Quantum Limits to Sensitivity

Atomic magnetometers are based on optical manipulation and readout of the spin state of an atomic ensemble in the presence of a magnetic field. Light that is near-resonant with an optical transition spin polarizes the hyperfine levels of the ground state, which subsequently undergo Larmor spin precession in the magnetic field. The phase and amplitude of the transmitted light then encodes information about the spin precession, from which the magnetic field can be estimated.

The sensitivity of this measurement is fundamentally limited by quantum noise in both the optical readout and the spin of the atomic ensemble. Quantum noise in the spin states, referred to as projection noise, results from the projection of the atomic spin onto the measurement axis. The mean spin is oriented orthogonal to the

[3]This experiment was published after the quantum enhanced microscopy experiment reported in Chaps. 10 and 11 of this thesis (Ref. [165]), but before this was extended to spatially resolved imaging as described in Chap. 12 (Ref. [166]). Consequently, this thesis reports the first experiment to achieve quantum enhanced microscopy, though Ref. [125] was the first to demonstrate quantum enhanced microscopic imaging.

measurement axis to provide optimal estimation of the spin precession. Projection noise then follows from the statistical fluctuations in the measurement. The optical readout can also be limited by quantum shot noise. While the dominant source of quantum noise depends on the details of the measurement, the contributions of projection noise and optical shot noise are comparable when the measurement is optimized [15].

1.2.7.2 Enhancement with Entangled Atoms

There has been much interest in the possibility to improve sensitivity beyond the projection noise and shot noise limits. Optical readout of the Faraday polarization rotation is a quantum non-demolition (QND) measurement of the spin polarization state along one axis [150] (Fig. 1.8). In a QND based magnetometer, each measurement both provides information about the magnetic field and projects the system onto a spin-squeezed state, increasing the sensitivity of subsequent measurements (Fig. 1.9).

An early theoretical analysis suggested that quantum correlations within the spin ensemble would be destroyed by spin relaxation, rendering spin squeezing effective only for measurements much shorter than the spin-relaxation time [15]. Later analysis has shown that the spin relaxation preserves quantum correlations, and that spin squeezing could be used to vastly improve the sensitivity on any timescale [97]. This has then been applied experimentally, with QND measurements used to induce spin squeezing in an atomic ensemble, resulting in improved sensitivity to magnetic fields [100, 149]. One variation of this approach is to use QND measurements to induce anticorrelated noise in two separate vapor cells, such that the resulting two-mode squeezing (or equivalently, entanglement) suppresses the measured projection noise [179]. This approach enabled an absolute sensitivity approaching that achieved in state-of-the-art atomic magnetometers. Another related approach applied QND measurements to a scalar atomic magnetometer and achieved the most sensitive scalar magnetic field sensitivity to date, even without demonstrating spin squeezing [151].

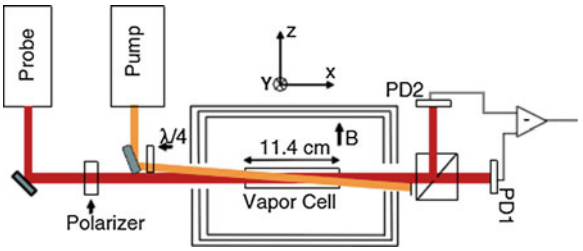

Fig. 1.8 Layout for QND atomic magnetometry. A pump field is used to spin polarize an atomic vapor. After this a probe field is passed through the cell, and the magnetic field estimated from the Faraday polarization rotation. Reproduced with permission from Ref. [150]

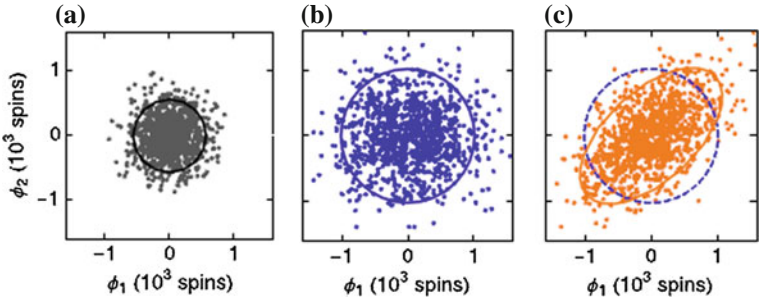

Fig. 1.9 Measurements with spin squeezing. The measurement statistics of QND measurements were studied, first with no atoms in the trap to characterize the readout noise (**a**) and then independently prepared coherent spin states (**b**), with the measured distribution corresponding to the projection noise. The *solid curves* indicate 2σ radii for Gaussian fits. **c** When a single coherent spin state is prepared and sampled sequentially, the successive measurements squeeze the spin variance below the projection noise limit (*dashed circle*) along one axis. Reproduced with permission from Ref. [149]

1.2.7.3 Use of Quantum Correlated Light

In addition to the enhancement by spin squeezing, non-classical states of light have also been used to overcome the quantum noise on the optical readout [84, 184, 185]. The optical magnetometer in Ref. [184] achieved sensitivity better than the shot-noise limit using a polarization-squeezed probe tuned near the atomic resonance (Fig. 1.10). In that work, however, the atomic vapor was not spin polarized, but instead kept in a thermal state, which resulted in poor absolute sensitivity. A similar experiment was reported later in Ref. [84], though there the absolute sensitivity was vastly improved and the frequency range of squeezing was extended into the biologically relevant sub-kHz regime. Such an enhancement could be particularly important once it is applied in a QND based magnetometer, because it acts both to improve

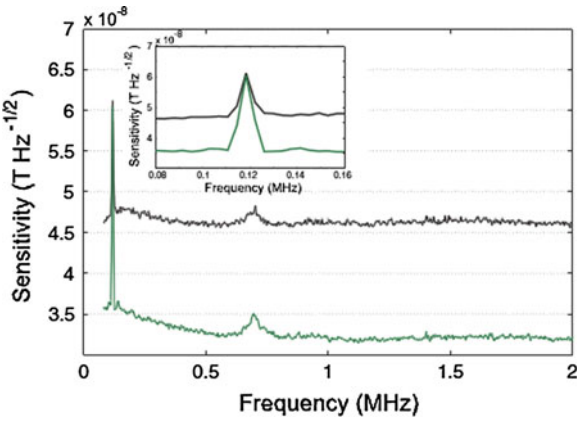

Fig. 1.10 Magnetic field measurements with squeezed (*dark green line*) and coherent (*black line*) light. The use of squeezed light lowers the detection noise floor without affecting the applied signal field at 120 kHz, and thus improves the field sensitivity by 3.2 dB. Reproduced with permission from Ref. [184]

the measurement sensitivity and also to improve the spin squeezing. Overall, this improves the fundamental limit on sensitivity for a QND based magnetometer [15, 184]. To achieve this, it is important that there is no increase in spin decoherence induced by the probe when using quantum correlated light. To test for this, Ref. [185] applied two-photon NOON states to perform optical readout in atomic magnetometry. By characterizing the photon scattering and atomic excitations, they could verify that entangled light induced less decoherence in the spin state than coherent light which achieved the same sensitivity.

By using squeezed light in a QND measurement to condition the spin-states of the atomic ensemble, it should be possible to achieve extremely high sensitivity. Once this is achieved in state-of-the-art magnetometers, it should allow magnetic field sensors which outcompete SQUIDs, and can be expected to have important biological and clinical applications.

1.2.8 Conclusion

Measurements which apply engineered quantum correlations are a newly emerging technology. Though no practical biological applications of such measurements have been demonstrated, they have been shown to have much potential and are likely to be important in the coming years. In particular, squeezed states of light have been proven to enable unprecedented sensitivity in non-biological measurements [1], and could hold important applications in biological sensing. However, no technology has been demonstrated which could apply squeezed light in optical measurements of biology; a challenge which is addressed in Part III of this thesis.

1.3 Introductory Theory of Optical Tweezers

Optical tweezers combine single particle tracking with controlled micromanipulation. Particles are tracked with sub-nanometer sensitivity [40] within a confining optical trap. With suitable calibration, this allows forces to be characterized with sub-piconewton precision [60, 117]. This allows dynamic characterization of both forces and displacements at the single molecule level, which has led to a vast range of biophysical discoveries. This section introduces the field of optical tweezers, briefly overviews some of the key achievements of the field, and introduces the theory of optical confinement of particles. This provides the background information, context, and relevance of quantum enhanced precision in particle tracking. This section incorporates the following publication [163].

1.3.1 Relevance of Optical Tweezers

Following the development of optical tweezers in 1986 [10], optical tweezers rapidly became a key tool in a wide range of biophysical experiments. These started with trapping of single cells [11] and viruses [8], and soon after the manipulation of intracellular organelles [9]. Such intracellular studies could then reveal the biophysical forces which propel organelles through the cellular cytoplasm [12]. For instance, it enabled characterization of the molecular motor kinesin, which carries cargo through cells along microtubule structures. In these experiments, kinesin would move down a microtubule while dragging a larger bead. This bead was tracked using optical tweezers, with the measured motion revealing both the molecular motion [24] and the applied molecular force [103]. When measured with sufficient precision, this has revealed that the induced motion is not continuous, but follows a step-like pattern [158].

Another notable application of optical tweezers is in microrheology, where the viscous and elastic properties of a medium are studied via their influence on the motion of an embedded test particle [26, 188]. Such micrometer scale measurement of the viscoelasticity can reveal information not available to bulk rheometers, such as the properties of microscale objects such as living cells [170], or directional properties of materials with nanoscale structure [51]. Materials are typically characterized by the complex shear modulus $G^* = G' + iG''$, where G' and G'' are the loss and storage moduli corresponding to viscosity and elasticity respectively. A Newtonian fluid is incompressible ($G'' = 0$) and has constant viscosity G'. In general, however, both moduli are non-zero and vary with frequency. By characterizing the thermal motion of a bead, the viscoelasticity can be characterized over the full bandwidth of the detection system [134, 162].

The thermal motion of particles in a Newtonian fluid such as water follows well-known Brownian motion. If the medium also exhibits elasticity, this partially confines the particle by introducing a path-dependent force which opposes its motion [73]. Optical tweezers can be used to characterize the resulting "subdiffusive" motion within living cells, thus determining both the viscosity and elasticity of the cellular cytoplasm [70, 113]. Within the cytoplasm, almost all thermal motion is subdiffusive because proteins and other macromolecules resist the movement of particles [181]. Subdiffusive motion is extremely important to the operation of a cell, as it mediates important processes such as chemical reactions [42], protein folding [63], and structural changes in DNA [157]. The extent of the particle confinement can strongly effect chemical reactions, for instance, as it slows the initial approach of chemical reactants to one another but also decreases the likelihood that they will pass without interacting. In some regimes this improves the efficiency of the reaction, while in others it can suppress reactions [74, 148]. The viscoelasticity is not a simple static parameter, but has been found to follow nanoscale structure in places [173], and to vary as the cell undergoes reproduction [147]. However, more study is still required to establish the full biological implications of these mechanical properties [74].

In addition to allowing the mechanical properties of a bulk fluid to be characterized, optical tweezers are also capable of probing the elastic response of single molecules such as DNA. The mechanical properties of DNA are far from trivial, and are heavily effected by bending, stretching, wrapping and unwinding. These properties have significant biological relevance to such cellular processes as replication and transcription [30]. Optical tweezers have provided a key tool in the study of such mechanical properties. By using DNA to tether a bead to a fixed surface, optical tweezers can be used to move the bead and stretch the DNA. This has allowed the elasticity of the DNA to be measured, and when using large forces, revealed the existence of a stable overstretched form of DNA [155, 178]. Further studies revealed several other force-induced mechanical transitions [34]. The attractive force which binds the complementary strands in the double-helix of DNA together has also been measured by immobilizing one strand on a fixed surface and the other strand to a bead, and applying a force to the bead [108]. Further extensions of this method have allowed measurement of the forces associated with unzipping the double-helix of DNA base-by-base [52], which is found to be substantially smaller than the force required to pull the entire DNA molecule apart at once. In addition to these lateral forces, optical tweezers have also been used to study the response of DNA to an applied torque by rotating the immobilized section of DNA, which has revealed even more structural transitions [30]. Similar studies have also been performed with RNA, and these have also revealed vast levels of molecular complexity [33]. Despite these advances, the mechanical properties of DNA and RNA still raise many unanswered questions. For instance, it is not yet known how DNA is wrapped into the compact form of a chromosome [174], and the mechanical response of DNA is not well understood in the presence of inhomogeneities which exist in biological environments [29]. The biological significance of these mechanical properties also raises many questions, including the role they play in gene expression [176]. Furthermore, numerous RNA strands have been discovered which act as thermometers, with temperature sensitivity via poorly understood effects that appear to rely on mechanical compliance [99]. These molecular thermometers play an important role in cellular function by regulating cellular activity in response to changing temperatures, and are also believed to stimulate bacterial pathogenic activity [99]. These open questions, and many more like them, are likely to be answered only with new technology and improved observations [29].

In addition to the many biological applications of optical tweezers, they have also been used to resolve a number of questions in fundamental physics. For instance, optical tweezers have also been used to demonstrate the non-trivial of thermodynamics of a microscale systems [114]. Macroscopic systems follow the second law of thermodynamics, which states that the entropy of any closed system must always increase. On a microscopic scale, however, all interactions are time-reversible, and individually are not constrained by this law. On average, each microscopic interaction increases the entropy, such that the second law holds when considering a system that is sufficiently large that the microscopic variability in the entropy is unmeasurable. This transition between the microscopic and macroscopic nature of the

second law was confirmed experimentally by studying the entropy of optical trapped particles [36, 177].

Optical tweezers also allow characterization of the thermal motion of a particle in a purely viscous fluid. The usual description of this, termed Brownian motion, assumes that the particle follows a random walk through the medium with no memory of its past trajectory. This requires velocity to be dissipated instantly [111]. At sufficiently short timescales, however, the motion deviates from this and thermally driven particles have a measurable velocity [86, 109]. In addition to this, motion in water also deviates from Brownian motion due to hydrodynamic effects. Since any surrounding fluid must be displaced in order for the particle to move, the surrounding fluid contains some memory of the past motion of the particle, which results in an effective modification to the thermal forces [90], and with a sufficiently strong optical trap produces a mechanical resonance in the particle motion [62].

Quantum physics can also be studied by optically trapping particles in vacuum and cooling the motion [6, 110]. With some improvements over current technology, this is expected to allow cooling to the quantum ground state [94]. Furthermore, the inherent optical control is expected to allow the quantum state to be engineered, enabling generation of mechanical entanglement [38]. Provided a levitating system could be controlled and measured with sufficient accuracy, it could then be used to resolve some of the central questions in quantum mechanics, including tests for non-Newtonian gravity at short distances [65], and the gravitationally induced wavefunction collapse predicted for a superposition state [16].

In addition to the important applications mentioned here, there are also many more which are not discussed. A comprehensive review of such experiments is beyond the scope of the current work. However, this brief overview allows the vast range and importance of the applications of optical tweezers to be appreciated. There are many reviews which can provide a more complete discussion of the biological applications of optical tweezers. For instance, Ref. [35] provides a thorough description of biomolecular force sensing experiments. For a thorough introduction to the underlying physics and capabilities of optical tweezers, see Ref. [25].

1.3.2 Optical Forces

An optical tweezers experiment fundamentally involves focusing a laser beam near a particle, and afterward measuring the light to infer particle position (see Fig. 1.11a). The focused laser field exerts an optical force on the particle which confines it near the focus. This interaction involves momentum exchange between the light and particle which therefore deflects the laser beam. The particle position is generally measured by estimating change in momentum of the transmitted light. This change in optical momentum is observable as a deflection of the laser beam, which is typically measured by collecting the transmitted light with an objective lens and directing it onto a quadrant detector [69]. To understand such a measurement, we now consider the optical forces exerted.

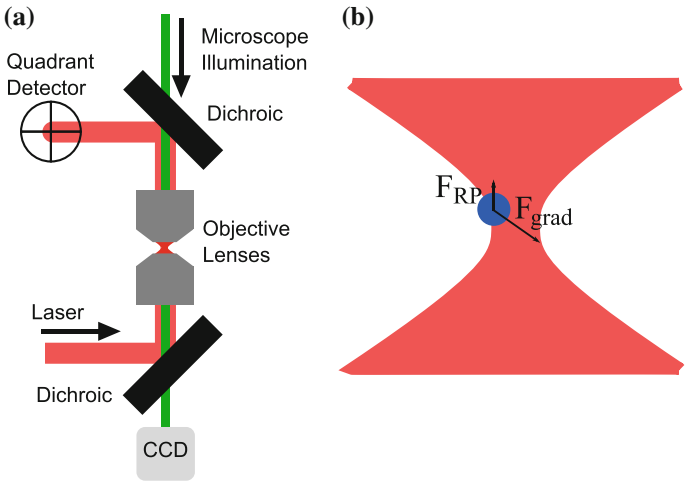

Fig. 1.11 The most basic elements of an optical tweezers experiment. **a** Laser light is focused to a point to trap particles, and then collected for measurement. In most cases, this measurement occurs on a quadrant detector as shown here. Microscope illumination is also used to allow visualization of the trapping region on a CCD (charge-coupled device) camera, which is not fundamentally required but is necessary for its practicality. **b** Provided the particle has greater refractive index than the surrounding fluid, it is trapped near the focus of the beam and is subject to two forces: a gradient force F_{grad} which points toward the intensity maxima (see Eq. 1.7), and radiation pressure F_{RP} which pushes in the direction of light propagation (see Eq. 1.8)

1.3.2.1 Dipole Approximation

The optical force exerted is simple to evaluate if the trapped particle is approximated as a point dipole [77]. In this case, the optical field $\mathbf{E}$ induces an oscillating dipole with polarization $\mathbf{p} = \alpha\mathbf{E}$, where α is the polarizability. Neglecting components at optical frequencies, the optical gradient force on the dipole is given by

$$\mathbf{F}_{\text{grad}} = (\mathbf{p} \cdot \bigtriangledown)\,\mathbf{E} = \frac{1}{2}\alpha \bigtriangledown E^2, \tag{1.7}$$

where the vector identity $\bigtriangledown E^2 = 2\,(\mathbf{E} \cdot \bigtriangledown)\,\mathbf{E} + 2\mathbf{E} \times (\bigtriangledown \times \mathbf{E})$ has been used, along with $\bigtriangledown \times \mathbf{E} = 0$ from Maxwell's equations [77]. The force described in Eq. 1.7 points toward maxima in intensity for particles with positive polarizability, or equivalently, a higher refractive index than the surrounding medium. In addition to this force, the radiation pressure of the trapping laser also pushes the particle along the optical axis $\hat{z}$, which tends to destabilize the trap (see Fig. 1.11b). This force is given by

$$\mathbf{F}_{\text{RP}} = \frac{k^4\alpha^2}{12\pi n^2 \epsilon_0} E^2 \hat{z}, \tag{1.8}$$

where k is the wavenumber, n the refractive index of the surrounding medium, and ϵ_0 the vacuum permittivity [77]. To enable stable trapping, the trapping force must dominate the radiation pressure. To achieve this, the laser is focused to the smallest spot possible, which maximizes the intensity gradient. The scattering rate is important because the gradient force scales as α while the radiation pressure scales as α^2. The scattering rate therefore should not be vanishingly small, as this produces minimal optical forces, but it also cannot be very large, as this produces large radiation pressure forces which destabilize the optical trap. Both the gradient and radiation pressure optical forces scale linearly with the light intensity, so within this analysis there is no upper limit on the optical power which can be used to trap particles. In practice, particles cannot be trapped in water if the trapping light causes excessive heating of the surrounding water.

1.3.2.2 Ray Optics Regime

While the dipole approximation described optical forces on particles much smaller than the wavelength, the ray optics approximation can be applied for particles much larger than the wavelength. Within the ray optics approximation, light is considered to propagate in rays, with deflection of the light occurring only through refraction at interfaces. In an optical trapping experiment, the only relevant interfaces are at the surface of the trapped particle. By considering the deflection of each ray of light that passes through the particle, the change in momentum of the trapping field can be estimated. Since momentum is conserved, a force is imparted on the particle which opposes the change in optical momentum [7]. When this force is estimated for a spherical particle of greater refractive index than its medium, the force is found to oppose small displacements such that the particle can be trapped at the focus; see Fig. 1.12.

Within the ray optics regime, the optical deflection is independent of the trapping wavelength. Although the optical momentum per photon depends on the wavelength, this is compensated by the energy per photon, so the momentum depends only on the optical power. Consequently, the force applied in the ray optics regime is independent of the trapping wavelength.

1.3.2.3 General Trapping Forces

If the particle size is comparable to the wavelength, the dipole approximation and ray optics analysis are both invalid. If the particle is a homogeneous sphere, the forces can be calculated with extended Mie theory. An exact solution for the scattered field (and hence the force) exists, though this solution is expressed as an infinite series of spherical harmonic functions [87]. The series is generally truncated to allow numerical evaluation of the scattered field, with precision limited only by the number of terms included in the analysis. For a more complete description of optical forces in the Mie scattering regime, see Ref. [136]. Alternatively, the Optical

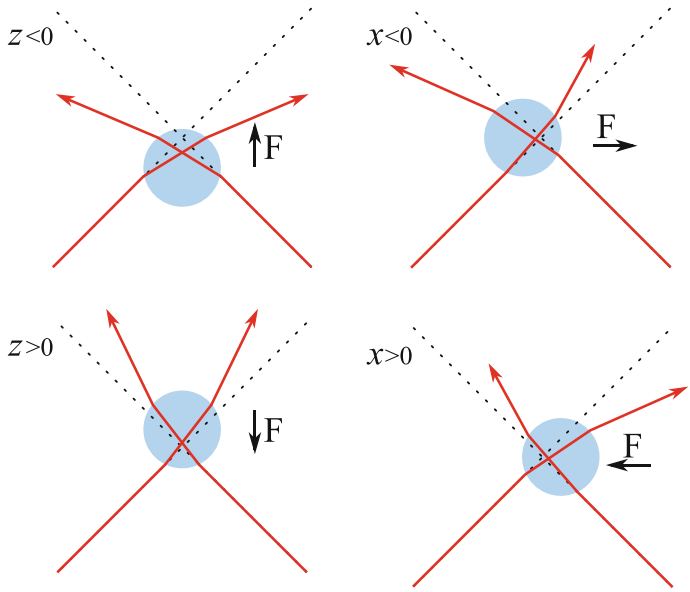

Fig. 1.12 Forces on a particle in the ray optics regime. The trapping light is deflected as the particle is displaced from the optical focus (indicated by *dashed lines*), which changes its momentum. The total momentum is conserved via an optical force on the particle which opposes the change in optical momentum. The particle refractive index is greater than the surrounding fluid in these diagrams, which leads to a trapping force that opposes small displacements. Particles with lower refractive index are not stably trapped

Tweezers Toolbox provides a numerical tool to allow rapid calculation of the forces exerted in an optical tweezers experiment [123, 124]. While the analysis for larger particles is more involved than that presented above, the qualitative conclusions remain similar. Particles can only be trapped if they have a higher refractive index than the surroundings. Traps are more stable when the light is more tightly focused, and when the refractive index contrast is small. Although the qualitative conclusions hold, neither the dipole approximation nor ray optics can correctly predict either the magnitude of the predicted forces or their scaling with experimental parameters within the Mie scattering regime.

1.3.3 Trapped Brownian Motion Spectra

Here we derive the expected thermal trajectory $x(t)$ of a trapped particle in the simple case of a purely viscous medium with no elasticity or hydrodynamic interactions. In this case, the equation of motion along one dimension is given by

$$m\ddot{x}(t) = -\gamma\dot{x}(t) - k_{\text{opt}}x(t) + F_T + F_{\text{ext}}, \tag{1.9}$$

for a particle mass m, friction coefficient γ, a harmonic optical force $-k_{\text{opt}}x(t)$, an external force F_{ext}, and a fluctuating thermal force $F_T = (2k_BT\gamma)^{1/2}\xi(t)$, with T the temperature and k_B Boltzmann's constant [20]. The fluctuating function has the properties $\langle\xi(t)\rangle = 0$ and $\langle\xi(t)\xi(t')\rangle = \delta(t-t')$. By taking the Fourier transform of Eq. 1.9 and rearranging, we find that

$$x(\omega) = \frac{(2k_BT\gamma)^{1/2}\xi(\omega) + F_{\text{ext}}(\omega)}{-m\omega^2 + i\omega\gamma + k_{\text{opt}}}. \tag{1.10}$$

Many experiments aim to measure an external force, such as those produced by protein motors. In such experiments, the external force directly competes with the fluctuating thermal force.

We can see that the inertial contribution $m\ddot{x}(t)$ to Eq. 1.10 is negligible at frequencies far below the rate at which the kinetic energy is lost through friction, $\omega \ll \gamma/m$. The friction is given by Stokes' law as $\gamma = 6\pi\mu R$, where R is the particle radius and μ is the fluid viscosity. Using this, it can be seen that the inertial contribution is measurable only at very short timescales; for instance, a 1 μm diameter silica microsphere in water has $m/\gamma = 120$ ns. This term is therefore typically neglected [20], with the resulting power spectra of trapped Brownian motion given by

$$\langle|x(\omega)|^2\rangle = \frac{2k_BT/\gamma + \langle F_{\text{ext}}(\omega)\rangle/\gamma^2}{\omega^2 + \omega_c^2}, \tag{1.11}$$

where we have used $\langle|\xi(\omega)^2|\rangle = 1$ and introduced the corner frequency $\omega_c \equiv k_{\text{opt}}/\gamma$. Any measurement of this thermal motion will also include a detection noise floor. Without an external force $F_{\text{ext}} = 0$, this results in spectra such as that shown in Fig. 1.13.

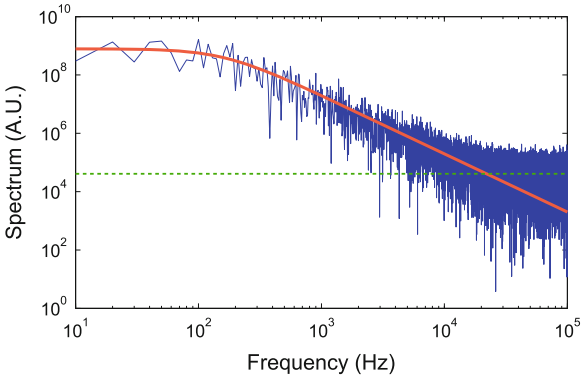

Fig. 1.13 This is the mechanical spectra which is typical for measurements of trapped Brownian motion. This follows the expectation value (*thick red line*), given by a Lorentzian mechanical profile (Eq. 1.11), along with a white noise floor (*dashed green line*)

1.3.4 Application to Sensing

In many optical tweezers experiments, a biological molecule exerts a force on a trapped particle, and the particle position is measured to determine the biomolecular force. Since such experiments are performed in an aqueous environment at room temperature, the desired force competes with the stochastic thermal force on the particle. Force resolution is therefore limited by both the absolute sensitivity of the apparatus and the background of thermal forces. These experiments are typically limited by detection drifts at sub-Hz frequencies, thermal noise over the bulk of the detection range, and are shot-noise limited only above a few tens of kHz [132]. For the example in Fig. 1.13, the characteristic Lorentzian spectral shape of trapped Brownian motion dominates over the measurement noise for frequencies below 10 kHz. In this frequency range, thermal forces limit any determination of the external force F_{ext}, and reduction in the measurement noise floor offers no improvement in the force sensitivity. At frequencies above 10 kHz, however, measurement noise dominates the imprecision in force sensing. Thus an improvement in measurement noise primarily increases the measurement bandwidth available for force sensing applications.

Although thermal fluctuations can limit the resolution of non-thermal forces, they also provide a method to probe the mechanical nature of the fluid surrounding the particle, since thermal motion of a particle is determined both by the thermal force and the mechanical properties of its surrounding medium. Provided the particle size is known, both the temperature and viscosity of the surrounding fluid can be determined easily from Eq. 1.11. In addition to this, several effects can also be characterized which are neglected in the derivation of Eq. 1.11. For instance the inertial term $m\ddot{x}(t)$ was neglected, although this dominates at fast time-scales [86, 93], as described in Sect. 1.3.1. By characterizing the particle velocity in this regime, one can directly test the Maxwell-Boltzmann distribution for particle velocities [93, 109]. Furthermore, the thermal force F_T is assumed to be a white noise process, which requires it to be completely memoryless. However, the surrounding fluid must be displaced to allow particle motion, which results in correlations between the fluid flow and particle motion, effectively causing the Brownian force to be non-white [62, 90, 112]. Similar hydrodynamic effects also couple the particle motion to surrounding walls [49, 130] and other particles [116]. Additionally, the surrounding fluid can exhibit elasticity, which effects both the damping and thermal force and thereby the thermal motion [70, 113]. This effect is common in complex fluids such as within biological systems, and has a profound effect on all chemical processes within the cell which are mediated by thermal motion. All of the above effects can be characterized by determining the profile of the thermal motion. The sensitivity of such experiments is limited by detection noise at all frequencies, so reducing the measurement noise allows characterization of such effects with improved bandwidth and precision. For a more detailed explanation of such experiments, see Ref. [188].

1.3.5 Applications for Quantum Enhanced Sensitivity

The use of non-classically correlated light in optical tweezers can allow enhanced sensitivity. As described in Sect. 1.2, this can increase the bandwidth and improve the precision of practical experiments. Here, several applications which are already known to require such improvements are discussed. This list is far from exhaustive, and we anticipate that quantum enhanced sensitivity could also hold relevance to the investigation of many other phenomena.

In the field of microrheology, the viscoelastic properties of a material are studied by the way they influence the motion of an embedded particle. This reveals mechanical properties of the medium, with important applications in understanding both biological structures and in the study of nanofluidic mechanics. Improved sensitivity would allow the viscoelastic response to be probed on shorter timescales, revealing both the properties of the cytoplasm and biological processes at higher frequency [31, 134]. For instance, the cytoskeleton is responsible for cell shape and movement, and intracellular transport of organelles and chromosomes for protein synthesis and cell division. It consists of a complex structure of interconnected semiflexible protein filaments, and exists in a dynamical non-equilibrium state due to the action of motor molecules and actin filament polymerization. To date, this has made quantitative measurements of its behavior challenging [13]. The recent development of low noise two-particle microrheology with 100 kHz bandwidth represents a significant advance in this area, and has allowed the observation of rich dynamical behavior in actin filaments, including new relaxation processes unique to semiflexible polymers [14, 95]. Using quantum optics techniques we expect that it will be possible to extend the bandwidth of such techniques well into the MHz frequency range, and potentially even into the GHz regime. This would open up a new window on the biological world.

The high bandwidth achievable with quantum enhancement could also enable the first observation of ultrafast biological processes. For instance, nanopores in the membrane of a cell can open and close on nanosecond timescales [126]. These nanopores are of approximately 1 nm size [127], and provide extremely effective control of the membrane permeability to water and ions [88]. Nanopores have been indirectly observed via measurements of membrane permeability [17, 127], and their function studied by characterizing synthetic nanopores [104]; however, due to their small size and transient nature, they have never been directly observed. Their exact structure and function is not fully understood, and the formation process is unknown [17]. Direct observation of nanopores forming and closing could provide a significant advance in the understanding of cell membranes. These dynamics can only be characterized with nanosecond time resolution, which is beyond the range of existing technology. The use of quantum technology to enter the high frequency regime may therefore enable this observation, and provide new insight into the structure of a cell membrane.

Furthermore, there is currently debate in the neurobiology community regarding the contribution of acoustic waves, rather than pure electrical signaling, to the propagation of signals down axons in nerve cells [5]. Although neural signaling

undoubtedly includes propagating electrical excitations, this excitation is accompanied by many other measurable effects, including rapid heating and cooling and volume changes in the axon [159, 161], stimulation of unconnected cells nearby [58], and changes in the axon's optical properties [160]. Although these changes have been shown to co-propagate with the electric signal [161], and both electrical and mechanical stimulation can produce neural activity [28, 39, 140], the biological role of these mechanical effects is not yet known. Some hypothesize that neural signaling occurs via transmission of a electric-acoustic soliton, with the electric pulse a side-effect of the mechanical signal [78, 79], while others maintain that the mechanical effects are a side-effect of the electrical signal [5]. This question lies at the very heart of neuroscience, which makes it extremely important to test the predictions of the hypotheses. The predicted mechanical vibrations, and particularly the dissipation, differ significantly between the models [4]. Although direct imaging allows some characterization of the mechanical excitation, it lacks the precision and bandwidth required to distinguish between the competing models. Laser tracking has also been used as this offers far greater sensitivity [28, 53, 54], though this approach is limited by the extreme photosensitivity of nerve cells [190], and observations to date have also lacked the required precision. By using quantum resources to improve the sensitivity, it may be possible to finally resolve the role of mechanical excitations in neural activity.

Quantum enhanced particle tracking could also hold important applications in investigations of the non-Brownian thermal motion of particles in water on very short timescales, as described earlier in Sect. 1.3.1. Observation of the instantaneous velocity of a particle in liquid requires exquisite precision, and was only reported in 2014 [93]. The ability to access this regime allows characterization of single-particle thermodynamic properties, which could provide new insights into non-equilibrium processes [93]. Furthermore, when a particle moves in liquid, it carries with it an envelope of the surrounding fluid [86]. At very fast time-scales the envelope motion decouples from the particle motion in a manner governed by the compressibility of the fluid [191]. Although water is close to incompressible, it does have an elastic component, which is required for the propagation of sound waves [59]. If the decoupling of the fluid envelope could be measured, this would both test longstanding theoretical predictions and allow a novel way of probing the mechanical properties of the liquid. The use of quantum correlated light could allow the improvement in sensitivity required to observe these phenomena.

As we see here, there are many important applications which could benefit from the use of quantum enhanced particle tracking. More generally, non-classically correlated light can also enhance a range of different biological measurements techniques, such as two-photon microscopy, super-resolution imaging, and absorption imaging [27, 66]. By demonstrating quantum enhancement in optical tweezers, we hope to lead the way for a broad range of biological applications of non-classically correlated light.

References

1. J. Aasi et al., Enhanced sensitivity of the LIGO gravitational wave detector by using squeezed states of light. Nat. Photon. **7**(8), 613–619 (2013)
2. J. Abadie et al., A gravitational wave observatory operating beyond the quantum shot-noise limit. Nat. Phys. **7**, 962–965 (2011)
3. I. Afek, O. Ambar, Y. Silberberg, High-NOON states by mixing quantum and classical light. Science **328**(5980), 879–881 (2010)
4. S.S. Andersen, A.D. Jackson, T. Heimburg, Towards a thermodynamic theory of nerve pulse propagation. Prog. Neurobiol. **88**(2), 104–113 (2009)
5. R. Appali, S. Petersen, U. v. Rienen, A comparision of Hodgkin-Huxley and soliton neural theories. Adv. Radio Sci. **8**(6), 75–79 (2010)
6. Y. Arita, M. Mazilu, K. Dholakia, Laser-induced rotation and cooling of a trapped microgyroscope in vacuum. Nat. Commun. **4**, 2374 (2013)
7. A. Ashkin, Forces of a single-beam gradient laser trap on a dielectric sphere in the ray optics regime. Biophys. J. **61**(2), 569–582 (1992)
8. A. Ashkin, J. Dziedzic, Optical trapping and manipulation of viruses and bacteria. Science **235**, 1517–1520 (1987)
9. A. Ashkin, J. Dziedzic, Internal cell manipulation using infrared laser traps. Proc. Natl. Acad. Sci. USA **86**(20), 7914–7918 (1989)
10. A. Ashkin, J.M. Dziedzic, J.E. Bjorkholm, S. Chu, Observation of a single-beam gradient force optical trap for dielectric particles. Opt. Lett. **11**(5), 288–290 (1986)
11. A. Ashkin, J. Dziedzic, T. Yamane, Optical trapping and manipulation of single cells using infrared laser beams. Nature **330**(6150), 769–771 (1987)
12. A. Ashkin, K. Schütze, J. Dziedzic, U. Euteneuer, M. Schliwa, Force generation of organelle transport measured in vivo by an infrared laser trap. Nature **348**, 346–348 (1990)
13. M. Atakhorrami, High bandwidth microrheology of complex fluids and biopolymer networks. Ph.D. thesis, Vrije Universiteit, Amsterdam, 2006
14. M. Atakhorrami, C. Schmidt, High-bandwidth one-and two-particle microrheology in solutions of wormlike micelles. Rheol. Acta **45**(4), 449–456 (2006)
15. M. Auzinsh, D. Budker, D. Kimball, S. Rochester, J. Stalnaker, A. Sushkov, V. Yashchuk, Can a quantum nondemolition measurement improve the sensitivity of an atomic magnetometer? Phys. Rev. Lett. **93**(17), 173002 (2004)
16. A. Bassi, K. Lochan, S. Satin, T.P. Singh, H. Ulbricht, Models of wave-function collapse, underlying theories, and experimental tests. Rev. Mod. Phys. **85**(2), 471 (2013)
17. H.T. Beier, C.C. Roth, G.P. Tolstykh, B.L. Ibey, Resolving the spatial kinetics of electric pulse-induced ion release. Biochem. Biophys. Res. Commun. **423**(4), 863–866 (2012)
18. S.J. Benkovic, J. Theriot, D. Ringe, Open questions-in brief: beyond-omics, missing motor proteins, and getting from molecules to organisms. BMC Biol. **11**(1), 8 (2013)
19. C.H. Bennett, D.P. DiVincenzo, Quantum information and computation. Nature **404**(6775), 247–255 (2000)
20. K. Berg-Sørensen, H. Flyvbjerg, Power spectrum analysis for optical tweezers. Rev. Sci. Instrum. **75**(3), 594–612 (2004)
21. G. Bison, R. Wynands, A. Weis, Dynamical mapping of the human cardiomagnetic field with a room-temperature, laser-optical sensor. Opt. Express **11**(3), 904–909 (2003)
22. G. Bison, R. Wynands, A. Weis, A laser-pumped magnetometer for the mapping of human cardiomagnetic fields. Appl. Phys. B **76**(3), 325–328 (2003)
23. G. Bison, N. Castagna, A. Hofer, P. Knowles, J.-L. Schenker, M. Kasprzak, H. Saudan, A. Weis, A room temperature 19-channel magnetic field mapping device for cardiac signals. Appl. Phys. Lett. **95**(17), 173701 (2009)
24. S.M. Block, L.S. Goldstein, B.J. Schnapp, Bead movement by single kinesin molecules studied with optical tweezers. Nature **348**, 348–352 (1990)
25. R.W. Bowman, M.J. Padgett, Optical trapping and binding. Rep. Prog. Phys. **76**(2), 026401 (2013)

26. R. Brau, J. Ferrer, H. Lee, C. Castro, B. Tam, P. Tarsa, P. Matsudaira, M. Boyce, R. Kamm, M. Lang, Passive and active microrheology with optical tweezers. J. Opt. A: Pure Appl. Opt **9**(8), S103–S112 (2007)
27. G. Brida, M. Genovese, I.R. Berchera, Experimental realization of sub-shot-noise quantum imaging. Nat. Photon. **4**, 227–230 (2010)
28. W.E. Brownell, F. Qian, B. Anvari, Cell membrane tethers generate mechanical force in response to electrical stimulation. Biophys. J. **99**(3), 845–852 (2010)
29. Z. Bryant, F.C. Oberstrass, A. Basu, Recent developments in single-molecule DNA mechanics. Curr. Opin. Struct. Biol. **22**(3), 304–312 (2012)
30. Z. Bryant, M.D. Stone, J. Gore, S.B. Smith, N.R. Cozzarelli, C. Bustamante, Structural transitions and elasticity from torque measurements on DNA. Nature **424**(6946), 338–341 (2003)
31. M. Buchanan, M. Atakhorrami, J.F. Palierne, F.C. MacKintosh, C.F. Schmidt, High-frequency microrheology of wormlike micelles. Phys. Rev. E **72**, 011504 (2005)
32. D. Budker, M. Romalis, Optical magnetometry. Nat. Phys. **3**(4), 227–234 (2007)
33. C. Bustamante, Unfolding single RNA molecules: bridging the gap between equilibrium and non-equilibrium statistical thermodynamics. Q. Rev. Biophys. **38**(4), 291–301 (2005)
34. C. Bustamante, Z. Bryant, S.B. Smith, Ten years of tension: single-molecule DNA mechanics. Nature **421**(6921), 423–427 (2003)
35. C. Bustamante, Y. Chemla, N. Forde, D. Izhaky, Mechanical processes in biochemistry. Annu. Rev. Biochem. **73**(1), 705–748 (2004)
36. D. Carberry, J.C. Reid, G. Wang, E.M. Sevick, D.J. Searles, D.J. Evans, Fluctuations and irreversibility: an experimental demonstration of a second-law-like theorem using a colloidal particle held in an optical trap. Phys. Rev. Lett. **92**(14), 140601 (2004)
37. C.M. Caves, Quantum-mechanical noise in an interferometer. Phys. Rev. D **23**, 1693–1708 (1981)
38. D.E. Chang, C.A. Regal, S.B. Papp, D.J. Wilson, J. Ye, O. Painter, H.J. Kimble, P. Zoller, Cavity opto-mechanics using an optically levitated nanosphere. Proc. Natl. Acad. Sci. USA **107**(3), 1005–1010 (2010)
39. A.C. Charles, J.E. Merrill, E.R. Dirksen, M.J. Sandersont, Intercellular signaling in glial cells: calcium waves and oscillations in response to mechanical stimulation and glutamate. Neuron **6**(6), 983–992 (1991)
40. I. Chavez, R. Huang, K. Henderson, E.-L. Florin, M.G. Raizen, Development of a fast position-sensitive laser beam detector. Rev. Sci. Instrum. **79**, 105104 (2008)
41. J. Clarke, SQUID fundamentals, in *SQUID Sensors: Fundamentals, Fabrication and Applications* (Springer, 1996), pp. 1–62
42. S. Condamin, V. Tejedor, R. Voituriez, O. Bénichou, J. Klafter, Probing microscopic origins of confined subdiffusion by first-passage observables. Proc. Natl. Acad. Sci. USA **105**(15), 5675–5680 (2008)
43. E. Corsini, V. Acosta, N. Baddour, J. Higbie, B. Lester, P. Licht, B. Patton, M. Prouty, D. Budker, Search for plant biomagnetism with a sensitive atomic magnetometer. J. Appl. Phys. **109**, 074701 (2011)
44. A. Crespi, M. Lobino, J. Matthews, A. Politi, C. Neal, R. Ramponi, R. Osellame, J. O'Brien, Measuring protein concentration with entangled photons. Appl. Phys. Lett. **100**(23), 233704 (2012)
45. J.-M. Cui, F.-W. Sun, X.-D. Chen, Z.-J. Gong, G.-C. Guo, Quantum statistical imaging of particles without restriction of the diffraction limit. Phys. Rev. Lett. **110**(15), 153901 (2013)
46. H. Dang, A. Maloof, M. Romalis, Ultrahigh sensitivity magnetic field and magnetization measurements with an atomic magnetometer. Appl. Phys. Lett. **97**(15), 151110 (2010)
47. R. Demkowicz-Dobrzański, J. Kołodyński, M. Guţă, The elusive Heisenberg limit in quantum-enhanced metrology. Nat. Commun. **3**, 1063 (2012)
48. J.P. Dowling, Quantum optical metrology-the lowdown on high-n00n states. Contemp. Phys. **49**(2), 125–143 (2008)
49. E. Dufresne, T. Squires, M. Brenner, D. Grier, Hydrodynamic coupling of two Brownian spheres to a planar surface. Phys. Rev. Lett. **85**(15), 3317–3320 (2000)

50. T. Eberle, S. Steinlechner, J. Bauchrowitz, V. Händchen, H. Vahlbruch, M. Mehmet, H. Müller-Ebhardt, R. Schnabel, Quantum enhancement of the zero-area Sagnac interferometer topology for gravitational wave detection. Phys. Rev. Lett. **104**(25), 251102 (2010)
51. D. Engström, M.C. Varney, M. Persson, R.P. Trivedi, K.A. Bertness, M. Goksör, I.I. Smalyukh, Unconventional structure-assisted optical manipulation of high-index nanowires in liquid crystals. Opt. Express **20**, 7741–8 (2012)
52. B. Essevaz-Roulet, U. Bockelmann, F. Heslot, Mechanical separation of the complementary strands of DNA. Proc. Natl. Acad. Sci. USA **94**(22), 11935–11940 (1997)
53. C. Fang-Yen, M.C. Chu, H.S. Seung, R.R. Dasari, M.S. Feld, Noncontact measurement of nerve displacement during action potential with a dual-beam low-coherence interferometer. Opt. Lett. **29**(17), 2028–2030 (2004)
54. C. Fang-Yen, S. Oh, Y. Park, W. Choi, S. Song, H.S. Seung, R.R. Dasari, M.S. Feld, Imaging voltage-dependent cell motions with heterodyne Mach-Zehnder phase microscopy. Opt. Lett. **32**(11), 1572–1574 (2007)
55. H.-B. Fei, B.M. Jost, S. Popescu, B.E. Saleh, M.C. Teich, Entanglement-induced two-photon transparency. Phys. Rev. Lett. **78**(9), 1679–1682 (1997)
56. R. Fenici, D. Brisinda, A.M. Meloni, Clinical application of magnetocardiography. Exp. Rev. Mol. Diagn. **5**, 291–313 (2005)
57. A.F. Fercher, W. Drexler, C.K. Hitzenberger, T. Lasser, Optical coherence tomography-principles and applications. Rep. Prog. Phys. **66**(2), 239 (2003)
58. R.D. Fields, Y. Ni, Nonsynaptic communication through ATP release from volume-activated anion channels in axons. Sci. Signal. **3**(142), ra73 (2010)
59. R.A. Fine, F.J. Millero, Compressibility of water as a function of temperature and pressure. J. Chem. Phys. **59**, 5529 (1973)
60. J.T. Finer, R.M. Simmons, J.A. Spudich, Single myosin molecule mechanics: piconewton forces and nanometre steps. Nature **368**, 113–119 (1994)
61. M. Fox, *Quantum Optics: An Introduction*, vol. 15 (Oxford University Press, Oxford, 2006)
62. T. Franosch, M. Grimm, M. Belushkin, F.M. Mor, G. Foffi, L. Forró, S. Jeney, Resonances arising from hydrodynamic memory in Brownian motion. Nature **478**, 85–88 (2011)
63. H. Frauenfelder, P. Fenimore, G. Chen, B. McMahon, Protein folding is slaved to solvent motions. Proc. Natl. Acad. Sci. USA **103**(42), 15469–15472 (2006)
64. J.G. Fujimoto, Optical coherence tomography for ultrahigh resolution in vivo imaging. Nat. Biotechnol. **21**(11), 1361–1367 (2003)
65. A.A. Geraci, S.B. Papp, J. Kitching, Short-range force detection using optically cooled levitated microspheres. Phys. Rev. Lett. **105**, 101101 (2010)
66. V. Giovannetti, S. Lloyd, L. Maccone, Quantum-enhanced measurements: beating the standard quantum limit. Science **306**(5700), 1330–1336 (2004)
67. V. Giovannetti, S. Lloyd, L. Maccone, Quantum metrology. Phys. Rev. Lett. **96**(1), 010401 (2006)
68. N. Gisin, G. Ribordy, W. Tittel, H. Zbinden, Quantum cryptography. Rev. Mod. Phys. **74**(1), 145–195 (2002)
69. F. Gittes, C.F. Schmidt, Interference model for back-focal-plane displacement detection in optical tweezers. Opt. Lett. **23**(1), 7–9 (1998)
70. F. Gittes, B. Schnurr, P. Olmsted, F. MacKintosh, C. Schmidt, Microscopic viscoelasticity: shear moduli of soft materials determined from thermal fluctuations. Phys. Rev. Lett. **79**(17), 3286–3289 (1997)
71. W.J. Greenleaf, S.M. Block, Single-molecule, motion-based DNA sequencing using RNA polymerase. Science **313**(5788), 801 (2006)
72. H. Grote, K. Danzmann, K. Dooley, R. Schnabel, J. Slutsky, H. Vahlbruch, First long-term application of squeezed states of light in a gravitational-wave observatory. Phys. Rev. Lett. **110**(18), 181101 (2013)
73. G. Guigas, C. Kalla, M. Weiss, Probing the nanoscale viscoelasticity of intracellular fluids in living cells. Biophys. J. **93**(1), 316–323 (2007)

74. G. Guigas, M. Weiss, Sampling the cell with anomalous diffusion-the discovery of slowness. Biophys. J. **94**(1), 90–94 (2008)
75. A.R. Guzman, M.R. Harpham, Ö. Süzer, M.M. Haley, T.G. Goodson III, Spatial control of entangled two-photon absorption with organic chromophores. J. Am. Chem. Soc. **132**(23), 7840–7841 (2010)
76. M. Hämäläinen, R. Hari, R.J. Ilmoniemi, J. Knuutila, O.V. Lounasmaa, Magnetoencephalographytheory, instrumentation, and applications to noninvasive studies of the working human brain. Rev. Mod. Phys. **65**(2), 413 (1993)
77. Y. Harada, T. Asakura, Radiation forces on a dielectric sphere in the Rayleigh scattering regime. Opt. Commun. **124**(5–6), 529–541 (1996)
78. T. Heimburg, A.D. Jackson, On soliton propagation in biomembranes and nerves. Proc. Natl. Acad. Sci. USA **102**(28), 9790–9795 (2005)
79. T. Heimburg, A.D. Jackson, The thermodynamics of general anesthesia. Biophys. J. **92**(9), 3159–3165 (2007)
80. F. Helmchen, W. Denk, Deep tissue two-photon microscopy. Nat. Methods **2**(12), 932–940 (2005)
81. W.R. Hendee, C.J. Morgan, Magnetic resonance imaging part I-physical principles. West. J. Med. **141**(4), 491 (1984)
82. U.B. Hoff, G.I. Harris, L.S. Madsen, H. Kerdoncuff, M. Lassen, B.M. Nielsen, W.P. Bowen, U.L. Andersen, Quantum-enhanced micromechanical displacement sensitivity. Opt. Lett. **38**(9), 1413–1415 (2013)
83. C. Hong, Z. Ou, L. Mandel, Measurement of subpicosecond time intervals between two photons by interference. Phys. Rev. Lett. **59**(18), 2044–2046 (1987)
84. T. Horrom, R. Singh, J.P. Dowling, E.E. Mikhailov, Quantum-enhanced magnetometer with low-frequency squeezing. Phys. Rev. A **86**(2), 023803 (2012)
85. D. Huang, E.A. Swanson, C.P. Lin, J.S. Schuman, W.G. Stinson, W. Chang, M.R. Hee, T. Flotte, K. Gregory, C.A. Puliafito et al., Optical coherence tomography. Science **254**(5035), 1178–1181 (1991)
86. R. Huang, I. Chavez, K.M. Taute, B. Lukić, S. Jeney, M.G. Raizen, E.-L. Florin, Direct observation of the full transition from ballistic to diffusive Brownian motion in a liquid. Nat. Phys. **7**, 576–580 (2011)
87. D.R. Huffman, C.F. Bohren, *Absorption and Scattering of Light by Small Particles* (Wiley-VCH, New York, 2008)
88. B.L. Ibey, C.C. Roth, A.G. Pakhomov, J.A. Bernhard, G.J. Wilmink, O.N. Pakhomova, Dose-dependent thresholds of 10-ns electric pulse induced plasma membrane disruption and cytotoxicity in multiple cell lines. PLoS ONE **6**(1), e15642 (2011)
89. B. Jagatap, W.J. Meath, On the competition between permanent dipole and virtual state two-photon excitation mechanisms, and two-photon optical excitation pathways, in molecular excitation. Chem. Phys. Lett. **258**(1), 293–300 (1996)
90. A. Jannasch, M. Mahamdeh, E. Schäffer, Inertial effects of a small Brownian particle cause a colored power spectral density of thermal noise. Phys. Rev. Lett. **107**(22), 228301 (2011)
91. C.N. Johnson, P. Schwindt, M. Weisend, Multi-sensor magnetoencephalography with atomic magnetometers. Phys. Med. Biol. **58**(17), 6065 (2013)
92. Z. Kam, Microscopic differential interference contrast image processing by line integration (LID) and deconvolution. Bioimaging **6**(4), 166–176 (1998)
93. S. Kheifets, A. Simha, K. Melin, T. Li, M.G. Raizen, Observation of Brownian motion in liquids at short times:iInstantaneous velocity and memory loss. Science **343**(6178), 1493–1496 (2014)
94. N. Kiesel, F. Blaser, U. Delić, D. Grass, R. Kaltenbaek, M. Aspelmeyer, Cavity cooling of an optically levitated submicron particle. Proc. Natl. Acad. Sci. USA **110**, 14180–14185 (2013)
95. G.H. Koenderink, M. Atakhorrami, F.C. MacKintosh, C.F. Schmidt, High-frequency stress relaxation in semiflexible polymer solutions and networks. Phys. Rev. Lett. **96**, 138307 (2006)
96. M. Kolobov, C. Fabre, Quantum limits on optical resolution. Phys. Rev. Lett. **85**(18), 3789–3792 (2000)

97. I. Kominis, Sub-shot-noise magnetometry with a correlated spin-relaxation dominated alkali-metal vapor. Phys. Rev. Lett. **100**(7), 073002 (2008)
98. I. Kominis, T. Kornack, J. Allred, M. Romalis, A subfemtotesla multichannel atomic magnetometer. Nature **422**(6932), 596–599 (2003)
99. J. Kortmann, F. Narberhaus, Bacterial RNA thermometers: molecular zippers and switches. Nat. Rev. Microbiol. **10**(4), 255–265 (2012)
100. M. Koschorreck, M. Napolitano, B. Dubost, M. Mitchell, Sub-projection-noise sensitivity in broadband atomic magnetometry. Phys. Rev. Lett. **104**(9), 093602 (2010)
101. D.E. Kuhl, R.Q. Edwards, Image separation radioisotope scanning. Radiology (US) **80** (1963)
102. P. Kukura, H. Ewers, C. Müller, A. Renn, A. Helenius, V. Sandoghdar, High-speed nanoscopic tracking of the position and orientation of a single virus. Nat. Methods **6**, 923 (2009)
103. S.C. Kuo, M.P. Sheetz, Force of single kinesin molecules measured with optical tweezers. Science **260**(5105), 232–234 (1993)
104. V. Kurz, E.M. Nelson, J. Shim, G. Timp, Direct visualization of single-molecule translocations through synthetic nanopores comparable in size to a molecule. ACS Nano **7**(5), 4057–4069 (2013)
105. M.F. Langhorst, J. Schaffer, B. Goetze, Structure brings clarity: structured illumination microscopy in cell biology. Biotechnol. J. **4**(6), 858–865 (2009)
106. J. Lavoie, R. Kaltenbaek, K.J. Resch, Quantum-optical coherence tomography with classical light. Opt. Express **17**(5), 3818–3825 (2009)
107. D.-I. Lee, T. Goodson, Entangled photon absorption in an organic porphyrin dendrimer. J. Phys. Chem. B **110**(51), 25582–25585 (2006)
108. G.U. Lee, L.A. Chrisey, R.J. Colton, Direct measurement of the forces between complementary strands of DNA. Science **266**(5186), 771–773 (1994)
109. T. Li, S. Kheifets, D. Medellin, M.G. Raizen, Measurement of the instantaneous velocity of a Brownian particle. Science **328**(5986), 1673–1675 (2010)
110. T. Li, S. Kheifets, M.G. Raizen, Millikelvin cooling of an optically trapped microsphere in vacuum. Nat. Phys. **7**, 527–530 (2011)
111. T. Li, M.G. Raizen, Brownian motion at short time scales. Ann. Phys. **525**, 281–295 (2013)
112. B. Lukić, S. Jeney, C. Tischer, A.J. Kulik, L. Forró, E.-L. Florin, Direct observation of nondiffusive motion of a Brownian particle. Phys. Rev. Lett. **95**, 160601 (2005)
113. T. Mason, K. Ganesan, J. Van Zanten, D. Wirtz, S. Kuo, Particle tracking microrheology of complex fluids. Phys. Rev. Lett. **79**(17), 3282–3285 (1997)
114. L.I. McCann, M. Dykman, B. Golding, Thermally activated transitions in a bistable three-dimensional optical trap. Nature **402**(6763), 785–787 (1999)
115. M. Mehmet, H. Vahlbruch, N. Lastzka, K. Danzmann, R. Schnabel, Observation of squeezed states with strong photon-number oscillations. Phys. Rev. A **81**(1), 013814 (2010)
116. J.-C. Meiners, S.R. Quake, Direct measurement of hydrodynamic cross correlations between two particles in an external potential. Phys. Rev. Lett. **82**(10), 2211–2214 (1999)
117. J.R. Moffitt, Y.R. Chemla, S.B. Smith, C. Bustamante, Recent advances in optical tweezers. Annu. Rev. Biochem. **77**, 205–228 (2008)
118. T. Nagata, R. Okamoto, J. O'Brien, K. Sasaki, S. Takeuchi, Beating the standard quantum limit with four-entangled photons. Science **316**(5825), 726–729 (2007)
119. M.B. Nasr, B.E.A. Saleh, A.V. Sergienko, M.C. Teich, Demonstration of dispersion-canceled quantum-optical coherence tomography. Phys. Rev. Lett. **91**, 083601 (2003)
120. M.B. Nasr, B.E. Saleh, A.V. Sergienko, M.C. Teich, Dispersion-cancelled and dispersion-sensitive quantum optical coherence tomography. Opt. Express **12**(7), 1353–1362 (2004)
121. M.B. Nasr, D.P. Goode, N. Nguyen, G. Rong, L. Yang, B.M. Reinhard, B.E. Saleh, M.C. Teich, Quantum optical coherence tomography of a biological sample. Opt. Commun. **282**(6), 1154–1159 (2009)
122. K.C. Neuman, E.H. Chadd, G.F. Liou, K. Bergman, S.M. Block, Characterization of photodamage to Escherichia coli in optical traps. Biophys. J. **77**, 2856–2863 (1999)
123. T. Nieminen, V. Loke, A. Stilgoe, G. Knöner, A. Brańczyk, N. Heckenberg, H. Rubinsztein-Dunlop, Optical tweezers computational toolbox. J. Opt. A: Pure Appl. Opt **9**(8), S196 (2007)

124. T.A. Nieminen, V.L.Y. Loke, A.B. Stilgoe, Y. Hu, G. Knoener, A.M. Brańczyk, Optical tweezers toolbox 1.3 (2013), http://www.physics.uq.edu.au/people/nieminen/software.html
125. T. Ono, R. Okamoto, S. Takeuchi, An entanglement-enhanced microscope. Nat. Commun. **4**, 2426 (2013)
126. A.G. Pakhomov, R. Shevin, J.A. White, J.F. Kolb, O.N. Pakhomova, R.P. Joshi, K.H. Schoenbach, Membrane permeabilization and cell damage by ultrashort electric field shocks. Arch. Biochem. Biophys. **465**(1), 109–118 (2007)
127. A.G. Pakhomov, A.M. Bowman, B.L. Ibey, F.M. Andre, O.N. Pakhomova, K.H. Schoenbach, Lipid nanopores can form a stable, ion channel-like conduction pathway in cell membrane. Biochem. Biophys. Res. Commun. **385**(2), 181–186 (2009)
128. S.C. Park, M.K. Park, M.G. Kang, Super-resolution image reconstruction: a technical overview. IEEE Signal Process. Mag. **20**(3), 21–36 (2003)
129. J. Peřina, B.E. Saleh, M.C. Teich et al., Multiphoton absorption cross section and virtual-state spectroscopy for the entangled n-photon state. Phys. Rev. A **57**(5), 3972 (1998)
130. G. Perkins, R. Jones, Hydrodynamic interaction of a spherical particle with a planar boundary: II. Hard wall. Phys. A **189**(3), 447–477 (1992)
131. E.J. Peterman, F. Gittes, C.F. Schmidt, Laser-induced heating in optical traps. Biophys. J. **84**(2), 1308–1316 (2003)
132. E.J. Peterman, M.A. van Dijk, L.C. Kapitein, C.F. Schmidt, Extending the bandwidth of optical-tweezers interferometry. Rev. Sci. Instrum. **74**(7), 3246–3249 (2003)
133. M.E. Phelps, Positron emission tomography provides molecular imaging of biological processes. Proc. Natl. Acad. Sci. USA **97**(16), 9226–9233 (2000)
134. D. Preece, R. Warren, R. Evans, G.M. Gibson, M.J. Padgett, J.M. Cooper, M. Tassieri, Optical tweezers: wideband microrheology. J. Opt. **13**(4), 044022 (2011)
135. S. Rankowitz, J. Robertson, W. Higinbotham, M. Rosenblum, Positron scanner for locating brain tumors. Technical report, Brookhaven National Lab., (BNL) Upton, NY (1961)
136. A. Rohrbach, E. Stelzer, Trapping forces, force constants, and potential depths for dielectric spheres in the presence of spherical aberrations. Appl. Opt. **41**(13), 2494–2507 (2002)
137. O. Roslyak, C.A. Marx, S. Mukamel, Nonlinear spectroscopy with entangled photons: manipulating quantum pathways of matter. Phys. Rev. A **79**(3), 033832 (2009)
138. M.J. Rust, M. Bates, X. Zhuang, Sub-diffraction-limit imaging by stochastic optical reconstruction microscopy (STORM). Nat. Methods **3**(10), 793–796 (2006)
139. B.E. Saleh, B.M. Jost, H.-B. Fei, M.C. Teich, Entangled-photon virtual-state spectroscopy. Phys. Rev. Lett. **80**(16), 3483 (1998)
140. M.J. Sanderson, A. Charles, E.R. Dirksen, Mechanical stimulation and intercellular communication increases intracellular Ca2+ in epithelial cells. Cell Regul. **1**(8), 585–596 (1990)
141. I. Savukov, V. Zotev, P. Volegov, M. Espy, A. Matlashov, J. Gomez, R. Kraus Jr, MRI with an atomic magnetometer suitable for practical imaging applications. J. Magn. Res. **199**(2), 188–191 (2009)
142. R. Schmidt, C.A. Wurm, S. Jakobs, J. Engelhardt, A. Egner, S.W. Hell, Spherical nanosized focal spot unravels the interior of cells. Nat. Methods **5**(6), 539–544 (2008)
143. J.M. Schmitt, Optical coherence tomography (OCT): a review. IEEE J. Sel. Top. Quant. Electron. **5**(4), 1205–1215 (1999)
144. M. Schubert, The attributes of nonclassical light and their mutual relationship. Ann. Phys. **499**(1), 53–60 (1987)
145. O. Schwartz, D. Oron, Improved resolution in fluorescence microscopy using quantum correlations. Phys. Rev. A **85**(3), 33812 (2012)
146. O. Schwartz, J.M. Levitt, R. Tenne, S. Itzhakov, Z. Deutsch, D. Oron, Superresolution microscopy with quantum emitters. Nano Lett. **13**(12), 5832–5836 (2013)
147. C. Selhuber-Unkel, P. Yde, K. Berg-Sørensen, L.B. Oddershede, Variety in intracellular diffusion during the cell cycle. Phys. Biol. **6**(2), 025015 (2009)
148. E.N. Senning, A.H. Marcus, Actin polymerization driven mitochondrial transport in mating S. cerevisiae. Proc. Natl. Acad. Sci. USA **107**, 721–725 (2010)

149. R. Sewell, M. Koschorreck, M. Napolitano, B. Dubost, N. Behbood, M. Mitchell, Magnetic sensitivity beyond the projection noise limit by spin squeezing. Phys. Rev. Lett. **109**(25), 253605 (2012)
150. V. Shah, G. Vasilakis, M. Romalis, High bandwidth atomic magnetometery with continuous quantum nondemolition measurements. Phys. Rev. Lett. **104**(1), 013601 (2010)
151. D. Sheng, S. Li, N. Dural, M. Romalis, Subfemtotesla scalar atomic magnetometry using multipass cells. Phys. Rev. Lett. **110**(16), 160802 (2013)
152. H. Shroff, C.G. Galbraith, J.A. Galbraith, E. Betzig, Live-cell photoactivated localization microscopy of nanoscale adhesion dynamics. Nat. Methods **5**(5), 417–423 (2008)
153. R. Slusher, Quantum optics in the 80's. Opt. Photonics News **1**(12), 27–30 (1990)
154. R. Slusher, A. Porta, B. Yurke, P. Grangier, Squeezed states, interferometric limits and back-action evasion, in *Frequency Standards and Metrology*, ed. by A. Marchi (Springer, Berlin Heidelberg, 1989), pp. 343–348
155. S.B. Smith, Y. Cui, C. Bustamante, Overstretching B-DNA: the elastic response of individual double-stranded and single-stranded DNA molecules. Science **271**(5250), 795–799 (1996)
156. M. Stefszky, C. Mow-Lowry, S. Chua, D. Shaddock, B. Buchler, H. Vahlbruch, A. Khalaidovski, R. Schnabel, P. Lam, D. McClelland, Balanced homodyne detection of optical quantum states at audio-band frequencies and below. Class. Quant. Grav. **29**(14), 145015 (2012)
157. O. Stiehl, K. Weidner-Hertrampf, M. Weiss, Kinetics of conformational fluctuations in dna hairpin-loops in crowded fluids. New J. Phys. **15**(11), 113010 (2013)
158. K. Svoboda, C.F. Schmidt, B.J. Schnapp, S.M. Block, Direct observation of kinesin stepping by optical trapping interferometry. Nature **365**, 721 (1993)
159. I. Tasaki, T. Nakaye, Heat generated by the dark-adapted squid retina in response to light pulses. Science **227**(4687), 654–655 (1985)
160. I. Tasaki, A. Watanabe, R. Sandlin, L. Carnay, Changes in fluorescence, turbidity, and birefringence associated with nerve excitation. Proc. Natl. Acad. Sci. USA **61**(3), 883 (1968)
161. I. Tasaki, K. Kusano, P. Byrne, Rapid mechanical and thermal changes in the garfish olfactory nerve associated with a propagated impulse. Biophys. J. **55**(6), 1033–1040 (1989)
162. M. Tassieri, G.M. Gibson, R. Evans, A.M. Yao, R. Warren, M.J. Padgett, J.M. Cooper, Measuring storage and loss moduli using optical tweezers: Broadband microrheology. Phys. Rev. E **81**, 026308 (2010)
163. M.A. Taylor, W.P. Bowen, Quantum noise in optical tweezers. J. Phys.: Conf. Ser. **467**, 012007 (2013)
164. M.A. Taylor, W.P. Bowen, Quantum metrology and its application in biology. arXiv:1409.0950, 2014
165. M.A. Taylor, J. Janousek, V. Daria, J. Knittel, B. Hage, H.-A. Bachor, W.P. Bowen, Biological measurement beyond the quantum limit. Nat. Photon. **7**, 229–233 (2013)
166. M.A. Taylor, J. Janousek, V. Daria, J. Knittel, B. Hage, H.-A. Bachor, W.P. Bowen, Subdiffraction-limited quantum imaging within a living cell. Phys. Rev. X **4**(1), 011017 (2014)
167. M.C. Teich, B.E. Saleh, Squeezed and antibunched light. Phys. Today **43**, 26–34 (1990)
168. M.C. Teich, B.E. Saleh, Entangled-photon microscopy. Česk. Čas. Fyz. **47**, 3–8 (1997)
169. M.C. Teich, B.E. Saleh, F.N. Wong, J.H. Shapiro, Variations on the theme of quantum optical coherence tomography: a review. Quantum Inf. Process. **11**(4), 903–923 (2012)
170. I.M. Tolić-Nørrelykke, E.-L. Munteanu, G. Thon, L. Oddershede, K. Berg-Sørensen, Anomalous diffusion in living yeast cells. Phys. Rev. Lett. **93**, 078102 (2004)
171. N. Treps, U. Andersen, B. Buchler, P.K. Lam, A. Maître, H.-A. Bachor, C. Fabre, Surpassing the standard quantum limit for optical imaging using nonclassical multimode light. Phys. Rev. Lett. **88**, 203601 (2002)
172. N. Treps, N. Grosse, W.P. Bowen, C. Fabre, H.-A. Bachor, P.K. Lam, A quantum laser pointer. Science **301**, 940–943 (2003)
173. Y. Tseng, J. Lee, T. Kole, I. Jiang, D. Wirtz, Micro-organization and visco-elasticity of the interphase nucleus revealed by particle nanotracking. J. Cell Sci. **117**(10), 2159–2167 (2004)

174. F. Uhlmann, Open questions: chromosome condensation-why does a chromosome look like a chromosome. BMC Biol. **11**(9), 9 (2013)
175. L. Upton, M.R. Harpham, O. Suzer, M. Richter, S. Mukamel, T.G. Goodson III, Optically excited entangled states in organic molecules illuminate the dark. J. Phys. Chem. Lett. **4**, 2046–2052 (2013)
176. V. Vijayan, R. Zuzow, E.K. O'Shea, Oscillations in supercoiling drive circadian gene expression in cyanobacteria. Proc. Natl. Acad. Sci. USA **106**(52), 22564–22568 (2009)
177. G. Wang, E.M. Sevick, E. Mittag, D.J. Searles, D.J. Evans, Experimental demonstration of violations of the second law of thermodynamics for small systems and short time scales. Phys. Rev. Lett. **89**(5), 050601 (2002)
178. M.D. Wang, H. Yin, R. Landick, J. Gelles, S.M. Block, Stretching DNA with optical tweezers. Biophys. J. **72**(3), 1335–1346 (1997)
179. W. Wasilewski, K. Jensen, H. Krauter, J.J. Renema, M. Balabas, E.S. Polzik, Quantum noise limited and entanglement-assisted magnetometry. Phys. Rev. Lett. **104**(13), 133601 (2010)
180. K. Watanabe, Y. Ishida, Y. Yamamoto, H. Haus, Y. Lai, Femtosecond squeezed-vacuum-state generation in mode-locked soliton lasers. Phys. Rev. A **42**(9), 5667–5674 (1990)
181. M. Weiss, M. Elsner, F. Kartberg, T. Nilsson, Anomalous subdiffusion is a measure for cytoplasmic crowding in living cells. Biophys. J. **87**(5), 3518–3524 (2004)
182. J. Welzel, Optical coherence tomography in dermatology: a review. Skin Res. Technol. **7**(1), 1–9 (2001)
183. K.I. Willig, R.R. Kellner, R. Medda, B. Hein, S. Jakobs, S.W. Hell, Nanoscale resolution in GFP-based microscopy. Nat. Methods **3**(9), 721–723 (2006)
184. F. Wolfgramm, A. Cerè, F.A. Beduini, A. Predojević, M. Koschorreck, M.W. Mitchell, Squeezed-light optical magnetometry. Phys. Rev. Lett. **105**, 053601 (2010)
185. F. Wolfgramm, C. Vitelli, F.A. Beduini, N. Godbout, M.W. Mitchell, Entanglement-enhanced probing of a delicate material system. Nat. Photon. **7**, 28–32 (2013)
186. H. Xia, A. Ben-Amar, Baranga, D. Hoffman, M. Romalis, Magnetoencephalography with an atomic magnetometer. Appl. Phys. Lett. **89**(21), 211104 (2006)
187. S. Yamada, D. Wirtz, S.C. Kuo, Mechanics of living cells measured by laser tracking microrheology. Biophys. J. **78**, 1736–1747 (2000)
188. A. Yao, M. Tassieri, M. Padgett, J. Cooper, Microrheology with optical tweezers. Lab Chip **9**(17), 2568–2575 (2009)
189. Z. Zhai, J. Gao, Low-frequency phase measurement with high-frequency squeezing. Opt. Express **20**(16), 18173–18179 (2012)
190. F. Zhang, V. Gradinaru, A. Adamantidis, R. Durand, R. Airan, L. De Lecea, K. Deisseroth, Optogenetic interrogation of neural circuits: technology for probing mammalian brain structures. Nat. Protoc. **5**(3), 439–456 (2010)
191. R. Zwanzig, M. Bixon, Compressibility effects in the hydrodynamic theory of Brownian motion. J. Fluid Mech. **69**(part 1), 21–25 (1975)

Part I
The Quantum Limit to Particle Tracking Sensitivity

Part I of this thesis consists of three chapters which characterize in detail the quantum limit to particle tracking sensitivity. The first of these chapters determines the total information content of the measured light, assuming it is in a coherent state. Even a perfect measurement cannot extract more information than this, so it establishes an ultimate limit for classical experiments. This chapter does not, however, determine how the derived limit applies to nonclassically correlated light.

Particle tracking relies on extraction of information from a scattered field, and no particle tracking scheme to date can capture the complex spatial structure of the field which carries this information. As such, real experiments are unable to approach the ultimate limit, and Chap. 3 derives the limit imposed by quantum noise in real experiments. It also establishes how the use of quantum correlated light can improve the measurement sensitivity, and increase the per photon information content of the scattered light. By determining the sensitivity limit in the regime of real experiments, this chapter also provides insight into how to classically optimize the measurement to extract all of the information.

Finally, Chap. 4 presents a computational tool which characterizes particle tracking measurements with the commonly used quadrant detection scheme. This tool allows researchers to theoretically characterize the sensitivity and signal amplitude in their experiments without requiring any technical calculations, and can thus provide a wide range of researchers with the benefit of rigorous theoretical predictions.

Altogether, these theoretical tools allow a thorough characterization of the capabilities of existing technology, how to improve upon this, and what such developments could allow.

Chapter 2
The Total Information Carried by the Light

This chapter theoretically establishes the quantum limit on the total information carried by the collected light, using a simple approach analogous to the Heisenberg microscope. This sets a limit on the sensitivity attainable with a perfect measurement within a given optical setup. This ultimate limit provides a view to what may be possible in future; real experimental systems cannot perfectly capture the complex spatial profile of the scattered light, so the limit derived here is not achieved in any experiment, even when the sensitivity is limited by quantum noise. The theory presented in this chapter was published in the following paper [25].

2.1 Introduction

The position sensitivity in optical tweezers is usually limited by technical noise sources, such as laser noise, electronic noise in the detector, or drifts of mirrors in the experiment. Substantial efforts have been made to minimize such technical sources of error [2, 14, 17]. With sufficient improvements in the technical noise, the sensitivity per photon must eventually be limited by noise due to the quantization of light [13]. The resulting quantum noise limit is an important consequence of quantum mechanics, and is becoming increasingly relevant in experiments. So, what is the precision at the quantum limit? And how closely are experiments approaching this? The quantum limit has previously only been derived in the paraxial optics regime with Rayleigh scattering [3, 23], making the calculated limit inapplicable to most experiments.

Here we follow the simple principles of the Heisenberg Microscope to derive the maximum information content of a scattered optical field, and the corresponding quantum sensitivity limit for particle tracking in optical tweezers. A more detailed analysis of the quantum limit following standard quantum formalism is given in Chap. 3. The simple approach followed here can be straightforwardly applied to particles with arbitrary shape and size, yields analytic solutions in the Rayleigh scattering regime, and allows analysis of a wide range of optical setups.

M. Taylor, *Quantum Microscopy of Biological Systems*, Springer Theses,
DOI 10.1007/978-3-319-18938-3_2

The approach is also relevant to other measurements such as microscopy with fluorescent particles [7]. Our results show that leading experiments are already within two orders of magnitude of the quantum noise limit.

2.2 How Much Information Can a Photon Carry?

Particles in optical tweezers are tracked by measuring their perturbing influence on the electric field as they scatter photons. The scattered light is collected with a high numerical aperture lens, providing an image of the particle. Motion of the particle displaces the image, with the displacement typically measured via a resulting power imbalance on a quadrant detector [9]. Each scattered photon carries some information about the position of the particle from which it scatters. This information is fundamentally constrained by the Heisenberg uncertainty relation, which places a limit on the localization of a photon [8] of $\Delta q_i \geq \frac{\hbar}{2\Delta p_i}$, where Δp_i is the photons momentum uncertainty for each axis $i \in \{x, y, z\}$, z is the direction of optical propagation, x the axis of linear polarization, and $\hbar$ is the reduced Planck constant. Consequently, the location of the scattering event which produced the photon can be established with a minimum uncertainty of Δq_i. This also defines the particle position uncertainty when the scattered field originates from the center of the particle, as is the case for Rayleigh scattering. In general, however, the origin of the scattered field may be offset, lying between the center of the particle and that of the optical trap. For example, if the trapped particle is larger than the trap width and displaced such that its center lies outside the trap, scattering can only originate from the part of the particle contained within the trap field. This leads to a smaller displacement in the scattering origin than that of the particle itself. Such effects increase the absolute uncertainty in the particle position, so that in this case, Δq_i establishes a lower bound on particle position uncertainty.

A useful constraint on momentum uncertainty Δp_i is that it must be within the total photon momentum $p_{ph} = \frac{2\pi n_m \hbar}{\lambda}$, where n_m is the refractive index of the medium[1] and λ is the vacuum wavelength, because

$$\Delta p_i^2 = \langle p_i^2 \rangle - \langle p_i \rangle^2 \leq \sum_{i=x,y,z} \langle p_i^2 \rangle - \langle p_i \rangle^2 = p_{ph}^2 - \sum_{i=x,y,z} \langle p_i \rangle^2. \tag{2.1}$$

We introduce parameters f_i to characterize Δp_i along each axis, such that

$$\Delta p_i = f_i \, p_{ph}, \tag{2.2}$$

[1]The momentum flux of light in a medium has been highly controversial, with Abraham and Minkowski separately deriving it to be $\frac{P_0}{n_m c}$ and $\frac{n_m P_0}{c}$ respectively, and with both forms confirmed by experiments [16]. The different forms have been shown to describe different physical quantities, as described in detail in Ref. [16]. It is the Minkowski form $\frac{n_m P_0}{c}$ which is appropriate to this problem, as this conserves kinetic momentum in light-matter interactions.

leading to the condition $f_x^2 + f_y^2 + f_z^2 \leq 1$. This relation becomes an equality for a photon which is scattered with no preferred direction ($\langle p_i \rangle = 0$). Using this, a position measurement is limited to an uncertainty of

$$\Delta q_i \geq \frac{\lambda}{4\pi n_m f_i}. \tag{2.3}$$

Perhaps unsurprisingly, this condition has a similar form to the Rayleigh criterion [4], which establishes an approximate limit to the resolution of a given microscope system without regard for the exact features of the scattering process. By contrast, Eq. 2.3 provides a rigorous bound which accounts for the scattered field profile. This is crucial for establishing accurate quantum limits to the precision of particle tracking experiments, particularly in the Mie scattering regime where the scattering exhibits both complex spatial structure and resonance phenomena.

In particle tracking experiment, the position of a particle is measured with $\langle N_s \rangle = \kappa \langle N_0 \rangle$ scattered photons, where N_0 incident photons have a scattering probability of κ. Without quantum correlations in the light, each photon detection event provides an independent measurement of the particle position with uncertainty Δq_i. While the standard deviation of these position measurements will be limited to Δq_i, the particle position can be reliably established with a much smaller standard error δq_i given by

$$\delta q_i \geq \frac{\lambda}{4\pi n_m f_i \sqrt{\kappa \langle N_0 \rangle}}. \tag{2.4}$$

This places a lower limit on the particle position sensitivity achievable with uncorrelated photons. To derive the value of this limit, we only need to calculate the scattering probability κ and the momentum parameter f. As these parameters depend on the trapping field, the particle being tracked, and the refractive index of the surrounding medium, they must be evaluated for specific cases, although neither may ever reach unity. The condition that κ and f remain below one places a general lower bound of $\delta q \geq \frac{\lambda}{4\pi n_m \sqrt{N_0}}$ on the precision, which is imposed even if the scattering properties of the particle were cleverly engineered [12] and the measurement performed perfectly; for all realistic situations, the minimum resolvable displacement is larger than this. To determine the limit for real experiments, we evaluate the quantum limit for the common case of homogeneous spheres in a Gaussian trap.

2.3 Optimal Tracking of a Rayleigh Particle

Both the scattering rate κ and momentum distribution parameter f can be calculated analytically in the Rayleigh scattering regime, in which the particle diameter $d \ll \lambda$. If an incident TEM_{00} mode is focused on the particle to a waist of w, the scattering rate is

$$\kappa = \frac{128\pi^4 a^6}{3\lambda^4 w^2}\left(\frac{n_p^2 - n_m^2}{n_p^2 + 2n_m^2}\right)^2, \tag{2.5}$$

where n_p is the refractive index of the particle [11]. For Rayleigh scatterers polarized along the x axis, the scattered photons enter the mode ψ, with amplitude given by

$$|\psi|^2 = \frac{3}{8\pi}\frac{1-(x/r)^2}{r^2}, \tag{2.6}$$

where r is the radial distance [11]. Assuming the photons to be moving radially outward, this mode determines the momentum profile of the scattered light. In most experiments, any scattered photon which reaches the detector has passed through the aperture of an objective. This constrains the momentum range of the detected photons, thereby increasing the position uncertainty. The measurement then only includes the light present in the area A of this aperture. For this measurement, the parameter f is calculated to be

$$f_x^2 = \int |\psi|^2 (x/r)^2 dA - \left(\int |\psi|^2 (x/r) dA\right)^2. \tag{2.7}$$

The second term in Eq. 2.7 is zero for all cases considered here, as photons scattered from centered particles have no preferred transverse direction. The ultimate sensitivity limit is given when we evaluate this over a spherical shell; here this gives $f_x^2 = \frac{1}{5}$, $f_y^2 = \frac{2}{5}$ and $f_z^2 = \frac{2}{5}$. Since the sensitivity predicted from this can only be achieved with perfect imaging of all scattered photons, it also determines the measurement back-action upon the particle. For measurements subject to a limited aperture size, Eq. 2.7 can be integrated analytically, with the corresponding quantum limit plotted in Fig. 2.1. In this, the aperture size is expressed in terms of the NA for a particle suspended in water. This shows near-perfect agreement with the equivalent numerical calculations performed in Ref. [23].

2.4 Sensitivity in the Mie Scattering Regime

Optical tweezers experiments usually operate with particles which are too large to be accurately approximated as Rayleigh scatterers. For these particles, the scattering profile is complicated by such effects as multiple internal reflections and the interference between optical paths of different length. For spherical particles in focused optical fields, this scattering regime is described mathematically by extended Mie theory [11]. We evaluate the scattering profiles numerically with the Optical Tweezers Toolbox [19]. These profiles are integrated as described in Eq. 2.7 to find the quantum sensitivity limit for particle tracking. The quantum limit is shown in Fig. 2.2 for polystyrene beads suspended in water, measured with 1064 nm light and an NA = 1.3

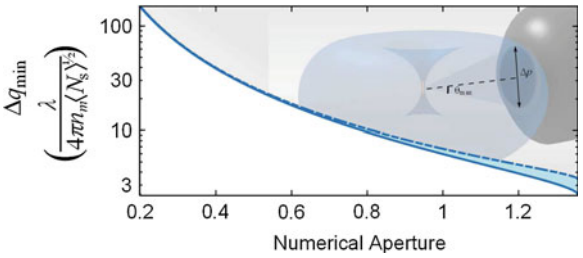

Fig. 2.1 Light scatters from a small particle with a defined spatial profile, shown here as Rayleigh scattering. The field which enters the objective aperture is measured to determine the particle position. The scattered photons which propagate towards the aperture ($\theta > \theta_{\min}$) have a momentum distribution Δp which defines the fundamental lower bound on sensitivity with which the particle position can be determined, as plotted here as a function of the condenser NA for Rayleigh particles suspended in water, illuminated by linearly polarized light. The sensitivity limit is shown for motion both perpendicular (*solid line*) and parallel (*dashed line*) to the polarization axis. Sensitivity improves with NA, as high NA lenses collect scattered photons with a larger momentum range. Because of the anisotropic scattering profile, this improvement is greatest for motion which is perpendicular to the polarization axis. Together with the scattering rate κ, this sensitivity defines the quantum limit on displacement resolution per incident photon

objective and condenser. Examining this, we see a number of noteworthy features. For small particles, where Rayleigh scattering is valid, forward and back scatter offer an equally sensitive measurement. However, as the particle size increases, the scatter becomes preferentially forward, with less information carried by back-scattered photons. Polarization has little effect on the sensitivity for beads larger than the wavelength. Two different resonant effects are evident in Fig. 2.2 for large particles. The direction of scattering is periodically modulated by an effect which is approximately given by thin-film interference. This causes a significant modulation of the sensitivity available through back-scatter measurements; however, maximizing back-scattered sensitivity may not be advantageous for high-refractive index particles, as this regime also has the weakest trapping potential [22]. In addition to this, Mie resonances suppress the particle position information encoded in the phase of the outgoing field when propagation through the particle increases the optical path length by an integer multiple of the wavelength (see Fig. 2.2 insets). This degrades the measurement sensitivity without affecting the trapping potential, as the trapping is determined purely by the optical amplitude.

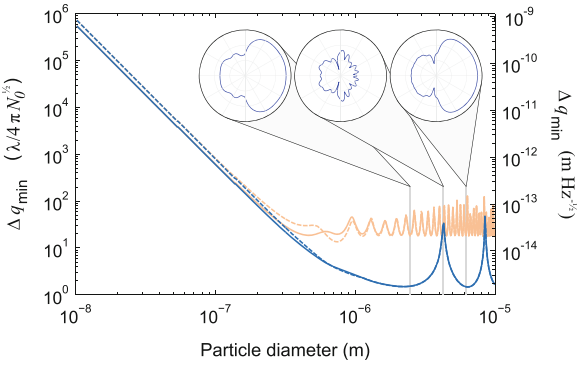

Fig. 2.2 The quantum limit on position sensing polystyrene beads ($n = 1.58$) suspended in water with a 1.3 NA objective as a function of diameter. The faint and dark lines representing measurement of back-scatter and forward-scatter respectively, and *dashed* and *solid lines* representing measurements parallel and perpendicular to the plane of polarization. The axis on the right shows the best sensitivity possible for a measurement based on 1 mW of optical power. *Insets* Logarithmically scaled scattered field intensity profiles for bead diameters of 2.5, 4.3 and 6.2 μm, calculated in the plane of polarization. The 4.3 μm bead forward-scatters far less light than either of the other two, because resonant effects reduce the interaction of the incoming field with the bead, such that most of the light remains in the incident mode. However, the back-scatter is of a similar magnitude for all three

2.5 Relevance of This Limit

2.5.1 Resolving Zero-Point Motion

One application of this calculation is to determine the conditions required to observe the zero-point motion of a levitating sphere. When this can be measured, it is possible to generate squeezed mechanical states or cool to the ground state [1], and also provides a means to search for the non-Newtonian gravity predicted at small scales [6]. The average amplitude of zero-point motion is given by [1]

$$\Delta q_{\mathrm{zpm}} = \left(\frac{\hbar}{2m\Omega}\right)^{1/2} \tag{2.8}$$

for a mechanical frequency Ω and mass m. For most interesting applications, the measurement time must be short compared to the average time for one bath phonon to enter or leave the mechanical mode [1], which is given by $\tau = \frac{2\pi}{\Gamma n}$ for a mean phonon occupancy $n = \frac{k_B T}{\hbar\Omega}$ and decay rate Γ. Although feedback is often used to cool motion, it does not influence this coupling rate, as feedback can only reduce the phonon occupancy by introducing mechanical dissipation which increases Γ, keeping the product unchanged. In order to measure the movement Δq_{zpm} over a time τ, the incident power must exceed the minimum threshold which we calculate

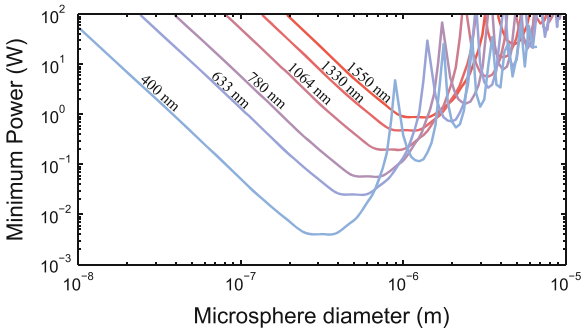

Fig. 2.3 This is the optical power required to observe the zero-point motion of a levitating silica bead in vacuum, for six different laser wavelengths. A refractive index of 1.46, a temperature of $T = 298$ K, and a decay rate of $\Gamma = 2\pi \times 0.1$ Hz have been used, along with NA $= 0.8$ objective and condenser. This plot can be easily extrapolated to other physical parameters because the required power scales linearly with both the decay Γ and temperature T. Although the decay rate used for this calculation is similar to that in recent experiments [15], future experiments may attain much lower decay rates, with predicted rates of order 10^{-6} Hz [1, 6]

here. Conveniently, an increase in the mechanical frequency Ω reduces both the mechanical amplitude Δq_{zpm} and phonon occupancy n such that the power threshold is independent of the frequency. This means that the trapping potential need not be considered, and the derived power limit is valid even if there are additional trapping fields. The power threshold is calculated as a function of sphere radius and shown in Fig. 2.3. This shows that for a given laser, the optimal bead diameter is somewhat smaller than the wavelength. In the Rayleigh scattering regime, the required power scales as λ^7, making a short wavelength laser a practical choice. For large beads, the preferred wavelength is determined entirely by the Mie resonances. The dependence of the zero-point motion on particle mass generally makes its observation more difficult in larger beads. To observe zero-point motion in any silica bead with a diameter larger than 6 μm would be prohibitively difficult at the assumed decay rate of 0.1 Hz, as it requires a quantum limited measurement of over 10 W of optical power.

Although the power predicted in Fig. 2.3 should make the zero-point motion observable, it will also impart back-action onto the bead motion. The back-action will be greater than the zero-point momentum, since only the forward-scattered photons are included in the measurement. This consideration is particularly severe in the Rayleigh scattering regime, where the back-scatter carries as much information as the forward-scatter. If zero-point motion of a Rayleigh particle were resolvable with the NA $= 0.8$ condenser considered here, back-action will exceed the zero-point momentum by a factor of 2.9. By contrast, deep within the Mie scattering regime most of the information is in the forward-scattered light, and the zero-point motion can be resolved while imparting back-action which only exceeds the zero-point momentum by a factor of 1.06. However, if the measurement is in any way non-optimal, this will enlarge the relative back-action. In real experiments, optical loss and the use of

split detectors [23] ensure a non-optimal position measurement. This is a significant limitation, as non-optimal measurement prevents ground state cooling and minimum uncertainty squeezing [18].

2.5.2 Experimental Sensitivity

With our calculations, we can characterize the gap between experimental results and the quantum limit. A recent experiment achieved a sensitivity of 1.7×10^{-14} m Hz$^{-1/2}$ when tracking 1 μm diameter polystyrene beads in water with 700 mW of 1064 nm light, and collecting only the forward-scatter [2]. Assuming the objective and condenser have NA = 1.3, we find that $\kappa^{1/2} f_x = 0.380$, and the 3.7×10^{18} incident photons per second should limit the sensitivity to 1.1×10^{-16} m Hz$^{-1/2}$, which is within a factor of 145 of the demonstrated result. Not all of the photons were measured, however, as the field was attenuated by 70 % before the detector, such that the remaining photons were measured with sensitivity within a factor of 80 of the quantum limit. In another recent experiment, silica beads in vacuum were tracked at 3.9×10^{-14} m Hz$^{-1/2}$ using 120 mW of 1064 nm light, and NA = 0.68 objective and condenser [15]. For this case, $\kappa^{1/2} f_x = 0.203$ and the quantum limit is 5.2×10^{-16} m Hz$^{-1/2}$, only 75 times lower than the experimental sensitivity. In this experiment, the measurement for each axis was performed on separate detectors, so each detector had fewer photons available for measurement. Although both of these experiments used non-optimal split detectors, they operate well within two orders of magnitude of the quantum limit. If further improvements to sensitivity are required, it would be useful to characterize the contributions to this gap arising from optical loss, non-optimal detection, and various noise sources. This characterization would indicate the aspects of the measurement which could be most effectively improved. Some classical strategies to reduce this gap are discussed in Part II of this thesis. The quantum limit derived can only be overcome by using quantum correlated light to achieve sub-shot noise performance in a classically near-optimal measurement.

2.6 Lessons to Learn

The quantum limit calculated here has important implications for future experiments requiring better sensitivity than currently available. The thermal motion of particles in water has been observed to deviate from Brownian motion on very short timescales, due to hydrodynamic resonances [5] and ballistic motion [10]. However, there are further predicted effects which remain unobserved, such as oscillations arising from the elastic compressibility of water [10]. Direct observation of this phenomenon requires sensitivity of around 2×10^{-17} m Hz$^{-1/2}$ [10], which even with a quantum limited measurement requires 19 W of 1064 nm light. This presents a problem, as the surrounding water is heated by approximately 8 K/Watt of 1064 nm

trapping light [20], such that the boiling point is reached when the optical power is around 10 W. The only way to surpass the quantum limit is to use correlated photons which allow more information to be extracted per photon [8, 13]. Such quantum resources can be integrated into particle tracking experiments [24], and with existing technology, offer up to 10 dB of enhancement [21]. With this quantum enhancement, measurement of the elastic compressibility of water would require a more achievable 2 W of optical power. Based on our calculations, and the advanced state of recent experiments, we conclude that quantum resources will play an important role in the next generation of high precision tracking experiments.

From the calculation presented here, it is clear that the minimum resolvable displacement improves as the objective NA increases, and as more scattered photons are measured. High sensitivity experiments should therefore utilize high NA objectives and capture as many scattered photons as possible. Neither of these conclusions should come as a surprise. The particles tracked in optical tweezers are assumed to be located at the centroid of the optical image, which is well known to improve with both of these parameters. This principle is applied in Chap. 5, where a method is presented to remove unscattered trapping light from the detection, and thus increase the scattered photon number which can be measured without saturating the detector.

References

1. D.E. Chang, C.A. Regal, S.B. Papp, D.J. Wilson, J. Ye, O. Painter, H.J. Kimble, P. Zoller, Cavity opto-mechanics using an optically levitated nanosphere. Proc. Natl. Acad. Sci. USA **107**(3), 1005–1010 (2010)
2. I. Chavez, R. Huang, K. Henderson, E.-L. Florin, M.G. Raizen, Development of a fast position-sensitive laser beam detector. Rev. Sci. Instrum. **79**, 105104 (2008)
3. W. Denk, W.W. Webb, Optical measurement of picometer displacements of transparent microscopic objects. Appl. Opt. **29**(16), 2382–2391 (1990)
4. R.W. Ditchburn, *Light* (Dover Publications, New York, 1991)
5. T. Franosch, M. Grimm, M. Belushkin, F.M. Mor, G. Foffi, L. Forró, S. Jeney, Resonances arising from hydrodynamic memory in Brownian motion. Nature **478**, 85–88 (2011)
6. A.A. Geraci, S.B. Papp, J. Kitching, Short-range force detection using optically cooled levitated microspheres. Phys. Rev. Lett. **105**, 101101 (2010)
7. G. Giannone, E. Hosy, F. Levet, A. Constals, K. Schulze, A. Sobolevsky, M. Rosconi, E. Gouaux, R. Tampé, D. Choquet, L. Cognet, Dynamic superresolution imaging of endogenous proteins on living cells at ultra-high density. Biophys. J. **99**(4), 1303–1310 (2010)
8. V. Giovannetti, S. Lloyd, L. Maccone, Quantum-enhanced measurements: beating the standard quantum limit. Science **306**(5700), 1330–1336 (2004)
9. F. Gittes, C.F. Schmidt, Interference model for back-focal-plane displacement detection in optical tweezers. Opt. Lett. **23**(1), 7–9 (1998)
10. R. Huang, I. Chavez, K.M. Taute, B. Lukić, S. Jeney, M.G. Raizen, E.-L. Florin, Direct observation of the full transition from ballistic to diffusive Brownian motion in a liquid. Nat. Phys. **7**, 576–580 (2011)
11. D. R. Huffman, C. F. Bohren, *Absorption and Scattering of Light by Small Particles* (Wiley, New York, 2008)
12. A. Jannasch, A.F. Demirörs, P.D.J. van Oostrum, A. van Blaaderen, E. Schäffer, Nanonewton optical force trap employing anti-reflection coated, high-refractive-index titania microspheres. Nat. Photon. **6**, 469–473 (2012)

13. M. Kolobov, C. Fabre, Quantum limits on optical resolution. Phys. Rev. Lett. **85**(18), 3789–3792 (2000)
14. P. Kukura, H. Ewers, C. Müller, A. Renn, A. Helenius, V. Sandoghdar, High-speed nanoscopic tracking of the position and orientation of a single virus. Nat. Methods **6**, 923 (2009)
15. T. Li, S. Kheifets, M.G. Raizen, Millikelvin cooling of an optically trapped microsphere in vacuum. Nat. Phys. **7**, 527–530 (2011)
16. P.W. Milonni, R.W. Boyd, Momentum of light in a dielectric medium. Adv. Opt. Photon. **2**(4), 519–553 (2010)
17. J.R. Moffitt, Y.R. Chemla, S.B. Smith, C. Bustamante, Recent advances in optical tweezers. Annu. Rev. Biochem. **77**, 205–228 (2008)
18. A. Naik, O. Buu, M. LaHaye, A. Armour, A. Clerk, M. Blencowe, K. Schwab, Cooling a nanomechanical resonator with quantum back-action. Nature **443**(7108), 193–196 (2006)
19. T. Nieminen, V. Loke, A. Stilgoe, G. Knöner, A. Brańczyk, N. Heckenberg, H. Rubinsztein-Dunlop, Optical tweezers computational toolbox. J. Opt. A: Pure Appl. Opt **9**(8), S196 (2007)
20. E.J. Peterman, F. Gittes, C.F. Schmidt, Laser-induced heating in optical traps. Biophys. J. **84**(2), 1308–1316 (2003)
21. M. Stefszky, C. Mow-Lowry, S. Chua, D. Shaddock, B. Buchler, H. Vahlbruch, A. Khalaidovski, R. Schnabel, P. Lam, D. McClelland, Balanced homodyne detection of optical quantum states at audio-band frequencies and below. Class. Quant. Grav. **29**(14), 145015 (2012)
22. A. Stilgoe, T. Nieminen, G. Knöener, N. Heckenberg, H. Rubinsztein-Dunlop, The effect of Mie resonances on trapping in optical tweezers. Opt. Express **16**(19), 15039–15051 (2008)
23. J.W. Tay, M.T.L. Hsu, W.P. Bowen, Quantum limited particle sensing in optical tweezers. Phys. Rev. A **80**(6), 063806 (2009)
24. M.A. Taylor, J. Janousek, V. Daria, J. Knittel, B. Hage, H.-A. Bachor, W.P. Bowen, Biological measurement beyond the quantum limit. Nat. Photon. **7**, 229–233 (2013)
25. M.A. Taylor, J. Knittel, W.P. Bowen, Fundamental constraints on particle tracking with optical tweezers. New J. Phys. **15**, 023018 (2013)

Chapter 3
The Quantum Noise Limit for a Specific Measurement

In this chapter, we follow a full quantum treatment of the optical fields to derive the quantum noise limit to real particle tracking experiments. Unlike the limit in Chap. 2, which can only be attained with a perfect experiment, the limit derived here is achieved for any quantum shot-noise limited experiment. This also provides an aid in designing new experiments by predicting the sensitivity achievable with any experimental procedure. This chapter expands on the theory presented in the supplementary information of the following paper [7].

3.1 Quantum Treatment of Fields

The quantum noise which is present in all optical measurements is a direct result of the commutation relation between the operators which describe an optical field. Here we introduce the conventions of quantum optics [4] which are then followed in calculation of this quantum noise. It is useful to decompose the optical electric field amplitude $\bar{\mathbf{E}}$ at position $\mathbf{X}$ on the detector into a collection of modes,

$$\bar{\mathbf{E}}(\mathbf{X}) = \sum_{n=0}^{\infty} \hat{\mathbf{E}}_n(\mathbf{X}) = i\sqrt{\frac{\hbar\omega}{2c\epsilon}} \sum_{n=0}^{\infty} \hat{a}_n \psi_n(\mathbf{X}) \mathbf{z}_n, \tag{3.1}$$

where the nth mode has a normalized mode shape of ψ_n, polarization $\mathbf{z}_n$ and the annihilation operator $\hat{a}_n$. This operator can be expressed as a mean value α_n and a fluctuating operator $\hat{\delta a}_n$,

$$\hat{a}_n = \alpha_n + \hat{\delta a}_n. \tag{3.2}$$

Here we work in the limit that quantum fluctuations are much smaller than the mean amplitude ($\hat{\delta a}_n \ll \alpha_n$), such that the mean photon number n of the mode is given by $n_n = |\alpha_n|^2$. We also define quadratures in the usual way as

M. Taylor, *Quantum Microscopy of Biological Systems*, Springer Theses,
DOI 10.1007/978-3-319-18938-3_3

$$\hat{X}_n^+ = \left(\hat{\delta a}_n + \hat{\delta a}_n^\dagger\right), \tag{3.3}$$

$$\hat{X}_n^- = -i\left(\hat{\delta a}_n - \hat{\delta a}_n^\dagger\right), \tag{3.4}$$

The variance of any state must always satisfy the Heisenberg uncertainty principle, which in this case is given by

$$\left\langle\left(\delta\hat{X}_n^+\right)^2\right\rangle\left\langle\left(\delta\hat{X}_n^-\right)^2\right\rangle \geq \left(\left\langle\frac{1}{2i}[\hat{X}_n^+, \hat{X}_n^-]\right\rangle\right)^2 \tag{3.5}$$

$$= \left(\left\langle[\hat{\delta a}_n^\dagger, \hat{\delta a}_n]\right\rangle\right)^2 \tag{3.6}$$

$$= 1, \tag{3.7}$$

where we have used $[\hat{\delta a}_n, \hat{\delta a}_n^\dagger] = 1$. For any of these quadratures, the fluctuation statistics for coherent, quantum noise limited modes and unoccupied vacuum modes are therefore given by

$$\left\langle\delta\hat{X}_n^\pm(\omega)\right\rangle = 0 \tag{3.8}$$

$$\left\langle\left(\delta\hat{X}_n^\pm(\omega)\right)^2\right\rangle = 1. \tag{3.9}$$

In most real optical states, there is additional laser noise on the state which increases the variance. A state can, however, have a lower variance than Eq. (3.9) in one quadrature, provided the other quadrature has a higher variance. This is termed a "squeezed" state, and requires non-classical photon correlations [4]. To simplify the notation, we represent the variances of the quadratures as $V^\pm \equiv \left\langle\left(\delta\hat{X}^\pm(\omega)\right)^2\right\rangle$. The uncertainty relation in Eq. 3.5 is then represented as

$$V^+V^- \geq 1. \tag{3.10}$$

Loss along the optical path can be represented with a beamsplitter which couples out some of the occupation of the mode, while introducing some vacuum fluctuations. When fields are detected with an efficiency of η, this is represented as a beamsplitter with transmission η followed by perfect detection. The measured field is thus given by

$$\alpha_n^{\text{det}} + \hat{\delta a}_n^{\text{det}} = \eta^{1/2}\alpha_n + \eta^{1/2}\hat{\delta a}_n + (1-\eta)^{1/2}\hat{\delta a}_n^0 \tag{3.11}$$

where $\hat{\delta a}_n^0$ is the vacuum fluctuation and the superscript "det" is used to denote a field at the detector.

3.2 The Quantum Limit for Position Sensing

In a typical particle tracking experiment, the two fields which are occupied at the detector are the trapping field $\mathbf{E}_T$ and the scattered field $\mathbf{E}_{\text{scat}}$ (see Fig. 3.1). The trap field acts to confine the particle, produce the scattered field, and also as the local oscillator for measurement. The particle is then tracked via a measurement of the interference between the trap and scattered fields. To find the dependence of the scattered field on a small particle displacement x, it can be expanded to first order as

$$\hat{E}_{\text{scat}} = \hat{E}_{\text{scat}}|_{x=0} + x\frac{d\hat{E}_{\text{scat}}}{dx}\Big|_{x=0}. \tag{3.12}$$

The component $\hat{E}_{\text{scat}}|_{x=0}$ can be considered as a stationary perturbation to the trapping field, such that at the detector this field is given by

$$\hat{E}_T^{\text{det}} = \eta^{1/2}\left(\hat{E}_T + \hat{E}_{\text{scat}}|_{x=0}\right) + (1-\eta)^{1/2}\hat{E}_T^0, \tag{3.13}$$

where $\hat{E}_T^0 = \hat{\delta a}_T^0 \psi_T$ is a vacuum fluctuation introduced with the optical losses into the detected trap mode ψ_T. All particle position information is within the component $x\frac{dE_{\text{scat}}}{dx}\Big|_{x=0} = \hat{a}_{\text{scat}}\psi'_{\text{scat}}x$, where $\psi'_{\text{scat}} = \frac{d\psi_{\text{scat}}}{dx}\Big|_{x=0}$, so this defines the ideal measurement mode shape. When these fields are measured on a detector, the resulting signal photocurrent is given by

$$i = \frac{2\epsilon}{\hbar\omega}\int_{-\infty}^{\infty} U(\mathbf{X})|\sum_{n=0}^{\infty}\hat{\mathbf{E}}_n^{\text{det}}|^2 d\mathbf{X} \tag{3.14}$$

$$= \frac{2\epsilon}{\hbar\omega}\int_{-\infty}^{\infty} U(\mathbf{X})|\hat{E}_T^{\text{det}} + \hat{E}_{\text{scat}}^{\text{det}} + \hat{E}_0^{\text{det}}|^2 d\mathbf{X}. \tag{3.15}$$

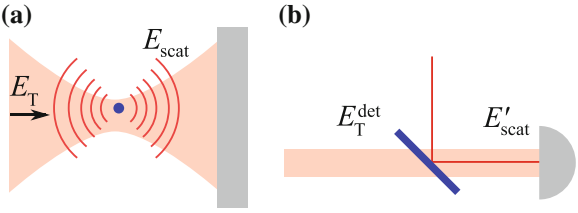

Fig. 3.1 This shows the relevant fields in a particle tracking measurement. **a** The incident trapping field E_T generates a scattered field E_{scat}, and these fields propagate together toward the detector. **b** Since the particle introduces the scattered field to the measurement, it is analogous to a highly transmissive beamsplitter which couples illuminating light onto the detector

Here the polarization vector has been dropped because the trap and scattered field are assumed to share polarization. This is a very close approximation provided the particle is rotationally symmetric and located near the optical focus, and the trapping field carries uniform polarization outside the objective [5]; all of which are typical of experimental conditions. Vacuum fluctuations in all unoccupied modes are included in the field $\hat{E}_0^{\text{det}} = \sum_{n=0}^{\infty} \delta\hat{a}_n^0 \psi_n$. These are only detectable via their interference with the occupied modes, and fluctuations orthogonal to the detection mode can be neglected. The spatial variation in the gain of the detector is described by $U(\mathbf{X})$; for a bulk detector, this is always 1, while for split detection, this is -1 on the left side and 1 on the right side. Defining the detection mode as $\psi_{\text{det}} = U(\mathbf{X})\psi_T$, the detected photocurrent is found to be

$$\begin{aligned} i = |\eta^{1/2}\alpha_T + \eta^{1/2}\delta\hat{a}_T + (1-\eta)^{1/2}\delta\hat{a}_T^0|^2\langle\psi_T|\psi_{\text{det}}\rangle \\ +\eta^{1/2}\alpha_T\delta\hat{X}_0^+\langle\psi_0|\psi_{\text{det}}\rangle + 2\eta\alpha_T\alpha_{\text{scat}}x\text{Re}\{\langle\psi'_{\text{scat}}|\psi_{\text{det}}\rangle\}, \end{aligned} \tag{3.16}$$

where the scattered field amplitude is assumed to be much smaller than the trap amplitude. The integral $\langle\psi_n|\psi_{\text{det}}\rangle = \int_{-\infty}^{\infty}\psi_{\text{det}}^*\psi_n d\mathbf{X}$ then defines the overlap between the mode n and the detection mode. If using a bulk detector, $U(\mathbf{X}) = 1$ throughout and $\psi_{\text{det}} = \psi_T$. Consequently, we see that $\langle\psi_T|\psi_{\text{det}}\rangle = 1$, while $\langle\psi_0|\psi_{\text{det}}\rangle = 0$ because the field $\hat{E}_0$ only includes vacuum fluctuations which are in unoccupied modes, all of which are orthogonal to ψ_T. By contrast, a split detector has $U(\mathbf{X}) = \text{sign}(X)$; provided the trapping field is centered on the detector, this results in $\langle\psi_T|\psi_{\text{det}}\rangle = 0$. One of the unoccupied vacuum modes then overlaps perfectly with the detection mode, such that $\psi_0 = \psi_{\text{det}}$ and $\langle\psi_0|\psi_{\text{det}}\rangle = 1$. This can be used to simplify the photocurrent in Eq. 3.16 for the specific case of a split detector, with

$$i = \eta^{1/2}\alpha_T\delta\hat{X}_0^+ + 2\eta\alpha_T\alpha_{\text{scat}}x\text{Re}\{\langle\psi'_{\text{scat}}|\psi_{\text{det}}\rangle\}. \tag{3.17}$$

The expectation value of this is

$$\langle i\rangle = 2\eta\alpha_T\alpha_{\text{scat}}\langle x\rangle\,\text{Re}\{\langle\psi'_{\text{scat}}|\psi_{\text{det}}\rangle\}, \tag{3.18}$$

$$= 0, \tag{3.19}$$

which uses $\langle x\rangle = 0$. Taking the Fourier transform of Eq. 3.17 and calculating the variance, we find

$$\left\langle i^2(\omega)\right\rangle = \eta n_T + 4\eta^2 n_T n_{\text{scat}}\left\langle x^2(\omega)\right\rangle\text{Re}\{\langle\psi'_{\text{scat}}|\psi_{\text{det}}\rangle\}^2, \tag{3.20}$$

where we have used $\left\langle\left(\delta\hat{X}_0^+(\omega)\right)^2\right\rangle = 1$, and neglected the small cross term. The displacement x is resolvable when the noise term (ηn_T) is equal to the signal (the last term in Eq. 3.20), giving the quantum noise limit

$$\left\langle x^2(\omega)\right\rangle_{\mathrm{QNL}} = \frac{1}{4\eta n_{\mathrm{scat}}\mathrm{Re}\{\langle\psi'_{\mathrm{scat}}|\psi_{\mathrm{det}}\rangle\}^2}, \tag{3.21}$$

$$= \frac{1}{4\kappa\eta n_T\mathrm{Re}\{\langle\psi'_{\mathrm{scat}}|\psi_{\mathrm{det}}\rangle\}^2}, \tag{3.22}$$

where we have used $n_{\mathrm{scat}} = \kappa n_T$. Although this equation was derived for split detection, the approach used is general and can be applied to any detection scheme. It is important to note that the scattered mode ψ_{scat} is normalized, but its derivative ψ'_{scat} is not. A comparison with the limit derived in Eq. 2.4 shows that the minimum resolvable displacement is arrived at if the measurement overlap $\langle\psi'_{\mathrm{scat}}|\psi_{\mathrm{det}}\rangle = kf_i$, where $k = \frac{2\pi n_m}{\lambda}$ is the wavenumber.

3.3 Particle Tracking with Squeezed States of Light

The above analysis reached the quantum noise limit following the assumption that the fluctuations in the detection mode followed the vacuum noise, with $\left\langle\left(\delta\hat{X}_0^+(\omega)\right)^2\right\rangle = V_0^+ = 1$. It should be possible to overcome this limit by replacing these vacuum fluctuations with a squeezed vacuum ($V_0^+ < 1$). This would then modify the photocurrent variance previously shown in Eq. 3.20 to

$$\left\langle i^2(\omega)\right\rangle = \eta n_T\left(\eta V_0^+(\omega) + (1-\eta)\right) + 4\eta^2 n_T n_{\mathrm{scat}}\left\langle x^2(\omega)\right\rangle\mathrm{Re}\{\langle\psi'_{\mathrm{scat}}|\psi_{\mathrm{det}}\rangle\}^2, \tag{3.23}$$

with a resulting minimum resolvable displacement of

$$\left\langle x^2(\omega)\right\rangle_{\mathrm{min}} = \left[1-\eta(1-V_0^+)\right]\left\langle x^2(\omega)\right\rangle_{\mathrm{QNL}}. \tag{3.24}$$

This shows that quantum enhanced particle tracking is possible. However, this configuration presents some technical problems. Most importantly, it is difficult to ensure that the squeezed vacuum mode will coincide with the detection mode, as propagation through microscope objectives and biological samples will cause a large unknown distortion. Distortion will be particularly significant around the discontinuity in the detection mode at $X = 0$. Furthermore, split detectors typically lack the bandwidth and efficiency required for such quantum enhanced measurements.

Instead of confining the analysis to split detection, we now consider particle tracking with a shaped local oscillator field E_{LO} and a bulk detector, such that $\psi_{\mathrm{det}} = \psi_{\mathrm{LO}}$. Using this, the photocurrent in Eq. 3.16 simplifies to

$$i = \eta n_{\mathrm{LO}} + \eta\alpha_{\mathrm{LO}}\delta\hat{X}^+_{\mathrm{LO}} + (\eta(1-\eta))^{1/2}\alpha_{\mathrm{LO}}\delta\hat{X}^{0+}_{\mathrm{LO}} + 2\eta\alpha_{\mathrm{LO}}\alpha_{\mathrm{scat}}x\mathrm{Re}\{\langle\psi'_{\mathrm{scat}}|\psi_{\mathrm{det}}\rangle\}, \tag{3.25}$$

where the trapping field E_T has been renamed the local oscillator E_{LO}, and the small terms $|\hat{\delta a}_{\mathrm{LO}}|^2$ and $|\hat{\delta a}^0_{\mathrm{LO}}|^2$ have been neglected. Unlike split detection, the mean photocurrent is now non-zero, with $\langle i \rangle = \eta n_{\mathrm{LO}}$. However, if the local oscillator is in a coherent state ($V^+_{\mathrm{LO}}(\omega) = 1$), this results in an identical photocurrent variance to that derived in Eq. 3.20 for all non-zero frequencies. Correspondingly, the quantum noise limit for this measurement approach is identical to that derived in Eq. 3.22 for split detection. Similarly, if the local oscillator is amplitude squeezed, with $V^+_{\mathrm{LO}}(\omega) < 1$, we find the minimum resolvable displacement to be

$$\left\langle x^2(\omega) \right\rangle_{\mathrm{min}} = \left[1 - \eta(1 - V^+_{\mathrm{LO}})\right] \left\langle x^2(\omega) \right\rangle_{\mathrm{QNL}}, \tag{3.26}$$

similar to the result in Eq. 3.24 for split detection. In this scheme, the detection mode and squeezed mode are both defined by the local oscillator, which ensures that the squeezing is measured perfectly. This also ensures that the phase of the squeezed field perfectly matches the detection, with no anti-squeezing entering the measurement. In standard interferometric measurements, the anti-squeezing cannot be perfectly eliminated from detection, and this can substantially limit the achievable quantum enhancement [3]. However, it requires that the local oscillator be spatially engineered to overlap with the mode ψ'_{scat} which contains the particle position information. This mode has previously been calculated for Rayleigh scattering particles [6], for which it is approximately given by the TEM01 mode. However, the TEM01 mode is poorly suited to trapping of particles, so an additional trapping field could be required to confine the particle. Provided the trapping field is kept orthogonal to the measurement, it will not interfere with the other optical fields. The resulting photocurrent is then a linear combination of the photocurrent due to the detection fields (Eq. 3.25) and the photocurrent due to the trapping field, such that

$$\begin{aligned} i = \eta n_{\mathrm{LO}} + \eta \alpha_{\mathrm{LO}} \delta \hat{X}^+_{\mathrm{LO}} + (\eta(1-\eta))^{1/2} \alpha_{\mathrm{LO}} \delta \hat{X}^{0+}_{\mathrm{LO}} \\ + \eta n_T + \eta \alpha_{\mathrm{T}} \delta \hat{X}^+_{\mathrm{T}} + (\eta(1-\eta))^{1/2} \alpha_{\mathrm{T}} \delta \hat{X}^{0+}_{\mathrm{T}} \\ + 2\eta \alpha_{\mathrm{LO}} \alpha_{\mathrm{scat}} x \mathrm{Re}\{\langle \psi'_{\mathrm{scat}} | \psi_{\mathrm{det}} \rangle\}. \end{aligned} \tag{3.27}$$

Following similar reasoning to above, and assuming the trapping field is in a coherent state ($V^+_T(\omega) = 1$), this then results in a minimum resolvable displacement of

$$\left\langle x^2(\omega) \right\rangle_{\mathrm{min}} = \frac{n_{\mathrm{LO}} \left(\eta V^+_{\mathrm{LO}}(\omega) + (1-\eta)\right) + n_T}{4 n_{\mathrm{LO}} \eta n_{\mathrm{scat}} \mathrm{Re}\{\langle \psi'_{\mathrm{scat}} | \psi_{\mathrm{det}} \rangle\}^2}, \tag{3.28}$$

$$= \frac{n_{\mathrm{LO}} \left(\eta V^+_{\mathrm{LO}}(\omega) + (1-\eta)\right) + n_T}{n_{\mathrm{LO}}} \left\langle x^2(\omega) \right\rangle_{\mathrm{QNL}}. \tag{3.29}$$

This shows that the trapping photons which reach the detector contribute additional quantum noise to the measurement which can substantially degrade the improvement achievable via squeezing. However, this approach does allow the local oscillator to be shaped to optimize its overlap with the information in the scattered field ($\mathrm{Re}\{\langle \psi'_{\mathrm{scat}} | \psi_{\mathrm{det}} \rangle\}$) without disrupting the optical trap.

3.4 Relation to the Quantum Limit for Phase Estimation

The expression in Eq. 3.22 generalizes the quantum noise limit imposed in phase estimation interferometry to situations in which information is included in spatial changes as well as phase shifts. For the case where no information is contained in the spatial profile, the limit in Eq. 3.22 reduces to the usual phase estimation quantum noise limit. Such a situation occurs if the motion x is movement of an interferometer mirror, as shown in Fig. 3.2, with the "scattered" field given by a phase modulated input mode ψ_{in},

$$\psi_{\text{scat}} = \psi_{\text{in}} e^{ikx}. \tag{3.30}$$

With this definition of the scattered mode,

$$\psi'_{\text{scat}} = \frac{d\psi_{\text{scat}}}{dx}\Big|_{x=0} = (ik)\psi_{\text{in}} e^{ikx} \approx (ik - k^2 x)\psi_{\text{in}}. \tag{3.31}$$

Choosing the optimum phase for the detection mode, one has $\text{Re}\{\langle\psi'_{\text{scat}}|\psi_{\text{det}}\rangle\} = k\langle\psi_{\text{in}}|\psi_{\text{det}}\rangle = k\eta_{\text{homo}}^{1/2}$, where η_{homo} is the overlap efficiency between the incident signal field and the local oscillator field. Since the the momentum is completely changed by the reflection, the momentum parameter $f_x = 1$ in the absolute quantum limit of Eq. 2.4. Thus, the limits in Eqs. 3.22 and 2.4 converge for an optimal measurement with $\eta_{\text{homo}} = 1$.

Substituting these expressions into Eq. 3.22, we find that the quantum noise limit is given by

$$\left\langle x(\omega)^2 \right\rangle_{\text{QNL}} = \frac{1}{4\eta\eta_{\text{homo}} n_{\text{scat}} k^2} = \frac{1}{4n_{\text{det}} k^2}, \tag{3.32}$$

where n_{det} is the number of scattered photons arriving in the homodyne detector in the correct detection mode ψ_{det}. As the phase being measured is given by $\phi = kx$, Eq. 3.32 can be rearranged to

$$\left\langle \phi(\omega)^2 \right\rangle_{\text{QNL}} = \frac{1}{4\eta\eta_{\text{homo}} n_{\text{scat}}} = \frac{1}{4n_{\text{det}}}, \tag{3.33}$$

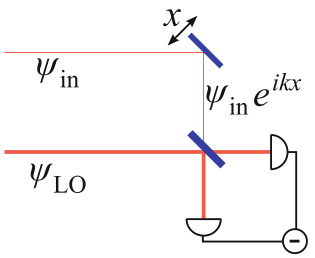

Fig. 3.2 This shows a simple setup in which the quantum noise limit derived here for particle tracking reduces to the usual quantum noise limit for phase estimation

which is the usual quantum noise limit for phase sensing of a weak signal field [1]. An alternative limit of $\left\langle \phi(\omega)^2_{\mathrm{QNL}} \right\rangle = 1/n_{\mathrm{det}}$ is used when the total photon number is constrained, rather than the signal photon number, with these photons divided equally between the signal and local oscillator fields [1]. In our case, since the measurements rely on a relatively weak scattered field and a much brighter local oscillator, Eq. 3.33 is the relevant limit.

3.5 Conclusion

This chapter shows that it is possible to enhance particle tracking measurements with squeezed states of light. As shown in Sect. 3.3, particle tracking via split detection or quadrant detection can be enhanced with the addition of a squeezed vacuum which is spatially engineered to match the detection mode. Alternatively, a local oscillator field which is spatially shaped to extract information can be used with a bulk detector. In this case, using a bright amplitude squeezed field for the local oscillator will offer enhanced performance. This approach has the advantage of ensuring perfect detection of the squeezed field, and also allowing the detection mode to be spatially optimized. We can also see that the classical sensitivity improves as the detection mode is optimized to extract information from the scattered field. Although previous research has sought to improve trapping forces by shaping the trapping field [2], no experimental procedure has been developed to optimize the detection mode.

References

1. R. Demkowicz-Dobrzański, J. Kołodyński, M. Guţă, The elusive Heisenberg limit in quantum-enhanced metrology. Nat. Commun. **3**, 1063 (2012)
2. K. Dholakia, T. Čižmár, Shaping the future of manipulation. Nat. Photon. **5**(6), 335–342 (2011)
3. S. Dwyer, L. Barsotti, T. Isogai, K. Kawabe, A. Khalaidovski, P. Lam, et al., Squeezed quadrature fluctuations in a gravitational wave detector using squeezed light. Opt. Express **21**(16), 19047–19060 (2013)
4. M. Fox, *Quantum Optics*: *An Introduction*, vol 15 (Oxford University Press, Oxford, 2006)
5. T.A. Nieminen, T. Asavei, V.L. Loke, N.R. Heckenberg, H. Rubinsztein-Dunlop, Symmetry and the generation and measurement of optical torque. J. Quant. Spectrosc. Radiat. Trans. **110**(14), 1472–1482 (2009)
6. J.W. Tay, M.T.L. Hsu, W.P. Bowen, Quantum limited particle sensing in optical tweezers. Phys. Rev. A **80**(6), 063806 (2009)
7. M.A. Taylor, J. Janousek, V. Daria, J. Knittel, B. Hage, H.-A. Bachor, W.P. Bowen, Biological measurement beyond the quantum limit. Nat. Photon. **7**, 229–233 (2013)

Chapter 4
Characterizing Quadrant Detection

The preceding chapter established a method to calculate the shot-noise limit to particle tracking sensitivity. While the theory is relatively straightforward, the scattered fields can be tedious to determine, and few researchers actually perform such calculations for their own experimental conditions. This chapter presents a computational tool which allows rapid characterization of quadrant detection based particle tracking, without requiring any manual calculations. This was presented in the following publication [18].

4.1 The Relevance of Computational Tools

Optical tweezers have proven an indispensable tool for modern biophysics, and have advanced our understanding of a wide range of single particle dynamic processes [1, 9]. Consequently, the optical forces exerted in optical tweezers have been extensively studied and calculated [6, 8, 15]. While it can be difficult and time-consuming to manually calculate the forces in a specific experiment, researchers can perform the difficult calculations with the freely available Optical Tweezers Toolbox [11, 12]. This determines the optical force for arbitrary incident fields and trapped particles, using a full vectorial field calculation, and allows researchers to rigorously model the trapping in their experiments in an easy and convenient manner. The theory of particle tracking has also been well established for quadrant detection [5, 16]. Additionally, the quantum limit to measurement sensitivity has been derived [17, 20], though this is only accessible with a perfect measurement which includes both the phase and amplitude of the light. Accurate calibration of an optical tweezers apparatus is important in almost all applications. Although particle tracking is well understood theoretically, currently no computational tool equivalent to the Optical Tweezers Toolbox is available to predict the response or sensitivity of such a system. Instead, researchers are required to repeat literature calculations for their specific apparatus. As a consequence, the use of theoretical tools to model detection is currently limited

M. Taylor, *Quantum Microscopy of Biological Systems*, Springer Theses,
DOI 10.1007/978-3-319-18938-3_4

to a small subset of the community. The availability of a straightforward tool to perform such calculations would enable optimization of experiments and quantitative comparisons with theory.

Here we present a computational tool for optical tweezers which calculates the position signal measured with a quadrant detector, and the corresponding shot-noise limit to position sensitivity. This piece of Matlab code is designed to function within the Optical Tweezers Toolbox [11, 12], and allows users to theoretically determine the measurement properties of their experiments without manually performing any calculations. Because the Optical Tweezers Toolbox can calculate the scattering of arbitrary optical fields from any trapped particle, this code inherits the same versatility. The source code is included in Appendix A, and was also published in the supplementary information of Ref. [18] which this chapter is based on.

The calculations performed by this code have several applications. For instance, in most optical tweezers measurements it is important to be able to determine the range over which the measurement is linear. The code allows this range to be directly predicted, and through this provides a convenient tool to optimize the linearity by varying experimental parameters such as numerical aperture or particle size. By providing the signal amplitude retrievable from a given apparatus, the code also makes it possible to determine whether a given phenomena will be measurable, and to optimize the experimental apparatus to maximize signal-to-noise where required.

4.2 Principle

In an optical tweezers experiment, an objective focuses an incident field to a spot, where particles are trapped by optical forces. This interaction includes a momentum exchange between the field and the particle, which therefore changes the propagation direction of the light. This has an overall effect of deflecting the transmitted field. To measure this deflection, the transmitted light is collected with a high numerical aperture (NA) condenser lens and measured at the back focal plane with a quadrant detector [5] (see Fig. 4.1). The condenser changes the spatial distribution of the light which passes through its aperture, without changing the photon flux arriving in each quadrant. Therefore, the signal measured on the quadrant detector can be evaluated by calculating the power within the four quadrants of the condenser aperture at the farfield of the particle [16] (see Fig. 4.1b).

Many real experiments do not place the detector at the back focal plane as shown in Fig. 4.1a, but use an additional lens to image the field at the back focal plane onto the detector. This additional lens also has a finite aperture width which introduces additional clipping, effectively reducing the condenser NA. In order to accurately model the measurement, the effective condenser NA which includes any additional clipping must be used.

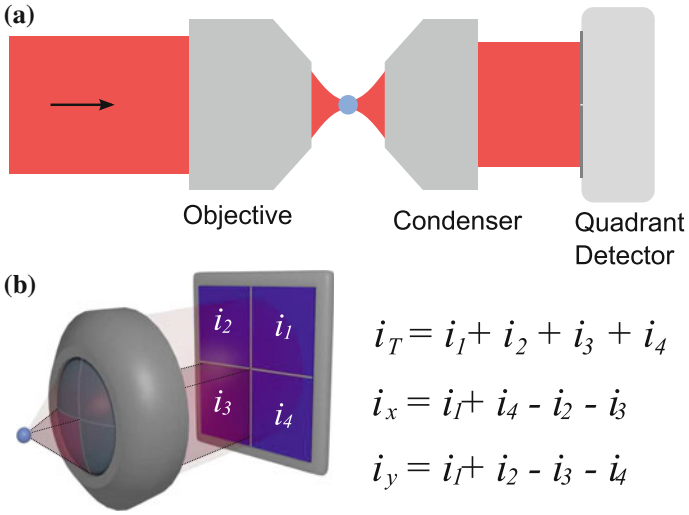

Fig. 4.1 This schematic describes the particle tracking setup which the code calculates. **a** The incident field is focused by the objective, and then interacts with a particle. The transmitted field is then collected by a condenser and directed onto a quadrant detector at the *back focal plane*. **b** The transmitted light which is in one quadrant at the condenser remains in this quadrant until it reaches the detector. The signal measured on the quadrant detector can be evaluated by calculating the intensity profile at the farfield of the particle, and integrating over the area within the condenser aperture in the relevant quadrants. The measurements are the two subtraction currents i_x and i_y, and the total photocurrent i_T which are defined as shown here

4.3 Calculation of the Signal

To use the supplied code, the user needs only to define the experimental parameters. The relevant parameters are the optical wavelength in vacuum, the refractive indices of the medium and particle, the particle radius (assuming spherical particles), the NA of the objective and condenser, the measured optical power, the optical polarization, and the spatial profile of the incident field in the Laguerre-Gaussian basis. Once these are defined, the code uses functions present in the Optical Tweezers Toolbox [11, 12] to decompose the incident field into an expansion of spherical harmonics, given by the coefficients a and b. Then the T-matrix is calculated for the scattering particle [10]. The location of the axial trapping point is determined following the examples in the toolbox. To find the measured signal, the scattered field coefficients p and q are calculated with the particle at a range of transverse displacements from the trapping point. The coefficients a, b, p and q fully determine the transmitted optical field, and therefore allow calculation of the optical force (which the Optical Tweezers Toolbox was designed for) and the intensity profile which is measured on the detector. The particle tracking response can also be calculated for scatterers which are not homogeneous spheres, with the files "Quadrant_measurement_layered.m" and "Quadrant_measurement_cube.m" respectively calculating the particle tracking response for a layered sphere and a cube.

The optical field is then calculated over an angular grid of points to find the photocurrent in each quadrant. This calculation can be performed with the "farfield" function in the toolbox, although this is not efficient when running a sequence of calculations with the same particle. To reduce the computation time, we use a modified version of this function which calculates two matrices A_p and B_q which implicitly contain the angular grid. The transmitted electric field is determined by the matrix multiplications

$$E(\theta, \phi) = A_p(\theta, \phi) \times (a + 2p) + B_q(\theta, \phi) \times (b + 2q)\,. \tag{4.1}$$

Then, the light intensity is integrated to determine the photon flux present in each of the quadrant detector signals. The particle tracking signals i_x and i_y are determined by subtracting the light incident on one half from the other, as defined in Fig. 4.1b. Additionally, the total photocurrent i_T is calculated as this can be used to determine the particle position along the z axis [3, 14]. These are calculated as photon numbers, so the total photocurrent $i_T = P/(\hbar\omega)$, where P is the detected optical power and $\hbar\omega$ is the energy per photon. Since detectors in real experiments are not perfectly efficient, not every incident photon is measured. To account for this, the theoretical power P should be lower than that used in experiments by a factor given by the detection efficiency. Examples of the calculated photocurrent signals are shown in Fig. 4.2, which agree well with previously published calculations [5, 16, 17].

4.4 Measurement Sensitivity

The sensitivity of most real experiments is limited by electronic noise in the detectors, though there are methods to improve this [2, 21]. With sufficient improvements, the detection will eventually be shot-noise limited. At this point the sensitivity can no longer be improved by reducing the electronic noise, and further improvements require use of alternative strategies [19, 22]. The code presented here determines this shot-noise limit from the calculated detector response to particle displacements, and thus allows the gap between the shot-noise limit and the experimentally achieved sensitivity to be quantified. This also provides a straightforward method to compare the strength of the detection signal that different particles or trapping configurations produce.

The subtraction photocurrent i_x responds linearly for small displacements along x, so in this limit we can define a gain G_x by

$$\langle i_x \rangle = \langle i_T \rangle G_x x, \tag{4.2}$$

where $\langle i_T \rangle$ is the mean total number of photons measured on the detector. If the light is in a coherent state, and there is no additional noise, then the photons follow Poissonian statistics [4] and the quantum shot noise of this measured signal is given by

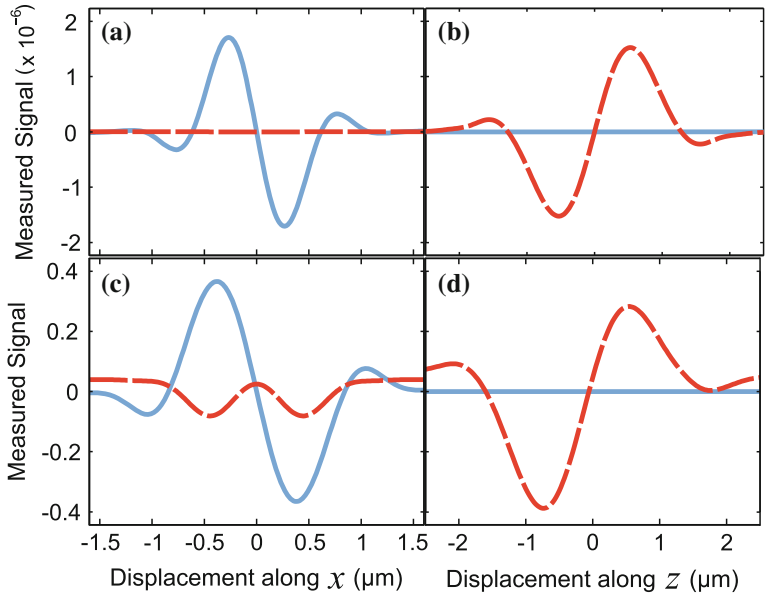

Fig. 4.2 The particle tracking signals photocurrents are shown for a measurement of a 10 nm (**a**, **b**) and a 1 μm (**c**, **d**) diameter polystyrene ($n = 1.58$) sphere in water ($n = 1.33$) as it moves transversely along the x axis (**a**, **c**) and axially along the z axis (**b**, **d**). The setup uses 1064 nm light polarized linearly along the x axis, and with objective and condenser NA of 1.2 and 1.0 respectively. The subtraction signal $i_x / \langle i_T \rangle$ (*solid blue line*) provides effective tracking of particle displacements along the x axis, where $\langle i_T \rangle$ is total photocurrent for the centered particle. The total collected light $(i_T - \langle i_T \rangle) / \langle i_T \rangle$ (*dashed red line*) provides information about the displacement along the z axis, although this is also affected by transverse motion, particularly for large beads (**c**)

$$\langle \Delta i_x^2 \rangle = \langle i_T \rangle. \tag{4.3}$$

Combining Eqs. 4.2 and 4.3, we find that the signal-to-noise ratio is given by

$$\frac{\langle i_x \rangle^2}{\langle \Delta i_x^2 \rangle} = \langle i_T \rangle G_x^2 x^2. \tag{4.4}$$

A displacement is resolvable when it yields a signal-to-noise ratio greater than 1, so the minimum resolvable displacement in units of m/Hz$^{-1/2}$ is

$$x_{\min} = \langle i_T \rangle^{-1/2} G_x^{-1}. \tag{4.5}$$

The gain G_x is defined by the calculated detector response, and this is used in the presented code to reveal the shot noise limit to position sensitivity. A similar calculation finds the shot noise limit along the y and z axes. For the data in Fig. 4.2c, d, for instance, a quadrant measurement which perfectly captures 1 mW of optical power should have a displacement sensitivity at the levels 9.3×10^{-15} and

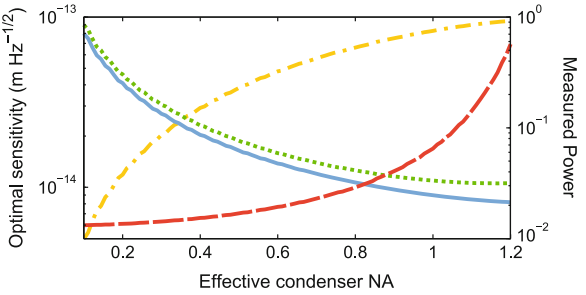

Fig. 4.3 The best displacement resolution possible with a quadrant detector, for a 1 μm polystyrene sphere in water tracked with 1 mW of 1064 nm light polarized linearly along the x axis, which is focused with an NA = 1.2 objective. As the effective condenser NA increases, the sensitivity along the x (*solid blue line*) and y (*green dotted line*) axes improves. The axial sensitivity (*red dashed line*), however, improves with decreasing condenser NA. The proportion of the trapping power which can be collected (*yellow dash-dot*) rises with increasing condenser NA, as this increases the angular range which can enter the detector

$1.7 \times 10^{-14}\mathrm{m/Hz}^{-1/2}$ along the x and z axes respectively. If this is measured with 1 μs time resolution, then the measurement bandwidth is 1 MHz and the minimum resolvable displacements along x and z are respectively 9.3 and 17 pm. Although such sensitivities are impressive, recent experiments have demonstrated a position sensitivity within a factor of 2 of the transverse prediction [2]. It is important to note that both axial and transverse motion effect the sum photocurrent i_T (see Fig. 4.2c), so the axial position cannot be accurately determined without accounting for a transverse displacement. Also, the sum photocurrent is sensitive to laser amplitude noise which cancels from the subtraction signals i_x and i_y. This means that the axial position sensitivity is likely to be further from optimal in a real experiment than the corresponding transverse sensitivities.

The code allows the shot noise limit to sensitivity of particle tracking in all three axes to be quantified for particles of any size, trapped in arbitrary optical fields, and measured with any condenser NA. For instance, the sensitivity attainable is calculated as a function of effective condenser NA, for a fixed objective (NA = 1.2) and 1 mW of measured optical power (shown in Fig. 4.3). In this case, the position sensitivity along the transverse directions improve with NA, while the axial sensitivity per measured photon degrades, as demonstrated in Refs. [3, 16]. As such, the optimal method for three-dimensional particle tracking is to use a quadrant with a large capture angle to monitor the transverse position, while a second bulk detector with a small capture angle monitors the axial position.

4.5 Particle Tracking Beyond Homogeneous Spheres

Although the particles studied in most optical tweezers experiments are homogeneous spheres, it can also be useful to track other types of particles. For instance, multiple layers on a sphere can act as an anti-reflection coating, suppressing back-

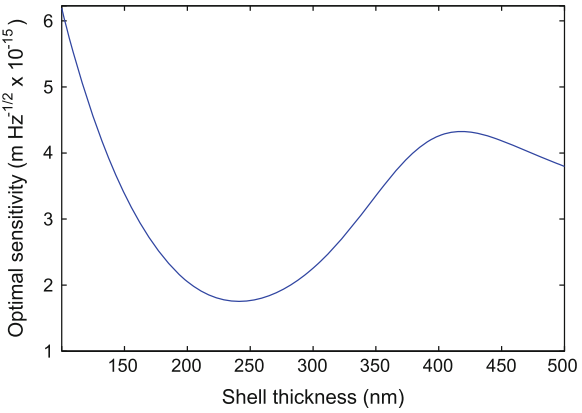

Fig. 4.4 This shows the minimum resolvable displacement with a quadrant detector for an anti-reflection coated bead in water, as a function of the shell thickness. The core diameter (500 nm) and refractive index (2.3), and the shell refractive index (1.78) match those from the experiments in Ref. [7]. In that work, a shell thickness of 230 nm was found to optimize the trapping forces. The calculations here show that this condition also optimizes the particle tracking sensitivity

reflection and improving the trap stability. Such layering allows the stable trapping of high refractive index materials which cannot be trapped in a typical optical tweezers experiment, thus allowing improved trapping forces [7]. Alternatively, some experiments benefit from particles without rotational symmetry. For that case, the code presented here is also capable of characterizing particle tracking with cubic particles.

An example is shown in Fig. 4.4 which shows the minimum resolvable displacement for a layered sphere as a function of the shell thickness. The refractive indices and core size match those of the anti-reflection coated titania bead described in Ref. [7], while the shell thickness is varied. The optimal shell thickness for particle tracking is found to be 230 nm, which coincides with the optimal thickness determined for the trapping force [7]. This is not surprising, as an increased force results in an increased laser deflection, and consequently an improved measurement.

In other experiments, angular momentum is imparted to particles via higher order Laguerre-Gauss modes, which carry orbital angular momentum. Since spherical particles have complete rotational symmetry, the exerted torque is relatively weak compared to the torque exerted on non-symmetric particles [13]. However, because the quadrant detection signal is not trivially related to the particle position in such experiments, a separate field with a camera is typically used to infer its motion. The code presented here allows the quadrant detection signal to be estimated and characterized, as shown in Fig. 4.5. This characterization could allow non-spherical particles to be tracked with the higher bandwidth and sensitivity of quadrant detection. Additionally, this code could also be extended to birefringent particles, provided the scattering T-matrix could be calculated.

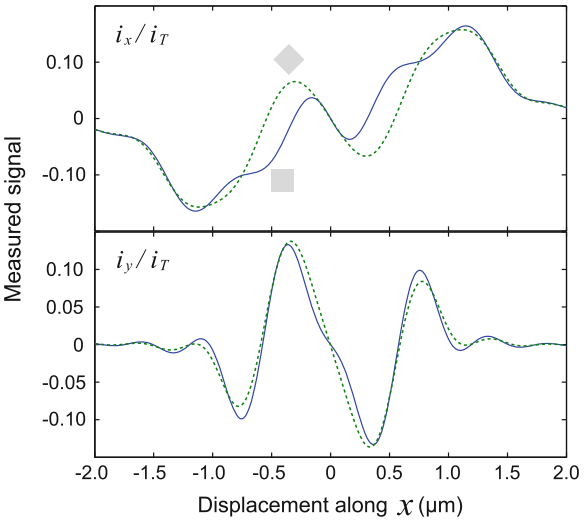

Fig. 4.5 The particle tracking response for a cubic particle trapped in water with circularly polarized light in the LG_{01} mode, similar to the optical setup of an "optical spanner". The cube has 1 μm side length and refractive index of 1.58, and is shown for cube orientations which are straight on (□, *blue line*) and rotated about the optical axis by 45° (◇, *dashed line*). In this case, the signal i_x provides a poorer particle tracking response than does i_y for displacements along the x axis

4.6 Measurement Mode in Quadrant Detection

Although the sensitivity limit derived in Eq. 4.5 appears mathematically distinct from the limit of Eq. 3.23 in Chap. 3, the two are identical. To show this, we express the terms found in Eq. 4.5 in a way which follows the the framework of Chap. 3. The particle is tracked via the subtraction photocurrent, which can be expressed as

$$\langle i_x \rangle = 2\eta \int_{-\infty}^{\infty} \alpha_T^* \psi_{\text{det}}^* \left(\alpha_T \psi_T + \alpha_{\text{scat}} \psi_{\text{scat}}\right) d\mathbf{X}, \tag{4.6}$$

where α_T and α_{scat} are the trapping and scattered amplitudes respectively and η is the detection efficiency. In this case, the detection mode is given by

$$\psi_{\text{det}}(X, Y) = \text{sign}(X)\psi_T(X, Y). \tag{4.7}$$

It is not the absolute value of this subtraction photocurrent which defines the sensitivity, but rather its derivative, given by

$$\frac{d\langle i_x \rangle}{dx}\Big|_{x=0} = 2\eta\alpha_T^*\alpha_{\text{scat}} \int_{-\infty}^{\infty} \psi_{\text{det}}^* \psi'_{\text{scat}} d\mathbf{X} \tag{4.8}$$

$$= 2\kappa^{1/2}\eta|\alpha_T|^2 \text{Re}\{\langle \psi'_{\text{scat}} | \psi_{\text{det}} \rangle\}, \tag{4.9}$$

where we have used $\frac{d\psi_T}{dx} = 0$, $\frac{d\psi_{scat}}{dx}\big|_{x=0} = \psi'_{scat}$ and $\alpha_{scat} = \kappa^{1/2}\alpha_T$. Rearranging the photocurrent found in Eq. 4.2, and using $\langle i_T \rangle = \eta|\alpha_T|^2$, we can now express the photocurrent gain as

$$G_x \equiv \frac{1}{\langle i_T \rangle}\frac{d\langle i_x \rangle}{dx}\Big|_{x=0}, \tag{4.10}$$

$$= 2\kappa^{1/2}\mathrm{Re}\{\langle \psi'_{scat}|\psi_{det}\rangle\}, \tag{4.11}$$

Using this definition of G_x, Eq. 4.5 converges to the limit already found in Eq. 3.23. As expected, although the approach here is simpler and more intuitive than the mathematical framework of Chap. 3, the limit derived is equally rigorous.

4.7 Conclusion

In this chapter we have presented a piece of Matlab code which operates alongside the Optical Tweezers Toolbox to calculate the response of a quadrant detector to particle displacements, and the associated shot-noise limit to displacement sensitivity. The calculation supports particles with arbitrary size, any optical fields and any combination of objective and condenser.

This concludes Part I of the thesis. At this point, the quantum noise limit in particle tracking is well established theoretically, and we turn our attention to developing experimental strategies which can both classically improve the sensitivity, and make optical tweezers compatible with non-classically correlated light.

References

1. C. Bustamante, Y. Chemla, N. Forde, D. Izhaky, Mechanical processes in biochemistry. Annu. Rev. Biochem. **73**(1), 705–748 (2004)
2. I. Chavez, R. Huang, K. Henderson, E.-L. Florin, M.G. Raizen, Development of a fast position-sensitive laser beam detector. Rev. Sci. Instrum. **79**, 105104 (2008)
3. J. Dreyer, K. Berg-Sorensen, L. Oddershede, Improved axial position detection in optical tweezers measurements. Appl. Opt. **43**(10), 1991–1995 (2004)
4. M. Fox, *Quantum Optics*: *An Introduction*, vol. 15 (Oxford University Press, Oxford, 2006)
5. F. Gittes, C.F. Schmidt, Interference model for back-focal-plane displacement detection in optical tweezers. Opt. Lett. **23**(1), 7–9 (1998)
6. Y. Harada, T. Asakura, Radiation forces on a dielectric sphere in the Rayleigh scattering regime. Opt. Commun. **124**(5–6), 529–541 (1996)
7. A. Jannasch, A.F. Demirörs, P.D.J. van Oostrum, A. van Blaaderen, E. Schäffer, Nanonewton optical force trap employing anti-reflection coated, high-refractive-index titania microspheres. Nat. Photon. **6**, 469–473 (2012)
8. J. Lock, Calculation of the radiation trapping force for laser tweezers by use of generalized Lorenz-Mie theory. I. Localized model description of an on-axis tightly focused laser beam with spherical aberration. Appl. Opt. **43**(12), 2532–2544 (2004)

9. J.R. Moffitt, Y.R. Chemla, S.B. Smith, C. Bustamante, Recent advances in optical tweezers. Annu. Rev. Biochem. **77**, 205–228 (2008)
10. T. Nieminen, V. Loke, A. Stilgoe, N. Heckenberg, H. Rubinsztein-Dunlop, T-matrix method for modelling optical tweezers. J. Mod. Opt. **58**(5–6), 528–544 (2011)
11. T. Nieminen, V. Loke, A. Stilgoe, G. Knöner, A. Brańczyk, N. Heckenberg, H. Rubinsztein-Dunlop, Optical tweezers computational toolbox. J. Opt. A: Pure Appl. Opt **9**(8), S196 (2007)
12. T.A. Nieminen, V.L.Y. Loke, A.B. Stilgoe, Y. Hu, G. Knoener, A.M. Brańczyk, Optical tweezers toolbox 1.3 (2013) http://www.physics.uq.edu.au/people/nieminen/software.html
13. T.A. Nieminen, S. Parkin, N.R. Heckenberg, H. Rubinsztein-Dunlop, Optical torque and symmetry. Proc. SPIE **5514**, 254–263 (2004)
14. A. Pralle, M. Prummer, E.-L. Florin, E. Stelzer, J. Hörber, Three-dimensional high-resolution particle tracking for optical tweezers by forward scattered light. Microsc. Res. Tech. **44**(5), 378–386 (1999)
15. A. Rohrbach, E. Stelzer, Trapping forces, force constants, and potential depths for dielectric spheres in the presence of spherical aberrations. Appl. Opt. **41**(13), 2494–2507 (2002)
16. A. Rohrbach, E.H.K. Stelzer, Three-dimensional position detection of optically trapped dielectric particles. J. Appl. Phys. **91**, 5474–5488 (2002)
17. J.W. Tay, M.T.L. Hsu, W.P. Bowen, Quantum limited particle sensing in optical tweezers. Phys. Rev. A **80**(6), 063806 (2009)
18. M.A. Taylor, W.P. Bowen, A computational tool to characterize particle tracking measurements in optical tweezers. J. Opt. **15**(8), 085701 (2013)
19. M.A. Taylor, J. Janousek, V. Daria, J. Knittel, B. Hage, H.-A. Bachor, W.P. Bowen, Biological measurement beyond the quantum limit. Nat. Photon. **7**, 229–233 (2013)
20. M.A. Taylor, J. Knittel, W.P. Bowen, Fundamental constraints on particle tracking with optical tweezers. New J. Phys. **15**, 023018 (2013)
21. M.A. Taylor, J. Knittel, W.P. Bowen, Optical lock-in particle tracking in optical tweezers. Opt. Express **21**, 8018–8024 (2013)
22. M.A. Taylor, J. Knittel, M.T.L. Hsu, H.-A. Bachor, W.P. Bowen, Sagnac interferometer-enhanced particle tracking in optical tweezers. J. Opt. **13**, 044014 (2011)

Part II
Classically Optimizing Sensitivity

Shot noise in particle tracking arises due to quantum noise in the optical fields. Without resorting to quantum resources, it may be suppressed by efficiently measuring the scattered photons which carry information about the desired biological process while minimizing detection of background photons. Many biological imaging techniques implicitly rely on this principle, including dark-field microscopy and florescence imaging, where background photon counts are greatly suppressed by spatially or spectrally separating the illumination field from the light carrying the desired signal.

Part II of this thesis presents techniques to improve the detection efficiency of the scattered photons. Chapter 5 demonstrates that the background photons can be suppressed through use of interferometry, without degradation of the scattered field. This allows higher field intensities without saturation of the detector, and consequently, an increased flux of scattered photons. Following this, Chap. 6 presents a new particle tracking method based on homodyne measurement, which thus allows tailoring of the detection mode for improved measurement efficiency. This method also improves the prospects for quantum enhanced particle tracking, as discussed earlier in Chap. 3.

In Chap. 7, a novel lock-in measurement is demonstrated which evades low frequency laser and electronic noise which could otherwise obscure the particle tracking signal. This allows shot-noise limited measurements at low frequencies, which could be beneficial to a wide range of classical experiments, and is essential in any attempt to achieve sub-shot noise limited sensitivity.

Chapter 8 then discusses the use of dark-field microscopy. Dark-field microscopy spatially separates the illuminating field from the detection, and allows a vast improvement in contrast. However, while the illumination can be completely suppressed at the detector, some background photons from extraneous scattering centers still remain. In this chapter, we show that the scattering background can also be suppressed by optimizing the illumination angle.

Finally, Chap. 9 provides an overview of the strategies used in the field to achieve high sensitivity measurements in optical tweezers. The field of optical

tweezers has seen tremendous progress over the past three decades, and a great number of the problems which any high precision experiment will face have already been addressed elsewhere. This chapter summarizes some of the expertise of the field. If a quantum enhanced particle tracking system is to be built which can outperform its classical competitors, it will be essential to avoid the pit-falls which have already been resolved in classical experiments.

Chapter 5
Interferometer Enhanced Particle Tracking

This chapter presents a novel interferometric method to filter unwanted light from detection. This allows a corresponding increase in the flux of scattered photons which can be measured without saturating the detector. This chapter contains material included in the following publication [12].

5.1 Basic Concept

Particle tracking sensitivity in optical tweezers is often optimized by using the maximum optical power which the sample under study can permit. In many cases this incident power exceeds the saturation threshold of the detector, and particle tracking measurements require an attenuator to be placed in the beam between the optical tweezers and the detector. While this attenuates the trapping beam and enables measurement, it also discards some of the light which scattered from the particle, degrading the detection sensitivity. An equivalent method is to add a second beam for use in particle tracking which is orthogonal to the trapping field either in polarization [8] or frequency [9]. Here we present an alternative approach, in which interferometry is used to filter unscattered photons from the detection, thus increasing the scattered photon number which can be measured without saturating the detector.

This is related to a method already used to improve the sensitivity of optical tweezers, in which the particle is tracked from measurement of the back-scattered rather than forward-scattered light. The bulk of the trapping light is then separated from the detector, with a weak back-reflection from the sample chamber acting as the local oscillator. This substantially reduces the detected trapping field intensity, reducing the shot noise with relatively little degradation of the detected signal [4, 6]. However, this technique does not allow classically optimal measurement, as the forward-scattered light contains the bulk of the information (see Chap. 2). Also, the local oscillator will be divergent with respect to the scattered field, as the stable trapping point is further from the objective than the focus of the reflected trapping

M. Taylor, *Quantum Microscopy of Biological Systems*, Springer Theses,
DOI 10.1007/978-3-319-18938-3_5

field. This will necessarily ensure non-optimal mode overlap and will limit the efficiency with which information can be extracted.

We apply Sagnac interferometry to enhance the detection of particles in optical tweezers, extending a recent demonstration of Sagnac interferometer based phase plate characterization [11]. In principle, this approach allows near-optimal measurements of bright optical fields. It requires the use of counter-propagating trap fields which are not typically used, but which improves the trap stability, as is necessary in some instances. One such situation is when trapping high refractive index particles [13, 14], which are strong scatterers. The use of counter-propagating traps cancels the radiation pressure in the direction of propagation and enables axial trapping. Also, since counter-propagating traps are typically much longer than the size of the particles they hold, they can confine multiple particles to a single trap and allow study of the multiparticle dynamics. In this case, the interaction of a single optical mode with multiple particles can give rise to an effective optical force between the particles which is stronger than the optical trap for a single particle [2, 10]. Another situation where a counter-propagating trap is necessary is when imaging the sample from the side [7]. In this case, lower numerical aperture (NA) lenses are required to increase the sample-objective separation. This reduces the trapping force, particularly in the axial direction, which can make a single-beam trap unstable.

With optical tweezers embedded in a Sagnac interferometer, selective interference attenuates the trapping field and hence reduces the detection shot noise, substantially improving the detection SNR when compared to using a standard attenuator. The particle tracking SNR is enhanced by a factor which increases as the interferometer visibility approaches 100 %, up to a maximum enhancement defined by the ratio of the trapping field power to the detector saturation threshold. In an experimental demonstration of this, optical tweezers were embedded within a Sagnac interferometer with a visibility of 93 %. This should allow the signal-to-noise ratio (SNR) to be enhanced by a factor of up to 29, which in the dipole scattering regime would enable tracking of 1.7 times smaller particles than the equivalent standard optical tweezers scheme.

5.2 Sensitivity of Particle Tracking

To compare the sensitivity achievable with direct detection of the field (Fig. 5.1a) to that achievable with Sagnac interferometry (Fig. 5.1b), we first calculate the sensitivity achievable with direct detection. The $\hat{\mathbf{Z}}$ axis is defined as the direction of propagation of the laser beam, $\hat{\mathbf{Y}}$ as normal to the plane of the diagrams in Fig. 5.1, and $\hat{\mathbf{X}}$ by $\hat{\mathbf{X}} = \hat{\mathbf{Y}} \times \hat{\mathbf{Z}}$, with the input field polarized along $\hat{\mathbf{X}}$. We also assume that the input trapping field E_0 is symmetric on reflection, so $E_0(X, Y) = E_0(-X, Y)$.

Throughout this work it is useful to separate the electric fields into normalized real modes $\psi(X, Y)$ and complex amplitudes A, such that

$$E_n(X, Y) = A_n \psi_n(X, Y), \tag{5.1}$$

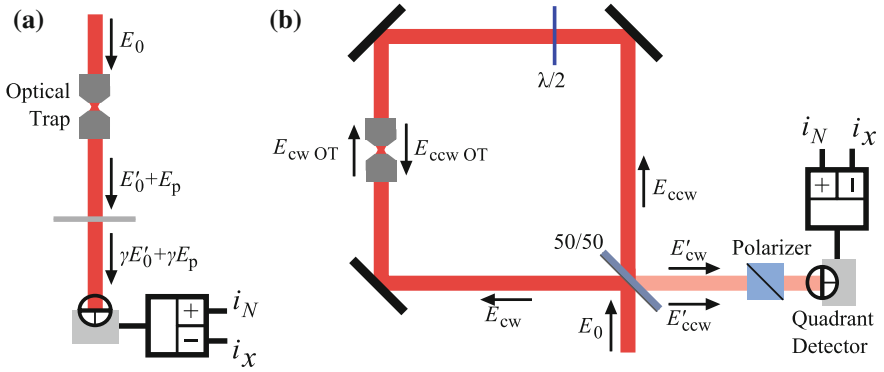

Fig. 5.1 Layout of the two optical tweezers detection schemes under comparison. **a** Direct detection, where the field enters the optical trap, interacts with the particle, and is then attenuated by a factor γ before detection on a quadrant detector. **b** Sagnac interferometer enhanced particle tracking, by contrast, uses interferometry instead of an attenuator to reduce the field intensity. The trapping field is split at the beamsplitter (50/50), with the transmitted field E_{ccw} traveling counterclockwise around the Sagnac interferometer, and the reflected field E_{cw} traveling clockwise. A half waveplate is used to prevent the fields from forming a standing wave in the optical trap. Once the fields reach the beam splitter again they recombine and interfere. The quadrant photodiode detects the light, producing sum and difference photocurrents i_N and i_x

where n is an arbitrary subscript, and ψ_n is normalized such that

$$\int_{-\infty}^{\infty}\int_{-\infty}^{\infty} \psi_n(X,Y)^2 dX\, dY \;=\; 1. \tag{5.2}$$

To begin with, we consider the fields involved in an experiment which utilizes direct detection, as shown in Fig. 5.1a. In this case, the field $E_0(X,Y)$ enters the optical trap, where it is distorted by the trapping optics and the particle into $E'_0(X,Y)$, and where some light scatters from the trapped particle into an antisymmetric field component $E_p(X,Y)$. The symmetric component of the scattered field is to first order independent of particle position, and is included as part of the distortion of the trapping field. After this interaction the field propagating to the detector is given by

$$\mathbf{E}(X,Y) \;=\; \left(E'_0(X,Y) + E_p(X,Y)\right)\hat{\mathbf{X}} \tag{5.3}$$

It is useful to separate the distorted trapping field into symmetric and antisymmetric components with mode shapes $\psi_{0,s}$ and $\psi_{0,a}$ respectively. Using the notation of Eq. 5.1, and neglecting the common polarization, the distorted trapping field and scattered field are respectively given by

$$E'_0(X,Y) = A_0\left(\sigma_s\psi_{0,s}(X,Y) + \sigma_a\psi_{0,a}(X,Y)\right), \tag{5.4}$$

$$E_p(X,Y) = \kappa_a\psi_p(X,Y). \tag{5.5}$$

Here, σ_s, σ_a and κ_a respectively represent the proportion of the incident trapping field which enters the symmetric and antisymmetric components of the trap mode, and the antisymmetric scattered mode. The scattered field depends on the particle position x implicitly, with $\kappa_a \propto x$ for small particle displacements. Here we work in the experimentally relevant limit that the proportion of the trapping field which enters the antisymmetric modes is very small, or equivalently, $\{\kappa_a,\ \sigma_a\} \ll 1$. Due to their symmetry, the modes have the properties

$$\psi_{0,s}(X, Y) = \psi_{0,s}(-X, Y) \tag{5.6}$$

$$\psi_{0,a}(X, Y) = -\psi_{0,a}(-X, Y) \tag{5.7}$$

$$\psi_p(X, Y) = -\psi_p(-X, Y). \tag{5.8}$$

The fields then propagate through an attenuator with transmission of γ, which for simplicity includes the loss of both the optical trap and the attenuator. After this, the mean photon number flux reaching each position in the detector is given by

$$\langle n(X, Y)\rangle = \frac{\epsilon_0 \lambda}{2h}\gamma E^*(X, Y)E(X, Y), \tag{5.9}$$

where h is Planck's constant and ϵ_0 is the vacuum permittivity. This is detected on a quadrant detector, and subtraction of the resulting photocurrents is performed in the standard manner to infer the position. We assume that the detector size is large compared to the beam size, such that clipping can be neglected. The sum and difference photocurrents are then given by

$$\langle i_T\rangle = \int_{-\infty}^{\infty}\int_{-\infty}^{\infty} \langle n(X, Y)\rangle dX\, dY \tag{5.10}$$

and

$$\langle i_x\rangle = \int_{-\infty}^{\infty}\int_{0}^{\infty} \langle n(X, Y)\rangle dX\, dY - \int_{-\infty}^{\infty}\int_{-\infty}^{0} \langle n(X, Y)\rangle dX\, dY, \tag{5.11}$$

where the photocurrents $\langle i_T\rangle$ and $\langle i_x\rangle$ are in units of electrons per second. $\langle i_T\rangle$ is the mean total photocurrent generated by the light hitting the detector. This also defines the shot noise variance $\Delta^2 i_T$, which for shot noise limited detection is the noise on the position measurement. This follows from a quantum treatment of the optical fields, as described in Chap. 3, and also follows from a simple assumption of Poissonian statistics for the detected photons [3]. Since the distortion of the field at the optical trap is represented as a lossless process, the total mean photocurrent is given by

$$\Delta^2 i_T^{\mathrm{dir}} = \langle i_T^{\mathrm{dir}} \rangle = \frac{\epsilon_0 \lambda}{2h} \gamma A_0^2, \tag{5.12}$$

with A_0 set to be real without loss of generality. An identical result also follows from a quantum treatment of the optical fields with shot noise being the result of vacuum noise, as described in Chap. 3. The mean photocurrent difference can be found in a similar manner. Since it is obtained by subtracting the flux on one half of the detector from that on the other, intrinsically symmetric terms such as $\psi_{0,s}^2$ and $\psi_{0,a}^2$ can be ignored. The result is that

$$\langle i_x^{\mathrm{dir}} \rangle = 2 \frac{\epsilon_0 \lambda}{h} \gamma A_0^2 \left(\int_{-\infty}^{\infty} \int_{0}^{\infty} \mathrm{Re}\{\sigma_s^* (\kappa_a \psi_p + \sigma_a \psi_{0,a}) \psi_{0,s}\} dX\, dY \right), \tag{5.13}$$

where only one integral is explicitly included because of the symmetries of the fields. To simplify this expression, we define overlap integrals η_p and η_0 as

$$\eta_p = 2 \int_{-\infty}^{\infty} \int_{0}^{\infty} \psi_p \psi_{0,s} dX\, dY, \tag{5.14}$$

and

$$\eta_0 = 2 \int_{-\infty}^{\infty} \int_{0}^{\infty} \psi_{0,a} \psi_{0,s} dX\, dY. \tag{5.15}$$

Using these, Eq. 5.13 simplifies to

$$\langle i_x^{\mathrm{dir}} \rangle = \frac{\epsilon_0 \lambda}{h} A_0^2 \left(\eta_p \mathrm{Re}\{\kappa_a \sigma_s^*\} + \eta_0 \mathrm{Re}\{\sigma_a \sigma_s^*\} \right). \tag{5.16}$$

The integrals η_p and η_0 determine how effectively the measurement captures the antisymmetric component of the scattered field and the objective distortion, respectively. Provided the distortion introduced by the objectives is static, its contribution to the subtraction photocurrent is to add a constant offset which effects the device calibration but does not influence the position sensitivity. Neglecting the offset due to distortion, this expression provides the measurement signal and Eq. 5.12 the shot noise variance, such that the shot noise limited SNR for particle tracking in the x direction is

$$\mathrm{SNR}_x^{\mathrm{dir}} = \frac{\langle i_x^{\mathrm{dir}} \rangle^2}{\Delta^2 i_N^{\mathrm{dir}}} = \frac{\epsilon_0 \lambda}{2h} \gamma A_0^2 \eta_p^2 \mathrm{Re}\{\kappa_a \sigma_s^*\}^2. \tag{5.17}$$

5.3 Theory of Sagnac Enhancement

The scheme proposed here utilizes optical tweezers embedded within a sagnac interferometer, as shown in Fig. 5.1b. The input optical field E_0 is split by a beam splitter, resulting in two optical fields propagating through the Sagnac interferometer, E_{ccw} traveling counterclockwise and E_{cw} traveling clockwise. These fields form an optical trap at the focus of the objective lenses. In a typical Sagnac interferometer, the two fields would form a standing wave, although here one polarization is rotated by 90° with a half waveplate to prevent this. For an optical trap, a standing wave provides some advantages; it greatly increases the axial field gradient, thereby improving the axial trap strength [15]. Since particles are trapped at maxima of the field, the trapping point will be at an antinode of the field. This intensifies the field at the particle, generating more scattered light and improving the measurement sensitivity. However, any phase drift within the interferometer will shift the position of the trapping point, effectively dragging the particle in and out of focus. If the phase drift is controlled to keep the trapping location stable, the waveplate is unnecessary, with the correct treatment included in the paper published on this method [12]. Here, we include it to reduce the experimental complexity required for stable trapping.[1]

When a particle is trapped, it will scatter light from both fields, modifying their spatial profiles. The fields then recombine at the beam splitter, with the trapping field constructively interfering when returning out the beam splitter port of incidence, henceforth termed the *light port*, as is standard for a Sagnac interferometer. The quadrant detector used to extract particle position information is placed at the other *dark port*, where the trapping field destructively interferes. By contrast, the component of the scattered field containing particle position information constructively interferes when leaving the dark port, provided the interferometer has an odd number of internal reflections.

The number of interferometer mirrors is kept general in the following theory to illustrate the necessity for an odd number of internal reflections. Phase shifts upon hard boundary reflection from mirrors have no effect on the interference of the clockwise and counterclockwise fields, as both fields experience the same number of reflections. For simplicity we therefore neglect them.

We now calculate the particle tracking sensitivity achievable with sagnac interferometry, following a similar approach to that used above for direct detection. The enhancement achievable with interferometry depends crucially on the interferometer visibility. Although there are several experimental constraints which can degrade the visibility, here we represent these with imperfection in the beamsplitter ratio, and also the field distortion due to the optical trap. The transmittance and reflectance of the beam splitter are given by T and R respectively, so that the transmitted and reflected fields, E_{ccw} and E_{cw}, are given by

$$\mathbf{E}_{\mathrm{ccw}}(X, Y) = \sqrt{T} E_0(X, Y)\hat{\mathbf{X}} \tag{5.18}$$

[1] The theory in this chapter differs slightly from its associated publication, which described Sagnac interferometer enhanced optical tweezers without the waveplate, and with the standing wave.

and

$$\mathbf{E}_{\mathrm{cw}}(X,Y) \;=\; -\sqrt{R}E_0(X,Y)\hat{\mathbf{X}}, \tag{5.19}$$

where the negative sign is due to a hard boundary reflection at the beam splitter. The counterclockwise traveling field propagates a distance of L_1 to the optical tweezers, and picks up a phase shift of e^{ikL_1}, where $k = \frac{2\pi}{\lambda}$ is the wavenumber. Likewise the clockwise propagating field picks up a phase shift of e^{ikL_2} as it travels a distance of L_2 to the optical trap, while additionally changing polarization from $\hat{\mathbf{X}}$ to $\hat{\mathbf{Y}}$ as it passes the waveplate. The electric field at the trapping point is then given by

$$\mathbf{E}_{\mathrm{OT}}(X,Y) \;=\; \left(e^{ikL_1}\sqrt{T}\hat{\mathbf{X}} - e^{ikL_2}\sqrt{R}\hat{\mathbf{Y}}\right)E_0(X,Y). \tag{5.20}$$

The effect of distortion, clipping and loss within the objectives and sample chamber then modifies the shape of the circulating fields in a similar manner to that described for direct detection. The circulating fields will be equal in the two directions of propagation, as they are equal as they enter the trap, and interact with the same optical setup. After interacting with the optical trap the counterclockwise and clockwise propagating fields are given by

$$\begin{aligned}\mathbf{E}_{\mathrm{ccw\ OT}}(X,Y) \;=\; & e^{ikL_1}\sqrt{T}A_0\left(\sigma_s\psi_{0,s}(X,Y)+\sigma_a\psi_{0,a}(X,Y)+\kappa_a\psi_p(X,Y)\right)\hat{\mathbf{X}} \\ & - e^{ikL_2}\sqrt{R}A_0\kappa_b\psi_b(X,Y)\hat{\mathbf{Y}}, \end{aligned}\tag{5.21}$$

$$\begin{aligned}\mathbf{E}_{\mathrm{cw\ OT}}(X,Y) \;=\; & -e^{ikL_2}\sqrt{R}A_0\left(\sigma_s\psi_{0,s}(X,Y)+\sigma_a\psi_{0,a}(X,Y)+\kappa_a\psi_p(X,Y)\right)\hat{\mathbf{Y}} \\ & + e^{ikL_1}\sqrt{T}A_0\kappa_b\psi_b(X,Y)\hat{\mathbf{X}}, \end{aligned}\tag{5.22}$$

where κ_b denotes the proportion of the trapping field which scatters backward into the mode $\psi_b(X,Y)$.

Each reflection off a mirror causes a reflection of the beam profile in the x direction. This is shown graphically in Fig. 5.2. As seen in Eq. (5.8), this results in a change in the sign of the antisymmetric modes $\psi_{0,a}$ and ψ_p, but does not effect the trapping mode $\psi_{0,s}$. As a result, the antisymmetric field components which contain the particle

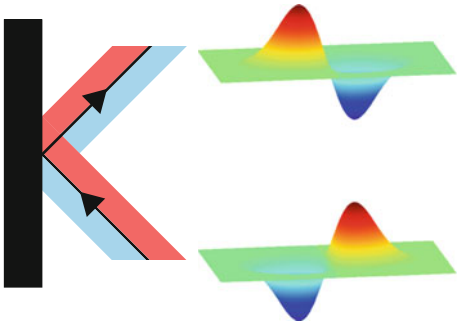

Fig. 5.2 Phase induced by reflection of an antisymmetric field off a mirror. *Left* Reflection of an antisymmetric field off a mirror. *Right* Spatial profiles of field before and after reflection. The example spatial profile shown here is a TEM01 mode

position information pick up an additional π phase shift on each reflection compared to the symmetric field components.

After interaction with the particle, both counterclockwise and clockwise fields propagate back to the beam splitter, such that they both travel a distance $L = L_1 + L_2$. The counterclockwise field now passes the waveplate which switches the polarization between $\hat{\mathbf{X}}$ and $\hat{\mathbf{Y}}$. The counterclockwise and clockwise fields experience g and f reflections respectively before reaching the beam splitter, with each reflection inducing a π phase shift on their antisymmetric components. Dropping the explicit spatial dependence for the sake of brevity, with with $\psi_n(X, Y)$ written as ψ_n throughout, the fields at the beam splitter are then

$$\mathbf{E}'_{\text{ccw}} = e^{ikL}\sqrt{T}A_0\left(\sigma_s\psi_{0,s} + (-1)^g(\sigma_a\psi_{0,a} + \kappa_a\psi_p)\right)\hat{\mathbf{Y}} - e^{2ikL_2}\sqrt{R}A_0\kappa_b\psi_b\hat{\mathbf{X}}, \tag{5.23}$$

$$\mathbf{E}'_{\text{cw}} = -e^{ikL}\sqrt{R}A_0\left(\sigma_s\psi_{0,s} + (-1)^f(\sigma_a\psi_{0,a} + \kappa_a\psi_p)\right)\hat{\mathbf{Y}} + e^{2ikL_1}\sqrt{T}A_0\kappa_b\psi_b\hat{\mathbf{X}}. \tag{5.24}$$

The field leaving the light port is given by $E_L = -\sqrt{R}E'_{\text{ccw}} + \sqrt{T}E'_{\text{cw}}$, where the negative sign in the first expression is due to the reflection of the counterclockwise field from a hard boundary at the beam splitter. Similarly, the field leaving the dark port is given by $E_D = \sqrt{T}E'_{\text{ccw}} + \sqrt{R}E'_{\text{cw}}$, which can be expanded as

$$\begin{aligned}\mathbf{E}_D = A_0[(T-R)\sigma_s\psi_{0,s} + A_0\left((-1)^gT - (-1)^fR\right)(\sigma_a\psi_{0,a} + \kappa_a\psi_p)]e^{ikL}\hat{\mathbf{Y}} \\ + \sqrt{TR}A_0\kappa_b\psi_b\left(e^{2ikL_1} - e^{2ikL_2}\right)\hat{\mathbf{X}}.\end{aligned} \tag{5.25}$$

The back-scattered term which is polarized along the $\hat{\mathbf{X}}$ axis is removed with a polarizer, and we now neglect both the global phase e^{ikL} and polarization $\hat{\mathbf{Y}}$. Notice that all symmetric field components which exit through the dark port suffer destructive interference due to the prefactor $(T - R)$, and cancel exactly when $T = R$, which corresponds to perfect interferometer visibility. By contrast, constructive interference can be achieved for the antisymmetric scattered field through an appropriate choice of g and f. The term in Eq. (5.25) relating to the antisymmetric scattered field can be simplified by defining the difference in the number of reflections experienced by the clockwise and counterclockwise fields after interaction with the particle, $m = f - g$, so that

$$\mathbf{E}_D = A_0(T-R)\sigma_s\psi_{0,s} + (-1)^gA_0\left(T - (-1)^mR\right)(\sigma_a\psi_{0,a} + \kappa_a\psi_p). \tag{5.26}$$

It apparent that the sign of the antisymmetric coefficient will depend on g. The only effect this has is to alter the sign of the detected photocurrent i_x, with the sensitivity of the measurement left unchanged. Hence, without loss of generality we set $g = 2$ as in Fig. 5.1. We can then find

$$E_{D,\,m\ \text{odd}} = A_0(T-R)\sigma_s\psi_{0,s} + A_0\,(T+R)\,(\sigma_a\psi_{0,a} + \kappa_a\psi_p), \tag{5.27}$$

$$E_{D,\,m\ \text{even}} = A_0(T-R)\sigma_s\psi_{0,s} + A_0(T-R)(\sigma_a\psi_{0,a} + \kappa_a\psi_p). \tag{5.28}$$

In the case that m is odd, the antisymmetric part of the scattered field constructively interferes at the dark port, as shown by the presence of a $(T+R)$ prefactor on ψ_a. In contrast, if m is even all of the fields destructively interfere, as shown by the $(T-R)$ prefactor. SNR enhancement requires constructive interference of the antisymmetric term. If the total number of mirrors in the interferometer is odd, m is odd and this condition is met. Henceforth we only consider this case, with A_0 set to be real without loss of generality. The total photocurrent can now be evaluated as

$$\langle i_T\rangle = \frac{\epsilon_0\lambda}{2h}A_0^2\left((T-R)^2|\sigma_s|^2 + (T+R)\iint|\sigma_a\psi_{0,a} + \kappa_a\psi_p|^2 dX\,dY\right). \tag{5.29}$$

This expression is somewhat more complicated than Eq. 5.12 due to the general nature of the field distortion. However, it can be simplified in the limiting case that the objective distortion is almost perfectly symmetric. Then, neglecting antisymmetric terms of $O(2)$, we find that

$$\Delta^2 i_T \approx \langle i_T\rangle = \frac{\epsilon_0\lambda}{2h}A_0^2(T-R)^2|\sigma_s|^2, \tag{5.30}$$

The difference photocurrent is also evaluated as

$$\langle i_x\rangle = 2\frac{\epsilon_0\lambda}{h}A_0^2(T-R)\,(T+R)\int_{-\infty}^{\infty}\int_{0}^{\infty}\text{Re}\{\sigma_s^*(\kappa_a\psi_p + \sigma_a\psi_{0,a})\psi_{0,s}\}dX\,dY. \tag{5.31}$$

$$= \frac{1}{\gamma}(T-R)\,(T+R)\,\langle i_x^{\text{dir}}\rangle \tag{5.32}$$

This then yields a shot-noise limited SNR for particle tracking in the x direction of

$$\text{SNR}_x = \frac{\langle i_x\rangle^2}{\Delta^2 i_N} = \frac{\epsilon_0\lambda}{2h}\,(T+R)^2\,A_0^2\eta_p^2 \tag{5.33}$$

$$= (T+R)^2\,\gamma^{-2}\text{SNR}_x^{\text{dir}}. \tag{5.34}$$

Since typical trapping powers are of the order 1 W (for example see Ref. [1]), and typical photodiodes used for detection have saturation thresholds below 10 mW,[2] the optical field is attenuated prior to detection. To enable a fair comparison between the two schemes, the attenuation in the direct detection is set to $\gamma = (T-R)$ such that the total photocurrents in Eqs. 5.12 and 5.30 are equal. With this condition, the interferometric SNR is substantially enhanced when $T \approx R$. Explicitly, the SNR

[2]For example, the commonly used Thorlabs PDQ30C quadrant detector has a 1 mW saturation threshold.

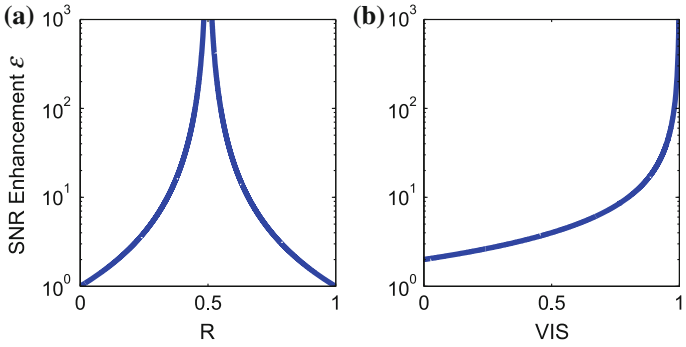

Fig. 5.3 SNR enhancement of the Sagnac interferometer over direct detection, as a function of, **a** beam-splitter reflectivity and, **b** Sagnac interferometer visibility. $T + R = 1$ has been used, which assumes there is no loss in the Sagnac beam splitter

enhancement factor $\mathcal{E}$ for the Sagnac over direct detection is

$$\mathcal{E} = \frac{\mathrm{SNR}_x}{\mathrm{SNR}_x^{\mathrm{dir}}} = \frac{(T+R)^2}{(T-R)^2} \tag{5.35}$$

which is shown as a function of R in Fig. 5.3a, assuming a loss-less beam splitter such that $T = 1 - R$. Note that $\mathcal{E}$ tends to infinity as $(T-R)$ goes to zero. This is unrealistic since it corresponds to perfect interference on the Sagnac beam splitter, which requires perfect polarization and spatial overlap as well as $R = T$. A physically useful parameter which includes various non-ideal effects is the interferometer visibility VIS, given by

$$\mathrm{VIS} = \frac{\langle n_L \rangle - \langle n_D \rangle}{\langle n_L \rangle + \langle n_D \rangle} = 1 - 2\frac{(T-R)^2}{(T+R)^2}, \tag{5.36}$$

where $\langle n_L \rangle$ and $\langle n_D \rangle$ respectively denote the photon numbers at the light and dark ports. The visibility quantifies the mode overlap between the two beams in the interferometer, with a visibility of 1 indicating perfect mode matching. Using this and Eq. (5.35), we can express the enhancement factor in terms of the visibility as

$$\mathcal{E} = \frac{2}{(1 - \mathrm{VIS})}, \tag{5.37}$$

where we have assumed a lossless beamsplitter, such that $T + R = 1$. The enhancement $\mathcal{E}$ as a function of VIS is shown in Fig. 5.3b. We see that as the mode overlap goes to unity, the enhancement again approaches infinity.

In realistic experiments, the interferometer visibility may be limited by something other than a non-ideal beamsplitter ratio. However, the expression derived in Eq. 5.37 holds for any sufficiently high experimental visibility. For instance, the visibility may

be limited by non-optimal polarization control. In this case, one of the fields in the interferometer reaches the beamsplitter polarized along $\hat{\mathbf{Y}}$ while the other is polarized along $\sqrt{\eta}\hat{\mathbf{Y}} + \sqrt{1-\eta}\hat{\mathbf{X}}$, such that the overlap is $\sqrt{\eta}$. If all else is ideal, this results in an interferometer visibility of $VIS_p = \sqrt{\eta}$, and a SNR enhancement of.

$$\mathcal{E}_p = \frac{2}{(1-\sqrt{\eta})}. \tag{5.38}$$

This results in a relation between the enhancement and visibility which is identical to Eq. 5.37. Back-reflections from the sample coverslip can also present an additional complication to experiments. While these should in principle be eliminated with the polarizing beamsplitter, perfect isolation is not possible if the optical trap includes some birefringence which rotates the polarization of the circulating fields. As with imperfect polarization control, realistic levels of back-reflection degrades the SNR enhancement in a way that is fully accounted for in Eq. (5.37) from the modest degradation to the visibility.

To show this, the back-reflected field in Eq. 5.25 can be included in the detection rather than being perfectly removed with the polarizing beamsplitter. Should this back-reflection interfere with the other fields, it could add substantial complexity to the analysis. However, in addition to being orthogonal in polarization, it will also have low spatial overlap with the other fields, as reflections from the coverslip are not collimated, but rather diverge rapidly. Thus, the addition of a back-reflected field can be treated as a perturbation on the total light intensity which contributes to the shot-noise while leaving the detection unchanged.

Within these constraints the back-reflected fields can be treated as a separate additional Michelson interferometer which introduces some light to the dark port. The added intensity depends on the phase $\left(e^{2ikL_1} - e^{2ikL_2}\right)$. Taking the worst-case scenario, in which this is equal to 2, we find the total photocurrent to gain an additional photon flux of

$$I_b = \left(\frac{\epsilon_0 \lambda}{2h} A_0 |\kappa_b|\right)^2 \tag{5.39}$$

which acts to degrade the interferometer visibility by

$$\mathrm{VIS}_r = \mathrm{VIS} - |\kappa_b|^2. \tag{5.40}$$

A separate calculation of the SNR, including the increase in shot noise due to the back-reflected intensity, gives

$$\mathrm{SNR}_r = \frac{\mathrm{SNR}}{(1 + |\kappa_b|^2/(T-R)^2)}, \tag{5.41}$$

which gives the same change in SNR enhancement as does substituting the modified visibility in Eq. 5.40 into Eq. 5.37. This means that the expression for SNR

enhancement as a function of interferometer visibility in Eq. 5.37 already accounts for back-reflections.

Antisymmetric distortion of the trapping field at the optical trap also degrades the interferometer visibility. For sufficiently high visibility, this merely adds unwanted shot-noise and a spurious offset to the measured signal. As calculated for back-reflections above, the SNR enhancement accounts for the addition of unwanted fields such as this. However, if the antisymmetric distortion becomes large, such that it dominates the visibility, the approximation in Eq. 5.30 fails, and the SNR is not accurately predicted by in Eq. 5.37.

The maximum enhancement possible is limited by the ratio of the trapping field intensity to the detector saturation threshold. In order to compare Sagnac interferometer based detection to standard detection, the optical intensity in standard detection is attenuated by a factor of $(T-R)^2$. However, once the optical power is below the saturation threshold of the detector, it is no longer sensible to apply more attenuation. Once this limit has been reached, no further advantage can be had from improving the visibility of the Sagnac, since there is no requirement to further reduce the optical power reaching the detector.

Practically, the maximum enhancement conferred by the Sagnac interferometer is achieved when it is used to reduce the detected light intensity to the point that the total photocurrent defined in Eq. 5.30 is just within the saturation threshold $\langle i_{\mathrm{sat}}\rangle$,

$$\langle i_{\mathrm{T}}\rangle = \frac{\epsilon_0 \lambda}{2h}(T-R)^2 A_0^2 = \langle i_{\mathrm{sat}}\rangle. \tag{5.42}$$

Rearranging this, we find

$$(T-R)^2 = \frac{2h}{\epsilon_0 \lambda}\frac{\langle i_{\mathrm{sat}}\rangle}{A_0^2}. \tag{5.43}$$

If we substitute this into Eq. (5.35), and model a lossless, ideal beamsplitter with $T = R = \frac{1}{2}$, we find that the maximum enhancement is

$$\mathcal{E}_{\mathrm{max}} = \frac{\epsilon_0 \lambda}{2h}\frac{A_0^2}{\langle i_{\mathrm{sat}}\rangle} = \frac{\langle i_{T\,0}\rangle}{\langle i_{\mathrm{sat}}\rangle}, \tag{5.44}$$

where $\langle i_{T\,0}\rangle$ is the mean photocurrent that would result from the trapping field without attenuation. The condition that $T = R = \frac{1}{2}$ is not critical for this calculation, as this limit will be approximately accurate for any splitting ratio which is close to 50/50. The value of this limit will depend on the trapping field intensity and the specific detector used. For instance, if a trapping intensity of 1 W is used as in Ref. [1], and detection occurs on a detector with 1 mW saturation threshold, such as the Thorlabs PDQ30C quadrant detector, the absolute maximum enhancement possible would be approximately 1000. It is unlikely that an interferometer could be constructed which is capable of exceeding this maximum enhancement, so this upper limit is not likely to constrain any real experiments.

Finally, we note that the described theory is only valid for the enhancement the x position detection, because the interfered beams are only flipped in the x direction on reflection against interferometer mirrors. While there is some enhancement of the y position detection, this is not independent of x, as we would like. Reflections of both the x and the y directions are required in order to fully extend this technique to enhanced x–y position detection. This can be achieved with a 3-dimensional layout of mirrors.

5.4 Experimental Verification

The theory presented in this chapter shows that antisymmetric fields generated within a Sagnac interferometer are selectively directed to the dark port of the interferometer. By implementing optical tweezers within a Sagnac interferometer, this property can be used to enhance optical tweezers based particle tracking. To achieve significant enhancement, it is critical to obtain high interferometer visibility. Since optical tweezers require the trap beam to be strongly focused in high NA objectives, this is a significant technical challenge.

An experiment was set up to test the theory presented above, though this setup did not include the waveplate shown in Fig. 5.1b. The laser source is an Innolight Prometheus laser, which produces the two counter-propagating 100 mW 1064 nm trapping fields for a horizontally oriented optical tweezers trap within a Sagnac interferometer. The trap itself is formed by a pair of long working distance, NA = 0.4 objectives (OFR LMH-20X-YAG).

This apparatus achieved a visibility of 93 % in the absence of large trapped particles, demonstrating the feasibility of the proposed method. The trapping field was focused onto a CCD camera, with the resulting images of a particle clearly showing the predicted behavior (Fig. 5.4). In these images, a 2 μm silica bead is fixed to the coverslip and moved about controllably. The background trapping field is suppressed when we image the bead at the Sagnac interferometer dark port. The relatively high visibility achieved allow clear imaging of particles at the Sagnac dark port, and is predicted by Eq. 5.37 to give a SNR enhancement of 29. In the Rayleigh scattering regime this enhancement would allow a reduction in the minimum detectable particle size when compared to standard detection of $29^{\frac{1}{6}}$, or approximately 1.7 times.

The primary challenge in achieving this was to ensure that the phasefronts of the clockwise and counterclockwise fields remain matched after transmission through both objectives, and to ensure that all of the objective distortion remained symmetric around the optical axis. A particularly sensitive experimental parameter is the alignment of the objectives to each other. Any mismatch in the diffraction of the fields was minimized by placing the optical trap in the center of the Sagnac, so each beam propagates an equal distance from the trap to the beamsplitter. An additional concern was clipping within the objectives, which has the effect of altering the intensity distributions of the two counter-propagating fields. This was avoided by under-filling

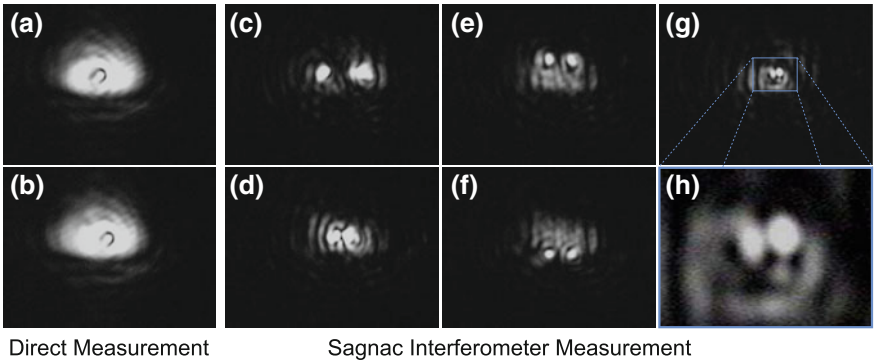

Fig. 5.4 Direct detection of the trapping field is compared here to the use of Sagnac interferometry. **a** 2 μm diameter silica bead was fixed on the cover-glass and imaged with a CCD camera, both with direct imaging (**a** and **b**) and with Sagnac interferometry (**c**–**h**, with the particle in a variety of locations). The trapping field results in a bright background in direct imaging, which is heavily suppressed in the interferometric case. Since the particle is imaged by both counterpropagating fields in the Sagnac interferometer case, a double-image results when the particle is off-center. When the particle is centered, this double-image also exhibits destructive interference (**g** and **h**)

the objectives and ensuring that both fields are centered on the optical axis of the objectives, and therefore experience both minimal clipping and symmetric distortion. Provided the beams are perfectly centered, the loss of intensity due to clipping effects the SNR in Sagnac based detection and back-focal plane detection in the same manner, and therefore has no effect on the level of enhancement.

5.5 Alternative Interferometric Configurations

5.5.1 Sagnac-Michelson Interferometry

The setup described here allows monitoring of the back-reflected light by placing a detector at the empty output of the polarizing beamsplitter. This would allow the relative back-reflected phase $\left(e^{2ikL_1} - e^{2ikL_2}\right)$ to be monitored, as in a Michelson interferometer. If the back-reflection is dominated by back-scatter from the particle, this provides a highly precise method to track the axial position of the particle.

The feasibility of this approach was tested with the apparatus described above. In this case, it was found that back-reflections from the glass coverslip dominated the back-scatter from the particle, and the Michelson signal provided no useful information. Because an air gap was present between the objective and sample, the glass coverslips which enclosed the sample reflected at least 4 % of the incident light, which is far greater than the particle back-scatter. However, these back-reflections could be vastly reduced by using oil-immersion or water-immersion objectives.

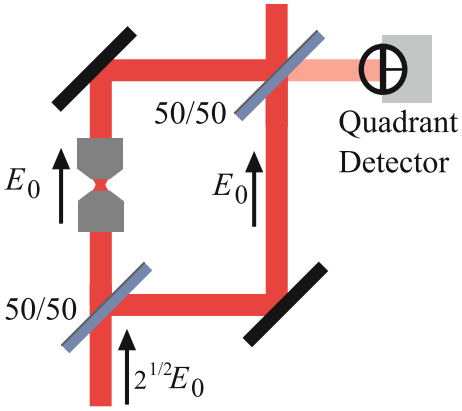

Fig. 5.5 This shows optical tweezers within a Mach-Zehnder interferometer, which is an alternative interferometric configuration which utilizes interference to suppress the unwanted trapping field

A more advanced setup with reduced back-reflections may be able to utilize the Michelson signal for highly precise axial tracking.

5.5.2 Mach-Zehnder Interferometry

While we consider Sagnac interferometry here, the same principle of using interference to filter out the unwanted trapping field may be applied with other configurations. An example, which was demonstrated in Ref. [5] following the publication of this theory, is use of Mach-Zehnder interferometry to enhance sensitivity, as shown in Fig. 5.5. In this case one field propagates through the optical trap while the other does not. This will simplify the alignment of the optical tweezers, potentially making it easier to construct. However, the phasefronts of the two fields will differ if there is any distortion due to the trapping optics. Trapping optics can heavily distort fields, particularly when aberrations are present, so this could set a relatively low limit on the achievable interferometer visibility. However, it is very possible that Sagnac interferometry does not offer the most practical method for removing the trapping field, and it is worthwhile to consider alternative methods such as those explored in Ref. [5].

5.6 Conclusion

By using an interferometric detection scheme, the signal-to-noise ratio for particle tracking in optical tweezers with counter-propagating trap beams is enhanced by a factor which increases as the interferometer visibility approaches 100 %, up to a maximum enhancement defined by the ratio of the trapping field intensity to the detector saturation threshold. This improvement comes about because the interfer-

ometer causes destructive interference of the trapping field at the dark port without affecting the information carrying part of the scattered field.

References

1. A. Ashkin, J. Dziedzic, Optical trapping and manipulation of viruses and bacteria. Science **235**, 1517–1520 (1987)
2. R.W. Bowman, M.J. Padgett, Optical trapping and binding. Rep. Prog. Phys. **76**(2), 026401 (2013)
3. M. Fox, *Quantum Optics: An introduction*, vol. 15 (Oxford University Press, Oxford 2006)
4. P. Kukura, H. Ewers, C. Müller, A. Renn, A. Helenius, V. Sandoghdar, High-speed nanoscopic tracking of the position and orientation of a single virus. Nat. Methods **6**, 923 (2009)
5. T. Li, *Fundamental tests of physics with optically trapped microspheres*. (Springer 2013)
6. K. Lindfors, T. Kalkbrenner, P. Stoller, V. Sandoghdar, Detection and spectroscopy of gold nanoparticles using supercontinuum white light confocal microscopy. Phys. Rev. Lett. **93**, 037401 (2004)
7. I. Perch-Nielsen, P. Rodrigo, J. Glückstad, Real-time interactive 3D manipulation of particles viewed in two orthogonal observation planes. Opt. Express **13**(8), 2852–2857 (2005)
8. H. Sehgal, T. Aggarwal, M. Salapaka, Characterization of dual beam optical tweezers system using a novel detection approach. Proc. ACC **1**, 4234 (2007)
9. R.M. Simmons, J.T. Finer, S. Chu, J.A. Spudich, Quantitative measurements of force and displacement using an optical trap. Biophys. J. **70**(4), 1813–1822 (1996)
10. S. Tatarkova, A. Carruthers, K. Dholakia, One-dimensional optically bound arrays of microscopic particles. Phys. Rev. Lett. **89**(28 Part 1), 283901–283901 (2002)
11. J.W. Tay, M.A. Taylor, W.P. Bowen, Sagnac-interferometer-based characterization of spatial light modulators. Appl. Opt. **48**(12), 2236–2242 (2009)
12. M.A. Taylor, J. Knittel, M.T.L. Hsu, H.-A. Bachor, W.P. Bowen, Sagnac interferometer-enhanced particle tracking in optical tweezers. J. Opt. **13**, 044014 (2011)
13. A. van der Horst, P.D.J. van Oostrum, A. Moroz, A. van Blaaderen, M. Dogterom, High trapping forces for high-refractive index particles trapped in dynamic arrays of counterpropagating optical tweezers. Appl. Opt. **47**(17), 3196–3202 (2008)
14. D.L.J. Vossen, A. van der Horst, M. Dogterom, A. van Blaaderen, Optical tweezers and confocal microscopy for simultaneous three-dimensional manipulation and imaging in concentrated colloidal dispersions. Rev. Sci. Instrum. **75**, 2960 (2004)
15. P. Zemánek, A. Jonáš, L. Šrámek, M. Liška, Optical trapping of Rayleigh particles using a Gaussian standing wave. Opt. Commun. **151**, 273–285 (1998)

Chapter 6
Homodyne Based Particle Tracking

The theoretical framework of Part I establishes that the quantum limit to particle tracking sensitivity improves as the measured flux of scattered photons increases and the spatial mode overlap improves. Chapter 5 presented a method to increase the measured photon flux, and thus improve the shot-noise limit. Here we introduce a novel detection method, which unlike conventional quadrant detection, allows engineering of the spatial mode overlap and thus optimization of the shot-noise limit. In principle, this allows construction of a classically optimal tracking scheme.

6.1 Homodyne Measurements

Quadrant detection provides an easy and effective particle tracking method. However, it is not an optimal measurement, as it does not capture all of the information present in the scattered field. Quadrant detection attempts to estimate the deflection of the trapping field intensity $I(X, Y)$ by the measured photocurrent

$$i_{\text{quadrant}} = \int \text{sign}(X)\, I(X, Y)\, dX\, dY. \tag{6.1}$$

This is a fundamentally non-optimal measurement of the mean deflection, defined as

$$\langle X \rangle = \int X\, I(X, Y)\, dX\, dY \tag{6.2}$$

There are alternatives to quadrant detection which avoid this problem. One is the position sensitive detector, which has a position dependent gain such that it performs an optimal measurement of the displacement of the measured beam,

$$i_{\text{PSD}} = \int X\, I(X, Y)\, dX\, dY. \tag{6.3}$$

M. Taylor, *Quantum Microscopy of Biological Systems*, Springer Theses,
DOI 10.1007/978-3-319-18938-3_6

Since the laser is displaced through a momentum interaction with the particle, this is equivalent to an optimal measurement of the optical force. For Mie scattering particles, however, this still misses information encoded into the phase of the transmitted light. It is only with a phase and amplitude sensitive detection scheme with an optimal detection mode that it is possible to extract all of the particle position information from the scattered field (see Chap. 2).

Homodyne detection is an alternative method which, when optimized, allows fields to be measured at the Cramér-Rao informational bounds [2, 3]. Such measurements generally involve mixing a small signal field with a specific local oscillator, as shown in Fig. 6.1. In the commonly used spatial homodyne measurement, shown in Fig. 6.1a, a local oscillator E_{LO} and signal E_s field are mixed on a 50/50 beamsplitter. The measured fields at the two detectors are then given by

$$E_{\mathrm{det}\ 1} = \sqrt{1/2}\,(E_{\mathrm{LO}} + E_s)\,, \tag{6.4}$$

$$E_{\mathrm{det}\ 2} = \sqrt{1/2}\,(E_{\mathrm{LO}} - E_s)\,, \tag{6.5}$$

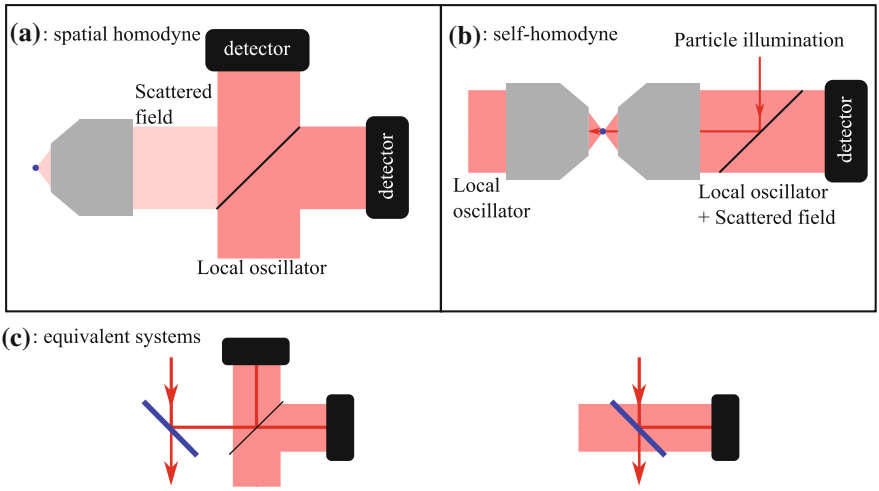

Fig. 6.1 Two different homodyne measurements of the scattered field. **a** Spatial homodyne is commonly used to measure small signal fields, as it offers optimal measurement with and an arbitrary detection mode. **b** The self-homodyne approach used here is closely related, and with appropriate engineering of the local oscillator will also provide optimal measurement with an arbitrary detection mode. **c** In both cases, the scattered field is produced via illumination of the scattering particle. The particle can be viewed as a beamsplitter which couples a small amount of the illuminating light into the detection mode. Particle tracking relies on an accurate measurement of this scattered light. The primary difference between the spatial homodyne and self-homodyne approaches described here is that the self-homodyne also has the local oscillator propagating through the particle, and thus requires only one detector

with corresponding intensities of

$$|E_{\text{det }1}|^2 = \frac{1}{2}|E_{\text{LO}}|^2 + \frac{1}{2}|E_s|^2 + \text{Re}\{E_{\text{LO}}^* E_s\}, \tag{6.6}$$

$$|E_{\text{det }2}|^2 = \frac{1}{2}|E_{\text{LO}}|^2 + \frac{1}{2}|E_s|^2 - \text{Re}\{E_{\text{LO}}^* E_s\}. \tag{6.7}$$

These fields are then detected, with the measurement relying on the subtraction signal which is given as

$$i_{\text{det}} = \frac{\epsilon_0 \lambda}{2h}\left(\int E_{\text{det }1}|^2 dA - \int |E_{\text{det }2}|^2 dA\right), \tag{6.8}$$

$$= \frac{\epsilon_0 \lambda}{2h}\int 2\text{Re}\{E_{\text{LO}}^* E_s\} dA, \tag{6.9}$$

$$\approx \frac{\epsilon_0 \lambda}{2h}\int 2\text{Re}\{\bar{E}_{\text{LO}}^* E_s\} dA \tag{6.10}$$

where $\bar{E}_{\text{LO}}$ is the mean of the local oscillator field, and the approximation is valid in the limit that $E_{\text{LO}} \gg E_s$. The factor of $\frac{\epsilon_0 \lambda}{2h}$ normalizes the fields into photon number, with h Planck's constant and ϵ_0 the vacuum permittivity. The interference between the local oscillator and scattered fields is parameterized by the efficiency

$$\eta = \frac{\int \bar{E}_{\text{LO}} \cdot \bar{E}_s \, dA}{\left(\int |\bar{E}_{\text{LO}}|^2 \, dA \int |\bar{E}_s|^2 \, dA\right)^{1/2}}. \tag{6.11}$$

The mean amplitude $\bar{E}_s$ and fluctuations δE_s generally occupy the same spatial mode, such that η defines the overlap of both of these signal field components with the local oscillator. The photocurrent variance is then given by

$$\langle i_{\text{det}}^2 \rangle - \langle i_{\text{det}} \rangle^2 = \eta^2 i_{\text{LO}} \frac{\epsilon_0 \lambda}{2h} \langle \delta E_s^2 \rangle, \tag{6.12}$$

where i_{LO} is the mean photon flux of the local oscillator field. In this case, $\langle \delta E_s^2 \rangle$ includes the vacuum fluctuations, and it cannot approach zero even if the signal field is removed ($\bar{E}_s = 0$). We can see that this scheme effectively measures the amplitude of the signal field, while to first order cancelling any noise from the local oscillator. The signal field in a particle tracking experiment is given by the derivative of the scattered field with respect to particle position, as described in Chap. 3. By measuring the amplitude of this signal, spatial homodyne could allow particles to be tracked with precision at the quantum limit [3].

Here, instead of using spatial homodyne, we measure particle motion with a self-homodyne scheme, as represented in Fig. 6.1b. In this case, the particle is illuminated to produce a scattered field. This scattered field co-propagates with the local oscillator toward a single detector, which produces a photocurrent of

$$i_{\text{det}} = \frac{\epsilon_0 \lambda}{2h} \int |E_{\text{LO}}|^2 + |E_s|^2 + 2\text{Re}\{E_{\text{LO}}^* E_s\}\, dA \tag{6.13}$$

$$= i_{\text{LO}} + i_s + \frac{\epsilon_0 \lambda}{2h} \int \bar{E}_{\text{LO}} \cdot \left(\bar{E}_s + \delta E_{\text{LO}} + \delta E_s\right) dA. \tag{6.14}$$

When the constant offset $i_{\text{LO}} + i_s$ is subtracted, this measurement closely resembles that in Eq. 6.10. Although this does not cancel the noise variance on the local oscillator from the measurement, the optimal performance is identical to the conventional homodyne setup. One might imagine that self-homodyne would include additional vacuum noise, as the spatial homodyne setup allows cancellation of the vacuum fluctuations present on the local oscillator. However, the vacuum noise which is detected in the two schemes is simply that which was on the scattered field mode. In the case of the self-homodyne scheme, these fluctuations occur on a single optical mode in which scattered field and local oscillator co-propagate (see Fig. 6.1c).

6.2 Self-homodyne Tracking Setup

A particle tracking experiment was built as shown in Fig. 6.2 which applied self-homodyne to measure particle motion. In this demonstration, the local oscillator was shaped as a "flipped" Gaussian at the back-focal plane of the objective, with a π phase shift applied to one half of its transverse profile [1]. Since the trapping field E_T is Gaussian, this effectively sets the local oscillator field profile to $E_{LO}(X, Y) = \text{sign}(X) E_T(X, Y)$, where X and Y are position coordinates on the detector. The interference between the scattered field E_s and the spatially engineered local oscillator results in a photocurrent of

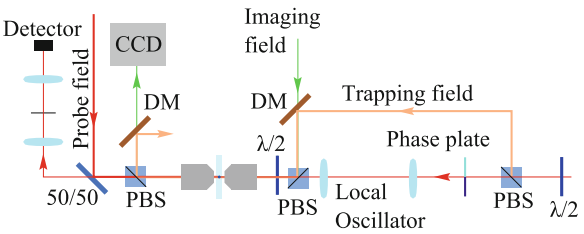

Fig. 6.2 Experimental layout of a self-homodyne tracking experiment. Particles are confined by the counter-propagating trapping and probe fields, which have orthogonal polarization. Particle tracking is achieved via interference between the back-scattered light from the probe field and a shaped local oscillator, which is shaped with a phase plate to have a π phase shift on one half of its transverse profile. The measured fields propagate to the bulk detector via a 50/50 beamsplitter, which loses half of the light, and a telescope with an aperture, to remove unwanted back-reflections from the sample chamber. The trapping field is isolated from the detection with a polarizing beamsplitter. A further imaging field at a different wavelength is used to image the particles onto a CCD camera

$$i = \int_{-\infty}^{\infty}\int_{-\infty}^{\infty} |E_s + E_{LO}|^2 dX\, dY \tag{6.15}$$

$$= \int_{-\infty}^{\infty}\int_{-\infty}^{\infty} |E_T|^2 + |E_s|^2 + 2\text{sign}(X)\text{Re}(E_s^* E_T) dX\, dY. \tag{6.16}$$

The self-homodyne measurement is similar to quadrant detection, in which the position is inferred by subtracting the light intensity on one half of the detector from the other, with a photocurrent of

$$i_x = \int_{-\infty}^{\infty} \left(\int_0^{\infty} |E_s + E_T|^2 dX - \int_{-\infty}^{0} |E_s + E_T|^2 dX \right) dY, \tag{6.17}$$

$$= \int_{-\infty}^{\infty}\int_{-\infty}^{\infty} \text{sign}(X) \left(|E_T|^2 + |E_s|^2 + 2\text{Re}(E_s^* E_T) \right) dX\, dY. \tag{6.18}$$

The particle tracking signal derived from each method is identical. The only qualitative difference between quadrant detection and our self-homodyne scheme is that the mean subtraction current in Eq. 6.18 is zero, and similar to spatial homodyne measurements, classical amplitude noise on the light is canceled. While split detection is widely used and known to perform well, the measurement sensitivity can be improved by optimizing the spatial profile of the detection mode. Although the local oscillator shape was not optimized here, the proof-of-principle demonstration of self-homodyne is an important step towards implementing classically optimal detection.

For the experimental demonstration, separate fields are used to interrogate the particle and to act as the local oscillator (see Fig. 6.2). A Gaussian probe field which propagates away from the detector enters the optical trap and illuminates the particles, with back-scattered light providing the signal field. This scattered light is mixed with the flipped Gaussian local oscillator field, which acts to define the detection mode, and the transmitted intensity is directly measured to infer particle position along one axis.

The self-homodyne particle tracking scheme shown in Fig. 6.2 was built and characterized. In this experiment, a particle is trapped in water between two objectives with 0.4 numerical aperture (NA) by 1064 nm light. Due to the low NA objectives used, trapping is not possible with a single beam. Two orthogonally polarized counter-propagating fields are used instead to confine particles, with only one of these contributing to the measurement. The additional trapping field is isolated from the detector using a polarizing beamsplitter with a manufacturer specified extinction ratio of 23 dB. The residual trapping field to reach the detector should carry an orthogonal polarization to the measured fields, such that it only affects the measurement process via a small contribution of noise. If higher NA objectives were used, the separate trapping field would not be needed. A Gaussian probe field which

propagates away from the detector enters the optical trap and illuminates the particles, with back-scattered light providing the signal field. This scattered light is mixed with the flipped Gaussian local oscillator field, which acts to define the detection mode, and the transmitted intensity is directly measured to infer particle position along one axis. The phase between the local oscillator and scattered field was locked by modulating the probe field at 2 MHz and monitoring the amplitude of the detected modulation. This measurement was processed with a PID controller, and used to lock the optical phases by feeding back to a piezo-mounted mirror in the path of the probe field.

In addition to backscattered light, the measurement also captures probe light which reflects from the sample coverslip. This light is highly divergent as the focus of the reflected field is displaced from the focal plane of the objective. An aperture is used to remove the diverging component of the optical field, which suppresses the detection of back-reflected light. However, some of the back-reflected light still reaches the detector and introduces a spurious signal. Since the glass coverslips are essentially stationary, the spurious signal has an extremely low frequency, and cannot be observed over the particle motion above 1 Hz.

With this setup, 1 μm polystyrene particles were tracked in water with a sensitivity of 3×10^{-12} m $\mathrm{Hz}^{-1/2}$ (see Fig. 6.3). Then, the measurement scheme was tested to verify whether the measured signal corresponded to motion along the x axis. A 1 kHz sinusoidal modulation with 5 V peak-to-peak amplitude was applied to the piezo drivers along the x and y axes of the positioning stage (Nanomax MAX302).

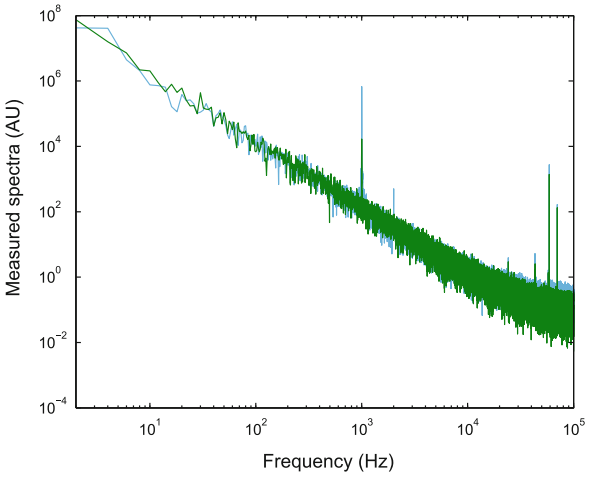

Fig. 6.3 Characterization of the cross-talk in homodyne particle tracking. The sample position was modulated along both the x and y axes, with measured spectra shown in light blue and green respectively. When the x axis was modulated, the resulting measurement yields a strong signal at 1 kHz as well as a weaker second harmonic at 2 kHz. Modulation of the y axis produced a smaller signal at 1 kHz and no response at 2 kHz. Both spectra also show the spectra of Brownian motion, with a measurement sensitivity of 3×10^{-12} m $\mathrm{Hz}^{-1/2}$. The peaks above 30 kHz are additional unwanted modulations associated with the phase lock

The resulting power spectra for the measured signal are shown in Fig. 6.3. When the x axis was modulated, the resulting measurement yields a strong signal at 1 kHz. By contrast, the response at 1 kHz is 40 times smaller for a modulation along the y axis. This clearly demonstrates that the measurement predominantly samples the particle motion along the x axis. Since the stage itself is imperfect, the observed cross-talk may have originated in either the positioning stage or imperfections in the detection.

Movement along the z axis shifts the relative phase between the scattered field and local oscillator. This phase is compensated with the phase lock, and to first order the residual phase difference does not affect the measured signal. Modulation of the z axis, however, introduced a large axial motion which the phase lock was unable to compensate. The feedback loop could not respond adequately to the driven motion, and the phase lock became unstable. This suggests that axial motion could produce more cross-talk than y axis motion. Without a stable phase lock it is not possible to perform reliable measurements, and the exact level of this axial cross-talk was not characterized.

References

1. V. Delaubert, D. Shaddock, P. Lam, B. Buchler, H. Bachor, D. McClelland, Generation of a phase-flipped Gaussian mode for optical measurements. J. Opt. A: Pure Appl. Opt **4**(4), 393 (2002)
2. V. Delaubert, N. Treps, C. Fabre, H.A. Bachor, P. Réfrégier, Quantum limits in image processing. Europhys. Lett. **81**, 44001 (2008)
3. J.W. Tay, M.T.L. Hsu, W.P. Bowen, Quantum limited particle sensing in optical tweezers. Phys. Rev. A **80**(6), 063806 (2009)

Chapter 7
Lock-In Particle Tracking

Chapters 5 and 6 present methods to optimize the shot-noise limit to particle tracking sensitivity. In many real experiments, however, technical noise dominates. In this case, it is more important to eliminate technical noise than to improve the shot-noise limit. This chapter presents a new optical lock-in method to eliminate low frequency noise, and incorporates the following publication [9].

7.1 Introduction

While shot-noise establishes the fundamental sensitivity limit for optical tweezers based measurements [6, 8, 10], real experiments are generally limited by technical noise sources such as laser noise, electronic noise in the detector, or drifts of mirrors in the experiment. These technical sources of error can be a significant hindrance to precision measurement, so much effort has gone into reducing them [1, 3, 5]. Here we develop an optical lock-in particle tracking scheme which allowed evasion of low-frequency technical noise without needing to remove the noise sources from the experiment. In principle, this optical lock-in particle tracking scheme offers near immunity to low frequency laser noise and electronic noise, which could make it a highly practical method for a wide range of experiments. Here we demonstrate optical lock-in particle tracking with both self-homodyne and conventional quadrant detection, and characterize the noise suppression attained. It is shown that lock-in based particle tracking allows evasion of low frequency electronic noise and laser intensity noise, and achieves equivalent sensitivity where the dominant noise source is fundamental shot-noise. The reduction in laser noise and electronic noise yields up to 20 dB of noise suppression below 1 kHz, where low frequency electronic noise is significant, and over 20 dB of noise suppression around 600 kHz where the laser crystal relaxation oscillations introduce an intensity noise feature. This allows shot-noise limited measurements at low frequencies, which is essential for the development of quantum enhanced particle tracking.

M. Taylor, *Quantum Microscopy of Biological Systems*, Springer Theses,
DOI 10.1007/978-3-319-18938-3_7

7.2 Basic Concept

The lock-in based particle tracking measurement demonstrated here is qualitatively similar to a continuous position tracking experiment. In optical tweezers based measurements, scattering particles are illuminated and the spatial distribution of the resulting scattered field is measured to infer particle position [2, 8]. Here this is extended by modulating the incident illumination. This modulation is carried onto the scattered field, shifting some of the optical power from the laser carrier frequency into side-bands. Once the scattered field is measured, the optical modulation translates into a modulation on the electrical signal, with the particle position information centered about the modulation frequency (see Fig. 7.1). The particle position can be recovered by demodulating this signal.

We may ask how the expected sensitivity of such a measurement compares to a usual continuous measurement. When optical fields are measured, the resulting photocurrent at time t is given by

$$I(t) = G \int U(X, Y)|E(t)|^2 dX\, dY + N_E(t) \tag{7.1}$$

where N_E is the electronic noise, G is the detector gain, E is the total electric field at the detector at the coordinates X and Y, and $U(X, Y)$ represents the spatial gain of the detector; for instance, if the photocurrent from two halves of a split detector are subtracted from one another, this is represented as $U(X, Y) = \text{sign}(X)$, while a bulk detector has $U(X, Y) = 1$. Here we assume that the fields present are a scattered field E_s which depends on particle position, and a local oscillator E_{LO} with which the scattered field interferes, such that $E = E_{\text{LO}} + E_s$. In most optical tweezers experiments, the local oscillator is simply given by the component of the trapping field which has not scattered from the particle. For lock-in experiments, the fields are separated to allow the particle illumination to be modulated independently of

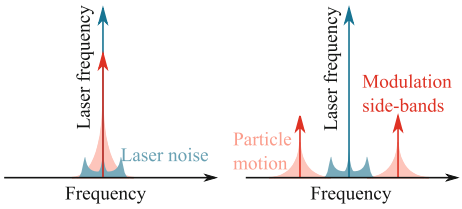

Fig. 7.1 An illumination optical field is modulated by its interaction with the particle (*red*). In order to measure this, it is mixed with another bright local oscillator field (*dark blue*). However, the local oscillator also has some low-frequency noise present. If the illumination field frequency matches the local oscillator frequency, as shown on the *left*, then the low-frequency noise competes with the low-frequency particle motion signal. However, if it is in amplitude modulated side-bands, as shown on the *right*, then the low-frequency particle motion can be isolated from the low-frequency noise, thereby improving the measurement sensitivity

the local oscillator. The scattered field is assumed to be much smaller than the local oscillator ($|E_s| \ll |E_{\mathrm{LO}}|$) as is typically the case, such that the measured photocurrent is given by

$$I(t) = G \int U(X,Y)|E_{\mathrm{LO}}(t)|^2 + 2U(X,Y)\mathrm{Re}\{E_{\mathrm{LO}}(t)E_s^*(t)\}dX\,dY + N_E(t). \tag{7.2}$$

The explicit time dependence of the scattered field may be separated from the spatial mode shape as $E_s = (A_s(t) + \xi(t))\psi_s(X,Y)$. Here $A_s(t)$ is a real parameter which represents the expectation value of the field amplitude given the particle position, and $\xi(t)$ represents all additional fluctuations such as laser noise and shot noise. $\psi_s(X,Y)$ is the complex spatial modeshape of the scattered field; this does not have explicit time dependence, but is modified as the particle moves. It is this spatial modification which is ultimately monitored to retrieve a particle tracking signal. To find the dependence of the scattered field on a small particle displacement $x(t)$, it can be expanded to first order as

$$E_s = E_s|_{x=0} + x(t)\frac{dE_s}{dx}\Big|_{x=0} = (A_s(t)+\xi(t))\psi_s(X,Y)|_{x=0} + x(t)(A_s(t)+\xi(t))\frac{d\psi_s(X,Y)}{dx}\Big|_{x=0}. \tag{7.3}$$

Substituting this expression into Eq. 7.2, the component of the photocurrent which gives a linear particle tracking signal can be seen to be

$$I_{\mathrm{sig}} = 2Gx(t)A_s(t)\int U(X,Y)\mathrm{Re}\{E_{\mathrm{LO}}\frac{d\psi_s^*(X,Y)}{dx}\Big|_{x=0}\}dX\,dY, \tag{7.4}$$

$$= gx(t)A_s(t) \tag{7.5}$$

where for brevity we define a gain $g = 2G\int U(X,Y)\mathrm{Re}\{E_{\mathrm{LO}}\frac{d\psi_s^*(X,Y)}{dx}\big|_{x=0}\}dX\,dY$. The position sensitivity is optimized when this gain is maximized, as occurs when both the phase and shape of the local oscillator field are optimized to perfectly interfere with the scattered field component $\frac{dE_s}{dx}\big|_{x=0}$ [6, 7]. Substituting this into Eq. 7.2, we can represent the measured photocurrent as

$$I(t) = N_{\mathrm{opt}}(t) + N_E(t) + gA_s(t)x(t), \tag{7.6}$$

where all the terms in the integrand which did not contribute to the tracking signal are included as optical noise N_{opt}. For a continuous measurement, the expectation value of the scattered field amplitude $A_s(t)$ should be constant. Alternatively, we can perform lock-in measurement if we modulate the scattered field amplitude at frequency ω such that $A_s(t) = \sqrt{2}\bar{A}_s\cos(\omega t)$, where the modulated amplitude has an RMS value of $\bar{A}_s$. Provided the modulation frequency is much faster than the mechanical motion, the position can then be extracted by demodulation;

$$I_{\text{lock-in}} = \sqrt{2}I\cos(\omega t) = \sqrt{2}\left(N_{\mathrm{opt}}(t) + N_E(t)\right)\cos(\omega t) + g\bar{A}_s x + g\bar{A}_s x\cos(2\omega t). \tag{7.7}$$

Thus, the effect of the lock-in is to shift the low frequency noise to high frequencies, and generate a second harmonic term proportional to x while leaving the signal term unchanged. The second harmonic term and the low frequency noise can then be removed via a low-pass filter, such that only the noise originally near the modulation frequency enters the measurement. Wherever low-frequency noise is dominant, lock-in measurement allows suppression of the noise floor. This does not influence white noise sources such as shot-noise, since these are equally present at low frequencies and around the modulation frequency. Thus, the fundamental shot-noise limit on position sensitivity is not influenced by a choice between continuous or lock-in measurement. The two schemes have equivalent shot-noise limits to sensitivity when the lock-in scattered amplitude $\bar{A}_s$ matches the amplitude A_s of a the continuous measurement, or equivalently, when the same number of scattered photons in modulation side-bands are collected for the lock-in measurement as are collected for a continuous measurement.

7.3 Self-homodyne Demonstration

To demonstrate the optical lock-in particle tracking method, the self-homodyne setup shown in Fig. 7.2 was built, and the sensitivity attainable with continuous and lock-in measurements characterized. This setup applies lock-in measurement in the self-homodyne experiment demonstrated in Chap. 6. Particles are trapped in water between two objectives with 0.4 numerical aperture (NA) by 1064 nm light produced by a low noise Innolight Prometheus Nd:YAG laser. The low NA objectives used do not allow stable trapping with a single beam, so two orthogonally polarized counter-propagating fields are used instead to confine particles. One of these is used to probe

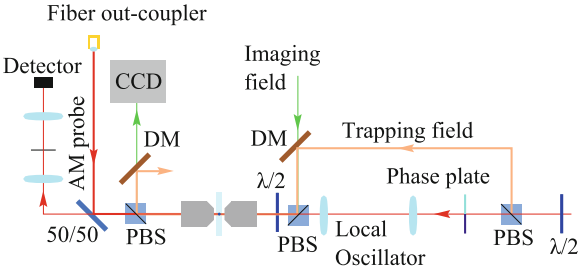

Fig. 7.2 Layout of the optical lock-in tracking scheme used here. *PBS* polarizing beamsplitter, *DM* dichroic mirror. The local oscillator is shaped with a phase plate which imparts a π phase shift to one half of the spatial profile. Particles are trapped by the counter-propagating probe and trap fields. The trap field is isolated from the detection, and if it is not required for stable trapping, can be removed altogether. The probe field scatters from trapped particles, and the particle motion tracked via the interference between this scattered light and the local oscillator. The probe is amplitude modulated at 2 MHz in a fiber Mach-Zehnder modulator. A separate green field is used to image the particles in the trap

the particles, with the resulting back-scattered light used to perform particle tracking. The other trapping field is removed with polarizing optics, and does not contribute to the measurement. The probe field is amplitude modulated at 2 MHz, which is a sufficiently high frequency that the resulting modulation of the trap strength does not measurably disturb the particle motion. The back-scatter from this modulated probe field is combined with a local oscillator field which also propagates through the trap. As described in Chap. 6, the local oscillator is shaped with a phase plate so that particle motion modulates the spatial overlap between the local oscillator and scattered field. Provided the phase between the local oscillator and scattered field is correctly chosen, the influence of the particle motion on the interference between these fields directly maps the position onto the transmitted light intensity, which is then measured on a New Focus 1811 bulk detector. Demodulation of the resulting signal at the amplitude modulation frequency allows both tracking of a scattering particle and also monitoring of the relative optical phases. The scattered light includes a large stationary term ($E_s|_{x=0}$ in Eq. 7.2), and the phase between this and the local oscillator can be determined from the amplitude of the measured modulation. This measured phase was processed with a PID controller and locked by feedback to a piezo-mounted mirror in the path of the probe field.

The amplitude modulation on the probe is chosen to leave approximately equal power in the central laser frequency and the first modulation side-band. This allows the continuous and pulsed measurements to occur simultaneously with a single detector, and with equivalent recording conditions. Some non-linearity in the modulator resulted in a number of higher harmonics being generated, which were suppressed in the data acquisition with analog electronic filters.

Using this setup, the Brownian motion of a 1 μm polystyrene bead was simultaneously measured both continuously and from side-bands around the 2 MHz modulation, with spectra shown in Fig. 7.3a, b respectively. The background noise was characterized by performing equivalent measurements in the absence of a trapped bead. As expected, the lock-in measurement is very similar to the continuous measurement, but with a reduction in the included electronic and laser noise. The reduction in included noise (shown in Fig. 7.3c) causes the measurement imprecision to improve markedly at the frequencies where laser and electronic noise are dominant. Between 10 and 5000 Hz, the imprecision is improved by an average of 20 dB, with even greater suppression of 35 dB in the frequency range 550–710 kHz where the laser crystal relaxation oscillations produce a prominent laser noise peak centered at 630 kHz. A comparison of the two measurements in the time domain also reveals both the clear suppression of noise on the lock-in trace and the otherwise close agreement between the measured displacements (Fig. 7.3d). These results verify that the lock-in measurement is equivalent to a continuous measurement, except that it evades low frequency technical noise.

With the optical layout used here, particle motion was tracked in a self-homodyne measurement on a single bulk detector rather than a quadrant photodiode. This is not required for lock-in particle tracking, which should work with any detection apparatus. However, it can be very advantageous; quadrant detectors are avoided in some high-speed experiments because they typically have low bandwidth [1, 4]. Further-

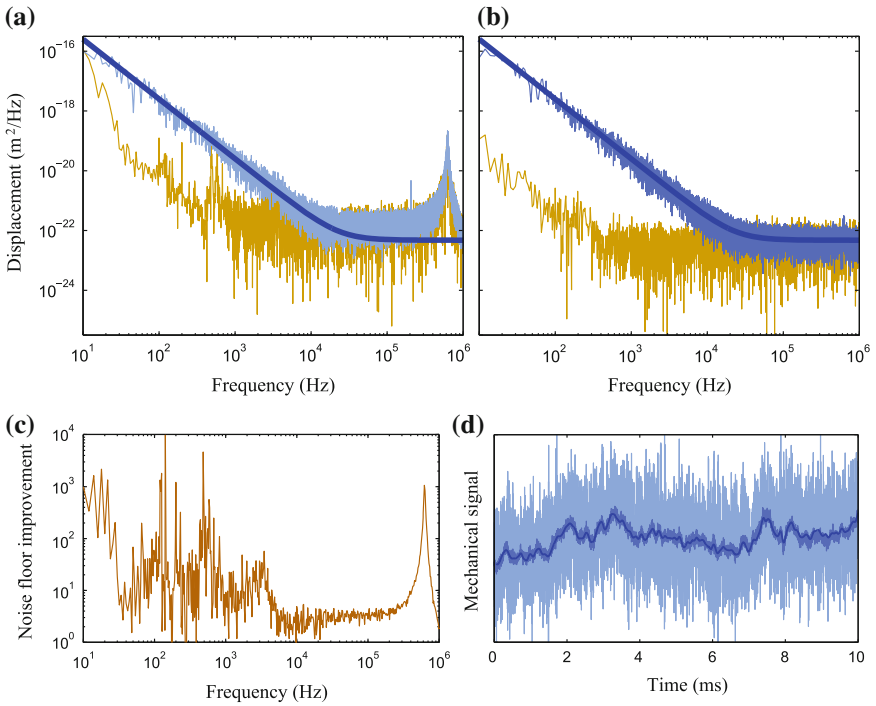

Fig. 7.3 Particle tracking spectra are shown from simultaneous continuous (**a**) and lock-in (**b**) measurements. The *light yellow* trace shows the noise floor present in the absence of a trapped particle which corresponds to the measurement imprecision, and the *blue* shows the measured signal with a 1 μm polystyrene bead held in the trap. The thick *darker blue* line fits the bead motion and the flat shot-noise floor. This matches the lock-in data well since it is shot-noise limited from 500 Hz, but does not follow the continuous spectra as this was limited by low frequency laser noise until 1 MHz. This noise includes a very prominent spectral peak around 630 kHz from the laser diode relaxation oscillations. Because the fitted floor corresponds to the shot-noise level, it drops below the measured data between 10 kHz and 1 MHz. The trap was very weak, as we used 0.4 NA objectives with a total of 30 mW trapping field. As such, the corner frequency is slightly below 10 Hz and not visible in the displayed data. By excluding low frequency noise, the lock-in measurement yields a measurement precision which is improved by the factor shown in (**c**). Subplot **d** shows the continuous (*light*) and lock-in (*medium*) time-traces after a low-pass filter at 1 MHz, revealing the clear noise improvement from lock-in measurement, and also shows the continuous data with a low-pass filter at 10 kHz (*dark*), which closely follows the higher bandwidth lock-in results

more, the quantum limit on sensitivity is accessible only with perfect interference between the local oscillator and scattered fields, which requires the local oscillator to be spatially engineered, as it is in a homodyne measurement such as this [6, 8]. A difficulty with the layout used here was that some of the probe field reflected from the sample chamber into the detector. Because air-gap objectives were used, the glass coverslip produced about 4 % reflection, which was of a greater intensity than the back-scatter from the particle. Thus phase shifts between the local oscillator and

scattered fields generated a spurious measured signal, but this was primarily below 5 Hz. In that low frequency range, our lock-in measurement performed worse than the continuous measurement. This problem could be solved by using oil-immersion objectives, where the refractive index mismatch between the medium and the coverslip is far smaller, and the resulting back-reflection far weaker. Alternatively, the reflections could be eliminated with anti-reflection coatings on the coverslips.

7.4 Experimental Verification in a Conventional Setup

To verify that this lock-in technique is applicable with the high NA objectives and quadrant detection typically used in optical tweezers experiments, the lock-in particle tracking apparatus was rebuilt to the design shown in Fig. 7.4. In this setup, a particle is trapped in water between two Nikon Plan Fluorite objectives with numerical aperture (NA) of 1.3. Because these objectives are high NA, the extra trapping field used in Sect. 7.3 was unnecessary and the particles were confined with a single beam optical trap with 30 mW of amplitude modulated trapping light. In this experiment the measurement bandwidth approached 1 MHz (see Fig. 7.5). It is necessary to modulate at a frequency which is greater than twice the measurement bandwidth to ensure that the continuous and lock-in measurements remained spectrally separated, so the frequency of the amplitude modulation was increased to 2.5 MHz. Once again, the modulation frequency is sufficiently high that the resulting modulation of the trap strength should not measurably disturb the particle motion. The back-scatter from this modulated field is combined with a 3 mW local oscillator field which also propagates through the trap. The resulting interference is then measured on a split detector to determine particle position [2]. The split detector follows the design used in Ref. [4], where the left and right halves of the laser beam are separated with a

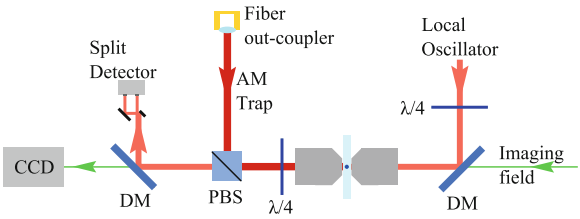

Fig. 7.4 Layout of the optical lock-in tracking scheme used here. *PBS* polarizing beamsplitter, *DM* dichroic mirror, $\lambda/4$ quarter waveplate. Particles are trapped with a 30 mW trapping field which has been amplitude modulated at 2.5 MHz in a fiber Mach-Zehnder modulator (*dark red*). Back-scattered light from this trapping field is combined with a 3 mW local oscillator field (*light red*). Since the back-scattered light passes through the quarter waveplate twice, its polarization is rotated and it passes straight through the polarizing beamsplitter. The interference between the scattered field and the local oscillator is measured on a split detector to track the particles. A separate green field is used to image the particles in the trap

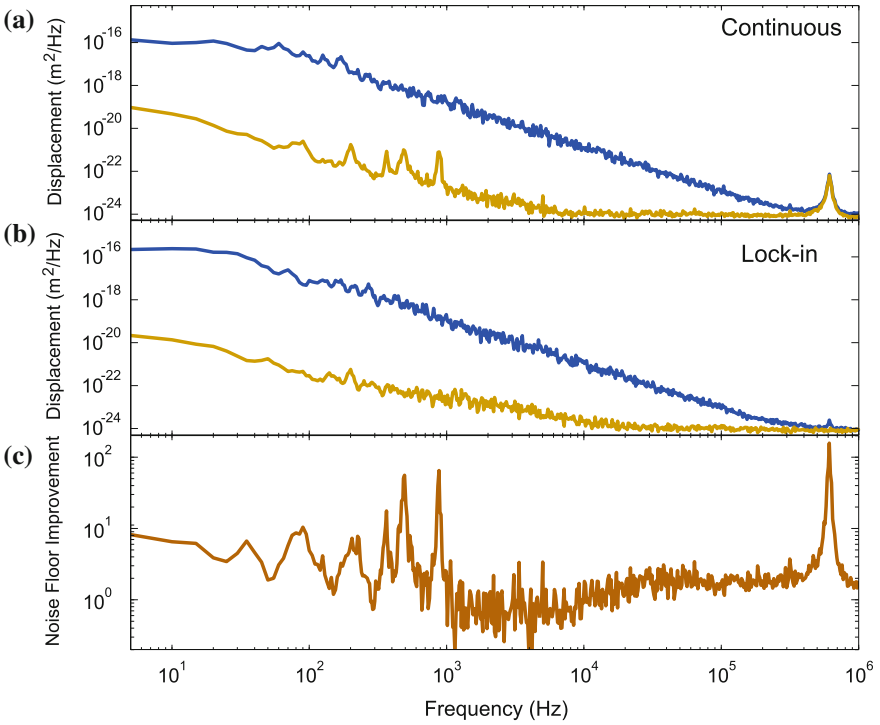

Fig. 7.5 Particle tracking spectra are shown from simultaneous continuous (**a**) and lock-in (**b**) measurements. The gold trace shows the noise floor present in the absence of a trapped particle which corresponds to the measurement imprecision, and the *blue* shows the measured signal with a 0.5 μm polystyrene bead held in the trap. For clarity, the traces are smoothed with a logarithmic width filter, and this broadens the sharp electrical noise features. The prominent spectral peak around 630 kHz in the continuous data is laser noise which arises from the laser diode relaxation oscillations, and this noise feature is barely visible in the lock-in results. Subplot **c** shows the factor by which the noise floor has been lowered for the lock-in results

mirror and measured with a balanced detector. The detector used in this experiment was a New Focus 1817 detector, which combines shot-noise limited performance with 80 MHz bandwidth.

Using a similar measurement procedure to Sect. 7.3, the Brownian motion of a 0.5 μm polystyrene bead was simultaneously measured both continuously and from side-bands around the 2.5 MHz modulation, with spectra shown in Fig. 7.5a, b respectively. The background noise was characterized by performing equivalent measurements in the absence of a trapped bead. As expected, the lock-in measurement is very similar to the continuous measurement, but with a reduction in the included electronic and laser noise. The reduction in included noise (shown in Fig. 7.5c) causes the measurement imprecision to improve at the frequencies where laser and electronic noise are dominant. Below 1 kHz, the noise floor was dominated by 1/f electronic noise, with some additional noise spikes. In this regime, the imprecision is improved

by an average of 8 dB, with peaks suppressed by up to 20 dB. A prominent laser noise peak was also present at 550–710 kHz due to the laser crystal relaxation oscillations, and this was also suppressed by 20 dB in the lock-in results. At higher frequencies the measurements are both shot-noise limited, and their noise floors converge. These results verify that the lock-in measurement is equivalent to a continuous measurement, except that it evades low frequency technical noise.

While the particle motion was only measured along a single axis in this experiment, lock-in particle tracking is fully compatible with the 3D tracking performed with quadrant detectors, provided the quadrant has sufficient bandwidth to capture the particle motion around the modulation side-bands. It should be noted that while lock-in particle tracking evades laser noise and electronic noise, this can only improve the sensitivity to the particle position relative to the optical fields. As with all other particle tracking experiments, the measurement remains sensitive to mirror drifts or air currents outside the trap which cause the trap center to drift, and conventional methods are needed to stabilize these noise sources.

7.5 Conclusion

In conclusion, we have demonstrated that lock-in measurement provides a simple and robust technique to reduce technical noise in an optical tweezers setup. Even when using a low noise laser and detector (shot-noise limited at 10 kHz; see Fig. 7.5), this results in a substantial improvement. Lock-in particle tracking is demonstrated to work in both a self-homodyne tracking setup and with a split detector, demonstrating that it is sufficiently versatile to operate in a wide range of apparatus designs. Since lock-in measurements eliminate low-frequency optical noise, it becomes relatively straightforward to perform experiments with quantum shot-noise limited sensitivity at low frequencies. This is an essential step for the development of quantum enhanced particle tracking apparatus. Furthermore, this elimination of noise can yield a substantial improvement in sensitivity, and could provide a practical benefit for many classical optical tweezers applications.

References

1. I. Chavez, R. Huang, K. Henderson, E.-L. Florin, M.G. Raizen, Development of a fast position-sensitive laser beam detector. Rev. Sci. Instrum. **79**, 105104 (2008)
2. F. Gittes, C.F. Schmidt, Interference model for back-focal-plane displacement detection in optical tweezers. Opt. Lett. **23**(1), 7–9 (1998)
3. P. Kukura, H. Ewers, C. Müller, A. Renn, A. Helenius, V. Sandoghdar, High-speed nanoscopic tracking of the position and orientation of a single virus. Nat. Methods **6**, 923 (2009)
4. T. Li, S. Kheifets, M.G. Raizen, Millikelvin cooling of an optically trapped microsphere in vacuum. Nat. Phys. **7**, 527–530 (2011)
5. J.R. Moffitt, Y.R. Chemla, S.B. Smith, C. Bustamante, Recent advances in optical tweezers. Annu. Rev. Biochem. **77**, 205–228 (2008)

6. J.W. Tay, M.T.L. Hsu, W.P. Bowen, Quantum limited particle sensing in optical tweezers. Phys. Rev. A **80**(6), 063806 (2009)
7. M.A. Taylor, J. Janousek, V. Daria, J. Knittel, B. Hage, H.-A. Bachor, W.P. Bowen, Biological measurement beyond the quantum limit. Nat. Photon. **7**, 229–233 (2013)
8. M.A. Taylor, J. Knittel, W.P. Bowen, Fundamental constraints on particle tracking with optical tweezers. New J. Phys. **15**, 023018 (2013)
9. M.A. Taylor, J. Knittel, W.P. Bowen, Optical lock-in particle tracking in optical tweezers. Opt. Express **21**, 8018–8024 (2013)
10. M.A. Taylor, J. Knittel, M.T.L. Hsu, H.-A. Bachor, W.P. Bowen, Sagnac interferometer-enhanced particle tracking in optical tweezers. J. Opt. **13**, 044014 (2011)

Chapter 8
Selective Measurement by Optimized Dark-Field Illumination Angle

The previous chapters establish methods which can be used to improve the sensitivity of single particle tracking in optical tweezers. In many real experiments, particularly in biology, the single particle under study is surrounded by extraneous scattering centers. In order to truly benefit from high precision measurements, it is important to minimize the contribution of these unwanted scatterers. This chapter shows that the contributions of different scatterers can be tuned by adjusting the angle of illumination in a dark-field microscopy setup. It is based on the following publication [24].

8.1 Dark-Field Microscopy

To optically image a microscopic structure, such as those within cells, light which has interacted with the structure is collected with a microscope objective. With dark-field illumination, the angle of incidence of the illuminating light is chosen to ensure that light can only enter the objective if it scatters from the sample [13, 19, 29]. This eliminates the bright background of unscattered light, which vastly improves the contrast and makes smaller features observable. This can allow biophysical experiments to proceed with far smaller markers than otherwise possible [9, 18, 23, 31], which then reveals previously unobservable dynamics of nanoscale objects such as protein motors [9, 18, 31]. The improved contrast also enables marker-free observation of small structures such as the rapidly moving bacterial flagella [13].

The only background light to enter a dark-field measurement is the unwanted scattering from scattering centers which are not under study. This background degrades the signal to noise of the measurement, which can be a limiting factor in dark-field experiments [19]. For instance, a dark-field image of the actin networks within the cellular cytoplasm includes a background of scattered light from organelles such as the cell nucleus and mitochondria. While this remaining background is typically much smaller than the background of unscattered light in bright-field microscopy, it can be significant when studying complex structures such as cells, where there are a vast collection of competing scatterers [7].

Here we calculate the collected flux of scattered photons for a range of spherical scattering particles, microscope objectives, and illumination angles, and show that the relative contribution of different particles to the measured signal can be tuned

M. Taylor, *Quantum Microscopy of Biological Systems*, Springer Theses,
DOI 10.1007/978-3-319-18938-3_8

by appropriately adjusting the illumination angle. This can be used to maximize the signal to noise, which can improve sensitivity in the limit that the measurement is limited by background scattering. Furthermore, the background scattering can be further suppressed by reducing the effective Numerical Aperture (NA) of the microscope objective. To take a specific example, these calculations are applied to the experiments which are later performed with squeezed light in Chaps. 11 and 12. In those experiments, lipid particles are tracked within yeast cells, and other centers within the cell contribute background noise. We calculate the scattering profiles of the cell nucleus, mitochondria, lipid granules, and cellular cytoplasm, and from this predict that the signal to noise ratio achieved with dark-field microscopy was over three orders of magnitude better than it would have been for an equivalent bright-field measurement. Our results also highlight the importance of selecting an appropriate illumination angle in dark-field microscopy, with the signal-to-noise varying by over two orders of magnitude as a function of illumination angle.

8.2 Calculations

In the basic setup considered here, an ensemble of particles are imaged via light which they scatter from an illumination field into the collection aperture of an objective, as shown in Fig. 8.1a. For simplicity, we only consider spherical particles, and approximate the total measured field as the sum of each of the individually calculated scattered fields. Although more accurate models to calculate biological scattering exist [6, 8], these approximations are widely used [1, 16, 21, 22] and have been found to provide realistic results [12, 30]. If the scattering particles consist of both particles which are to be measured and unwanted scattering centers, then it is desirable to maximize the desired scattered photon flux while minimizing the unwanted scatter. To study the scattered photon flux, we first evaluate the Mie scattering [11] profiles using the T-matrix method inbuilt in the Optical Tweezers Toolbox [17], which yields scattering intensity profiles as a function of scattering angle such as those shown in Fig. 8.1b. This calculation uses 1064 nm light which is p polarized and with an intensity at the scattering particle of 10 mW μm^{-2}. The scattering particle has a refractive index of 1.4, and is suspended in water with a refractive index of 1.33. As can be seen in Fig. 8.1b, small scatterers have an intensity profile which is well approximated by dipole scattering. The scattering from larger particles, by contrast, can include quite a complex spatial distribution, although there is generally a large maxima of scattering in the forward-propagation direction. Elsewhere on the spatial profile there are maxima and minima whose positions depend on the size and refractive index of the scattering sphere [11].

Once the intensity profile is calculated for each scatterer, it is integrated over the objective aperture area to find the collected photon flux, as shown in Fig. 8.1c for an objective with NA of 1.2. The illumination angles which correspond to dark-field microscopy are indicated by vertical lines, and defined by the range of angles for which the illumination cannot enter the objective either directly or via a back-

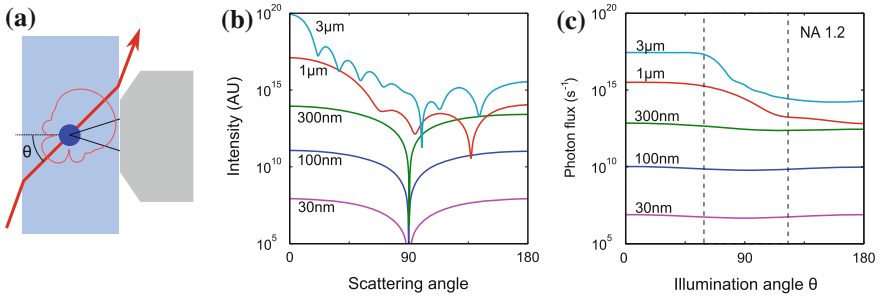

Fig. 8.1 We consider a microscopy measurement in which the illuminating light can be incident from any angle θ relative to the objective, as depicted in (**a**). In this example, the light is incident at the particle 45° from the objective axis, and the resulting scattered field which falls within the objective aperture is collected. The Mie scattering profile for 1064 nm p-polarized light striking with a refractive index of 1.4 suspended in water are shown in (**b**), for particles of diameter 30 nm, 100 nm, 300 nm, 1 μm and 3 μm. This intensity profile has substantial structure, with numerous maxima and minima for the larger particles, and a single minima at an angle of 90° for the dipole scatterers. In subplot **c**, the calculated flux of scattered photons through an NA = 1.2 objective is plotted as a function of the angle θ, for an illumination intensity of 10 mW μm^{-2} at the particle. Since the optical power is measured over a large aperture, the structure evident in the intensity profile is smoothed out. Dark-field measurement requires the illumination angle to be between the two dashed lines, where neither the illumination nor a back-reflection of the illumination will enter the objective aperture

reflection from the glass coverslip. Since this objective has a large aperture, the prominent spatial variation of the intensity profile is barely visible in the total photon flux. The smallest particles show the least spatial variation, and even the intensity minima along the direction of polarization makes little difference to the collected photon flux. Because larger particles scatter far more light in the forward direction, the relative contributions of these large particles can be tuned by orders of magnitude by changing the illumination angle.

Since the objective NA limits the range of possible dark-field illumination angles, most dark-field microscopes use objectives for which the NA is lower than 1.2. In Fig. 8.2 the dependence of the collected photon flux on the illumination angle is shown for a collection of lower NA objectives, with the same calculation parameters as above. The photon flux from 30 nm particles is small, and does not appear within the displayed range for objectives with a NA below 0.6. These 30 nm particles are well approximated as dipole scatterers, with a lower scattering rate but similar spatial dependence to the 100 nm particles. As the NA is reduced, the collected photon flux shows more of the spatial variation present in the intensity distribution. This allows the relative contributions of scattering from different sized particles to be tuned by varying the illumination angle, with greater tuning possible for lower NA objectives. For instance, if the desired signal is scattering from 300 nm particles, with smaller 100 nm particles produce the background, the illumination angle should be as low as possible, and the NA makes little difference to the relative strengths of the scatterers. If larger 1 μm scatterers produce the scattering background, the optimal illumination

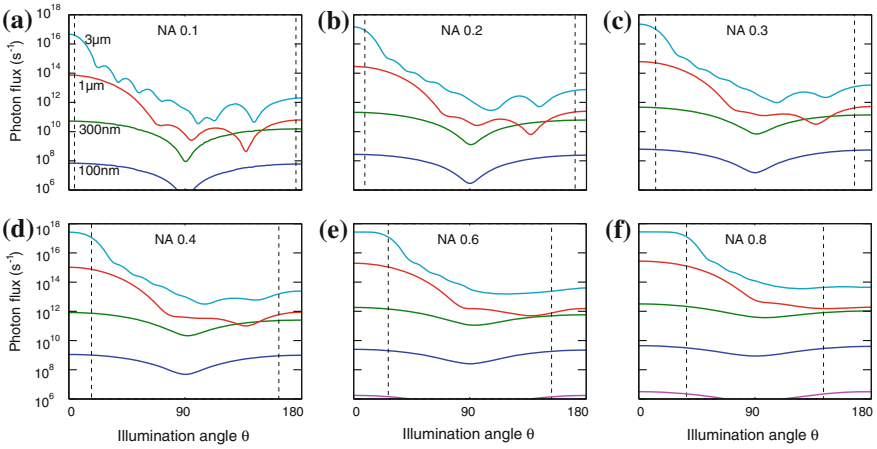

Fig. 8.2 The flux of scattered photons from the particles considered in Fig. 8.1 is calculated for various objectives as a function of the angle θ, with dark-field measurement requiring the illumination to lie between the *dashed lines*. The smallest particle with 30 nm diameter has a photon flux below the plotted range when the objective NA is below 0.6. As the numerical aperture drops, the profile of the collected power approaches the intensity profile shown in Fig. 8.1b. In the case that the measurement sensitivity is limited by background scatterers, this could provide a way to improve the measurement sensitivity. If large particles are being measured among a background of dipole scatterers, the scattering background can be suppressed by choosing an illumination angle of 90° and a low NA objective. Alternatively, if a 300 nm particle is under study, and the scattering background is produced by larger 1 μm particles, then the optimal measurement angle is around 140°, and the relative strength of the scattering background is reduced by reducing the objective NA

angle is around 140°, which then allows the 300 nm particles to dominate the scattered flux for NA below 0.4. However, reducing the NA also increases the diffraction limit and reduces the total photon flux collected, which will both degrade the overall sensitivity [25].

In a real measurement, particularly in biology, the sizes of all the scattering particles may not be precisely known. As such, it is useful to consider the collected photon flux from scatterers over some range of sizes. The dependence of the collected power on the particle size is shown in Fig. 8.3 for several fixed illumination angles. In the dipole scattering regime, the scattered power scales as d^6, where d is the particle diameter [10]. Outside of this regime, the behavior is more complicated. The forward-scatter continues to grow rapidly with particle size, and dominates over the scatter in any other direction. The scattered power collected to the side or back is modulated as scattering minima and maxima are sampled. However, we find that the collected power at the maxima scales as d^2; this suggests that the scattering cross-section scales with the cross-sectional area of the particle. Hence dark-field illumination at any angle will help to suppress the scattering background from a large scatterer (such as a cell nucleus), and this suppression is maximized when the measurement coincides with one of the collection minima.

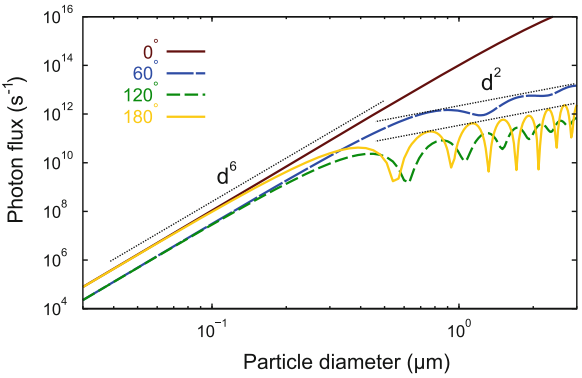

Fig. 8.3 The collected photon flux is plotted here at four separate illumination angles as a function of particle diameter, for an objective NA of 0.4. For dipole scatterers, the collected photon flux always scales as d^6. For larger particles, the side and back scatter photon flux is modulated, but the flux collected at the maxima scale as d^2. By contrast the forward-scatter grows far more rapidly than this

The calculations discussed above have used p polarized light with a wavelength of 1064 nm. This can be extrapolated to any wavelength of light, as Mie scattering depends only on the particle size relative to the wavelength. To apply these results to a different wavelength, the diameters must be adjusted to keep the relative particle size d/λ constant. For instance, if the particle diameters are halved, the results presented will correspond to green illumination at 532 nm. If s polarization is used instead, the scattering power is independent of the incident angle within the dipole scattering regime, while in the Mie scattering regime the angles of the scattering maxima and minima are shifted. However, the overall trends remain similar.

8.3 Application to Biological Measurement

When dark-field microscopy is applied to imaging living cells, many internal components can scatter light, which can produce a large scattering background. Cellular experiments are particularly relevant to this thesis, as the entire goal is to introduce quantum enhanced particle tracking to biological measurements. Here we consider a specific example of a biological experiment in which *Saccharomyces cerevisiae* yeast cells are probed in a dark-field particle tracking scheme, and the thermal motion of lipid granules racked. For such an experiment, the measurement sensitivity is likely to be limited by background scattering from the cell.

Overall, a living cell has a highly inhomogeneous refractive index, with a thin (10 nm) but high refractive index cell wall ($n \approx 1.46$) [7, 14] and an interior which typically varies from 1.36 to 1.40 [4]. Although the cell wall has a high refractive index, due to its small size it has been shown to contribute little to the total scattering

of the cell [7]. Within the cytoplasm, there are many distinct scatterers. In addition to their individual scattering properties, these are collectively considered via their contribution to the refractive index of the cytoplasm, which is considered here to be a large scattering particle. Within a yeast cell, the dominant scatterers are the nucleus, mitochondria, and lipid granules. The nucleus diameter typically varies from 1.5 to 2.8 μm [28], and has a refractive index which varies spatially from 1.36 to 1.39 [4]. Mitochondria are non-spherical with a volume which varies from approximately 0.07 to 1.5 μm^3 [16] and have an average refractive index of 1.40 [2, 26]. Lipid granules are spherical particles which typically have a diameter of 300 nm [27], and a refractive index of 1.50 [20].

To model the scattered field from the yeast cell (Fig. 8.4), we separately calculated the scattered fields of a single nucleus, collections of mitochondria and lipid granules, and the cytoplasm. The collected intensities of all four sources of scattering were then summed to determine the total collected photon flux. The model used a cell volume of 65 μm^3, which is within the range typically found [28]. The model cytoplasm refractive index was 1.36 [4, 5], while the extracellular fluid refractive index is 1.35

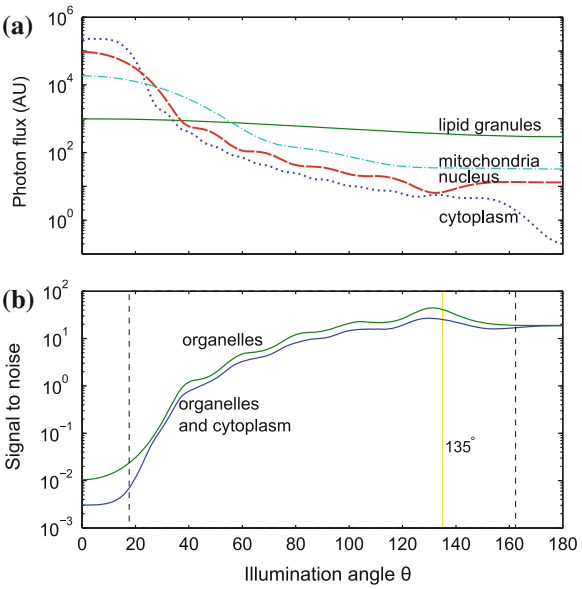

Fig. 8.4 The measured scattered field is calculated for an experiment where lipid granule motion within a yeast cell are measured in dark-field particle tracking with *s* polarized light and an objective NA of 0.4. **a** The dominant source of the collected scattered field varies with the collection angle from nucleus, mitochondria, to lipid granules at largest angles. **b** The signal to noise of the measurement is plotted here, which is defined as the lipid granule scatter power divided by the scattered power from all other contributions. As in Figs. 8.1 and 8.2, dark-field microscopy required the illumination angle to be between the two dashed vertical lines. The slight rise in the signal to noise around 130° results from a minima in the calculated field for the nucleus. Since the position of such minima in a real measurement is unlikely to be accurately given by our calculations, this maxima is not considered to be physically meaningful. For the experiments with squeezed light described in Part III, an illumination angle of 135° was chosen, as indicated by the light vertical line

[8, 14]. The model nucleus has a refractive index of 1.39 [3, 4] and is approximated as a 2.4 μm wide sphere, which thus occupies 9 % of the cell volume [28]. The mitochondria are modeled as a collection of 12 spheres with a refractive index of 1.40, and diameters ranging from 0.7 to 1.2 μm, with a total volume occupying 8.5 % of the cell [8]. The lipid granules are 300 nm across, have a refractive index of $n = 1.50$, and occupy 1.3 % of the cell volume [28].

The predicted photon flux from the different scatterers are shown in Fig. 8.4a. Due to the spatial profiles of the individual scattered fields, the total scattered field is dominated by all four of the scattering centers at different collection angles. Since the experiment aimed to measure lipid granules, the other scatterers produced the background. The resulting signal to noise ratio, defined as the collected flux which scattered from lipid granules divided by all other sources of scatter, is shown in Fig. 8.4b. This calculation is relevant to the experiments with squeezed light described in Part III. For those experiments, an illumination angle of 135° was chosen, which falls within the optimal range of collection angles from 100 to 160°. Within this range, the signal to noise is over three orders of magnitude higher than it would be for a bright-field measurement at $\theta = 0°$. At other dark-field illumination angles, the signal to noise could be over two orders of magnitude lower. This suggests that in addition to removing the bright background from the illuminating laser, the use of dark-field microscopy can suppress unwanted signals.

Some caution is required when attempting to derive absolute predictions from the calculations presented here. Firstly, all of the cellular components have been approximated as homogeneous spheres, while both the nucleus and mitochondria in a real cell are non-spherical and structured, which can significantly alter the scattering properties [15]. However, this simplified model has been shown to yield results which closely approximate real biological samples [1, 16, 21, 22]. Furthermore, interference between different scatterers has been neglected, although this can effect the scattered field [6]. Interference does not change either the total flux of scattered photons, or the total momentum of the scattered photons. Therefore while interference will introduce fringes in the measured light, it should not greatly change the photon flux over the entire aperture. Additionally, light may scatter multiple times within the cell. Multiple scattering can deflect the illumination angle, or cause the illumination to be inhomogeneous over the particle. However, the photon flux would not be influenced by a small change in illumination angle for any of the scatterers in Fig. 8.4a. Since the particle have a similar size to the wavelength, the spatial inhomogeneity in the illuminating field which multiple scattering introduces will typically be larger than the particles, and will not significantly effect the predicted outcome. Thus, although some features in the photon flux may be different in a real experiment to the calculations presented here, the general conclusion that dark-field illumination vastly increases the relative contribution of the lipid granules to the measured fields is valid.

8.4 Conclusion

We have calculated the collected flux of scattered photons in the Mie scattering regime, and determined how the measurement sensitivity depends on the illumination angle for various objectives and particles. In the limit that the dark-field measurement is limited by background scattering, we have shown that the sensitivity can be improved by lowering the objectives effective numerical aperture (NA) and tuning the illumination angle. For an example biological experiment which applies dark-field microscopy to track lipid granules within a yeast cell, the collected photon flux from different cellular components was approximately calculated. This suggests that the signal-to-noise varies by over three orders of magnitude with the illumination angle. For the experiments described in Part III, which demonstrate quantum enhanced particle tracking, this calculation is highly relevant, and an illumination angle is chosen which provides optimal signal to noise.

References

1. B. Beauvoit, T. Kitai, B. Chance, Contribution of the mitochondrial compartment to the optical properties of the rat liver: a theoretical and practical approach. Biophys. J. **67**(6), 2501–2510 (1994)
2. J. Beuthan, O. Minet, J. Helfmann, M. Herrig, G. Müller, The spatial variation of the refractive index in biological cells. Phys. Med. Biol. **41**(3), 369 (1996)
3. A. Brunsting, P.F. Mullaney, Differential light scattering from spherical mammalian cells. Biophys. J. **14**(6), 439–453 (1974)
4. W. Choi, C. Fang-Yen, K. Badizadegan, S. Oh, N. Lue, R. Dasari, M. Feld, Tomographic phase microscopy. Nat. Methods **4**(9), 717–719 (2007)
5. C.L. Curl, C.J. Bellair, T. Harris, B.E. Allman, P.J. Harris, A.G. Stewart, A. Roberts, K.A. Nugent, L. Delbridge, Refractive index measurement in viable cells using quantitative phase-amplitude microscopy and confocal microscopy. Cytometry A **65**(1), 88–92 (2005)
6. R. Drezek, A. Dunn, R. Richards-Kortum, Light scattering from cells: finite-difference time-domain simulations and goniometric measurements. Appl. Opt. **38**(16), 3651–3661 (1999)
7. A.K. Dunn, Light scattering properties of cells. Ph.D. thesis, University of Texas, Austin, 1997
8. A. Dunn, R. Richards-Kortum, Three-dimensional computation of light scattering from cells. IEEE J. Sel. Top. Quant. Electron. **2**(4), 898–905 (1996)
9. A.R. Dunn, J.A. Spudich, Dynamics of the unbound head during myosin V processive translocation. Nat. Struct. Mol. Biol. **14**(3), 246–248 (2007)
10. Y. Harada, T. Asakura, Radiation forces on a dielectric sphere in the Rayleigh scattering regime. Opt. Commun. **124**(5–6), 529–541 (1996)
11. D.R. Huffman, C.F. Bohren, *Absorption and Scattering of Light by Small Particles* (Wiley, New York, 2008)
12. M. Kalashnikov, W. Choi, C.-C. Yu, Y. Sung, R.R. Dasari, K. Badizadegan, M.S. Feld, Assessing light scattering of intracellular organelles in single intact living cells. Opt. Express **17**(22), 19674 (2009)
13. S. Kudo, Y. Magariyama, S. Aizawa, Abrupt changes in flagellar rotation observed by laser dark-field microscopy. Nature **346**, 677–680 (1990)
14. J.S. Maier, S.A. Walker, S. Fantini, M.A. Franceschini, E. Gratton, Possible correlation between blood glucose concentration and the reduced scattering coefficient of tissues in the near infrared. Opt. Lett. **19**(24), 2062–2064 (1994)

15. O.C. Marina, C.K. Sanders, J.R. Mourant, Correlating light scattering with internal cellular structures. Biomed. Opt. Express **3**(2), 296 (2012)
16. J.R. Mourant, J.P. Freyer, A.H. Hielscher, A.A. Eick, D. Shen, T.M. Johnson, Mechanisms of light scattering from biological cells relevant to noninvasive optical-tissue diagnostics. Appl. Opt. **37**(16), 3586–3593 (1998)
17. T. Nieminen, V. Loke, A. Stilgoe, G. Knöner, A. Brańczyk, N. Heckenberg, H. Rubinsztein-Dunlop, Optical tweezers computational toolbox. J. Opt. A: Pure Appl. Opt **9**(8), S196 (2007)
18. M. Nishiyama, E. Muto, Y. Inoue, T. Yanagida, H. Higuchi, Substeps within the 8-nm step of the ATPase cycle of single kinesin molecules. Nat. Cell Biol. **3**(4), 425–428 (2001)
19. N. Noda, S. Kamimura, A new microscope optics for laser dark-field illumination applied to high precision two dimensional measurement of specimen displacement. Rev. Sci. Instrum. **79**(2), 023704–023704 (2008)
20. L. Sacconi, I. Tolic-Nørrelykke, M. D'Amico, F. Vanzi, M. Olivotto, R. Antolini, F. Pavone, Cell imaging and manipulation by nonlinear optical microscopy. Cell Biochem. Biophys. **45**(3), 289–302 (2006)
21. I.S. Saidi, S.L. Jacques, F.K. Tittel, Mie and Rayleigh modeling of visible-light scattering in neonatal skin. Appl. Opt. **34**(31), 7410–7418 (1995)
22. J.M. Schmitt, G. Kumar, Optical scattering properties of soft tissue: a discrete particle model. Appl. Opt. **37**(13), 2788–2797 (1998)
23. S. Schultz, D.R. Smith, J.J. Mock, D.A. Schultz, Single-target molecule detection with non-bleaching multicolor optical immunolabels. Proc. Natl. Acad. Sci. USA **97**(3), 996–1001 (2000)
24. M.A. Taylor, W.P. Bowen, Enhanced sensitivity in dark-field microscopy by optimizing the illumination angle. Appl. Opt. **52**(23), 5718–5723 (2013)
25. M.A. Taylor, J. Knittel, W.P. Bowen, Fundamental constraints on particle tracking with optical tweezers. New J. Phys. **15**, 023018 (2013)
26. R. Thar, M. Kühl, Propagation of electromagnetic radiation in mitochondria? J. Theor. Biol. **230**(2), 261–270 (2004)
27. I.M. Tolić-Nørrelykke, E.-L. Munteanu, G. Thon, L. Oddershede, K. Berg-Sørensen, Anomalous diffusion in living yeast cells. Phys. Rev. Lett. **93**, 078102 (2004)
28. M. Uchida, Y. Sun, G. McDermott, C. Knoechel, M. Le Gros, D. Parkinson, D. Drubin, C. Larabell, Quantitative analysis of yeast internal architecture using soft X-ray tomography. Yeast **28**(3), 227–236 (2011)
29. H. Ueno, S. Nishikawa, R. Iino, K.V. Tabata, S. Sakakihara, T. Yanagida, H. Noji, Simple dark-field microscopy with nanometer spatial precision and microsecond temporal resolution. Biophys. J. **98**(9), 2014–2023 (2010)
30. J.D. Wilson, T.H. Foster, Mie theory interpretations of light scattering from intact cells. Opt. Lett. **30**(18), 2442–2444 (2005)
31. R. Yasuda, H. Noji, M. Yoshida, K. Kinosita, H. Itoh, Resolution of distinct rotational substeps by submillisecond kinetic analysis of F1-ATPase. Nature **410**(6831), 898–904 (2001)

Chapter 9
Technical Constraints on Sensitivity

In the preceding chapters, several new methods to improve the particle tracking sensitivity have been presented. These methods add to an already extensive depth of knowledge within the field of particle tracking. This chapter summarizes some of the important technical problems which can constrain particle tracking experiments, and methods which are in use to allow high sensitivity measurements.

9.1 Aberrations

Optical tweezers rely on a tightly focused optical field to trap and measure a particle. This is often limited by aberrations in the objective which distort the optical field and broadens the focus. Such aberrations can severely degrade both the trap strength and the measurement sensitivity.

9.1.1 Spherical Aberrations

An essential component in any optical trapping experiment is the trapping objective. Often oil-immersion objectives are used, though it is also possible to use water immersion, or immersion-free objectives (as used in this thesis). The NA of the objective is fundamentally limited by the refractive index of the immersion medium, such that immersion-free objectives are constrained to an NA below 1. Since the trap performance improves with NA, most experiments are performed with higher NA oil-immersion or water-immersion objectives. However, it is important to note the designed function of the objective, as even the highest quality objectives suffer from aberrations if used outside of their design specifications. Oil-immersion objectives are typically designed to focus light through oil and a glass coverslip. Optical trapping experiments typically require the light to be focused into water, and the propagation through water introduces spherical aberrations (see Fig. 9.1). Likewise,

M. Taylor, *Quantum Microscopy of Biological Systems*, Springer Theses,
DOI 10.1007/978-3-319-18938-3_9

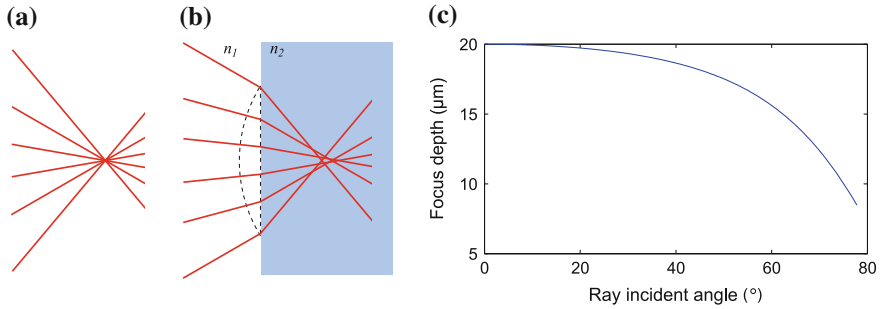

Fig. 9.1 Spherical aberrations. **a** When an objective focuses light, all of the rays should converge to a single spot. **b** If the light is being focused from one material with a refractive index of n_1 into a second material with n_2, the rays are refracted at the interface between the two materials. This is equivalent to adding a spherical lens with a refractive index of n_1 in a medium with n_2, as represented by the *dashed lines*. When focusing into a lower refractive index medium ($n_2 < n_1$), this brings the focus closer, with the high angle rays focused at a smaller depth than the low angle rays. **c** The depth at which the rays converge in water, as a function of the incident angle. This calculation uses NA = 1.3 oil immersion objectives with $n_1 = 1.50$ and $n_2 = 1.33$, with low angle rays focused into the water at a depth of 20 μm. Spherical aberration shifts the focal depth by more than 10 % for all incident angles above 46°

immersion-free objectives are not generally designed to focus into water, and also suffer spherical aberrations. This can vastly broaden the point-spread function of the objective, degrading the optical forces [20] and rendering optical traps unstable past a depth of approximately 20 μm [15]. This also degrades the measurement sensitivity by distorting the measurement mode (as described in Chap. 3), thus preventing efficient extraction of information from the scattered field. Furthermore, by reducing the trapping field intensity at the particle, aberration also lowers the rate of photon scattering, with a corresponding loss of sensitivity. The simplest method to remove spherical aberrations is to use high quality water-immersion objectives. In principle, since these are designed to allow light to propagate through water, they should not suffer any spherical aberrations [17].

9.1.2 Other Aberrations

In addition to suffering from spherical aberrations, the individual lenses within an objective have a refractive index which varies with wavelength. This results in chromatic aberrations, where the focal length varies with wavelength. An objective contains multiple lenses which are typically arranged to cancel out the overall wavelength dependence. However, this is only possible over a finite wavelength range. Most objectives are designed for light microscopy with visible light, while optical trapping experiments often use 1064 nm laser light. As such, the objective may not be

designed optimally for the trapping light, which can introduce aberrations on the focus [17].

The laser power used in optical trapping is also typically far higher than most objectives are designed for. Absorption in the objective can thus heat the lenses, which will degrade the focus. Heating will change the refractive index and deform the lens surface, which aberrates the overall focal properties, and also causes stress-induced birefringence [7]. The birefringence results in astigmatism, where rays in the horizontal plane focus at a different depth to rays in the vertical plane [13]. Thermal heating can therefore aberrate the focus severely, so it is important to use low absorption objectives even in classical experiments.

The above aberrations can result when near-perfect objectives are used outside of their design range. Additionally, non-ideal objectives also suffer aberrations due to imperfect design or construction. Astigmatism can result from unwanted stress in the mounting or imperfect angular alignment of the lenses within the objective [13, 18]. Coma aberrations result when the focus of off-axis incident light is distorted. However, these aberrations are not typically as serious to trapping applications, and the bulk of the literature attention is on spherical aberrations.

9.1.3 Aberrations in the Sample Chamber

While most aberrations are associated with the objective, the chamber which holds the particles under study can also aberrate the focus. The sample chamber typically includes a small cavity between glass coverslips which is filled with the sample solution. This is mounted and sealed with a waterproof adhesive, typically nail polish [19]. If the coverglass is stressed when it is glued in place, the resulting stress induced birefringence will lead to astigmatism [2]. Although there is no way to completely eliminate the stress associated with the gluing process, the astigmatism can be minimized with an appropriate design of the sample chamber. If the sample chamber is circularly symmetric, as shown in Fig. 9.2, the symmetry in the stress should minimize any resulting aberrations.

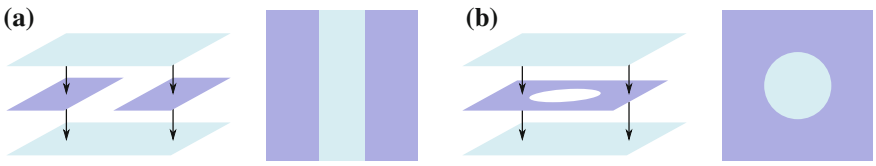

Fig. 9.2 The sample chamber is constructed with two glass coverslips (*faint blue*) separated by a spacer (*purple*). For the experiments in this thesis, this was arranged as shown in (**a**), although this can introduce astigmatism via stress induced birefringence. In this approach, the sample chamber is constructed, then filled with solution and sealed with adhesive [19]. **b** An alternative which avoids the astigmatism is to use a circularly symmetric sample chamber. Two coverslips are separated with a thin spacer, in which a circular hole is cut to house the solution. This requires the chamber to be filled with solution during the construction process

Furthermore, optical trapping experiments which are conducted within in vivo also suffer from aberrations due to the surrounding biological sample [8]. Since this aberration depends on the specific geometry and structure of the sample, it is not possible to design the optical trap to avoid it. The only possible way to avoid this is to apply active aberration compensation.

9.1.4 Aberration Compensation

It is possible to compensate for aberrations by engineering the incident trapping light [18]. If the aberrations within the system are known, then the conjugate phase can be applied to the field before it enters the experiment to correct the focal spot. For instance, a first order Zernike polynomial which represents spherical aberrations can be applied with a spatial light modulator to improve the focus [16]. Other aberrations can also be represented as Zernike polynomials, and compensated in a similar manner [11, 18]. Since an improvement in the focus will increase the optical forces, the quality of the aberration compensation is typically estimated from measurements of the trap stiffness. The optimal correction is found by adjusting the amplitude of each Zernike polynomial on the spatial light modulator to maximize the trap stiffness.

Although this optimization of the trapping field can improve the performance, it is not guaranteed to allow optimal performance, particularly if any aberrations are present which are not represented by the Zernike polynomials. To overcome this limitation, adaptive algorithms such as a genetic algorithm can instead be used to optimize the phase applied to the spatial light modulator [9, 14]. However, the genetic algorithm is an inefficient method to find the optimal solution. A deterministic method of aberration compensation is to measure the phase of the aberrated light, and apply the calculated optimal phase compensation to the spatial light modulator [5, 8].

In order to apply these compensation techniques, it is necessary to incorporate a spatial light modulator into the optical tweezers setup. This in itself introduces some experimental difficulties. For more on the use of optical tweezers with spatial light modulators, including design strategies and aberration compensation, see Ref. [12].

9.2 Long-Term Stability

Slow drifts in an experiment can cause a spurious signal which masks the true particle motion. For instance, the stage holding the sample under study often drifts over a timescale of order minutes [10]. This can be reduced by using an ultra-stable sample mount, but this does not completely eliminate the drift. The drift can also be compensated by measuring the drift and applying active feedback to the sample stage. The long-term precision of the particle tracking measurement is then given by the precision with which the stage drift can be measured. In typical experiments,

the drift is measured by immobilizing a reference particle on the sample chamber somewhere within the field of view of the imaging optics and tracking this particle with either the CCD camera, which can provide a few nm stability, or with a second measurement laser, which provides sub-nm long-term stability [6].

Also, since the particle position is measured relative to the laser beam center, any movement of the laser focus directly appears in the measured results. The focus shifts when the pointing direction of the incident trapping laser changes, as will result from any drifts in the mirrors. Mirror drifts are minimized with vibration isolation, used together with ultra-stable mirror mounts [10]. Additionally, the laser beam can be deflected by air currents, as air pressure gradients result in a gradient in the refractive index. To minimize air currents, the trapping setup is often confined in a box [10]. To reduce the spurious signal produced by the remaining currents, the air can be replaced with Helium, which has a lower refractive index and therefore produces less deflection for a given pressure gradient [1].

Despite the vast effort and resources which have been invested into improving classical experiments in this low frequency range, so far these experiments remain limited by low frequency technical noise. Quantum noise is therefore not relevant at low frequencies. It is therefore unlikely that quantum enhanced precision will be achieved below a few Hz while using existing technology.

9.3 Measurement Noise

The drifts described above are a form of technical noise which can obscure the measured signal. There are also various other sources of measurement noise, such as electronic noise in the detection, laser noise, and high frequency mechanical resonances in the sample chamber or optical mounts. Electronic flicker noise is a particularly significant noise source at low frequencies, as it scales as the inverse of frequency. This can be minimized by using low-noise detectors and amplifiers. When the measured signal extends into the MHz regime, the sensitivity can be degraded if the circuitry is not properly impedance-matched. Laser noise can also substantially degrade measurements, and use of a low-noise laser is essential for highly sensitive particle tracking. However, both laser noise and low frequency electronic noise can be eliminated with lock-in measurement, and can therefore be effectively managed.

Acoustic noise, however, cannot be eliminated with lock-in measurement, as discussed in Chap. 7. This noise is most disruptive if there are any mechanical resonances in the system. Long, cantilevered structures in particular can increase the impact of mechanical disturbances on sensitive measurements [4]. To reduce the degrading effect of such vibrations, most optical tweezers systems are built on air-isolated optical tables [4]. Often the acoustic noise needs to be reduced even further, so experiments are performed in quiet times such as weekends [10].

It is also important to consider the effects of aliasing in the detection electronics. This both degrades precision by increasing the frequency range of technical noise which can enter the measurement, and also distorts the spectra of the particle motion.

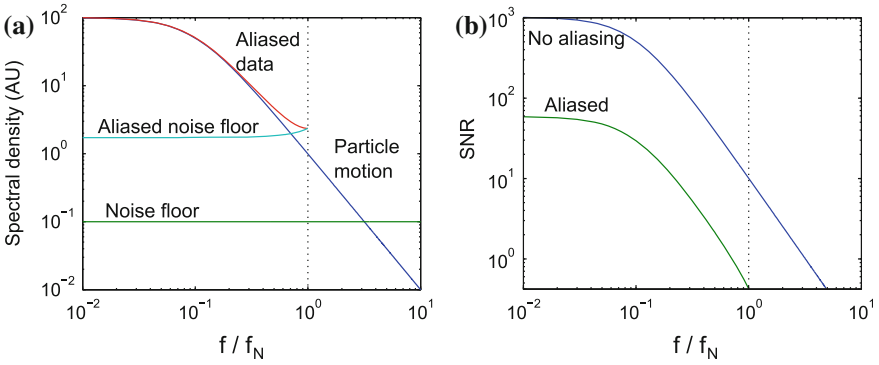

Fig. 9.3 Aliasing of a measured signal. **a** Calculated spectral densities are shown for a particle following trapped Brownian motion and a flat white measurement noise floor. If this is measured with a bandwidth 10 times the Nyquist frequency f_N, then the noise floor enters the measurement 10 times over. Additionally, the measured signal deviates from the true motion due to the high frequency particle motion which is aliased into the measurement. **b** The overall signal-to-noise of the measurement, for measurements both with and without aliasing. For this example calculation, aliasing degrades the sensitivity by a factor of approximately 20

This is particularly detrimental if the experiment aims to accurately characterize the spectra of motion, since aliasing causes high frequency particle motion to be measured at lower frequencies, which misrepresents the true mechanical response of the particle. This effectively converts high frequency particle tracking signal into lower frequency noise, which can severely degrade an otherwise high sensitivity measurement (as represented in Fig. 9.3). In many cases, however, the purpose of the measurement is to estimate the mechanical properties of the optical trap. Since the motion above the Nyquist frequency is determined by the same properties, inclusion of this in the measurement record can provide additional information. However, it is only beneficial if aliasing is accounted for appropriately in the signal analysis [3]. Aliasing can be suppressed substantially by applying a low-pass filter prior to digital recording.

References

1. E.A. Abbondanzieri, W.J. Greenleaf, J.W. Shaevitz, R. Landick, S.M. Block, Direct observation of base-pair stepping by RNA polymerase. Nature **438**(7067), 460–465 (2005)
2. C. Ai, J.C. Wyant, Testing stress birefringence of an optical window, in *8th International Symposium on Gas Flow and Chemical Lasers. International Society for Optics and Photonics* (1992), pp. 165–172
3. K. Berg-Sørensen, H. Flyvbjerg, Power spectrum analysis for optical tweezers. Rev. Sci. Instrum. **75**(3), 594–612 (2004)
4. R.W. Bowman, M.J. Padgett, Optical trapping and binding. Rep. Prog. Phys. **76**(2), 026401 (2013)

5. R.W. Bowman, A.J. Wright, M.J. Padgett, An SLM-based Shack-Hartmann wavefront sensor for aberration correction in optical tweezers. J. Opt. **12**(12), 124004 (2010)
6. A. Carter, G. King, T. Ulrich, W. Halsey, D. Alchenberger, T. Perkins, Stabilization of an optical microscope to 0.1 nm in three dimensions. Appl. Opt. **46**(3), 421–427 (2007)
7. H. Chen, H. Yang, X. Yu, Z. Shi, Simulated and experimental study of laser-beam induced thermal aberrations in precision optical systems. Appl. Opt. **52**(18), 4370–4376 (2013)
8. T. Čižmár, M. Mazilu, K. Dholakia, In situ wavefront correction and its application to micromanipulation. Nat. Photon. **4**(6), 388–394 (2010)
9. D.B. Conkey, A.N. Brown, A.M. Caravaca-Aguirre, R. Piestun, Genetic algorithm optimization for focusing through turbid media in noisy environments. Opt. Express **20**(5), 4840–4849 (2012)
10. F. Czerwinski, A.C. Richardson, L.B. Oddershede, Quantifying noise in optical tweezers by allan variance. Opt. Express **17**, 13255–13269 (2009)
11. M. Dienerowitz, G. Gibson, R. Bowman, M. Padgett, Holographic aberration correction: optimising the stiffness of an optical trap deep in the sample. Opt. Express **19**(24), 24589–24595 (2011)
12. E. Martín-Badosa, M. Montes-Usategui, A. Carnicer, J. Andilla, E. Pleguezuelos, I. Juvells, Design strategies for optimizing holographic optical tweezers set-ups. J. Opt. A: Pure Appl. Opt **9**(8), S267–S277 (2007)
13. I. Moshe, S. Jackel, Influence of birefringence-induced bifocusing on optical beams. J. Opt. Soc. Am. B **22**(6), 1228–1235 (2005)
14. M. Müllenbroich, N. McAlinden, A. Wright, Adaptive optics in an optical trapping system for enhanced lateral trap stiffness at depth. J. Opt. **15**(7), 075305 (2013)
15. K. Neuman, S. Block, Optical trapping. Rev. Sci. Instrum. **75**(9), 2787–2809 (2004)
16. T. Ota, T. Sugiura, S. Kawata, M.J. Booth, M.A. Neil, R. Juskaitis, T. Wilson, Enhancement of laser trapping force by spherical aberration correction using a deformable mirror. Jpn. J. Appl. Phys. **42**(6B; ISSU 391), L701–L703 (2003)
17. S.N.S. Reihani, S.A. Mir, A.C. Richardson, L.B. Oddershede, Significant improvement of optical traps by tuning standard water immersion objectives. J. Opt. **13**(10), 105301 (2011)
18. Y. Roichman, A. Waldron, E. Gardel, D.G. Grier, Optical traps with geometric aberrations. Appl. Opt. **45**(15), 3425–3429 (2006)
19. S. Tolic-Nørrelykke, E. Schaffer, J. Howard, F. Pavone, F. Julicher, H. Flyvbjerg, Calibration of optical tweezers with positional detection in the back focal plane. Rev. Sci. Instrum. **77**(10), 103101–103101 (2006)
20. W.H. Wright, G. Sonek, M. Berns, Parametric study of the forces on microspheres held by optical tweezers. Appl. Opt. **33**(9), 1735–1748 (1994)

Part III
Quantum Enhanced Optical Tweezers

Part III of this thesis demonstrates quantum enhanced sensitivity in optical tweezers. Chapter 10 describes the development and characterization of our quantum enhanced particle tracking apparatus, which relies upon several of the classical technologies developed in Part II. This demonstrates both sub-shot noise limited particle tracking and application of squeezed states of light to microscopy for the first time. With this tool, it is possible to perform a broad range of quantum enhanced measurements in biology that were unfeasible with previous technologies.

Two such biophysical experiments were performed with this apparatus. We began in Chap. 11 by demonstrating the first biological measurements with sensitivity beyond the quantum noise limit. Naturally occurring lipid granules were tracked within *Saccharomyces cerevisiae* yeast cells, with amplitude squeezed light yielding a 2.4 dB enhancement in displacement sensitivity. By analyzing the thermal motion, we could characterize the mechanical properties of the cellular cytoplasm surrounding the lipid particles, with squeezed light allowing a precision enhancement of 22 %.

This experiment was then extended to spatially resolved quantum imaging of the cytoplasmic structure in Chap. 12. This experiment demonstrated both sub-diffraction limited quantum metrology and quantum enhanced spatial resolution for the first time in a biological context. By tracking lipid particles as they diffused through an extended region of the cell, spatial variations in the local mechanical properties of the cellular cytoplasm could be sampled. This spatial structure was resolved at length scales down to 10 nm, far below the diffraction limit. In this case the use of quantum correlated light was found to enhance the spatial resolution by 14 %.

Chapter 13 then concludes this part of the thesis with a discussion of the future directions of quantum enhanced particle tracking. Despite showing conclusive quantum enhancements, our proof-of-principle experiments are yet to surpass the sensitivity of an optimized classical detection scheme. This chapter discusses the strategies required to combine quantum enhancement with classical optimization, and the important applications which such an apparatus could hold.

Chapter 10
Surpassing the Quantum Limit

As described in Part I, quantum noise establishes a fundamental limit for particle tracking sensitivity. This limit can be surpassed only by using non-classical states of light, in which quantum correlations in the photon statistics are used to suppress the quantum noise. This chapter describes the development of the first optical tweezers experiment with quantum enhanced particle tracking sensitivity. The particle tracking method reported in this chapter was described in the following publication [25].

10.1 Using Squeezed Light to Enhance Particle Tracking

In any optical measurement, quantum noise sets a fundamental limit on the sensitivity achievable per photon [11, 14]. This limit can only be surpassed if quantum correlations are used to suppress the quantum noise, such that more information is extracted per photon [9, 17]. Hence, use of such correlations allows high sensitivity measurements to proceed with a lower light intensity than classically possible [4, 28], which in the presence of optical power constraints allows sensitivity that can outperform any classical competitor.

Biological measurements are one important field in which optical power must be constrained. Incident light disrupts and damages cells via both optical heating [21] and photochemical effects [18]. Even the most gentle optical probe will effectively write lithographic changes through the specimen, which can perturb many of the parameters under study and limit biological observations. Use of quantum correlated light in biological measurements could allow reduction of the optical power and the associated optical damage, thus improving observations and potentially reveal new phenomena.

In typical laser-based particle tracking, the presence of a particle causes light to be scattered out of an incident field. The subsequent interference between scattered and transmitted fields manifests itself as a deflection of the incident field proportional to the displacement x of the particle from the beam center. This deflection is usually detected with a quadrant photodiode. The quantum noise limit is enforced by the

M. Taylor, *Quantum Microscopy of Biological Systems*, Springer Theses,
DOI 10.1007/978-3-319-18938-3_10

probabilistic nature of photon detection events on either side of the photodiode. Quadrant photodetection is a special case of spatial homodyne detection [23] where information contained in the field mode of interest is extracted via interference with a bright spatially shaped local oscillator field (see Chap. 6). In this framework, particle position measurement in optical tweezers is formally equivalent to an interferometric phase measurement. It is well known that phase measurements can be improved with nonclassical light [9, 11], with the recent demonstrations of sub-quantum noise limited sensitivity in gravitational wave detectors being a notable example [1, 2]. The complex scattering pattern from microscopic particles in tracking experiments necessitates a generalization of the usual quantum noise limit for phase measurement. Including spatial structure, and expressed in terms of the position x of the particle, the quantum noise limit was shown in Chap. 3 to be

$$\Delta x^2_{\mathrm{QNL}} = \frac{1}{4}\eta^{-1} n^{-1}_{\mathrm{scat}} \mathrm{Re}\{\langle \psi'_{\mathrm{scat}} | \psi_{\mathrm{det}} \rangle\}^{-2}, \tag{10.1}$$

where η is the detection efficiency of the scattered light; n_{scat} is the mean flux of scattered photons; ψ_{scat} and ψ_{det} are respectively the mode shapes of the scattered mode and a detection mode defined by the local oscillator field and detection method; and $\psi'_{\mathrm{scat}} = \frac{d\psi_{\mathrm{scat}}}{dx}\big|_{x=0}$ in the limit of small particle displacement. Since the quantum noise limit applies to tracking of *single* particles, it is not constrained by the Rayleigh criterion which determines the resolvable separation of *two* particles [14].

Using an optical field with amplitude quadrature variance V in the detection mode ψ_{det} at the plane of the particle, the achievable sensitivity is

$$\Delta x^2_{\mathrm{meas}} = [1 - \eta(1 - V)] \times \Delta x^2_{\mathrm{QNL}} \tag{10.2}$$

(see Chap. 3). In the coherent state limit with $V = 1$, the quantum noise limit is exactly reached. Using amplitude squeezed light, exhibiting non-classical photon anti-bunching, however, the variance V may be suppressed below unity, allowing the quantum noise limit to be surpassed. Although Eq. 10.2 was derived for squeezed light, when $V \to 0$ in the limit of high photon flux it sets an ultimate limit which cannot be surpassed with any quantum resource. When using bright optical fields subject to non-negligible losses, squeezed states approach this ultimate limit, and outperform more elaborate non-classical states such as NOON states [9].

Two technical barriers have previously prevented the use of squeezed light in biological measurements or particle tracking. First, the parameters which are of interest in such experiments typically produce mechanical displacements at low frequencies, where classical noise sources constrain the possibility of generating squeezing [16, 29]. Although state-of-the-art squeezing now reaches down to 10 Hz [22], this is based on extensive technical stabilization techniques which cannot be easily reproduced. Here, we instead applied the optical lock-in technique described in Chap. 7 to measure the low-frequency particle motion in the MHz frequency band of the squeezing. Although Yurke et al. proposed a similar lock-in method in 1987 to achieve quantum enhanced sensitivity at low frequencies [31], and theoretical

investigation of this scheme still continues [33], the experiments performed here constitute the first demonstration of low frequency measurements enhanced with high frequency squeezing. The second barrier is that propagation through high numerical aperture lenses and biological samples distorts the spatial mode of the squeezed light and prevents it from matching the detection mode. Due to its immense internal structure, there is no way to reliably calculate the scattering profile of a cell. Likewise, it is completely unrealistic to neglect spatial perturbations on light which propagates through a cell. Thus, it is necessary to find some way to ensure that the squeezed mode and detection mode coincide at detection, given unknown perturbations on the optical modes. To ensure that the squeezed mode would overlap perfectly with the detection mode, we applied the self-homodyne particle tracking technique described in Chap. 6. A bright amplitude squeezed field was used as the local oscillator, which ensured that the detection mode was given by the squeezed mode, despite the unknown distortion of the optical modes.

In biological experiments, it is also necessary to know which subcellular component gives rise to the scattered field which is measured. Since cells contain a vast array of scattering centers, the competing scattered fields from the desired component needs to be isolated to allow a reliable interpretation of any measured data. This is achieved here by choosing an appropriate illumination angle to maximize signal-to-noise, as explained in Chap. 8.

10.2 Particle Tracking Method

The particle tracking apparatus developed here is shown schematically in Fig. 10.1. Rather than relying on a single incident field to both interrogate the particle and act as the local oscillator, two separate fields are used. A Gaussian probe field propagating at an angle of 70° to the optical trapping axis acts as a dark-field illumination, interrogating the particle and producing scattering. As in Chap. 6, the local oscillator field is shaped as a "flipped" Gaussian, with a π phase shift applied to one half of its transverse profile. This propagates along the trap axis and acts to define the detection mode. Direct detection of the interference between the flipped local oscillator and scattered light on a single photodiode provides equivalent particle position information to the quadrant photodiode in standard particle tracking (see Chap. 6). Now, however, the local oscillator can be amplitude squeezed to allow quantum enhanced precision, and the probe field can be stroboscopically pulsed to shift the particle tracking information to MHz frequencies.

To allow particle motion to be studied for an extended length of time, an optical trap was used to confine them near the focus of the objectives. The optical force of the focused laser beam has two components; radiation pressure pushes particles along the direction of propagation, while the electric field gradient induces a force toward the focus of the laser beam. The waist of the field at the focus decreases with the NA of the objective lenses, and this correspondingly increases the gradient force

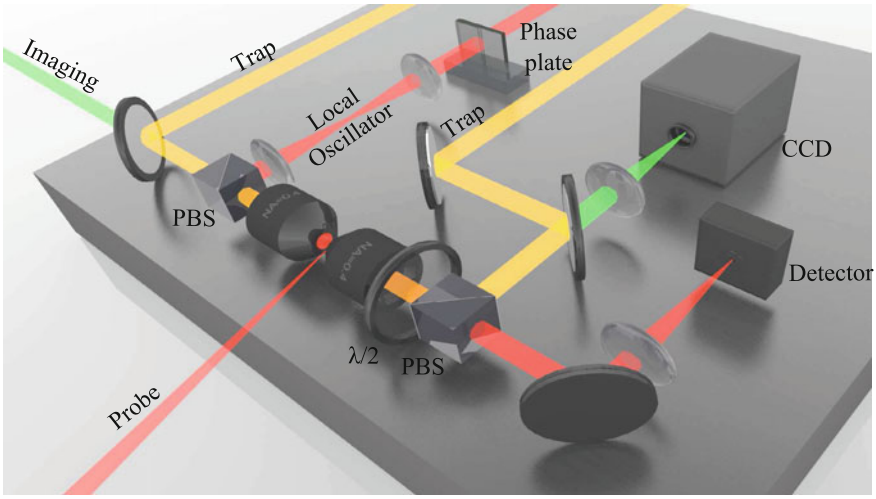

Fig. 10.1 Experimental layout. *PBS* polarizing beamsplitter, $\lambda/2$: half waveplate. An Nd:YAG laser produces 10–500 mW of 1064 nm trapping field (*orange*), which forms a counter-propagating optical trap to immobilize particles. Polarizing optics are used to isolate the trapping field from the detector. An imaging field (*green*) at 532 nm images the plane of the optical trap onto a CCD camera, allowing particles to be identified visually. A separate Nd:YAG laser produces the 1064 nm fields of the probe and local oscillator (*red*), which are used to measure particle position. For the full experimental layout, including the squeezed light source and field preparation, see Fig. 10.8

while leaving the radiation pressure approximately unchanged. As such, a single laser beam cannot stably trap particles if the objective NA is too low.

In our experiment, the optical tweezers were formed with two NA = 0.4 microscope objectives (LMH-20X-YAG). Counter-propagating trapping fields which have opposing radiation pressure forces were used to trap particles stably, as the NA was too low to permit single beam trapping. The objectives were chosen because their anti-reflection coatings ensure low loss (2–4 %) at our laser wavelength of 1064 nm, which is necessary to preserve non-classical correlations [9]. The trapping fields were orthogonal to the probe and local oscillator in polarization, and were isolated from the detection with polarizing optics. The trapping fields were also generated with a different laser to the measurement fields with sufficient frequency detuning to prevent any interference and further reduce any influence that the trapping fields could have on the measurement.

10.2.1 Production of the Probe Field

The particle tracking measurements here relied on interference between a squeezed local oscillator and light which scattered from the particle under study. This scattered

light was produced by illuminating the particle with a probe field, which entered the trap in a dark-field configuration [24]. Dark-field illumination was used as it offers near-perfect isolation of the probe field from the detector, with background scattering contributing the only unwanted probe photons to the measurement (Chap. 8). Without this isolation, the scattered light would interfere with both the probe and local oscillator fields, which would distort the detection mode (see Chap. 3). Furthermore, isolating the probe field from detection also prevented it from contributing laser noise to the measurement, which would reduce the benefit of applying squeezing to the local oscillator.

The dark-field probe was not focused through the objectives, but rather directed into the sample chamber as a free-space field. The intensity was maximized at the particle by focusing the probe with a 125 mm focal length lens. The illumination angle was chosen to allow the probe to propagate through the setup without clipping on the objectives, as clipping was found to scatter light in all directions and cause a large background of unwanted probe light to reach the detector. The unwanted background of scattered light was further reduced by choosing an illumination angle within the optimal range calculated in Chap. 8 for our biological experiments. In free space, the illumination angle was 110° from the optical axis of the local oscillator, though refraction of the field as it entered the water within the sample chamber shifted the angle to 135°.

To perform the lock-in measurement described in Chap. 7, the probe field was amplitude modulated at 3.522 MHz to a depth of 93 %. This modulation frequency was chosen to sit well within the squeezing bandwidth (see Fig. 10.5), while avoiding the modulations between 1 and 10 MHz which were used to lock the laser to the mode-cleaning cavities and squeezing cavity. The scattered field which was produced by illuminating a particle also carried this modulation, as did the measured photocurrent. Upon demodulation, the particle tracking signal was recovered while all the noise which had formerly been at low frequencies was shifted to the MHz regime. A simple low-pass analog filter was then used to remove this technical noise and avoid aliasing. In addition to this amplitude modulation, the probe also carried a weak phase modulation at 6.5 MHz which was used to generate an error signal for locking the phase between the probe and local oscillator. The measured photocurrent was also demodulated at 6.5 MHz, and the resulting signal fed into a high-speed digital PID controller. This was then used to lock the phase between the probe and local oscillator fields via feedback to a piezo mounted mirror. The optical setup used to prepare this probe field is included in the full layout in Fig. 10.8.

10.2.2 Engineering the Local Oscillator

The scattered field was measured by interfering it with a local oscillator to determine the particle position. The local oscillator field was shaped to produce a particle tracking signal which is equivalent to measurement with a split detector. To achieve this, a phase plate was used to apply a π phase shift to one half of its transverse profile.

Since the incident field was in a Gaussian mode, the phase plate shaped the local oscillator into a "flipped" Gaussian. The phase plate was constructed by our collaborators at the Australian National University, following the procedure described in Ref. [8]. The phase plate consisted of two glass sheets with differing thicknesses held alongside one another. Light which propagates through the thicker plate gains a π phase shift with respect to light which propagates through the thinner plate. To generate the desired local oscillator shape, the incident field was centered on the step between the two plates. Although the surfaces of the phase plate were AR coated to ensure high transmission, some light scattered from the step in the center of the plate, such that the phase plate introduced 5 % loss.

The phase profile generated at the phase plate was then mapped to the back focal plane of the objectives via $4f$ imaging with two lenses of focal length 150 mm. The phase plate was placed 150 mm from the first lens, which was 300 mm from the second lens, which was then 150 mm from the objective back-focal plane. This configuration ensured that both the phase and amplitude of the field at the phase plate was preserved at the back focal plane of the objective [12]. The local oscillator then propagates through the trap where some scattered light is added, and after this the optical field is focused onto a detector. Interference between the local oscillator and probe maps the particle position onto the transmitted light intensity (see Fig. 10.2).

The local oscillator defines the detection mode for the scattered light, provided its amplitude is much greater than the scattered amplitude. Although the power of the local oscillator was only 100 μW, which is much less than the 5.2 mW power of the probe, the scattering rate of the particles was sufficiently small that the scattered field could be treated as a small perturbation on the local oscillator.

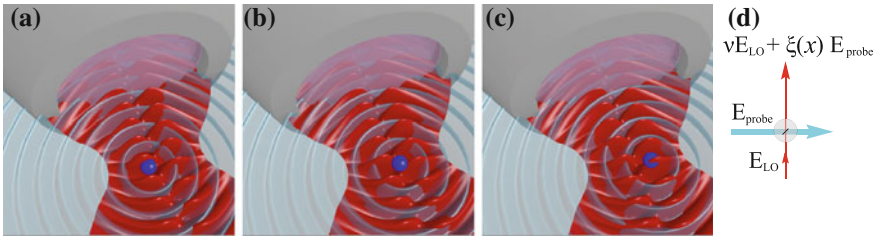

Fig. 10.2 Schematic of the particle tracking method. **a–c** A trapped particle acts as the source of scattered light (*faint blue*). This scattered light is combined with the spatially antisymmetric local oscillator field (*red*), collected in an objective, and the interference is measured as intensity fluctuations. The phase of the probe light is locked such that when the scattering particle is centered, as in (**b**), the fields are $\pi/2$ out of phase. When the particle moves *left* (**a**), the scattered wavefront shift closer to the local oscillator field maxima on both the *left* and *right*, due to the spatial antisymmetry of the local oscillator. This leads to constructive interference; similarly moving *right* leads to destructive interference as represented in (**c**). Hence the particle position is encoded on the detected light intensity. **d** The scattering particle can be thought of as a beamsplitter with a position dependent reflectivity, such that a measurement of the transmitted amplitude will yield the particle position. This is different to the strategies used to estimate macroscopic mirror motion, which typically rely on a phase shift imparted to a reflected field. In this case, the local oscillator amplitude is transmitted with $\nu = 0.98$, while only a very small fraction $\zeta \sim 7 \times 10^{-5}\ \mu\text{m}^{-1}$ of the incident probe amplitude scatters into the detection mode

10.3 Classically Characterizing the Experiment

The probe and local oscillator fields together should allow particle motion to be tracked along the x axis. To verify the efficacy of this technique, we trapped 2 μm diameter silica beads in water and monitored the detected signal (with an example shown in Fig. 10.3a). This measurement is expected to follow the trapped Brownian motion described in Sect. 1.3, with a power spectrum given by

$$\langle |x(\omega)|^2 \rangle = \frac{2D}{\omega^2 + \omega_c^2}, \tag{10.3}$$

where D is the diffusion constant, and ω_c is the corner frequency. The corner frequency scales linearly with the effective spring constant k_{opt} of the optical trap, and therefore ω_c provides a reasonable estimate for the optical trapping forces. Measurements were performed with a range of trapping powers and the resulting spectra compared to this theory (Fig. 10.3b). Since the corner frequency could be observed to increase with trapping power, these measurements confirmed that the measured signal corresponded to the mechanical motion of the trapped bead.

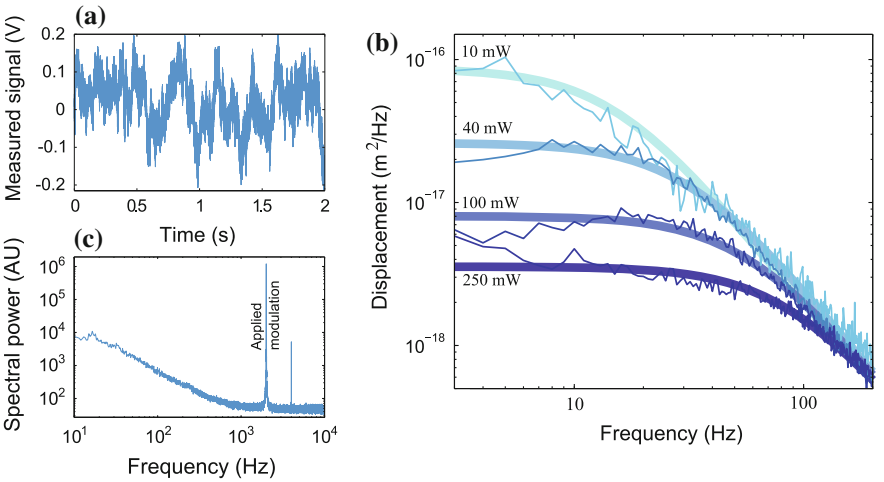

Fig. 10.3 **a** The measurement produces an electrical signal, with an example shown here. **b** The measured spectra for four different trapping powers: 10, 40, 100 and 250 mW. These are normalized into displacements by using the known value of the diffusion constant D in Eq. 10.3. The *thick lines* are a fit of Eq. 10.3 to the data, which show that the corner frequency ω_c increases with trap power. The dependence of the measured signal on the trap power verifies that the measured signal corresponds to particle motion. **c** To calibrate the setup, a 2 kHz mechanical modulation was applied to the sample holder. The resulting displacement is clearly visible in the spectra, and can be used to be convert the signal from voltage to physical displacement. This normalization agrees well with normalization by fitting measured spectra to Eq. 10.3

There was, however, some variation in the trapping force with time. This was because the two trapping fields carried the same polarization and thus formed a standing wave. By forming nodes and antinodes in the field, this greatly increases the field gradient along the optical axis, and improves the axial confinement of particles [32]; however, it also means that the stable trapping point must be on an antinode of the field, and the position of this can drift if the relative phase drifts. In this proof-of-principle demonstration, the trapping fields were not phase locked to one another, so the trapping point could drift with air currents and mirror motion. These drifts occurred over a timescale of minutes. The data collection was not adversely effected as this occurred over a much shorter timescale. However, the trap stiffness drifted in time, such that the corner frequency ω_c was not found to scale linearly with the trapping power.

Since diffusion is a well understood process and the constant D is known, the power spectra of beads in water can be normalized by simply fitting the measured data to theory. This only requires that we know the particle size, the viscosity of the surrounding medium, and that there are no nearby boundaries. In this work, the particles were trapped near the center of a 120 μm water-filled chamber, so all three conditions should be met. However, as the stable trapping point drifted in time, so too did the factor which should normalize the data. To establish the reliability of the data, a coherent 2 kHz modulation with an rms amplitude of 54 nm was applied to the stage which held the sample chamber, similar to the method in Ref. [27] (see Fig. 10.3c). This modulation provided another method to convert the signal from volts to meters, which was found to agree well with the quantitative predictions of Eq. 10.3. This confirmed that while the system lacked long-term stability, its measurements were otherwise reliable.

10.4 Incorporating Squeezed States of Light

10.4.1 Generating Squeezed Light

To achieve quantum enhanced sensitivity, squeezed light was integrated into the particle tracking setup. The optical parametric amplifier (OPA) which was used to generate squeezed light in this experiment was constructed earlier and had already been applied in several experiments [3]. In this OPA, squeezed light is generated by a nonlinear interaction between a strong 532 nm pump and a weak 1064 nm seed field. The fields are phase-matched and spatially overlap to allow efficient parametric amplification. Parametric amplification is a phase sensitive quantum amplification procedure which simultaneously amplifies one quadrature of the optical field while de-amplifying the other. In the limit of zero loss, this is a reversible process which will transform a coherent state into a minimum uncertainty squeezed state.

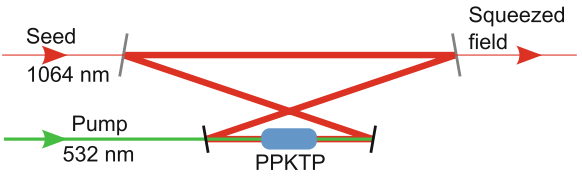

Fig. 10.4 The OPA which produced the squeezed light. A periodically poled $KTiOPO_4$ (PPKTP) crystal provides a nonlinear interaction between the incident seed field at 1064 nm and the pump at 532 nm which reduces the amplitude fluctuations of the seed field below the vacuum level. This nonlinear interaction is enhanced by an optical cavity which is kept resonant with the seed field

In the experiments, the OPA is formed by an optically nonlinear crystal (periodically poled KTP) which is placed inside a bowtie shaped optical cavity to enhance the nonlinear interaction (see Figs. 10.4 and 10.8). This OPA was driven by an Innolight Diablo laser which produces light at both 1064 and 532 nm. The 1064 nm light is kept resonant to enhance its nonlinear interaction, while the free-space 532 nm field is used to pump the nonlinear crystal. The faces of the nonlinear crystal were anti-reflection coated using the ion beam sputtering technique to provide ultra-low loss for the intra-cavity circulating field. The cavity mirrors were also custom made with reflectivity exceeding 99.95 %. The squeezed field exits the cavity through an output-coupler with 10 % transmission. The OPA is seeded with a bright laser beam such that bright amplitude squeezed light is produced. The resulting level of squeezing was calibrated by measuring the squeezed field with spatial homodyne, and comparing the measured variance to the vacuum noise. This revealed that the squeezing level was approximately −6 dB below the QNL at the sideband detection frequency 3.5 MHz [3]. For a more detailed and complete discussion of squeezed light generation, see Ref. [15].

10.4.2 Optical Losses

Squeezing degrades sharply with added loss, as loss is an inherently random process. To avoid this, high-efficiency optics were used for the optical tweezers, including low loss objectives (OFR-LMH-20X-YAG). As these have a relatively low numerical aperture of 0.4, they also impose minimal spatial distortion to the optical modes. The local oscillator encountered 19 % loss in the optical setup, with 16 % of this at the optical trap, and a further 3 % at the phase plate. The objectives together contributed 7 % loss, which is within the rated transmission of 96–98 %. Most commercially available objectives have much more loss than this; for instance the Zeiss Objective A-Plan 20x/0.45 has around 85 % transmission at 1064 nm. The sample was suspended in a 120 μm thick water chamber between two glass slides. The loss in the chamber was minimized by anti-reflection coating both of the air-glass interfaces, such that the chamber itself added around 5 % loss, with a further 4 % lost

from a trapped glass bead. Numerical calculations with Mie theory confirm that this loss results primarily from scattering of the field, rather than absorption. After the optical trap, the remaining 81 μW of local oscillator light was measured on a high efficiency, home-made bulk detector. This detector has efficiency >95 %, and, at the optical power used, the electronic noise floor was determined to be 14 dB below the shot noise level. Hence, the local oscillator was detected with an efficiency of $\eta_{LO} = 0.76$ when tracking the silica beads. In the biological experiments, the yeast cells in the optical trap caused 9 % more loss than the beads did, such that the local oscillator detection efficiency way $\eta_{LO} = 0.67$. The efficiency η_{LO} characterizes the loss which the squeezed local oscillator experiences, and therefore determines the maximum quantum enhancement possible. However, the local oscillator photons carry no information about the particle position; this information is carried by scattered photons, and these photons are only sensitive to loss between the scattering particle and the detector. Thus, the scattered photons which leave the yeast cell or silica bead are measured with a higher efficiency of approximately $\eta = 0.89$.

10.4.3 Amount of Quantum Enhancement

In order to characterize the quantum enhanced measurements, the probe illuminated a small defect in the sample chamber, producing scattered light to interfere with the local oscillator. The detector output was then studied with a spectrum analyzer, with traces shown in Fig. 10.5 for both squeezed and coherent light. The amplitude modulation from the probe is visible as a peak at 3.522 MHz. At this frequency the quantum noise limit is achieved for classical light; while for squeezed light it

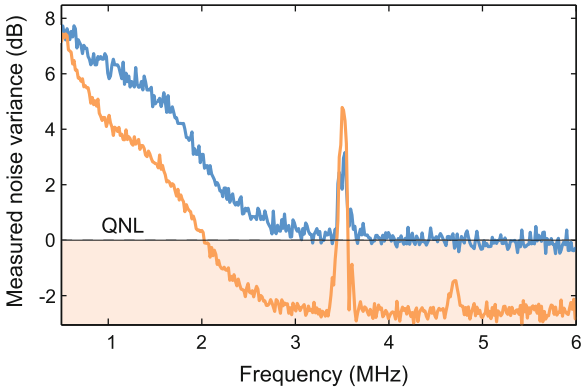

Fig. 10.5 The noise spectrum measured at the detector without a trapped particle, for coherent (*blue*) and squeezed (*orange*) local oscillator. The probe was amplitude modulated at 3.522 MHz, and illuminated a defect in the sample to allow observation of this large peak. The small peak visible at 4.7 MHz is caused by the modulations used for locking the laser

is surpassed by 2.8 dB, corresponding to a detected squeezed variance of $V_{\text{det}} = 1 - \eta_{LO}(1 - V) = 10^{-2.8/10} = 52\,\%$. Given 6 dB of incident squeezing, this detected squeezing would suggest a detection efficiency of 0.63, which is lower than the measured 0.76. This discrepancy may suggest that there were additional unknown losses in the system. At frequencies lower than 3 MHz, where typical optical particle tracking experiments operate, the noise floor is dominated by technical noise. This noise would preclude reaching the quantum noise limit using a continuous measurement. However, it is evaded with the stroboscopic approach demonstrated here. This allows sub-quantum noise limited measurements at frequencies down to 10 Hz, matching the lowest frequency previously reported in the literature [22]. It is worth noting that at low frequencies technical noise sources such as $1/f$ noise and laser noise are a common issue in conventional laser based particle tracking experiments [19].

10.5 Experimental Characterization

The trapped thermal motion of 2 μm silica beads in water was then measured with quantum enhanced precision. Both coherent and squeezed light allowed the characteristic Lorentzian mechanical spectrum to be observed, as shown in Fig. 10.6a. At high frequencies the mechanical amplitude scales inversely with frequency, such that motion above 1 kHz is difficult to detect. It is in this high frequency region that the simplistic model of Brownian motion breaks down, and complex dynamic effects become significant [10]. To observe the effect of squeezing more closely, this section of the observed mechanical spectrum is shown in Fig. 10.6b. The squeezed light can be clearly seen to improve the sensitivity, and extend the frequency range over which the mechanical motion is detectable. The classical sensitivity achieved with this photon flux was 1.3×10^{-10} m $\text{Hz}^{-1/2}$, while squeezed light improved this sensitivity to 9.3×10^{-11} m $\text{Hz}^{-1/2}$. Correspondingly, the quantum noise limit was surpassed here by 2.6 dB. As shown in Fig. 10.6c, the measured squeezing degraded as the trapping power increased, as expected from theory. At low trapping power, squeezed light enhanced the measurements by up to 2.7 dB. As the trapping power increased, however, the detection included an increased flux of trap photons, which contributed to the shot noise floor while adding nothing to the measured signal.

To test the frequency range over which squeezed light gave an improvement to the mechanical measurements, the probe power was vastly reduced. The resulting spectra (Fig. 10.6d) were then dominated by quantum noise for frequencies above 10 Hz. Here, the use of squeezed light restored information which was not previously observable, demonstrating that squeezing could enhance the sensitivity at frequencies as low as 10 Hz.

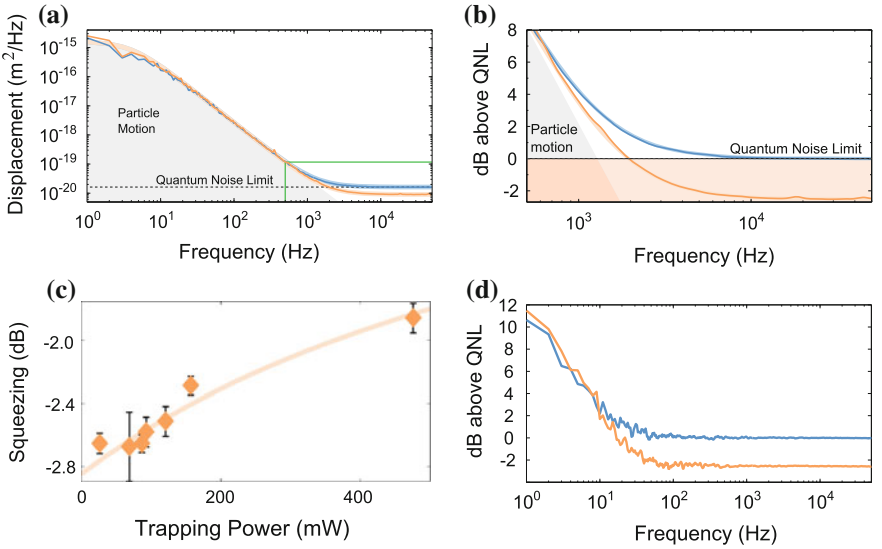

Fig. 10.6 This shows the enhancement achieved through squeezed light when tracking silica beads in water. **a** Typical measured spectra for a trapping power of 121 mW are shown for classical (*blue*) and squeezed (*orange*) local oscillator. Squeezed light lowers the noise floor but otherwise is entirely equivalent to the coherent measurement. To observe the improvement in noise floor more closely, the high frequency area within the box is shown in (**b**), where the two data sets diverge. In this case, the squeezing suppressed the noise floor by 2.6 dB. **c** The total degree of squeezing varied with the trapping power as a small fraction (7×10^{-5}) of trapping photons would reached the detector and contribute shot noise. The measured squeezing (diamonds) is well fitted by this simple model over a wide range of trapping powers, without fitting parameters. **d** The probe power was then vastly reduced, such that the bead motion became nearly irresolvable, and squeezed light was shown to restore some of the information lost through the reduced light intensity. This shows that squeezed light can offer substantial benefits for measurements where the scattering rate is very low, or very low-power illumination is required. It also demonstrates that the quantum enhancement is present down to 10 Hz

10.6 Comparison with Theory

The quantum limit in Eq. 10.1 depends on the detection efficiency of the scattered light η, the flux of scattered photons n_{scat}, the local oscillator mode shape ψ_{LO}, and both the shape and amplitude of the scattered mode derivative $\psi'_{\mathrm{scat}} = \frac{d\psi_{\mathrm{scat}}}{dx}\big|_{x=0}$. To make quantitative predictions, these parameters must all be known. Firstly, we consider the resolution achievable per measured photon, which is given by $\left(2\mathrm{Re}\{\langle\psi'_{\mathrm{scat}}|\psi_{\mathrm{det}}\rangle\}\right)^{-1}$.

To find this displacement, we evaluate the change in scattered field shape with particle position at the far-field of the particle with the Optical Tweezers Toolbox computational tool [20], with the transverse profile of this mode shown in Fig. 10.7a. We also know the local oscillator profile which entered the optical trap. In the experiment, the local oscillator mode ψ_{LO} was distorted somewhat by the trapped particles.

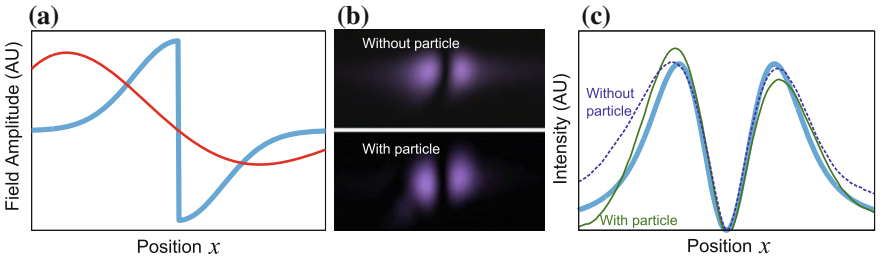

Fig. 10.7 Characterizing the detection mode in this experiment. **a** The calculated profiles of the detection mode (*thick blue*) and the mode ψ'_{scat} containing particle position information (*red*). The information mode is slightly asymmetric because the illumination is off-axis, such that the Mie scattering profile is not symmetric over the objective aperture. **b** To quantify whether the trapping optics distorted this detection mode, the intensity profile of the local oscillator was measured after the optical trap both with and without a trapped particle, corresponding to the Fourier transform of the detection mode. **c** Corresponding 1D intensity profiles through the intensity maxima in y, as a function of the position x. The expected profile (*thick blue line*) approximately describes the actual profiles in both cases

To determine the extent of this distortion, the detector was replaced with a CCD camera and the intensity profile of the local oscillator measured (Fig. 10.7b, c). The local oscillator profile approximately matched the expected Fourier transform of the flipped Gaussian, both in the absence of any trapped particles, and when a 2 μm diameter silica particle is trapped, as shown in Fig. 10.7. Without the trapped particle, the intensity distribution falls off more slowly, which is possibly due to spherical aberrations. Overall, these measurements suggest that the distortion was not severe. We therefore neglect this effect, and approximate ψ_{LO} with the input local oscillator mode. The overlap $\text{Re}\{\langle\psi'_{\text{scat}}|\psi_{\text{LO}}\rangle\}$ cannot change with propagation of the optical fields, so we evaluate this at the far-field of the scattering particle, where the local oscillator is given by the flipped Gaussian mode $\psi_{\text{LO}} \approx \text{sign}(x)\exp(-\sin^2\theta/\sin^2\theta_w))$ with an angular waist θ_w determined from beam profile measurements.

Using these modes, the overlap between the detection and information modes is found to be 3.8 %, and the corresponding minimum resolvable displacement is then given by 2.0 μm for each measured photon. This overlap is particularly low because the local oscillator under-filled the objective apertures, while the information mode fills the entire objective aperture and clips at the edges. The quantum noise limit can then be calculated from the flux of scattered photons reaching the detector.

The probe illumination held 5.2 mW of power, although this was reduced to 3.7 mW by a 28 % reflective sample chamber wall. This field was only weakly focused with a 125 mm focal length lens, and thus had a focal width of at least 68 μm and an intensity of approximately 1 W/mm^2. Since the bulk of the probe light missed the particle altogether, the fraction of the incident photons which were scattered into the objective aperture for collection was only 4.3×10^{-8}. Hence, we could collect about 8.5×10^8 photons per second. However, only 47 % of these were in the modulation side-bands and were thus used for measurement (see Chap. 7).

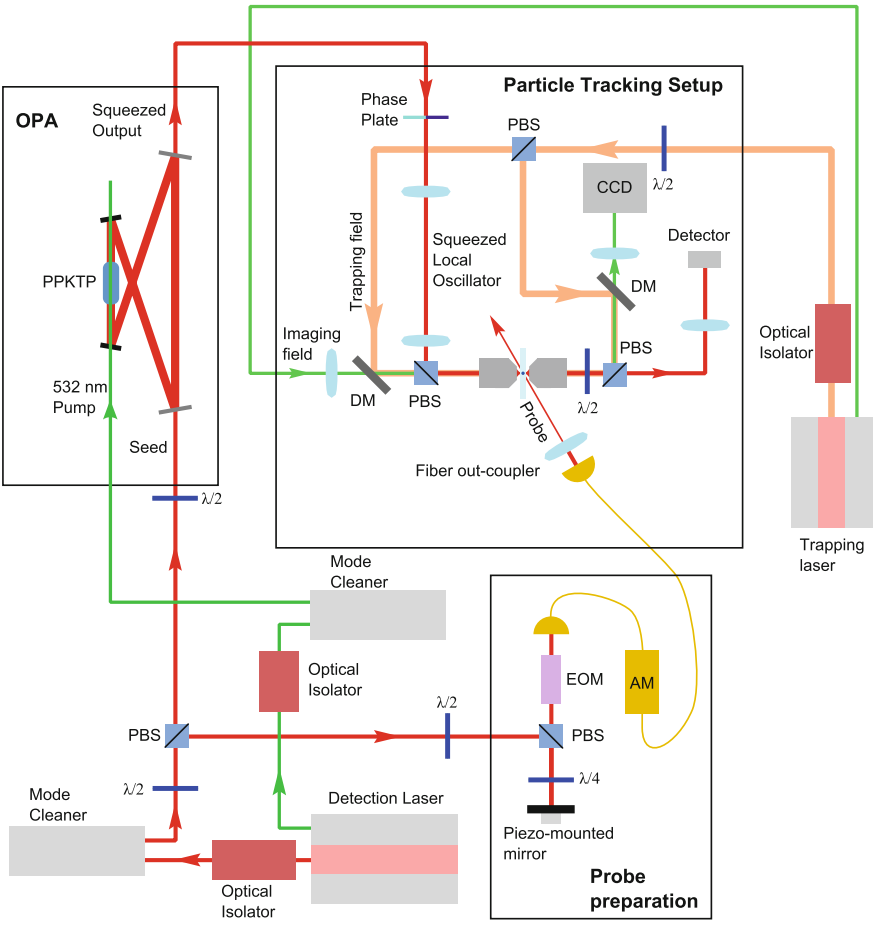

Fig. 10.8 The full experimental layout used for quantum enhanced particle tracking. This is separated into three main parts, the *OPA*, where squeezed light is generated (also shown in Fig. 10.4), the *Probe preparation*, where the probe field is prepared, and the *Particle Tracking Setup*, where all these elements are combined in an optical tweezers experiment to allow quantum enhanced particle tracking (also shown in Fig. 10.1). For clarity, only the dichroic (DM) and OPA cavity mirrors are included

The measurement efficiency for scattered photons was 0.89, which leaves 3.6×10^8 photons per second for the measurement. Combining the predicted measurement sensitivity per photon with the measured photon flux, we predict a displacement sensitivity of 1.05×10^{-10} m Hz$^{-1/2}$. This is only 17 % below the measured precision of 1.26×10^{-10} m Hz$^{-1/2}$. This small discrepancy could easily arise from distortion of the measured mode, which was neglected.

10.6.1 Relationship to the Standard Quantum Limit

These experiments demonstrate that microscopic particles can be tracked with sensitivity surpassing the quantum noise limit. The quantum noise limit is used to characterize the improvement which quantum resources confer to a measurement with a given apparatus, and is relevant in determining the practical benefit of a quantum enhancement. This is generally used in experiments similar to ours, where bright optical fields are used for continuous measurements [2, 30]. Many quantum metrology experiments instead compare their sensitivity to the more stringent *standard quantum limit*. The standard quantum limit characterizes the ultimate limit on sensitivity classically achievable given the number of photons, and is reached with a perfect measurement with coherent light and 100 % efficient detection.

Due to the stringent requirements on measurement apparatus and detection efficiency it is challenging, in general, to surpass the standard quantum limit. This is particularly the case for microparticle tracking experiments, where the scattered field has complex spatial structure and is not collimated. The detection apparatus must be able to near-optimally extract information from this complex spatial mode over 4π steradians. Even the best classical microparticle tracking experiments remain more than a factor of 1000 in power from the standard quantum limit.

10.7 Conclusion

The results reported here demonstrate that squeezed light may be used to surpass the quantum noise limit in particle tracking microscopy. Quantum enhanced particle tracking holds increasing relevance, with several experiments approaching quantum limited performance [26], and a wide range of potential applications as discussed in more detail in Sect. 1.3. In microrheology experiments, improved sensitivity allows the viscoelastic response of the medium to be probed on smaller timescales, revealing both the properties of the cytoplasm and biological processes at higher frequency [5]. Several recent experiments have investigated the non-Brownian thermal motion of particles in water on very short time-scales, observing hydrodynamic memory [10] and the average ballistic motion at fast time-scales [13]. However, there are predictions which remain untested that elastic properties of fluid will influence hydrodynamic motion over very short timescale [13, 34]. Direct observation of this without quantum resources would require over 19 W of 1064 nm optical power (see Chap. 2), increasing the water temperature [21] by over 100 K. Further applications include optomechanical experiments in which the quantum state of a trapped levitating particle is measured and controlled [6]; such systems could benefit from enhanced sensitivity both to improve optomechanical cooling, and to engineer non-classical states of the trapped particle [6].

References

1. J. Aasi et al., Enhanced sensitivity of the LIGO gravitational wave detector by using squeezed states of light. Nat. Photon. **7**(8), 613–619 (2013)
2. J. Abadie et al., A gravitational wave observatory operating beyond the quantum shot-noise limit. Nat. Phys. **7**, 962–965 (2011)
3. S. Armstrong, J.-F. Morizur, J. Janousek, B. Hage, N. Treps, P.K. Lam, H.-A. Bachor, Programmable multimode quantum networks. Nat. Commun. **3**, 1026 (2012)
4. G. Brida, M. Genovese, I.R. Berchera, Experimental realization of sub-shot-noise quantum imaging. Nat. Photon. **4**, 227–230 (2010)
5. M. Buchanan, M. Atakhorrami, J.F. Palierne, F.C. MacKintosh, C.F. Schmidt, High-frequency microrheology of wormlike micelles. Phys. Rev. E **72**, 011504 (2005)
6. D.E. Chang, C.A. Regal, S.B. Papp, D.J. Wilson, J. Ye, O. Painter, H.J. Kimble, P. Zoller, Cavity opto-mechanics using an optically levitated nanosphere. Proc. Natl. Acad. Sci. USA **107**(3), 1005–1010 (2010)
7. A. Crespi, M. Lobino, J. Matthews, A. Politi, C. Neal, R. Ramponi, R. Osellame, J. O'Brien, Measuring protein concentration with entangled photons. Appl. Phys. Lett. **100**(23), 233704 (2012)
8. V. Delaubert, D. Shaddock, P. Lam, B. Buchler, H. Bachor, D. McClelland, Generation of a phase-flipped Gaussian mode for optical measurements. J. Opt. A: Pure Appl. Opt. **4**(4), 393 (2002)
9. R. Demkowicz-Dobrzański, J. Kołodyński, M. Guţă, The elusive Heisenberg limit in quantum-enhanced metrology. Nat. Commun. **3**, 1063 (2012)
10. T. Franosch, M. Grimm, M. Belushkin, F.M. Mor, G. Foffi, L. Forró, S. Jeney, Resonances arising from hydrodynamic memory in Brownian motion. Nature **478**, 85–88 (2011)
11. V. Giovannetti, S. Lloyd, L. Maccone, Quantum-enhanced measurements: beating the standard quantum limit. Science **306**(5700), 1330–1336 (2004)
12. J.W. Goodman, *Introduction to Fourier Optics* (McGraw-Hill, New York, 2004)
13. R. Huang, I. Chavez, K.M. Taute, B. Lukić, S. Jeney, M.G. Raizen, E.-L. Florin, Direct observation of the full transition from ballistic to diffusive Brownian motion in a liquid. Nat. Phys. **7**, 576580 (2011)
14. M. Kolobov, C. Fabre, Quantum limits on optical resolution. Phys. Rev. Lett. **85**(18), 3789–3792 (2000)
15. P.K. Lam, Applications of quantum electro-optic control and squeezed light. Ph.D. thesis, Australian National University, 1998
16. K. McKenzie, N. Grosse, W. Bowen, S. Whitcomb, M. Gray, D. McClelland, P. Lam, Squeezing in the audio gravitational-wave detection band. Phys. Rev. Lett. **93**(16), 161105 (2004)
17. T. Nagata, R. Okamoto, J. O'Brien, K. Sasaki, S. Takeuchi, Beating the standard quantum limit with four-entangled photons. Science **316**(5825), 726–729 (2007)
18. K.C. Neuman, E.H. Chadd, G.F. Liou, K. Bergman, S.M. Block, Characterization of photodamage to Escherichia coli in optical traps. Biophys. J. **77**, 2856–2863 (1999)
19. K.C. Neuman, A. Nagy, Single-molecule force spectroscopy: optical tweezers, magnetic tweezers and atomic force microscopy. Nat. Methods **5**, 491–505 (2008)
20. T. Nieminen, V. Loke, A. Stilgoe, G. Knöner, A. Brańczyk, N. Heckenberg, H. Rubinsztein-Dunlop, Optical tweezers computational toolbox. J. Opt. A: Pure Appl. Opt. **9**(8), S196 (2007)
21. E.J. Peterman, F. Gittes, C.F. Schmidt, Laser-induced heating in optical traps. Biophys. J. **84**(2), 1308–1316 (2003)
22. M. Stefszky, C. Mow-Lowry, S. Chua, D. Shaddock, B. Buchler, H. Vahlbruch, A. Khalaidovski, R. Schnabel, P. Lam, D. McClelland, Balanced homodyne detection of optical quantum states at audio-band frequencies and below. Class. Quant. Grav. **29**(14), 145015 (2012)
23. J.W. Tay, M.T.L. Hsu, W.P. Bowen, Quantum limited particle sensing in optical tweezers. Phys. Rev. A **80**(6), 063806 (2009)
24. M.A. Taylor, W.P. Bowen, Enhanced sensitivity in dark-field microscopy by optimizing the illumination angle. Appl. Opt. **52**(23), 5718–5723 (2013)

25. M.A. Taylor, J. Janousek, V. Daria, J. Knittel, B. Hage, H.-A. Bachor, W.P. Bowen, Biological measurement beyond the quantum limit. Nat. Photon. **7**, 229–233 (2013)
26. M.A. Taylor, J. Knittel, W.P. Bowen, Fundamental constraints on particle tracking with optical tweezers. New J. Phys. **15**, 023018 (2013)
27. S. Tolic-Nørrelykke, E. Schaffer, J. Howard, F. Pavone, F. Julicher, H. Flyvbjerg, Calibration of optical tweezers with positional detection in the back focal plane. Rev. Sci. Instrum. **77**(10), 103101–103101 (2006)
28. N. Treps, N. Grosse, W.P. Bowen, C. Fabre, H.-A. Bachor, P.K. Lam, A quantum laser pointer. Science **301**, 940–943 (2003)
29. H. Vahlbruch, S. Chelkowski, B. Hage, A. Franzen, K. Danzmann, R. Schnabel, Coherent control of vacuum squeezing in the gravitational-wave detection band. Phys. Rev. Lett. **97**(1), 011101 (2006)
30. F. Wolfgramm, A. Cerè, F.A. Beduini, A. Predojević, M. Koschorreck, M.W. Mitchell, Squeezed-light optical magnetometry. Phys. Rev. Lett. **105**, 053601 (2010)
31. B. Yurke, P. Grangier, R.E. Slusher, Squeezed-state enhanced two-frequency interferometry. J. Opt. Soc. Am. B **4**, 1677–1682 (1987)
32. P. Zemánek, A. Jonáš, L. Šrámek, M. Liška, Optical trapping of Rayleigh particles using a Gaussian standing wave. Opt. Commun. **151**, 273–285 (1998)
33. Z. Zhai, J. Gao, Low-frequency phase measurement with high-frequency squeezing. Opt. Express **20**(16), 18173–18179 (2012)
34. R. Zwanzig, M. Bixon, Compressibility effects in the hydrodynamic theory of Brownian motion. J. Fluid Mech. **69**(part 1), 21–25 (1975)

Chapter 11
Biological Measurement Beyond the Quantum Limit

Chapter 10 described the development of an optical tweezers apparatus with quantum enhanced sensitivity. This chapter applies this device to biophysical experiments. The thermal motion of lipid particles within a living yeast cell was characterized with quantum enhanced precision, and from this the mechanical properties of the cellular cytoplasm could be inferred. The use of squeezed light improved the particle tracking precision by 2.4 dB, which improved the precision with which the α parameter could be determined by 22 %. This demonstrated for the first time that quantum correlated light could be used to surpass the quantum noise limit in biological measurements. This experiment was described in the following publication [18].

11.1 Microrheology

This chapter describes quantum enhanced microrheology measurements of the cytoplasm within a living yeast cell. In microrheology experiments, the viscoelasticity of a fluid is determined from its influence on the motion of an embedded particle [6, 10]. This can involve measuring the mechanical response to either an applied force or the thermal force, which continually pushes the particle in random directions. To infer useful information from the thermal diffusion of the particle, the key parameter of interest is generally the mean squared displacement (MSD). The MSD of a free particle undergoing thermal motion is defined as

$$\left\langle \Delta x^2(\tau) \right\rangle = \left\langle (x(t) - x(t-\tau))^2 \right\rangle, \tag{11.1}$$

where τ is the delay between measurements. The MSD thus characterizes the average distance that a particle will move over a given time range τ, and provided the MSD is dominated by thermal motion, has the form

$$\left\langle \Delta x^2(\tau) \right\rangle = 2D\tau^{\alpha}. \tag{11.2}$$

M. Taylor, *Quantum Microscopy of Biological Systems*, Springer Theses,
DOI 10.1007/978-3-319-18938-3_11

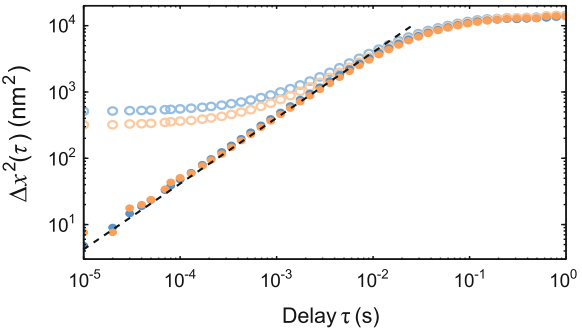

Fig. 11.1 The MSD of a trapped silica bead in water, with data recorded with both squeezed (*orange*) and coherent (*blue*) light. The noise floor enters the raw MSD data as a constant offset. Since squeezed light has lower noise, it has a lower offset. To analyze mechanical properties from such data, this noise floor is subtracted off (*closed circles*). Both the squeezed and classical data then closely follow the expected behavior for Brownian motion (*dashed line*) at short delays, with $\alpha = 1$ in Eq. 11.2. At long delays there is a plateau in the MSD due to the confinement of the optical trap

Here D is the diffusion constant and α a diffusive parameter determined by the viscoelasticity of the surrounding medium, with the ratio of loss to storage moduli given by $G''/G' = \tan(\pi\alpha/2)$ [11]. In a purely viscous medium, the particle follows Brownian motion which is characterized by $\alpha = 1$, whereas a viscoelastic medium results in subdiffusive motion with $\alpha < 1$ [7]. To determine the diffusive parameter, the MSD is determined from measurements of the particle motion. A discrete series of measurements x_n of the particle position x are performed at evenly spaced intervals dt in time, where n is the measurement number. These are used to determine the MSD by the relationship

$$\left\langle \Delta x^2(\tau = m\,dt) \right\rangle_{\text{exp}} = \sum (x_{n+m} - x_n)^2 - N_{\text{MSD}}, \tag{11.3}$$

where N_{MSD} is the mean noise variance. An example of such measured MSD traces for beads in water are shown in Fig. 11.1. This closely follows the expected $\alpha = 1$ at short delays, although at long delays there is a plateau in the MSD due to the particle confinement in the optical trap [25]. By analysing the MSD at short delays, the viscoelastic properties of surrounding fluid can be characterized. Alternatively, subdiffusive motion can also be characterized by analyzing the motion in the frequency domain, with the spectral density rolling off as $\omega^{-(1+\alpha)}$, as can be seen in Fig. 11.2b. However, analysis of the MSD intrinsically involves averaging which reduces the noise in the data when compared to the Fourier transform.

In addition to characterizing the viscoelasticity of the cytoplasm, microrheology measurements also shed light on cellular processes which rely on thermal motion. Almost all thermal motion within a living cell is subdiffusive because proteins and other macromolecules resist the movement of particles [23]. Subdiffusive motion is

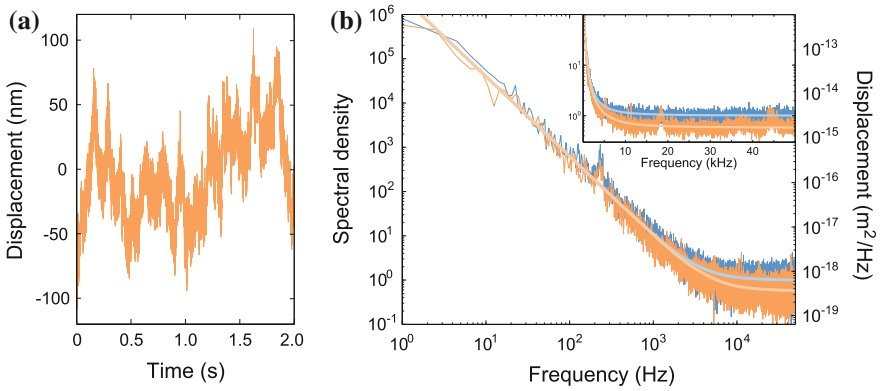

Fig. 11.2 Measured data from living yeast cells. **a** A typical time trace of data recorded with squeezed light probing a yeast cell. **b** The corresponding spectra, with amplitudes normalized to the shot-noise floor, and averaged over 100 data sets each. The *orange lines* are from data recorded with squeezed light, while the *blue colored lines* are recorded with coherent light. The fitting lines represent a frequency roll-off of $\omega^{-1.8}$ (corresponding to $\alpha = 0.8$), plus an additional flat noise floor. At low frequency, additional confinement causes the data to deviate from this fit. The inset shows the same spectra with a linearly scaled frequency axis, which allows the 2.4 dB of enhancement in precision (equivalently, 42 % lower noise) through squeezing to be seen more clearly. Some spurious peaks which resulted from modulations used to lock the squeezed light source have been removed from the spectra

extremely important to the operation of a cell, as it mediates important processes such as chemical reactions [3] and protein folding [4]. The extent of the particle confinement can strongly effect chemical reactions, for instance, as it slows the initial approach of chemical reactants to one another but also decreases the likelihood that they will pass without interacting. In some regimes this improves the efficiency of the reaction, while in others it can suppress reactions [8, 16]. Subdiffusion also has a strong effect on enzyme reactions [1, 14], and the formation of spatiotemporal patterns [22, 24]. The viscoelasticity is not a simple static parameter, but has been found to follow nanoscale structure in places [21], and to vary as the cell undergoes reproduction [15]. However, more study is still required to establish the full biological implications of these mechanical properties [8].

11.2 Quantum Enhanced Microrheology

To demonstrate the biological potential of the quantum particle tracking technique described in Chap. 10, we performed microrheology experiments within *Saccharomyces cerevisiae* yeast cells. It is known from intracellular measurements with a different yeast strain that the thermal motion of lipid granules in the cell is suppressed by networks of actin filaments within the cytoplasm, causing them to exhibit subdiffusive motion [20, 25]. To study the granule motion in our experiments, the host cell

was first immobilized by laser trapping with 170 mW of optical power, which also caused an estimated 1.5 K of cellular heating [13]. The amplitude modulated probe field was then incident on the yeast cells, at an illumination angle which provides optimal signal-to-noise for measurements of the lipid particles (see Chap. 8). This produced scattered light which was mixed with a shaped local oscillator and measured to extract lipid granule motion, with an example measurement in Fig. 11.2a. The sensitivity of the measurement depends on the overlap of the scattered field with the local oscillator, which in our experiment, was maximized for small particles near the focus, with the scattering profile from large structures yielding poor overlap. Because of this, measurements carried out in yeast cells preferentially extracted the motion of lipid granules. The measurement statistics confirm that lipid granules dominate the measured signal; in particular, see Sects. 12.4 and 12.5. However, it is not possible to fully exclude background scattering centers from the detection, and they are expected to contribute a noisy background to the measured signal. Similar to the bead tracking experiments in Chap. 10, squeezed light improved the measured sensitivity with the quantum noise limit surpassed by up to 2.4 dB (Fig. 11.2b). In circumstances where optical damage is a concern, this enhancement would allow the probe power to be reduced by 42 %.

The MSD was extracted over a range of delay times for both silica beads and yeast results, with typical traces shown in Fig. 11.3. Both the mean and uncertainty in the diffusive parameter α was determined through weighted linear regression of the MSD in a log-log basis. The results from silica beads in water match the well known profile of diffusive motion, with an ensemble of measurements finding that on average $\alpha = 0.994 \pm 0.006$. By contrast, the results extracted with yeast cells reveal clearly subdiffusive motion with a non-stationary value of α which varies on

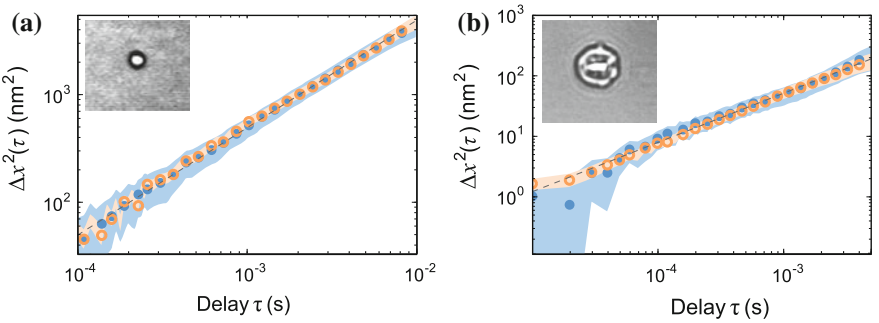

Fig. 11.3 Mean squared displacement data. Typical MSD measurements recorded over 0.1 s are shown in subplots **a** and **b** for silica beads and lipid granules in yeast respectively. Squeezed light measurements are shown as *orange open circles*, classical measurements as *blue closed circles*, and the *shaded regions* represent the standard error of the mean squared displacements. The *dashed lines* are linear fits to the data, which allow α to be determined. For the beads in water, this gives $\alpha = 0.999 \pm 0.006$, whereas it gives $\alpha = 0.815 \pm 0.008$ for the displayed yeast results. For yeast, the data is clearly subdiffusive; for comparison, a diffusive trend is plotted (*dotted line*) alongside this fit

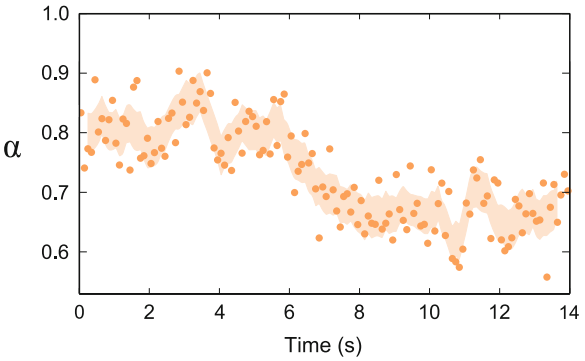

Fig. 11.4 This shows the variation of α with time on a subset of data recorded with squeezed light, with *dots* representing separate measurements and the *shaded region* representing the running mean and standard error over 6 points. The observed variations are far larger than the statistical uncertainty

sub-second timescales within the range of 0.6 to 1 as the lipid particles interact with different parts of the local environment (Fig. 11.4), similar to other measurements in the literature [15]. As expected, the MSD observed with squeezed light is similar to that observed with coherent light, but with improved precision. For instance, after a delay of 20 μs, the particle motion shown in Fig. 11.3b is unresolvable using coherent light but can be resolved using squeezing, with MSDs of 0.8 ± 1.1 nm^2 and 1.8 ± 0.6 nm^2 respectively.

Over all the measured biological data, α spanned from 0.6 to 1.0 with a mean of 0.81 ± 0.01. Because α was non-stationary, it was not possible to estimate the statistical uncertainty in each determination of α by the standard deviation of the ensemble. Instead, the statistical uncertainty in each determination was estimated with weighted linear regression. This uncertainty was found to be on average 22 % smaller when using squeezed light than equivalent measurements with coherent light. Consequently, squeezed light allows the ratio of the viscoelastic moduli to be characterized with 22 % enhanced precision. Alternatively, the precision can be maintained while averaging over fewer data points, with a 64 % increase in measurement rate allowed through the use of squeezed light. Thus dynamic changes in α could be observed over shorter timescales, providing more information about the inhomogeneity of the local environment around the granule.

11.2.1 The Effect of the Trapping Laser

In this experiment the optical trap was necessary to immobilize the cells in the correct location for measurement, although in principle the particle tracking method does not require an optical trap. Sometimes the trap also attracted additional particles which could disrupt the measurement, in which case the sample chamber was moved and a new yeast cell probed. More importantly, since the trapping laser was relatively bright,

it could have disrupted the cell function and influenced the measured properties. To test this, the lipid motion was studied as the trap power was varied from 44 mW to 308 mW. When trapping the cell with 308 mW, we expect approximately 2.5 K of cellular heating [13], and photo-oxidation to cause a lethal buildup of chemicals in approximately 3 min [12]. At the low trapping power of 44 mW, however, a more moderate 0.4 K of heating is expected [13] and photo-oxidation is expected to take over 20 min to kill the cell [12]. As such, the conditions within the cell are likely to vary with power. Our measurements, however, did not find any statistically significant variation in the diffusive parameter α with optical power, with measurements at different powers all yielding a similar range and mean of α (Fig. 11.5). As such, we conclude that the trapping laser did not effect the measured viscoelastic properties in our experiment.

The measurements of α could also have been influenced by drift in the background temperature, as the temperature of the sample stage was not stabilized. While it is not possible to fully exclude this possibility, the results described above suggest that α is not strongly dependent on the temperature. Optical heating should induce temperature changes greater than 2 K between those tests. Since α was not found to vary

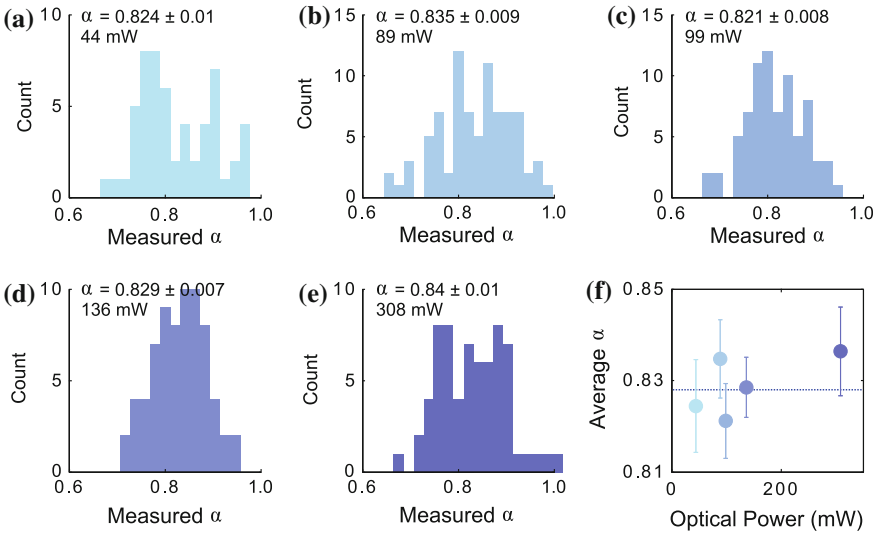

Fig. 11.5 To test whether the trapping fields disrupted the microrheology experiments, the values of α determined from a MSD analysis of the lipid motion are plotted in histograms for trapping powers of **a** 44 mW, **b** 89 mW, **c** 99 mW, **d** 136 mW and **e** 308 mW, following a similar approach to Ref. [15]. The data here was recorded in three different cells, as additional particles would occasionally enter the optical trap, such that it was necessary to either remove the foreign particle or probe a new cell; one cell was measured for data (**b**), one for data (**c**), and another for (**a**), (**d**) and (**e**). However, the data here shows no discernible variation between the different yeast cells. Each plot includes 80 measurements of 1 s length. The measured values of α vary quite substantially, but the mean α found in these measurements (plotted in **f**) all lie within a single standard error (*errorbar*), so there is no statistically significant dependence on the optical power

measurably between tests, it follows that a temperature change of 2 K is insufficient to alter the mean of α. Much smaller temperature changes are expected when the power is held constant, so thermal drift is not expected to contribute significantly to the fluctuations in α.

In addition to the viscoelasticity in the cytoplasm, which is characterized by α, the lipid granules also experience additional confinement. This can be characterized by the corner frequency, at which the spectra begins to roll off with the $\omega^{-(1+\alpha)}$ dependence (see Fig. 11.2). This was also fitted to the data, and was found to cover a similar range for all trapping powers (Fig. 11.6). Although these did show statistically significant changes with the power, the changes were not consistent with optical trapping; the highest corner frequency (and hence, the tightest confinement) was recorded with the lowest trap power. This indicates that the dominant confinement of the particles was not the trapping laser, and is most likely a cage-like particle confinement by the intracellular structure [9]. The changes in corner frequency is most likely due to changes in the relative position of boundaries such as the cell wall, as these sets of data were recorded many minutes apart and sometimes in different cells. It is noteworthy that even though the data was recorded in three different yeast cells, the data shows no discernible variation from cell to cell.

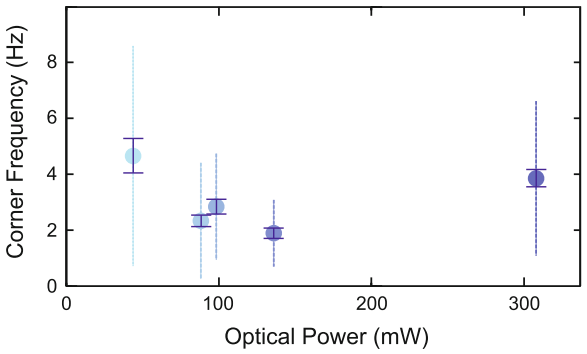

Fig. 11.6 This data shows that the optical trap did not significantly effect the motion of lipid particles within the yeast cells. The corner frequency of the measured spectrum was calculated for a range of trapping powers (from the same data as in Fig. 11.5). This corner frequency determines the transition between a low frequency plateau and high frequency roll-off with $\omega^{-(1+\alpha)}$ dependence, and indicates the confinement of the particle. Although the measurements show statistically significant differences between the mean corner frequencies, the corner frequency is not found to increase with power as would be expected if the particle confinement was dominated by the optical trap. All the measurements cover a similar range, as shown by the overlapping standard deviations (*dotted lines*)

11.3 Conclusion

The results reported here demonstrate that squeezed light may be used to surpass the quantum noise limit on tracking particles within a biological sample. The absolute sensitivity achieved was competitive with previous classical microrheology experiments [20]; however, the quantum noise limit itself could be lowered if more scattered photons were collected [17, 19]. If 74 % more photons were collected, the classical sensitivity would match our quantum enhanced sensitivity. For this setup, this would require increased sample illumination, since even completely eliminating optical loss would only increase the collection of scattered photons by 12 %. While it is generally easier to increase the light intensity than introduce squeezed light, high light intensities can cause biological damage [12, 13] so biophysical experiments must operate with constrained optical power. Under such constraints, the enhancement demonstrated provides a way to improve measurement sensitivity without increasing the risk of optical damage to the sample, thus allowing biological systems to be studied with improved bandwidth and precision. More generally, by demonstrating that biological measurements can be improved using quantum correlated light, our results pave the way for other applications in areas such as two-photon microscopy, super-resolution, and absorption imaging [2, 5].

References

1. H. Berry, Monte Carlo simulations of enzyme reactions in two dimensions: fractal kinetics and spatial segregation. Biophys. J. **83**(4), 1891 (2002)
2. G. Brida, M. Genovese, I.R. Berchera, Experimental realization of sub-shot-noise quantum imaging. Nat. Photon. **4**, 227–230 (2010)
3. S. Condamin, V. Tejedor, R. Voituriez, O. Bénichou, J. Klafter, Probing microscopic origins of confined subdiffusion by first-passage observables. Proc. Natl. Acad. Sci. USA **105**(15), 5675–5680 (2008)
4. H. Frauenfelder, P. Fenimore, G. Chen, B. McMahon, Protein folding is slaved to solvent motions. Proc. Natl. Acad. Sci. USA **103**(42), 15469–15472 (2006)
5. V. Giovannetti, S. Lloyd, L. Maccone, Quantum-enhanced measurements: beating the standard quantum limit. Science **306**(5700), 1330–1336 (2004)
6. F. Gittes, B. Schnurr, P. Olmsted, F. MacKintosh, C. Schmidt, Microscopic viscoelasticity: shear moduli of soft materials determined from thermal fluctuations. Phys. Rev. Lett. **79**(17), 3286–3289 (1997)
7. G. Guigas, C. Kalla, M. Weiss, Probing the nanoscale viscoelasticity of intracellular fluids in living cells. Biophys. J. **93**(1), 316–323 (2007)
8. G. Guigas, M. Weiss, Sampling the cell with anomalous diffusion-the discovery of slowness. Biophys. J. **94**(1), 90–94 (2008)
9. J.-H. Jeon, V. Tejedor, S. Burov, E. Barkai, C. Selhuber-Unkel, K. Berg-Sørensen, L. Oddershede, R. Metzler, In vivo anomalous diffusion and weak ergodicity breaking of lipid granules. Phys. Rev. Lett. **106**(4), 048103 (2011)
10. T. Mason, K. Ganesan, J. Van Zanten, D. Wirtz, S. Kuo, Particle tracking microrheology of complex fluids. Phys. Rev. Lett. **79**(17), 3282–3285 (1997)
11. T.G. Mason, Estimating the viscoelastic moduli of complex fluids using the generalized Stokes-Einstein equation. Rheol. Acta **39**, 371–378 (2000)

12. K.C. Neuman, E.H. Chadd, G.F. Liou, K. Bergman, S.M. Block, Characterization of photodamage to Escherichia coli in optical traps. Biophys. J. **77**, 28562863 (1999)
13. E.J. Peterman, F. Gittes, C.F. Schmidt, Laser-induced heating in optical traps. Biophys. J. **84**(2), 1308–1316 (2003)
14. S. Schnell, T. Turner, Reaction kinetics in intracellular environments with macromolecular crowding: simulations and rate laws. Prog. Biophys. Mol. Biol. **85**(2), 235–260 (2004)
15. C. Selhuber-Unkel, P. Yde, K. Berg-Sørensen, L.B. Oddershede. Variety in intracellular diffusion during the cell cycle. Phys. Biol. **6**(2), 025015 (2009)
16. E.N. Senning, A.H. Marcus, Actin polymerization driven mitochondrial transport in mating S. cerevisiae. Proc. Natl. Acad. Sci. USA **107**, 721–725 (2010)
17. J.W. Tay, M.T.L. Hsu, W.P. Bowen, Quantum limited particle sensing in optical tweezers. Phys. Rev. A **80**(6), 063806 (2009). Dec
18. M.A. Taylor, J. Janousek, V. Daria, J. Knittel, B. Hage, H.-A. Bachor, W.P. Bowen, Biological measurement beyond the quantum limit. Nat. Photon. **7**, 229–233 (2013)
19. M.A. Taylor, J. Knittel, M.T.L. Hsu, H.-A. Bachor, W.P. Bowen, Sagnac interferometer-enhanced particle tracking in optical tweezers. J. Opt. **13**, 044014 (2011)
20. I.M. Tolić-Nørrelykke, E.-L. Munteanu, G. Thon, L. Oddershede, K. Berg-Sørensen, Anomalous diffusion in living yeast cells. Phys. Rev. Lett. **93**, 078102 (2004)
21. Y. Tseng, J. Lee, T. Kole, I. Jiang, D. Wirtz, Micro-organization and visco-elasticity of the interphase nucleus revealed by particle nanotracking. J. Cell Sci. **117**(10), 2159–2167 (2004)
22. M. Weiss, Stabilizing turing patterns with subdiffusion in systems with low particle numbers. Phys. Rev. E **68**(3), 036213 (2003)
23. M. Weiss, M. Elsner, F. Kartberg, T. Nilsson, Anomalous subdiffusion is a measure for cytoplasmic crowding in living cells. Biophys. J. **87**(5), 3518–3524 (2004)
24. M. Weiss, T. Nilsson, In a mirror dimly: tracing the movements of molecules in living cells. Trends Cell Biol. **14**(5), 267–273 (2004)
25. S. Yamada, D. Wirtz, S.C. Kuo, Mechanics of living cells measured by laser tracking microrheology. Biophys. J. **78**, 17361747 (2000)

Chapter 12
Subdiffraction-Limited Quantum Imaging of a Living Cell

This chapter extends the biological experiments described in Chap. 11 to allow observation of spatial structure, and in doing so, demonstrates both subdiffraction-limited quantum metrology and quantum enhanced spatial resolution for the first time in a biological context. As in the previous experiment, thermal motion of embedded lipid nanoparticles is used to study the mechanical properties of the cytoplasm of a yeast cell. Here, however, the thermal motion is characterized with quantum enhanced precision through an extended region of the cell, with the gradual drift of the particle bringing it into contact with new cellular structure. This quantum enhanced photonic force microscope allows spatial structure within the cell to be mapped at length scales down to 10 nm. Control experiments in water show a 14 % resolution enhancement compared to experiments with coherent light. This confirms the longstanding prediction that quantum correlated light can enhance spatial resolution at the nanoscale and in biology. In this demonstration, however, the nanoparticle motion is only characterized along a single axis, and the unknown motion along the other two axes precludes any reliable reconstruction of the underlying structure. The challenge remains to combine this technique with 3D particle tracking, which would allow construction of quantum enhanced images of nanoscale biological structure. This chapter is based on the following paper [38].

12.1 Quantum Imaging with PFM

The emerging field of quantum imaging utilizes quantum effects to overcome classical imaging constraints. In particular, non-classical states of light can allow the shot-noise and diffraction limits to be surpassed [16], and quantum engineered artificial atoms allow new approaches to sensing [24]. The primary motivation for such techniques is in biological imaging [4, 24, 27, 29, 42], where any improvement in imaging technology can reveal new levels of cellular complexity. Since sub-cellular structures often have nanometer size scales, spatial resolution surpassing the diffraction limit is particularly beneficial. However, neither subdiffraction-limited res-

M. Taylor, *Quantum Microscopy of Biological Systems*, Springer Theses,
DOI 10.1007/978-3-319-18938-3_12

olution nor quantum enhanced resolution have previously been achieved in biology. To date, the only reported demonstration of biological imaging with non-classical light has been in dispersion compensation for optical coherence tomography [27]. Even in non-biological demonstrations, both the absolute sensitivity and resolution of optical quantum imaging has been constrained to levels far inferior to state-of-the-art classical technology [4, 29, 31]. While unprecedented sensitivity is in principle achievable using squeezed states of light [16, 42], no method has been experimentally demonstrated capable of utilizing squeezed light in biological imaging.

Here we propose and demonstrate a new quantum imaging method which applies squeezed light in photonic force microscopy (PFM) [8]. This allows both quantum enhanced resolution and subdiffraction-limited quantum imaging in biology for the first time, with resolution comparable to leading classical experiments. PFM is a classical subdiffraction-limited imaging technique closely analogous to atomic force microscopy (AFM), but with a nanoscale particle trapped in optical tweezers replacing the probe tip [8, 11]. As the nanoparticle explores a cell, environmental variations which affect its thermal diffusion can be mapped. PFM has been used to map both 3D surfaces [10, 40] and mechanical properties of fluids [32], and has been applied to study cell membranes [8], nanoscale protein motors [34], molecular interactions [33], and, similar to our work here, intracellular viscoelasticity [2]. As is typical of nanoprobe based microscopy techniques, the spatial resolution achievable in PFM is not constrained by the diffraction limit. The resolution lateral to the motion of the probe particle is constrained by its size. However, similar to AFM, the resolution along the direction of motion is typically limited by measurement signal-to-noise [10, 33]. Here we use non-classical light to improve the signal-to-noise, and thereby demonstrate quantum enhanced resolution in PFM.

The squeezed-light-enhanced PFM is used to construct one-dimensional profiles of spatial structures within a cell, with features observed at length scales down to 10 nm. Control measurements in water confirm that for fixed optical power, squeezed light provides 14 % enhancement over the resolution possible with coherent light. A 74 % increase in optical power would be required to achieve this level of enhancement without squeezing; increasing the potential for damage [28, 30] and photochemical disruption of cellular processes [22, 28], which are known to severely limit biological applications of PFM [33]. By demonstrating for the first time that non-classical light can improve resolution in a biological context, the PFM achieves the key requirement for quantum enhanced imaging in biology. Our results, further, constitute the first demonstration of quantum enhanced resolution using squeezed light in any context.[1] When combined with 3D particle tracking, quantum enhanced nanoscale images of biological structure could be constructed, placing practical applications of quantum imaging with non-classical light within reach.

The results presented here complement previous quantum imaging experiments using non-classical light. In imaging applications that simultaneously sample the entire field of view, many spatial modes are captured. Quantum enhancement

[1] Note that Ref. [5] claims to have enhanced resolution via use of squeezed light. We disregard this claim as unsubstantiated; for details see Appendix B.

then requires that quantum correlations are established between a large number of these modes. Such multimode non-classical light has been applied in proof-of-principle demonstrations of sub-shot noise absorption imaging [4], enhanced 2-photon microscopy [7], ghost imaging via photon correlations [31], improved image reconstruction against a noisy background [20], generation of entangled images [3], noiseless image amplification [21, 26], and to eliminate unwanted artifacts in optical coherence tomography [27]. However, practical applications have been precluded by a lack of both bright multi-mode sources of strongly non-classical light, and high bandwidth array detectors capable of efficiently detecting this light [18]. By contrast, in single or few-modes scenarios, such sources and detectors are readily available [1]. This has enabled quantum enhanced measurements of spatial parameters such as laser beam deflection [42, 43] and spatial quantum correlations [14]. However, these experiments suffer the apparent major drawback that quantum enhancement is only possible for a number of pixels at most equal to the number of available single-mode sources of quantum correlated light. Consequently, they have previously been limited to a maximum of 8 pixels [1]. This limitation can be overcome using a scanning probe as demonstrated here for the first time, or an optical raster scan as recently demonstrated in Ref. [29].

In PFM, a probe particle is tracked as it is scanned over the field of view. Variations in measured motion are then studied over a measurement time which is often of order minutes [10, 40]. Provided the microscope has sufficient stability [33], and that these variations are dominated by static intracellular structure, rather than dynamic cellular processes [35] or nanoscale motion of cellular constituents, this allows a map of the cellular structure to be constructed. The quantum PFM reported here utilizes the quantum enhanced nanoparticle tracking apparatus demonstrated in Chap. 10. Although this was also applied in Chap. 11 to study temporal fluctuations within living cells, the lack of spatial resolution was a critical shortcoming, preventing any conclusions from being drawn regarding the dominant source of fluctuations in the measured motion, and therefore application as a PFM. Here, spatial resolution is introduced and quantum PFM realized, with thermally driven motion used to scan the probe particle through an extended region of the cell [40].

12.2 Experimental Method

Saccharomyces cerevisiae yeast cells were immobilized with an optical trap, and lipid granules of approximately 300 nm diameter were tracked with either squeezed or coherent light as they diffused within the cellular cytoplasm. Since the characteristic thermal motion of any particle is determined by the mechanical properties of its surrounding medium, such intracellular particle tracking measurements are commonly used to study the mechanics of cellular cytoplasm [2]. Lipid granules are well suited for use as probe particles within yeast as they occur naturally and can be tracked precisely due to their high refractive index [35, 41]. In our experiment, the high frequency thermal motion of a lipid granule reveals the viscoelastic mechanical

properties of the surrounding cytoplasm, while for sufficiently long measurements its slow thermal drift provides spatial resolution by bringing it into contact with different parts of the cellular cytoplasm. Thus, spatial inhomogeneity in the viscoelasticity can be quantified by a single continuous measurement of the lipid granule position. In our experiment, the particle position $x(t)$ transverse from the trap center was measured by combining scattered light from the sample with a local oscillator field which was spatially shaped such that direct measurement of the total power yielded the particle position (Fig. 12.1a). In the same manner as in Chap. 11, mechanical properties of the cytoplasm directly surrounding the nanoparticle could be characterized from its mean squared displacement (MSD) after a delay τ,

$$\left\langle \Delta x^2(\tau) \right\rangle = \left\langle (x(t) - x(t-\tau))^2 \right\rangle, \tag{12.1}$$

with an example shown in Fig. 12.1b. Squeezed light improves the precision by reducing the error with which the MSD can be estimated. This improvement is shown in the measured power spectral density (Fig. 12.1d), with squeezed light lowering the noise floor by 2.4 dB. For short delays, the MSD is dominated by thermal motion and has the form

$$\left\langle \Delta x^2(\tau) \right\rangle = 2D\tau^{\alpha}, \tag{12.2}$$

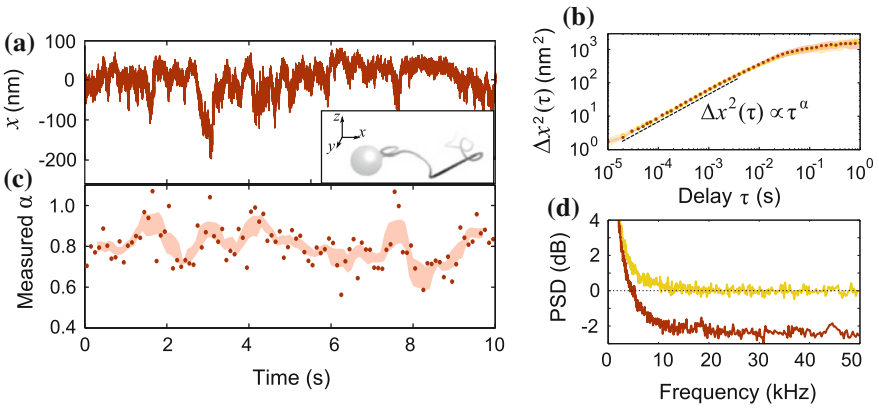

Fig. 12.1 This shows measurements of lipid motion within a yeast cell, similar to the results in Chap. 11. **a** Measured particle motion, which is the x projection of the 3D motion (shown schematically in the inset). **b** The MSD is constructed with both squeezed light (*dark red*) and coherent light (*gold*), and α determined by fitting this to Eq. 12.2. The classical and squeezed example traces here both yield $\alpha = 0.83$. **c** The raw data was divided into 100 ms segments and the value of α established for each (*solid dots*). The *light red shaded region* represents the moving mean and standard error with a 0.5 second width. **d** The normalized power spectral density (PSD) shows that squeezing suppressed the noise floor by 2.4 dB

where the diffusive parameter α carries information about the mechanical properties of the surrounding medium [12, 23]. α is determined for a set of data by fitting the MSD at short delays to Eq. 12.2. When $\alpha = 1$, the motion is diffusive, which is indicative of a random walk type of motion, whereas confinement of the particle causes subdiffusive motion ($0 < \alpha < 1$). Subdiffusive motion is an indicator that the cellular cytoplasm exhibits both viscosity and elasticity [12], since to constrict motion the cytoplasm must store mechanical energy. In our experiments, 100 ms of data was sufficient to precisely determine α. Consequently, the measured values of α allowed temporal variations in the cellular viscoelasticity to be characterized with 10 Hz bandwidth.

12.3 Spatially Resolved Measurements

As lipid particles undergo three dimensional (3D) thermal motion, they are exposed to different parts of the cell (Fig. 12.1a inset). In a full PFM, 3D motion is tracked through an extended region of the cell. By characterizing the changes in α that occur, it is then possible to construct 3D images of structure within the cellular cytoplasm [2]. Here, to demonstrate that non-classical light enables resolution surpassing that possible with coherent light, a proof-of-principle demonstration is achieved using 1D particle tracking along the x axis, with the co-ordinates y and z not determined. This allows 1D profiles of $\alpha(x)$ to be constructed following the projection of the trajectory onto the x axis.

A series of experiments were performed in which the motion of lipid particles was tracked with quantum enhanced precision for 10 s as they diffused through the cell. The data from each experiment was separated into 100 ms segments, with both α and the mean position along the x axis determined for each segment. As the particle diffused, a profile of α was generated as a function of x, with four representative profiles shown in Fig. 12.2. As can be seen, the particles explored a range of approximately 120 nm along the x axis over the 10 s measurement interval, consistent with the MSD in Fig. 12.1b extrapolated to longer delays. The directly obtained data exhibited substantial noise both from the measurement process and due to the unknown trajectory of the particle in the y and z directions. To identify statistically resolvable features, the running mean and standard error of α were calculated along the x axis, with a 10 nm averaging window defining the spatial resolution. A broader averaging window degrades the resolution, but improves the statistical uncertainty with which α can be determined, since a greater number of measurements are included in the averaging. As with any imaging procedure, features can only be observed if the image achieves sufficient contrast to distinguish it from its background; where the contrast here is limited by the statistical uncertainty in α. There exists an intrinsic compromise between spatial resolution and contrast, and it is necessary to choose a suitable spatial resolution to allow clear observation of spatial features. The choice of 10 nm spatial resolution was found to provide sufficient contrast to observe cellular structure in the images shown here. A significantly narrower choice of spatial resolution

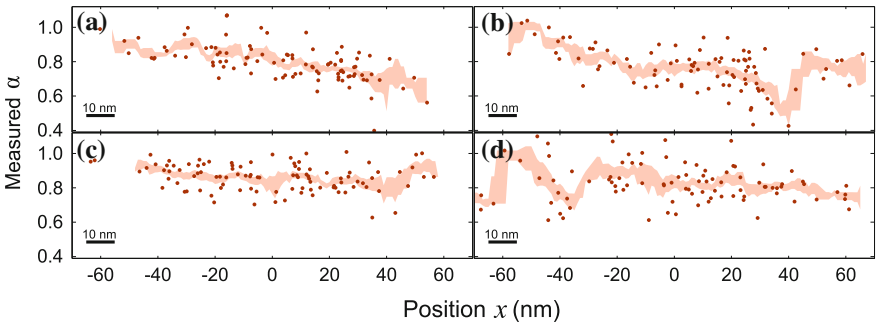

Fig. 12.2 1D profiles of α. Each *circle* represents a single measurement of α versus x using a 100 ms set of data. The *shaded regions* represent the running mean and standard error with 10 nm resolution (*thick black bar*). Each profile was recorded minutes apart to allow the particle time to diffuse to different regions of the cell with qualitatively different spatial structures. The particle confinement is greatest where α is lowest, such as the dip about 40 nm in (**b**), and the particle movement is most free when α is highest, such as the peak at –55 nm in (**d**)

led to numerous gaps in the profiles where there was insufficient data to construct the running average, while broader spatial resolution tended to average over some observable features.

The observed spatial structure varies between measurements of $\alpha(x)$ because the particle follows different 3D trajectories. Gradual linear changes in α were observed (e.g. Fig. 12.2a) which suggest a spatial gradient in the molecular crowding along the x axis [46], along with narrow dips in α (e.g. Fig. 12.2b at 40 nm) suggestive of barriers in the cytoplasm, areas of homogeneity (e.g. Fig. 12.2c), and peaks in α (e.g. Fig. 12.2d at –55 nm) which may follow from small voids in the cytoplasmic structure. Since only the projection of the particle motion onto the x axis was tracked, it is not possible to define the complete trajectory along which these 1D profiles are taken. This obscures the biological origin of observed features. For instance, the narrow dip in α seen in Fig. 12.2b could result from a range of subcellular components including an actin filament or the edge of a larger organelle, even though these have markedly different 3D profiles. The 3D motion of the particle also degrades the contrast of narrow features by averaging measurements of α from a range of positions along the y and z axes. These limitations could be resolved by incorporating our technique in a 3D PFM [8] which maps the complete trajectory of the particle. It may then be possible to generate a quantum enhanced 3D image of the cell, with quantum enhancement only required for one axis from which α could be determined.

12.4 Correlation Analysis of Images

Importantly, even though the biological origin of the profiles in Fig. 12.2 is obscured, the measured changes in α can be rigorously shown to originate from spatial structure within the cell. In a static spatially varying environment, spatial correlations between

$\alpha(x)$ profiles should decay exponentially with the time between the profiles, as the unknown motion along the y and z axes brings the particle into different regions of the cell.By contrast, temporal changes in the cell [35] or drifts in the apparatus which produce fluctuations in α should not exhibit any correlations between profiles. Thus, analysis of the correlations between subsequent images can determine whether temporal fluctuations or spatial structure in α are dominant. The correlations which result from spatial structure can be predicted with a simple model which assumes that α is perfectly correlated if the displacement dr along the y and z axes is below the length scale of structural variations r_c, and completely uncorrelated if $dr > r_c$. Then, assuming that the motion along each axis independently follows Eq. 12.2, and also assuming Gaussian probability distributions, the average correlation is given by the probability that the particle remains within r_c

$$P\,(dr < r_c) = 1 - \mathrm{Exp}\left[\frac{-\pi r_c^2}{4\langle dr^2\rangle}\right] = 1 - \mathrm{Exp}\left[\frac{-\pi}{4}\left(\frac{dt}{T_c}\right)^{-\alpha}\right], \tag{12.3}$$

where T_c is the average time that the particle takes to diffuse into an uncorrelated region of the cell, such that $\langle dr^2\rangle = r_c^2$. To determine whether the experimental data follows Eq. 12.3, a series of $\alpha(x)$ profiles were constructed at a rate of 20 s^{-1}, and the correlations between the subsequent images calculated as a function of delay. In this case, each profile was constructed from 50 measurements of α, each based on 1 ms of raw data. This experimental data was fitted to Eq. 12.3, with T_c and α used

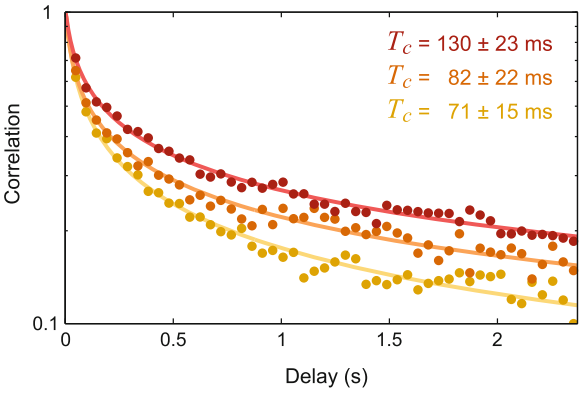

Fig. 12.3 To verify that the measured changes in α are spatial, correlations between sequential measurements of $\alpha(x)$ are analyzed for three sets of data. The *circles* are experimentally determined correlations between a series of measurements, which are well fitted by Eq. 12.3 (*lines*), which predicts the decay in correlations decays due to unknown motion along the y and z axes. The characteristic time T_c for the particle to diffuse into uncorrelated regions of the cell is estimated by fitting the data to Eq. 12.3. Note that the decay in correlation restricts the duration over which $\alpha(x)$ profiles can be constructed. Although the characteristic times found here are in the range of 0.1 s, correlations were found to persist for sufficient time to construct the 10 s $\alpha(x)$ profiles shown in Fig. 12.2

as fitting parameters. The data shows excellent agreement with the simple model, thus confirming that the α profiles reflect spatial structure rather than temporal fluctuations (Fig. 12.3). Furthermore, this analysis of correlations allows the local length scale of viscoelastic structure to be determined in the region of the nanoparticle. This length scale can be found by combining the MSD measured in Fig. 12.1b with the fitted characteristic time T_c over which the particle takes diffuses into an uncorrelated region of the cell. The length scales of the viscoelastic structure in three different regions were determined to be 46.9 ± 1.3 nm, 43.7 ± 2.4 nm, and 42.6 ± 1.9 nm (Fig. 12.3), demonstrating that changes in the characteristic length of spatial structure in different parts of the cell can be statistically distinguished with nanometer precision.

12.5 Background Scattering

The imaging method presented here intrinsically relies on single particle tracking. However, within the yeast cells there are many scattering centers which cannot be entirely separated from the tracked lipid granule. The resulting background of scattered light could contribute spurious signals to the measurement. This is common to any intracellular particle tracking experiment, though it is generally found to be safe to neglect the effects of the background structures [41]. In our experiment, the illumination angle of the dark-field illumination was chosen to maximize the measured scattering from the lipid granules, while minimizing the contributions of larger organelles such as mitochondria and the nucleus. Since the lipid granules have a higher refractive index than these larger organelles, their scattered field dominates at the wide angles which were sampled in this experiment (see Chap. 8). We can further confirm that the measured motion is dominated by lipid granule motion, since Ref. [41] also measured the motion of single lipid granules within yeast cells, and their equivalent data almost exactly follows that recorded here (see Fig. 12.4).

During measurements, the yeast cells were observed with light microscopy to identify the particles under study. The 0.4 numerical aperture of the objectives was relatively low due to the requirement for high quantum efficiency, and lack of commercially available objectives that combine high efficiency and numerical aperture at 1064 nm. Consequently, the resolution was insufficient to reliably resolve nearby lipid particles, and it was not possible to directly verify that only a single lipid granule entered the focus of the local oscillator. However, the measurement statistics are strongly consistent with single particle tracking and with previous measurements of single lipid particles in yeast [41]. In particular, the decay in correlations between subsequent images (discussed above) follows exactly the form expected for single particle measurements. A much faster decay would be expected if multiple particles contributed to the measured signal. Furthermore, the number density of lipid particles within yeast cells is low compared to the focal size of the local oscillator [41], such that it is statistically unlikely that multiple particles would be simultaneously measured.

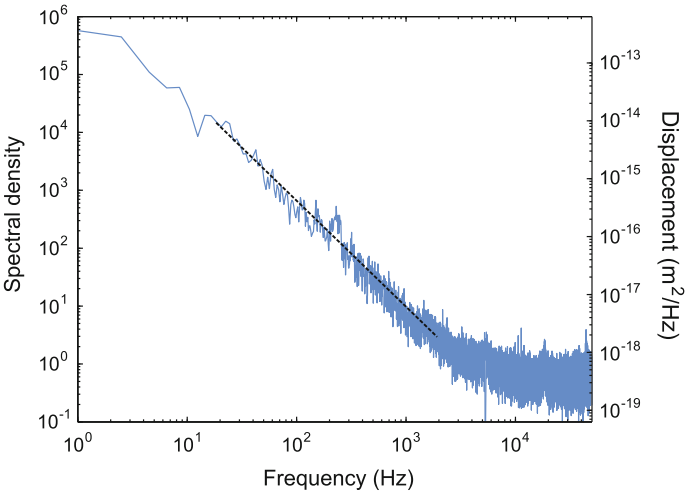

Fig. 12.4 The mechanical spectra measured within yeast cells. The data rolls off with a $\omega^{-1.8}$ relation at low frequencies, with a flat noise floor dominating at high frequencies. For comparison, the low frequency trend reported in Ref. [41] for single lipid granules within yeast cells is also shown (*dashed line*)

In future quantum PFM experiments, it will be important to rigorously quantify the effect of background scattering centers on the measured signal. Increased objective numerical aperture will be required to optimize the sensitivity, which will also improve the resolution of the conventional imaging system. This should allow lipid particles to be individually resolved, such that single-particle tracking can be guaranteed at all times. While this technical difficulty requires careful attention, it has already been addressed in previous classical measurements of anomalous diffusion within cells [41], and does not present a fundamental barrier to use of this quantum imaging technique in practical biological experiments.

12.6 Quantum Enhancement in Resolution

Due to the complexity of the intracellular environment, the quantum resolution enhancement achieved in the PFM was characterized via control experiments on 1 μm radius silica beads in water, rather than directly in vivo. This approach of using simple well understood control experiments is standard when calibrating resolution in PFM [8, 10, 33]. Although it would be preferable to use smaller beads which more closely approximate the lipid granules used in vivo, this would not affect the overall conclusion of this calibration. $\alpha(x)$ profiles were constructed from 80 s of data using both squeezed and coherent light. In this case, 2.5 dB of squeezing was measured, which closely approaches the enhancement achieved in biological measurements.

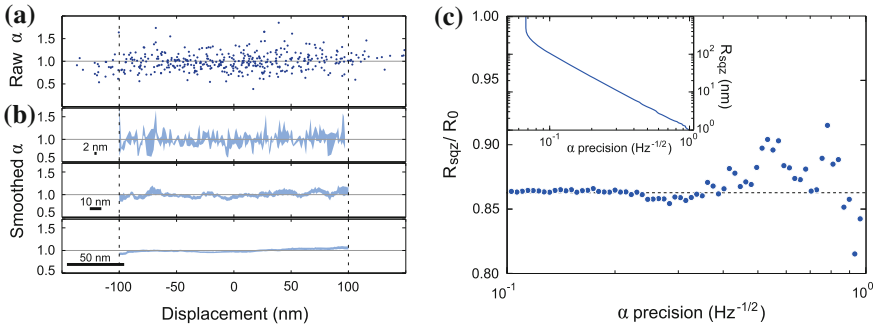

Fig. 12.5 Characterization of the spatial resolution. To calibrate the resolution enhancement achieved here, a profile of $\alpha(x)$ was constructed by tracking particles in water. The individual measurements are shown in (**a**), while (**b**) shows the corresponding moving mean and standard error calculated over a 200 nm range with spatial resolution of 2 nm, 10 nm, and 50 nm. The data closely follows the expected $\alpha = 1$ result (*horizontal line*). (**c**) The ratio of spatial resolutions with squeezed and coherent light is shown as a function of precision in α, which determines the contrast. The α precision values shown are normalized into units of $\mathrm{Hz}^{-1/2}$ to account for the improvement in absolute contrast as data is accumulated. For a fixed precision (or equivalently, contrast), the spatial resolution achievable with squeezing (R_{sqz}) is improved by approximately 14 % when compared to coherent light (R_0). The absolute spatial resolution achievable using squeezed light is plotted in the inset. Since the number of points being averaged is proportional to the spatial resolution, the sensitivity scales as the inverse square root of spatial resolution until the averaging window width becomes comparable to the spatial range of the measured data

These measurements show no statistically significant spatial structure (Fig. 12.5), with $\alpha = 1$ at all spatial locations as expected for Brownian motion. This lack of statistically significant variation provides further verification that the structure observed in vivo can be attributed to changes in α, rather than drifts in the apparatus.

Since water is homogeneous with $\alpha = 1$ throughout, the variation in this data allows the statistical uncertainty of our measurements of α to be determined. This precision was characterized as a function of spatial resolution by varying the width of the running average along x, as shown representatively in Fig. 12.5b. As the width increases, the spatial resolution is degraded, but the precision in α improves since more data is averaged at each position along x (see Fig. 12.5c inset), which improves the achievable image contrast. By comparing the resolution required to achieve a fixed precision with and without squeezed light, it was possible to confirm for the first time that squeezed light can be used to enhance spatial resolution. Furthermore, this also provides the first demonstration of quantum enhanced spatial resolution in a biological context. As shown in Fig. 12.5c, in this proof-of-principle experiment squeezed light allowed a 14 % improvement in resolution for precision in α ranging from 0.1–1 $\mathrm{Hz}^{-1/2}$.

To take a specific example, the biological profiles shown in Fig. 12.2 use 10 nm resolution and include 10 s of accumulated data. In our control experiments in water, this resolution and accumulation time would allow structures that alter α by 0.1 to be resolved (see Fig. 12.5c inset). By comparison, a resolution of 12 nm would be

required to resolve such features with coherent light. It is important to note that both the measurement sensitivity and the spatial range of diffusion differ between this calibration with silica beads and the measurements in biology. Consequently, the α precision determined here differs from that achieved *in vivo*, where the average standard error in α was 0.04. Importantly, the quantum resolution enhancement is independent of the absolute level of precision, as can be seen over an order of magnitude in Fig. 12.5c. Therefore, even though the absolute resolution differs between *in vivo* and control experiments, the quantum resolution enhancement predicted here can be expected to accurately represent the *in vivo* enhancement.

12.7 Theoretically Predicted Quantum Enhancement

This imaging method requires α to be accurately estimated from the thermal motion of a nanoparticle. The precision of this estimation is limited both by measurement noise and the stochastic nature of thermal motion. Although squeezed light can suppress the measurement noise and thereby enhance the spatial resolution, there is a non-trivial relationship between the resolution enhancement and the degree of squeezing achieved. Here this relationship was explored by analyzing simulated data to find the precision with which α can be estimated for different levels of measurement noise. This simulated data was analyzed in the same manner as the experimental results. A discrete series of measurements x_n of the particle position x were performed at evenly spaced intervals dt in time, where n is the measurement number. These were used to determine the mean squared displacement (MSD), by the relationship

$$\left\langle \Delta x^2(\tau = m\,dt) \right\rangle_{\text{exp}} = \sum (x_{n+m} - x_n)^2 - N_{\text{MSD}}, \tag{12.4}$$

where N_{MSD} is the mean variance. Although the expectation value of this experimental MSD is given by $2D\tau^{\alpha}$ (Eq. 12.2), a single trajectory will only asymptote towards this in the limit of infinite statistically independent measurements. The number of statistically independent measurements at any delay τ is given by T/τ, where T is the total measurement time. As such, even a perfectly noise-free determination of the particle motion cannot yield α with complete certainty in a finite measurement time. Thus, the stochastic nature of the MSD introduces an intrinsic uncertainty into the value of α in addition to any uncertainty associated with the measurement noise. This intrinsic uncertainty is greatest at long delays, where the number of independent measurements is lowest. Measurement noise, by contrast, is of approximately constant amplitude with delay, and therefore has the greatest relative effect at short delays where the expectation value of the MSD is smallest.

To quantitatively predict the enhancement achievable with squeezed light, Monte Carlo simulations were performed in which 10000 particle trajectories were simulated by a normally distributed random walk, with measurements including varying

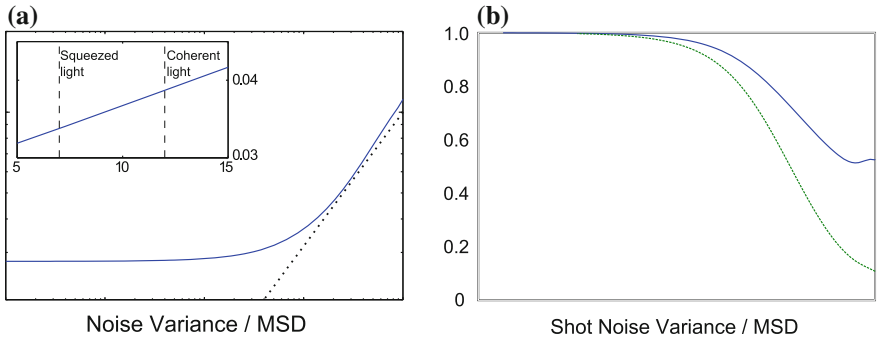

Fig. 12.6 The influence of measurement noise in viscoelastic imaging. (**a**) The precision with which α can be determined ($\delta\alpha$) is plotted against the measurement noise variance, normalized to the MSD at minimum delay. The *dotted line* scales as the square root of the noise variance, and approximately follows $\delta\alpha$ between variances of 10 and 100. The inset zooms in on this result in the regime of the experiments here, with the *vertical dashed lines* showing the noise variance on the experimental data. (**b**) The ratio of the spatial resolutions achievable with squeezed light and coherent light, with either 2.4 dB (*solid*) or 10 dB (*dashed*) of squeezing

levels of white noise. Each thermal trajectory was simulated by taking a normally distributed random step between each discrete measurement. After the trajectory was generated, the measurements were generated by adding Gaussian distributed noise with a range of variances. α was then determined from the simulated trajectories via weighted linear regression of the MSD in a log-log basis. The uncertainty $\delta\alpha$ was then given by the deviations of the predicted α from the ideal result of $\alpha = 1$ which should follow from such a random walk.

By repeating this for various levels of measurement noise, we could plot the uncertainty in α as a function of the measurement noise variance (Fig. 12.6a). In this case, the measurement length and fitting range matched the measurement conditions of the main text, and the noise variance was normalized to the MSD at minimum delay. When the noise is far smaller than the MSD (below 1 in Fig. 12.6a), the stochastic walk dominates the uncertainty in α, and techniques for noise reduction such as squeezing yield little improvement. When the measurement noise dominates the MSD at all analyzed delays, α cannot be determined with any reliability. As such, this region is not included in in Fig. 12.6. Between these two extremes, measurement noise only dominates the MSD at short delays, and the precision with which α can be determined scales approximately as the square root of the noise variance. The relative contribution of shot noise increases as the measurement rate increases or the measurement duration decreases, both of which are required to produce high precision images, or if the optical power is reduced. As such, quantum enhanced precision provides maximal enhancement in the regime which is both most challenging to reach in classical experiments and most relevant to biological imaging.

When performing spatially resolved experiments, the precision with which α can be determined at a specific location is given by $\delta\alpha_{\text{image}} = \delta\alpha N^{-1/2}$, where N is the mean number of data points averaged at each location. For 1D imaging, this is given by

$$N = N_{\text{tot}} \frac{dx}{x_{\text{FOV}}}, \tag{12.5}$$

where N_{tot} is the total number of measurements of α, x_{FOV} is the field of view, and dx is the spatial resolution. Thus, if a fixed precision $\delta\alpha_{\text{image}}$ is required in a 1D image, the spatial resolution scales as $dx \propto \delta\alpha^2$. Using this, the spatial resolution enhancement is plotted in Fig. 12.6b for both 2.4 dB and 10 dB of measured squeezing.

At the noise levels measured here, we can predict that 2.4 dB of measured squeezing should have allowed 21 % narrower spatial resolution in our experiment, which is greater than the measured 14 % enhancement. The discrepancy between predicted and achieved enhancements may be due to the technical noise in the experiment such as low frequency noise and unwanted inclusion of RF modulations that were used for phase locking of the squeezing cavity. If the measurement rate were increased, such that the shot noise variance was 100 times greater than the MSD at minimum delay, 2.4 dB of measured squeezing would allow a 45 % reduction in spatial resolution. If state-of-the art squeezing were used and the measured squeezing reached 10 dB, the quantum enhancement could then provide 90 % narrower spatial resolution. Alternatively, an even greater measurement rate could sufficiently increase the measurement noise to preclude determination of α from a classical experiment, while α could still be determined with squeezed light.

12.8 Outlook for the Future

In absolute terms, the resolution achieved here is comparable to that of leading classical PFM measurements of viscoelasticity [2, 34]. Furthermore, the resolution could be substantially improved using an increased level of squeezing. With 10 dB of measured squeezing, as reported in a number of experiments [25, 36], an order of magnitude enhancement should be feasible. This could potentially allow Angström level resolution. In principle, further enhancement may be possible by using more sophisticated quantum measurements [39, 44], with recent theoretical results predicting that an array of photon number resolving detectors could even allow particle tracking at the de Broglie limit [44].

When combined with the advances described above, the technology introduced here could help to answer important questions related to the nanoscale structure within cells. It has potential which extends beyond mapping of organelle positions, since thermal motion is critical to the operation of the cell and mediates important functions such as chemical reactions [6] and protein folding [9]. It has been shown that the optimal diffusive regime is different for storage, transport, and chemical reactions [13], and that in some regions of the cell, structures which influence diffusion are organized at the nanoscale [45]. It remains unknown to what extent these nanoscale structural variations reflect an underlying biological function. We anticipate that in the future, quantum imaging could play an important role in answering such questions.

Our results complement recent biological applications of quantum engineered diamond probes with Nitrogen Vacancy (NV) centers, which have enabled thermal [17] and magnetic cellular imaging [15, 19, 37]. None of these applications have achieved subdiffraction limited resolution, as they rely on optically resolvable arrays of stationary NV probes [15, 17, 19, 37], confining them to the study of relatively large cellular structures and organelles. The resolution achieved here is over an order of magnitude finer, providing the possibility to observe important nanoscale cellular structures such as membranes, actin networks, and individual proteins. Since the approach is in principle transferable to NV nanodiamond based imaging, it could also open the door to simultaneous subdiffraction-limited imaging of structure, temperature and magnetic fields.

In summary, we report the first application of quantum imaging techniques to subdiffraction-limited biological imaging, and demonstrate that non-classical light can improve spatial resolution in biological applications. The viscoelastic structure within a living yeast cell is sampled along the trajectory of a thermally driven nanoparticle, revealing spatial structure with length scales down to 10 nm. Control experiments in water show that the spatial resolution is enhanced by 14 % through use of squeezed light. Future experiments which apply this quantum enhanced photonic force microscope with improved technology may enable resolution of sub-nm structure *in vivo*.

References

1. S. Armstrong, J.-F. Morizur, J. Janousek, B. Hage, N. Treps, P.K. Lam, H.-A. Bachor, Programmable multimode quantum networks. Nat. Commun. **3**, 1026 (2012)
2. E. Bertseva, A. Singh, J. Lekki, P. Thévenaz, M. Lekka, S. Jeney, G. Gremaud, S. Puttini, W. Nowak, G. Dietler, L. Forró, M. Unser, A. Kulik, Intracellular nanomanipulation by a photonic-force microscope with real-time acquisition of a 3D stiffness matrix. Nanotechnology **20**(28), 285709 (2009)
3. V. Boyer, A.M. Marino, R.C. Pooser, P.D. Lett, Entangled images from four-wave mixing. Science **321**(5888), 544–547 (2008)
4. G. Brida, M. Genovese, I.R. Berchera, Experimental realization of sub-shot-noise quantum imaging. Nat. Photon. **4**, 227–230 (2010)
5. L. Chen, S.W. Bi, B.Z. Lu, Experimental study on the imaging of the squeezed state light at 1064 nm. Laser Phys. **21**(7), 1202–1207 (2011)
6. S. Condamin, V. Tejedor, R. Voituriez, O. Bénichou, J. Klafter, Probing microscopic origins of confined subdiffusion by first-passage observables. Proc. Natl. Acad. Sci. USA **105**(15), 5675–5680 (2008)
7. H.-B. Fei, B.M. Jost, S. Popescu, B.E. Saleh, M.C. Teich, Entanglement-induced two-photon transparency. Phys. Rev. Lett. **78**(9), 1679–1682 (1997)
8. E.-L. Florin, A. Pralle, J. Heinrich Hörber, E.H. Stelzer, Photonic force microscope based on optical tweezers and two-photon excitation for biological applications. J. Struct. Biol. **119**(2), 202–211 (1997)
9. H. Frauenfelder, P. Fenimore, G. Chen, B. McMahon, Protein folding is slaved to solvent motions. Proc. Natl. Acad. Sci. USA **103**(42), 15469–15472 (2006)
10. M. Friese, A. Truscott, H. Rubinsztein-Dunlop, N. Heckenberg, Three-dimensional imaging with optical tweezers. Appl. Opt. **38**(31), 6597–6603 (1999)

11. L.P. Ghislain, W.W. Webb, Scanning-force microscope based on an optical trap. Opt. Lett. **18**(19), 1678–1680 (1993)
12. F. Gittes, B. Schnurr, P. Olmsted, F. MacKintosh, C. Schmidt, Microscopic viscoelasticity: shear moduli of soft materials determined from thermal fluctuations. Phys. Rev. Lett. **79**(17), 3286–3289 (1997)
13. G. Guigas, M. Weiss, Sampling the cell with anomalous diffusion-the discovery of slowness. Biophys. J. **94**(1), 90–94 (2008)
14. J. Janousek, K. Wagner, J. Morizur, N. Treps, P. Lam, C. Harb, H. Bachor, Optical entanglement of co-propagating modes. Nat. Photon. **3**(7), 399–402 (2009)
15. S. Kaufmann, S. Steinert, L.P. McGuinness, B.C. Johnson, T. Ohshima, F. Caruso, et al., Detection of atomic spin labels in a lipid bi-layer using a single-spin nanodiamond probe. Proc. Natl. Acad. Sci. USA **110**(27), 10894–10898 (2013)
16. M. Kolobov, C. Fabre, Quantum limits on optical resolution. Phys. Rev. Lett. **85**(18), 3789–3792 (2000)
17. G. Kucsko, P. Maurer, N. Yao, M. Kubo, H. Noh, P. Lo, H. Park, M. Lukin, Nanometer scale quantum thermometry in a living cell. Nature **500**, 54–59 (2013)
18. M. Lassen, V. Delaubert, J. Janousek, K. Wagner, H.-A. Bachor, P.K. Lam, N. Treps, P. Buchhave, C. Fabre, C. Harb, Tools for multimode quantum information: modulation, detection, and spatial quantum correlations. Phys. Rev. Lett. **98**(8), 083602 (2007)
19. D. Le Sage, K. Arai, D. Glenn, S. DeVience, L. Pham, L. Rahn-Lee, M. Lukin, A. Yacoby, A. Komeili, R. Walsworth, Optical magnetic imaging of living cells. Nature **496**(7446), 486–489 (2013)
20. E. Lopaeva, I.R. Berchera, I. Degiovanni, S. Olivares, G. Brida, M. Genovese, Experimental realization of quantum illumination. Phys. Rev. Lett. **110**(15), 153603 (2013)
21. L. Lopez, N. Treps, B. Chalopin, C. Fabre, A. Maître, Quantum processing of images by continuous wave optical parametric amplification. Phys. Rev. Lett. **100**(1), 013604 (2008)
22. R. Lubart, R. Lavi, H. Friedmann, S. Rochkind, Photochemistry and photobiology of light absorption by living cells. Photomed. Laser Surg. **24**(2), 179–185 (2006)
23. T. Mason, K. Ganesan, J. Van Zanten, D. Wirtz, S. Kuo, Particle tracking microrheology of complex fluids. Phys. Rev. Lett. **79**(17), 3282–3285 (1997)
24. L.P. McGuinness, Y. Yan, A. Stacey, D.A. Simpson, L.T. Hall, D. Maclaurin, S. Prawer, P. Mulvaney, J. Wrachtrup, F. Caruso, R.E. Scholten, L.C.L. Hollenberg, Quantum measurement and orientation tracking of fluorescent nanodiamonds inside living cells. Nature Nanotech. **6**, 358–363 (2011)
25. M. Mehmet, H. Vahlbruch, N. Lastzka, K. Danzmann, R. Schnabel, Observation of squeezed states with strong photon-number oscillations. Phys. Rev. A **81**(1), 013814 (2010)
26. A. Mosset, F. Devaux, E. Lantz, Spatially noiseless optical amplification of images. Phys. Rev. Lett **94**(22), 223603 (2005)
27. M.B. Nasr, D.P. Goode, N. Nguyen, G. Rong, L. Yang, B.M. Reinhard, B.E. Saleh, M.C. Teich, Quantum optical coherence tomography of a biological sample. Opt. Commun. **282**(6), 1154–1159 (2009)
28. K.C. Neuman, E.H. Chadd, G.F. Liou, K. Bergman, S.M. Block, Characterization of photodamage to Escherichia coli in optical traps. Biophys. J. **77**, 2856–2863 (1999)
29. T. Ono, R. Okamoto, S. Takeuchi, An entanglement-enhanced microscope. Nat. Commun. **4**, 2426 (2013)
30. E.J. Peterman, F. Gittes, C.F. Schmidt, Laser-induced heating in optical traps. Biophys. J. **84**(2), 1308–1316 (2003)
31. T. Pittman, Y. Shih, D. Strekalov, A. Sergienko, Optical imaging by means of two-photon quantum entanglement. Phys. Rev. A **52**(5), R3429 (1995)
32. A. Pralle, E.-L. Florin, E. Stelzer, J. Hörber, Local viscosity probed by photonic force microscopy. Appl. Phys. A **66**, S71–S73 (1998)
33. A. Rohrbach, C. Tischer, D. Neumayer, E.-L. Florin, E.H. Stelzer, Trapping and tracking a local probe with a photonic force microscope. Rev. Sci. Instrum. **75**(6), 2197–2210 (2004)

34. T. Scholz, S.M. Altmann, M. Antognozzi, C. Tischer, J.-K. Heinrich, Hörber, B. Brenner, Mechanical properties of single myosin molecules probed with the photonic force microscope. Biophys. J. **88**(1), 360–371 (2005)
35. C. Selhuber-Unkel, P. Yde, K. Berg-Sørensen, L.B. Oddershede, Variety in intracellular diffusion during the cell cycle. Phys. Biol. **6**(2), 025015 (2009)
36. M. Stefszky, C. Mow-Lowry, S. Chua, D. Shaddock, B. Buchler, H. Vahlbruch, A. Khalaidovski, R. Schnabel, P. Lam, D. McClelland, Balanced homodyne detection of optical quantum states at audio-band frequencies and below. Class. Quant. Grav. **29**(14), 145015 (2012)
37. S. Steinert, F. Ziem, L. Hall, A. Zappe, M. Schweikert, A. Aird, G. Balasubramanian, L. Hollenberg, J. Wrachtrup, Magnetic spin imaging under ambient conditions with sub-cellular resolution. Nat. Commun. **4**, 1607 (2013)
38. M.A. Taylor, J. Janousek, V. Daria, J. Knittel, B. Hage, H.-A. Bachor, W.P. Bowen, Subdiffraction-limited quantum imaging within a living cell. Phys. Rev. X **4**(1), 011017 (2014)
39. M.A. Taylor, J. Knittel, W.P. Bowen, Fundamental constraints on particle tracking with optical tweezers. New J. Phys. **15**, 023018 (2013)
40. C. Tischer, S. Altmann, S. Finger, J. Horber, E.H. Stelzer, E.-L. Florin, Three-dimensional thermal noise imaging. Appl. Phys. Lett. **79**(23), 3878–3880 (2001)
41. I.M. Tolić-Nørrelykke, E.-L. Munteanu, G. Thon, L. Oddershede, K. Berg-Sørensen, Anomalous diffusion in living yeast cells. Phys. Rev. Lett. **93**, 078102 (2004)
42. N. Treps, U. Andersen, B. Buchler, P.K. Lam, A. Maître, H.-A. Bachor, C. Fabre, Surpassing the standard quantum limit for optical imaging using nonclassical multimode light. Phys. Rev. Lett. **88**, 203601 (2002). May
43. N. Treps, N. Grosse, W.P. Bowen, C. Fabre, H.-A. Bachor, P.K. Lam, A quantum laser pointer. Science **301**, 940–943 (2003)
44. M. Tsang, Quantum imaging beyond the diffraction limit by optical centroid measurements. Phys. Rev. Lett. **102**, 253601 (2009). Jun
45. Y. Tseng, J. Lee, T. Kole, I. Jiang, D. Wirtz, Micro-organization and visco-elasticity of the interphase nucleus revealed by particle nanotracking. J. Cell Sci. **117**(10), 2159–2167 (2004)
46. M. Weiss, M. Elsner, F. Kartberg, T. Nilsson, Anomalous subdiffusion is a measure for cytoplasmic crowding in living cells. Biophys. J. **87**(5), 3518–3524 (2004)

Chapter 13
Further Extensions

Chapter 10 of this thesis demonstrated quantum enhanced particle tracking, and Chaps. 11 and 12 applied this to biological measurements. This demonstrates that quantum measurement holds the potential to provide practical benefits in biological microscopy. However, this proof-of-principle demonstration did not provide absolute sensitivity surpassing that which is already available classically (see Fig. 13.1). Unprecedented sensitivity could be achieved if squeezed light is used in a classically optimized experiment. The developments in this thesis have provided the foundation for such an experiment. Here we discuss the requirements and the technical difficulties associated with achieving this.

13.1 Status of Experiments

The sensitivity achieved in our quantum particle tracking experiments is compared to a range of results from the literature[1] visually in Fig. 13.1 and numerically in Table 13.1. This shows that the absolute sensitivity achieved in our experiment is comparable to many published classical experiments (Fig. 13.1a), but is approximately two orders of magnitude behind leading biological experiments, and four orders of magnitude behind leading non-biological experiments. This can be attributed primarily to the low NA objectives and the low optical power used. The absolute sensitivity in the biological experiments was also limited by the small particle size, with classical biological experiments using a similar particle size only surpassing the achieved sensitivity by a factor of four. The classical lock-in particle tracking experiment of Chap. 7 achieved sensitivity which is competitive with leading experiments

[1] In addition to these publications, there are many more which are not shown because they did not provide results from which the sensitivity could be estimated. As such, this is not an exhaustive comparison. Experiments with sensitivity worse than 1 nm $Hz^{-1/2}$ have also been excluded.

M. Taylor, *Quantum Microscopy of Biological Systems*, Springer Theses,
DOI 10.1007/978-3-319-18938-3_13

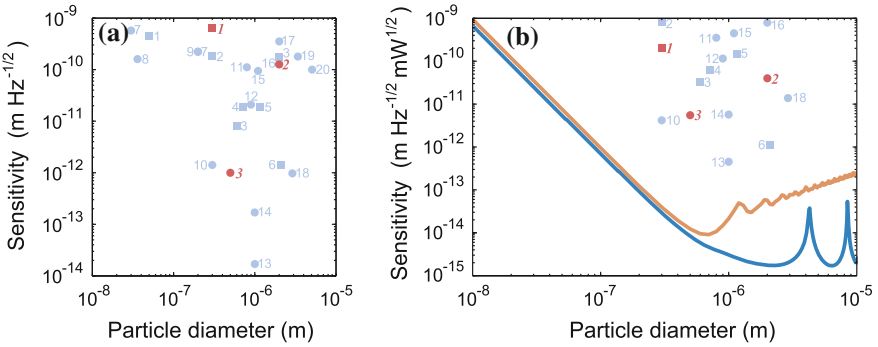

Fig. 13.1 A comparison of the sensitivity achieved in leading particle tracking experiments. **a** The absolute sensitivities, with *squares* and *circles* respectively denoting biological and non-biological experiments. The pale *blue* points correspond to classical experiments while the *dark red* points represent experiments in this thesis; **1** being the biological experiments of Chaps. 11 and 12, **2** the bead tracking characterization of Chap. 10, and **3** the classical lock-in optical tweezers of Chap. 7. These experiments cover a wide range of particle types, optical setups, and optical powers. The improvement in sensitivity with increasing optical power is compensated in **b**, which scales the sensitivity to that which would be achieved with 1 mW. In this plot, the *dark blue* line represents the fundamental limit as derived in Chap. 2 for polystyrene spheres in water tracked with 1064 nm light in the Gaussian mode, and an objective NA of 1.3. The *orange* line presents the limit to sensitivity achievable with a quadrant detector for these conditions, as derived in Chap. 4. The literature results here are listed in Table 13.1

by applying some of the techniques of the quantum particle tracking scheme but with the wider collection area of high NA objectives and higher optical power. This acts as a prototype for future quantum enhanced particle tracking experiments, and establishes that the quantum experiments in this thesis have the potential to provide field-leading sensitivity when applied with high NA objectives.

The experiments shown in Fig. 13.1 cover a wide range of optical setups. Because the sensitivity should improve with the optical power, Fig. 13.1b shows the sensitivity normalized to the value it would have for 1 mW of optical power. Our quantum experiments used far less light in measurement than most classical experiments, so in this normalized comparison our quantum experiments in biology are competitive with most leading experiments at that size scale. It is also of note that even the field-leading classical experiments which apply state-of-the-art technology do not closely approach the fundamental quantum limit to sensitivity (Fig. 13.1b). This is because technical limitations and inefficiencies prevent quantum limited particle tracking. As such, an optimized quantum enhanced particle tracking setup is expected to operate in a regime inaccessible to existing classical technology, even without breaching the fundamental quantum limit.

Table 13.1 Overview of particle tracking sensitivity

Point	Material	Diameter (μm)	Sensitivity (pm $Hz^{-1/2}$)	Normalized (pm $Hz^{-1/2}$ $mW^{1/2}$)
1 (Chap. 11)	Lipid	0.3	625	199
2 (Chap. 10)	Silica	2	126	39.9
3 (Chap. 7)	Silica	0.5	1	5.48
1 [3]	Lipid	0.05	445*	13000
	Lipid	2	177*	2300
2 [37]	Lipid	0.3	181*	812
3 [35]	Silica	0.6	8	33.0
4 [41]	Polystyrene sulfonate	0.8	19.2*	60.7#
5 [1]	Silica	1.16	18.5*	149
6 [11]	Silica	2	1.41	1.09
7 [14]	Gold	0.03	574*	12200
	Gold	0.2	222*	1570
8 [34]	Gold	0.036	160	1600
9 [13]	Gold	0.2	222*	1570
10 [7]	Latex	0.3	1.5	4.74
11 [6]	Polystyrene	0.3	111*	351#
12 [29]	Silica	0.9	21.0*	115
13 [4, 18]	Polystyrene	1	0.017	0.450
14 [19, 20]	AR titania	1	0.173	5.74
15 [38]	Titania	1.1	94.8*	444.5
16 [10]	Silica	2	130	791
17 [21]	Silicon	2	351*	1110
18 [8]	Resin	2	0.973*	13.8
19 [26]	Polystyrene	3.27	183*	1830
20 [39]	Silica	5.08	100	1000

Notes The literature results 1–6 were biological experiments, while 7–20 were non-biological experiments. Sensitivities marked with * are not specified in the publications, but were inferred from the measurable bandwidth of thermal motion. For the normalized sensitivities marked with #, the publication did not specify the optical power and we have assumed a rather moderate 10 mW

13.2 Key Challenges for Quantum Enhanced Particle Tracking

In order to achieve sensitivity which surpasses all classical competitors, some modifications to the experimental design are required. The primary short-coming of the apparatus demonstrated here was the use of low NA objectives. Future experiments will require high NA objectives, as a large collection area is pivotal to achieving high sensitivity. To maintain classically efficient detection, the detection mode should be

optimized, all sources of noise minimized, and care taken to avoid aberrations, which become increasingly important as the objective NA is improved. Chapter 9 discusses these considerations, which are identical for quantum and classical experiments. Additionally, the use of squeezed light requires high detection efficiency with losses throughout the system eliminated as much as possible.

One important consideration is the choice of the optical wavelength. While the experiments reported here used 1064 nm, a shorter wavelength might be advantageous. Use of a shorter wavelength would reduce optical heating, for instance, while increasing photochemical damage of cells (see Sect. 1.3). At fixed power it also offers improved precision; in general, the lower limit on a resolvable displacement scales as $\lambda^{1/2}$, though Rayleigh scattering particles offer a much stronger scaling of $\lambda^{5/2}$ (see Chap. 2). Furthermore, the transmission of most commercially available objectives is highest near the visible spectrum. In this thesis, 1064 nm light was chosen because this is the wavelength of the squeezed light source. Existing state-of-the-art squeezing technology has been developed for gravitational wave observatories, and has primarily operated at 1064 nm [25, 33]. For this reason, the following discussion assumes use of 1064 nm light. However, squeezed light is also generated at other wavelengths, with up to 7.6 dB demonstrated at 860 nm [24]. Such sources could also play an important role in future quantum measurements of biology.

An optimal quantum particle tracking experiment requires an objective which combines high transmission, minimal aberrations and high NA. Currently such objectives cannot be purchased commercially for 1064 nm light, and must be custom made at substantial expense. The first consideration when designing the objective is the immersion medium. Immersion-free objectives are unsuitable as they are fundamentally limited to a maximum NA of 1, and in practice are even more constrained. Oil-immersion objectives offer an NA which is commonly as high as 1.3, while the NA of water-immersion objectives is generally limited to 1.2 [31]. However, as discussed in Chap. 9, sensitivity can be vastly degraded by spherical aberrations when using oil-immersion objectives, while these are minimized for water immersion. Thus, despite the reduction in maximum NA, water-immersion objectives are likely to offer the best overall performance.

In addition to the objectives, loss is also introduced by the sample chamber containing the particles. In the experiments here this was minimized by use of anti-reflection coatings on the sample chamber. However, when using high NA objectives, the light is incident from a wide range of angles, and the optimal coating varies substantially with this incident angle. Furthermore, the light reflected from the coating and glass coverslip need to destructively interfere to provide optimal transmission, but for a tightly focused beam these two reflections will be divergent with respect to one another, making the coating ineffective. However, the reflectivity of the glass coverslips is relatively low for water immersion, as the glass coverslips have a small refractive index contrast. The resulting reflectivity predicted by Fresnel reflection is 0.4 % at normal incidence, and reaches 5.3 % for the *s* polarized component at the maximum convergence angle of 64°. Altogether, this will introduce a loss of 0.7 %

to an input Gaussian mode, with the four surfaces collectively producing 2.8 % loss. Higher order modes can suffer greater loss if these have greater components at large convergence angles.

13.3 Possible Designs

One of the aims for quantum enhanced particle tracking is to achieve sensitivity which outperforms classical competitors. In addition to this, some applications also require other capabilities such as 3D tracking or multi-particle tracking. For instance, the quantum imaging procedure described in Chap. 12 will only provide useful biological details if combined with 3D tracking. Multi-particle tracking also opens new avenues in microrheology, as this allows correlations between the motion of different particles to be studied. These correlations arise from transmission of vibrations between the objects, and thus provides a method to characterize the structures along which the vibrations propagate [5]. However, an apparatus would require squeezing across multiple spatial modes to achieve either multi-particle tracking or quantum enhancement along multiple axes, which could add considerable complexity to the experiment. Additionally, it would be desirable to integrate the quantum experiment with the Sagnac interferometry scheme described in Chap. 5 to further improve the sensitivity.

13.3.1 Incorporating Classical 3D Tracking

Figure 13.2 shows a proposed layout which could combine standard 3D particle tracking methods [30] with quantum enhancement along a single axis. Similar to the layout used for the lock-in experiments in Chap. 7, a probe field acts both to trap particles and to produce scattered light. The resulting back-scattered light is mixed with an amplitude squeezed local oscillator, and is efficiently directed toward a quadrant detector by polarizing optics. Since the sum photocurrent from the quadrant detector is a measurement of the total transmitted light, it provides a signal equivalent

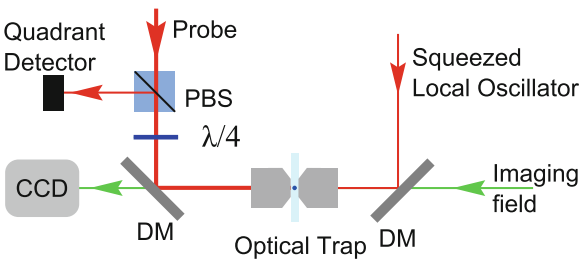

Fig. 13.2 A proposed design for future quantum optical tweezers. This is closely related to the layout used for the lock-in experiments in Chap. 7, though it is adjusted to allow 3D particle tracking with quantum enhancement along a single axis

to that of a bulk detector. This signal is used to track the particle position along the x axis, in the same manner as in the quantum enhanced particle tracking apparatus demonstrated here. Particle tracking along y and z is enabled by subtraction signals, similar to conventional 3D tracking. Since this approach relies on back-scattered light, it is better suited to tracking of small particles than large ones; for more details, see Chap. 2 or 8.

13.3.2 Incorporating Sagnac Interferometry

To further improve the future particle tracking setup, it can be combined with the Sagnac interferometry approach described in Chap. 5 and shown in Fig. 13.3. In this approach, the squeezed vacuum enters and exits through one port of the interferometer, while a bright probe field enters and exits from the other. In the limit of high visibility, only fields which experience an antisymmetric distortion within the interferometer will exit through a different port to the one it enters. Thus, the squeezed field and the antisymmetric component of the scattered field are preferentially combined and directed toward the detector.

As in the theory presented in Chap. 5, the unscattered probe photons which reach the detector then act as the local oscillator for measurement. Provided the squeezed vacuum can be appropriately mode-matched to the measurement mode, this combines the enhancements of both squeezing and Sagnac interferometry, and may thus offer a large improvement over conventional particle tracking experiments.

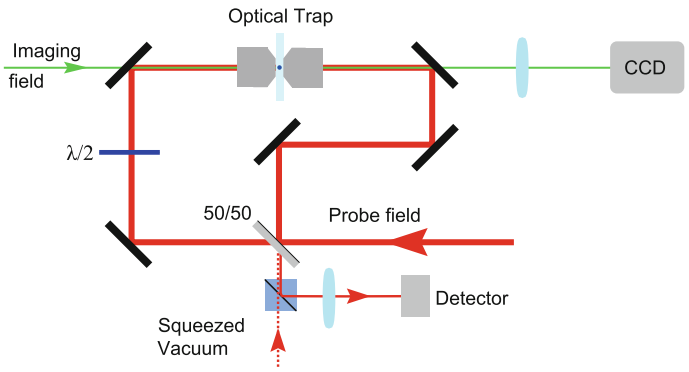

Fig. 13.3 A possible future design incorporating Sagnac interferometry

13.4 Applications

There are many potential applications for future implementations of quantum enhanced particle tracking, some of which are also discussed in Sect. 1.3. Some of these can be achieved once quantum enhanced sensitivity is achieved along one axis for a single particle, though some applications will require more elaborate setups.

A quantum particle tracking experiment which only achieves 1D tracking could be used to perform high bandwidth microrheology, extending the experiment in Chap. 11, with quantum enhanced sensitivity allowing the viscoelastic moduli of materials to be characterized in the MHz regime. High frequency mechanical properties are anticipated to be important in many materials, as highly localized relaxation processes with short characteristic length scales necessarily occur at high frequencies [22]. Such relaxation processes have been observed into the high kHz, though so far the MHz regime has been inaccessible to both bulk rheometers and microrheology experiments [40].

If classical particle tracking is integrated along the y and z axes, future experiments could perform 3D photonic force microscopy to image the interior of cells. This would extend the demonstration in Chap. 12 to allow 3D mapping of both organelle surfaces and the viscoelastic mechanical properties of the cellular cytoplasm. In addition to imaging cellular structures with nm resolution, this will also allow the study of perturbing effects which influence the measured structure. For instance, structural changes occur during cell division which change the average mechanical properties of the cell [32], and these should drastically change the measured 3D profiles. Alternatively, genetic activity can be stimulated by illumination, though the mechanism is not well understood [9, 12]. By imaging a cell before, during, and after illumination, it may be possible to determine which physical properties of cytoplasm are influenced by the light and provide new insights into the process of photostimulation.

Quantum enhanced particle tracking could also hold important applications in characterizing non-Brownian thermal motion with improved precision, as discussed in Sect. 1.3. By studying the instantaneous velocity of particles in water, it will be possible to measure the velocity distribution of particles in fluid for the first time [23]. Additionally, sufficiently high sensitivity and bandwidth will allow verification of an established theory in fluid dynamics. A moving particle in water is expected to carry with it an envelope of the surrounding fluid [18], which at very short time-scales decouples from the particle [42]. Observation of this decoupling requires sensitivity and bandwidth which both exceed the limits of current technology.

The high bandwidth achievable with quantum enhancement could also enable observation of ultrafast biological processes. These processes are extremely difficult to measure, and thus are poorly understood. For instance, nanopores in the membrane of a cell of approximately 1 nm size can open and close on ns timescales [2, 27]. Optical tweezers might allow direct observation of this process, possibly by binding a particle to a cell membrane and stimulating nearby nanopore formation. The dynamics of the formation process could then be characterized if nanopore formation

displaces the particle. However, such an experiment would require sensitivity of order 10^{-27} m^2/Hz. So far this has only been achieved in experiments that use power which is far too high for biological measurements [4]. Quantum enhanced optical tweezers might allow this level of sensitivity to be achieved with lower power, and thus allow the first direct observation of nanopore formation.

Further into the future, multi-particle tracking may allow even more applications. By studying the correlations between motion at different positions, it is possible to study vibration propagation along the intervening material. This allows important applications, such as characterization of the structural properties of cellular cytoskeleton [22]. It could also help to characterize the vibrational pulses which accompany signals propagating down axons in nerve cells [36]. As discussed in Sect. 1.3, these vibrational pulses are hypothesized to play an important role in neural transmission [15, 16]. A precise characterization of the vibrational pulse propagation may provide the evidence needed to rigorously test this hypothesis.

Finally, by combining quantum correlated light with living biology, it is conceivable that the quantum microscope may even allow the significance of quantum processes in biological systems to be tested. Several experiments have recently demonstrated that quantum coherence plays a role in biological processes such as photosynthesis, where it can improve the efficiency of light harvesting [17, 28]. However, it is quantum correlations which produce almost all uniquely quantum effects. To date, all experiments investigating quantum behavior in biological systems have studied quantum coherence, but not quantum correlations. Since this apparatus allows quantum correlated light to strongly interact with biological samples, it may be possible to map quantum correlations into biology. For instance, by stimulating photosynthesis with quantum correlated photons, the correlations should be maintained in the resulting excitations until destroyed by decoherence. By measuring the rate of energy transfer as a function of both the strength of quantum correlation and the spatial location of the absorption event, it may be possible to determine both the effect and the robustness of quantum correlations as a function of distance between the site of absorption and the reaction center. This would allow strong conclusions to be drawn about the importance of quantum mechanics in photosynthesis.

References

1. M. Atakhorrami, C. Schmidt, High-bandwidth one-and two-particle microrheology in solutions of wormlike micelles. Rheol. Acta **45**(4), 449–456 (2006)
2. H.T. Beier, C.C. Roth, G.P. Tolstykh, B.L. Ibey, Resolving the spatial kinetics of electric pulse-induced ion release. Biochem. Biophys. Res. Commun. **423**(4), 863–866 (2012)
3. P.M. Bendix, L.B. Oddershede, Expanding the optical trapping range of lipid vesicles to the nanoscale. Nano Lett. **11**(12), 5431–5437 (2011)
4. I. Chavez, R. Huang, K. Henderson, E.-L. Florin, M.G. Raizen, Development of a fast position-sensitive laser beam detector. Rev. Sci. Instrum. **79**, 105104 (2008)
5. J.C. Crocker, M.T. Valentine, E.R. Weeks, T. Gisler, P.D. Kaplan, A.G. Yodh, D.A. Weitz, Two-point microrheology of inhomogeneous soft materials. Phys. Rev. Lett. **85**(4), 888 (2000)

6. F. Czerwinski, A.C. Richardson, L.B. Oddershede, Quantifying noise in optical tweezers by allan variance. Opt. Express **17**, 13255–13269 (2009)
7. W. Denk, W.W. Webb, Optical measurement of picometer displacements of transparent microscopic objects. Appl. Opt. **29**(16), 2382–2391 (1990)
8. T. Franosch, M. Grimm, M. Belushkin, F.M. Mor, G. Foffi, L. Forró, S. Jeney, Resonances arising from hydrodynamic memory in Brownian motion. Nature **478**, 85–88 (2011)
9. M.A. Friedl, M. Schmoll, C.P. Kubicek, I.S. Druzhinina, Photostimulation of Hypocrea atroviridis growth occurs due to a cross-talk of carbon metabolism, blue light receptors and response to oxidative stress. Microbiology **154**(4), 1229–1241 (2008)
10. G.M. Gibson, J. Leach, S. Keen, A.J. Wright, M.J. Padgett, Measuring the accuracy of particle position and force in optical tweezers using high-speed video microscopy. Opt. Express **16**(19), 14561–14570 (2008)
11. F. Gittes, B. Schnurr, P. Olmsted, F. MacKintosh, C. Schmidt, Microscopic viscoelasticity: shear moduli of soft materials determined from thermal fluctuations. Phys. Rev. Lett. **79**(17), 3286–3289 (1997)
12. A. Gupta, P. Avci, M. Sadasivam, R. Chandran, N. Parizotto, D. Vecchio, W.C. Antunes-Melo, T. Dai, L.Y. Chiang, M.R. Hamblin, Shining light on nanotechnology to help repair and regeneration. Biotechnol. Adv. **31**, 607–631 (2012)
13. F. Hajizadeh, S.S. Reihani, Optimized optical trapping of gold nanoparticles. Opt. Express **18**(2), 551–559 (2010)
14. P.M. Hansen, V.K. Bhatia, N. Harrit, L. Oddershede, Expanding the optical trapping range of gold nanoparticles. Nano Lett. **5**(10), 1937–1942 (2005)
15. T. Heimburg, A.D. Jackson, On soliton propagation in biomembranes and nerves. Proc. Natl. Acad. Sci. USA **102**(28), 9790–9795 (2005)
16. T. Heimburg, A.D. Jackson, The thermodynamics of general anesthesia. Biophys. J. **92**(9), 3159–3165 (2007)
17. R. Hildner, D. Brinks, J.B. Nieder, R.J. Cogdell, N.F. van Hulst, Quantum coherent energy transfer over varying pathways in single light-harvesting complexes. Science **340**(6139), 1448–1451 (2013)
18. R. Huang, I. Chavez, K.M. Taute, B. Lukić, S. Jeney, M.G. Raizen, E.-L. Florin, Direct observation of the full transition from ballistic to diffusive Brownian motion in a liquid. Nat. Phys. **7**, 576–580 (2011)
19. A. Jannasch, A.F. Demirörs, P.D.J. van Oostrum, A. van Blaaderen, E. Schäffer, Nanonewton optical force trap employing anti-reflection coated, high-refractive-index titania microspheres. Nat. Photon. **6**, 469–473 (2012)
20. A. Jannasch, M. Mahamdeh, E. Schäffer, Inertial effects of a small Brownian particle cause a colored power spectral density of thermal noise. Phys. Rev. Lett. **107**(22), 228301 (2011)
21. S. Keen, J. Leach, G. Gibson, M. Padgett, Comparison of a high-speed camera and a quadrant detector for measuring displacements in optical tweezers. J. Opt. A: Pure Appl. Opt. **9**(8), S264–S266 (2007)
22. G.H. Koenderink, M. Atakhorrami, F.C. MacKintosh, C.F. Schmidt, High-frequency stress relaxation in semiflexible polymer solutions and networks. Phys. Rev. Lett. **96**, 138307 (2006)
23. T. Li, M.G. Raizen, Brownian motion at short time scales. Ann. Phys. **525**, 281–295 (2013)
24. G. Masada, T. Suzudo, Y. Satoh, H. Ishizuki, T. Taira, A. Furusawa, Efficient generation of highly squeezed light with periodically poled MgO: $LiNbO_3$. Opt. Express **18**(12), 13114–13121 (2010)
25. M. Mehmet, H. Vahlbruch, N. Lastzka, K. Danzmann, R. Schnabel, Observation of squeezed states with strong photon-number oscillations. Phys. Rev. A **81**(1), 013814 (2010)
26. O. Otto, F. Czerwinski, J.L. Gornall, G. Stober, L.B. Oddershede, R. Seidel, U.F. Keyser, Real-time particle tracking at 10,000 fps using optical fiber illumination. Opt. Express **18**(22), 22722–22733 (2010)
27. A.G. Pakhomov, A.M. Bowman, B.L. Ibey, F.M. Andre, O.N. Pakhomova, K.H. Schoenbach, Lipid nanopores can form a stable, ion channel-like conduction pathway in cell membrane. Biochem. Biophys. Res. Commun. **385**(2), 181–186 (2009)

28. G. Panitchayangkoon, D.V. Voronine, D. Abramavicius, J.R. Caram, N.H. Lewis, S. Mukamel, G.S. Engel, Direct evidence of quantum transport in photosynthetic light-harvesting complexes. Proc. Natl. Acad. Sci. USA **108**(52), 20908–20912 (2011)
29. E.J. Peterman, M.A. van Dijk, L.C. Kapitein, C.F. Schmidt, Extending the bandwidth of optical-tweezers interferometry. Rev. Sci. Instrum. **74**(7), 3246–3249 (2003)
30. A. Pralle, M. Prummer, E.-L. Florin, E. Stelzer, J. Hörber, Three-dimensional high-resolution particle tracking for optical tweezers by forward scattered light. Microsc. Res. Tech. **44**(5), 378–386 (1999)
31. S.N.S. Reihani, S.A. Mir, A.C. Richardson, L.B. Oddershede, Significant improvement of optical traps by tuning standard water immersion objectives. J. Opt. **13**(10), 105301 (2011)
32. C. Selhuber-Unkel, P. Yde, K. Berg-Sørensen, L.B. Oddershede, Variety in intracellular diffusion during the cell cycle. Phys. Biol. **6**(2), 025015 (2009)
33. M. Stefszky, C. Mow-Lowry, S. Chua, D. Shaddock, B. Buchler, H. Vahlbruch, A. Khalaidovski, R. Schnabel, P. Lam, D. McClelland, Balanced homodyne detection of optical quantum states at audio-band frequencies and below. Class. Quant. Grav. **29**(14), 145015 (2012)
34. K. Svoboda, S.M. Block, Optical trapping of metallic Rayleigh particles. Opt. Lett. **19**(13), 930–932 (1994)
35. K. Svoboda, C.F. Schmidt, B.J. Schnapp, S.M. Block, Direct observation of kinesin stepping by optical trapping interferometry. Nature **365**, 721 (1993)
36. I. Tasaki, K. Kusano, P. Byrne, Rapid mechanical and thermal changes in the garfish olfactory nerve associated with a propagated impulse. Biophys. J. **55**(6), 1033–1040 (1989)
37. I.M. Tolić-Nørrelykke, E.-L. Munteanu, G. Thon, L. Oddershede, K. Berg-Sørensen, Anomalous diffusion in living yeast cells. Phys. Rev. Lett. **93**, 078102 (2004)
38. A. van der Horst, P.D.J. van Oostrum, A. Moroz, A. van Blaaderen, M. Dogterom, High trapping forces for high-refractive index particles trapped in dynamic arrays of counterpropagating optical tweezers. Appl. Opt. **47**(17), 3196–3202 (2008)
39. G. Wang, R. Prabhakar, Y. Gao, E. Sevick, Micro-rheology near fluid interfaces. J. Opt. **13**(4), 044009 (2011)
40. N. Willenbacher, C. Oelschlaeger, Dynamics and structure of complex fluids from high frequency mechanical and optical rheometry. Curr. Opin. Colloid Interface Sci. **12**(1), 43–49 (2007)
41. N. Willenbacher, C. Oelschlaeger, M. Schopferer, P. Fischer, F. Cardinaux, F. Scheffold, Broad bandwidth optical and mechanical rheometry of wormlike micelle solutions. Phys. Rev. Lett. **99**(6), 068302 (2007)
42. R. Zwanzig, M. Bixon, Compressibility effects in the hydrodynamic theory of Brownian motion. J. Fluid Mech. **69**(part 1), 21–25 (1975)

Chapter 14
Summary and Conclusion

This thesis describes the development and application of quantum enhanced particle tracking, with the overall aim of introducing the techniques of quantum metrology to practical biological experiments. Toward this goal, the quantum limit to sensitivity was characterized for the first time, and classical strategies developed to improve sensitivity and make optical tweezers compatible with quantum metrology. Following this, we have demonstrated particle tracking with quantum enhanced sensitivity, and used this to enhance both sensitivity and spatial resolution for the first time in biological experiments. This has advanced the field of biological quantum metrology, and shown a route to future experiments in which quantum resources allow unprecedented sensitivity.

14.1 Part I: Characterization of the Quantum Limit

Shot noise in particle tracking arises due to quantum noise in the optical fields. The first part of this thesis characterized the constraining influence of this quantum noise on particle tracking sensitivity. Prior to the work in this thesis, investigations of this limit have relied on approximations which are inapplicable to real particle tracking experiments. Chapter 2 determines the total information contained in a measured coherent field, which establishes an ultimate limit for classical particle tracking experiments. The sensitivity achieved in leading experiments is found to be within two orders of magnitude of this limit, which thus constrains future advances in classical particle tracking technology.

Since this quantum limit is only approachable for a perfect measurement, it is not of primary relevance to real experimental systems. Particle tracking relies on extraction of information from a scattered field, and no particle tracking scheme to date can capture the complex spatial structure of the field which carries this information. The quantum shot noise limit in real experiments is derived in Chap. 3. This also provides insight into how to classically optimize the measurement to extract all of

M. Taylor, *Quantum Microscopy of Biological Systems*, Springer Theses,
DOI 10.1007/978-3-319-18938-3_14

the information. Furthermore, this chapter establishes how to use quantum correlated light to improve the measurement sensitivity and increase the per photon information content of the scattered light.

Although these calculations rigorously characterize particle tracking sensitivity, evaluation of the limits requires manual calculation of scattered fields, which can be difficult and time-consuming for a non-expert. To allow a wide range of researchers to benefit from rigorous theoretical predictions, Chap. 4 presents a computational tool which characterizes particle tracking measurements with the commonly used quadrant detection scheme. This can theoretically characterize the sensitivity and signal amplitude for an experiment without requiring any manual calculations. Altogether these theoretical tools allow a thorough characterization of the capabilities of existing technology, show how to improve upon this, and predict the progress that such advances could enable.

14.2 Part II: Strategies to Improve Sensitivity

The theory from Part I establishes the requirements for efficient measurement of the scattered photons which carry information about the position of a nanoparticle. The second part of the thesis presents techniques to improve this detection efficiency, while minimizing detection of background photons that introduce noise. Chapter 5 demonstrates that the field used to trap the particles can be suppressed through use of interferometry, without degradation of the scattered field. This allows higher field intensities at the optical trap without saturation of the detector, and consequently, an increased flux of scattered photons and corresponding improvement in sensitivity. Following this, Chap. 6 presents a new particle tracking method based on homodyne measurement. This allows the detection mode to be engineered arbitrarily, and if optimized, will allow classically optimal particle tracking. This method also provides additional benefits for quantum enhanced particle tracking by providing improved control over the detection mode.

In Chap. 7, a novel lock-in measurement is demonstrated which evades low frequency laser and electronic noise which could otherwise obscure the particle tracking signal. This allows shot-noise limited measurements at low frequencies, which could be beneficial to a wide range of classical experiments, and is essential in any attempt to achieve sub-shot noise limited sensitivity. Chapter 8 then discusses the use of dark-field microscopy. Dark-field microscopy spatially separates the illuminating field from the detection, and allows a vast improvement in contrast. However, while the illumination can be completely suppressed at the detector, some background photons from extraneous scattering centers still remain. This chapter shows that the scattering background can also be suppressed by optimizing the illumination angle.

Chapter 9 then concludes this part of the thesis with an overview of the strategies commonly used to achieve high sensitivity measurements in optical tweezers. For any optical tweezers experiment to achieve high sensitivity measurements, it must avoid the technical pitfalls of aberration, drift, and noise. All of these problems can place

serious limitations on classical experiments, and unless dealt with appropriately, will also limit quantum experiments. Since these have already been addressed many times in classical experiments, it is essential to take note of the expertise of the field which is summarized in this chapter. Avoidance of these problems is a prerequisite for any experiment which aims to use quantum correlated light to outperform classical competitors.

14.3 Part III: Quantum Enhanced Measurements

The theoretical and experimental developments in Parts I and II together show the way to design a quantum enhanced optical tweezers experiment. In Part III of this thesis, quantum enhanced particle tracking is finally demonstrated and applied in biological experiments. It begins with the development and characterization of a quantum enhanced optical tweezers apparatus in Chap. 10. Squeezed states of light are applied to microscopy for the first time, and allow sub-shot noise limited particle tracking for the first time. This provides the first technology capable of performing a broad range of quantum enhanced measurements in biology.

To demonstrate that the quantum shot noise limit can be overcome for measurements of living systems, quantum enhanced microrhoelogy experiments were performed within *Saccharomyces cerevisiae* yeast cells. As described in Chap. 11, naturally occurring lipid granules were tracked as they thermally diffused through the cell, with amplitude squeezed light yielding a 2.4 dB enhancement in displacement sensitivity. Analysis of the thermal motion allowed the mechanical properties of the cellular cytoplasm to be characterized, with squeezed light allowing a precision enhancement of 22 %.

Following this, Chap. 12 extended this experiment to spatially resolved quantum imaging of the cytoplasmic structure. Here, sub-diffraction-limited quantum metrology and quantum enhanced spatial resolution were both demonstrated for the first time in a biological context. By tracking lipid particles as they diffused through an extended region of the cell, spatial variations in the local mechanical properties of the cellular cytoplasm could be sampled. This spatial structure was resolved at length scales down to 10 nm, far below the diffraction limit. Quantum correlated light was found to enhance the spatial resolution in this experiment by 14 %.

Chapter 13 then concludes the body of the thesis with a discussion of the future directions of quantum enhanced particle tracking. The experiments reported in this thesis demonstrate with finality that quantum correlated light can provide a practical benefit to biological microscopy. However, these proof-of-principle experiments were not conducted with sensitivity surpassing the classical competition, and the challenge remains to implement quantum correlated light in a classically optimized experiment. This chapter discusses the strategies required to build such an apparatus, and the important applications which it could allow.

14.4 Outlook for the Future

The experiments in this thesis have established that quantum correlated light is capable of enhancing biological microscopy experiments, and shown the way for future applications of this technique. Once a quantum enhanced particle tracking experiment is built which applies both the technologies developed here and the improvements described in Chap. 13, it is likely to provide sensitivity beyond the capabilities of classical technology. At that point, the quantum experiment will be capable of resolving features that no classical competitor can resolve, and will likely be applied in a wide range of measurements. Perhaps in a few decades, similar quantum techniques will be applied routinely in microscopy.

Appendix A
Source Code for Quadrant Detection

A.1 Quadrant Detection

The following Matlab program is used to calculate the response of a quadrant detector.

```
tic

% This file will calculate the measurement signal for displacements along
% the x axis, and minimum resolvable displacement for a spherical particle
% in optical tweezers, with particle tracking via a quadrant detector at
% the back-focal plane of a condenser.


%%%%%%%%%%%%%%%%%%%%%%%%%%%%%%%%%%%%%%%%%%%%%%%%%%%%%%%%%%%%%%%%%%%%%%%%%%%%%%%
% First, define the particle properties: %%%%%%%%%%%%%%%%%%%%%%%%%%%%%%%%%%%%%%%

% Specify refractive indices of the medim and particle
n_medium = 1.33; % Water

% n_particle = 1.46; %Silica
n_particle = 1.58;% Polystyrene


% Particle size
radius = 5e-7; % In units of m

% Next define the measurement setup: %%%%%%%%%%%%%%%%%%%%%%%%%%%%%%%%%%%%%%%%%%

% The vacuum wavelength in m
wavelength=1064e-9;

% Objective NA; this defines the trapping beam width. Note, this assumes an
% aberration free objective.
NA=1.25;

% Effective condenser NA
NA_condenser=1.25;
```


M. Taylor, *Quantum Microscopy of Biological Systems*, Springer Theses,
DOI 10.1007/978-3-319-18938-3

```
% Polarisation. [ 1 0 ] is plane-polarised along the x-axis, [ 0 1 ] is
% y-polarised, and [ 1 -i ] and [ 1 i ] are circularly polarised.
polarisation = [ 1 0 ];

% Define the spatial mode of the incident light, in the Laguerre-Gauss
% basis. A Gaussian profile is [0, 0].
lg_mode=[0 0];

% To normalize the shot-noise limit, define measured power in W
Power=1e-3;


% What do we want to calculate: %%%%%%%%%%%%%%%%%%%%%%%%%%%%%%%%%%%%%%%%%%%%

% Which axis do we measure along: x=1, y=2, z=3
axis=1;

% Is the particle axially centered at the stable trap point (=1) or the beam focus (=0)?
Trap=1;

% All needed parameters are now defined. %%%%%%%%%%%%%%%%%%%%%%%%%%%%%%%%%%%%
%%%%%%%%%%%%%%%%%%%%%%%%%%%%%%%%%%%%%%%%%%%%%%%%%%%%%%%%%%%%%%%%%%%%%%%%%%%


% Creating the trapping field %%%%%%%%%%%%%%%%%%%%%%%%%%%%%%%%%%%%%%%%%%%%%%



% Location of the focal point relative to the particle. These are the
% [ x y z ] coordinates.
beam_offset = [ 0 0 0];


% Specify the beam width.
beam_angle = asin(NA/n_medium)*180/pi;
w0 = lg_mode_w0( lg_mode, beam_angle );

% Wavenumber
k = 2*pi*n_medium/wavelength;

% To what order do we expand the fields?
Nmax = ka2nmax(k*radius);
    if Nmax < 12
        Nmax = 12;
    end


% Create the trapping field:
% Use this for focused Gaussian field
[n,m,a0,b0] = bsc_pointmatch_farfield(Nmax,1,[ lg_mode w0 1 polarisation 90 beam_offset ]);
[a,b,n,m] = make_beam_vector(a0,b0,n,m);

% Normalize total power of wave sum to 1.
pwr = sqrt(sum( abs(a).^2 + abs(b).^2 ));
a=a/pwr;
b=b/pwr;
```

```
%********* Insert T-matrix here *********%
T = tmatrix_mie(Nmax,k,k*n_particle/n_medium,radius);
%*********                      *********%

if(Trap)
    % Calculate axial trapping point %%%%%%%%%%%%%%%%%%%%%%%%%%%%%%%%%%%%%%%%%%%%%%%%
    % Generally, the trapping position is not centred along the z axis.

% Specify points at which to evaluate the force.
% Note that these lengths are in units of the medium wavelength.
z = linspace(-5,4,100);
fz = zeros(size(z));

%calculate the force along z
for nz = 1:length(z)

    [A,B] = translate_z(Nmax,z(nz));
    a2 = ( A*a + B*b );
    b2 = ( A*b + B*a );

    pq = T * [ a2; b2 ];
    p = pq(1:length(pq)/2);
    q = pq(length(pq)/2+1:end);

    fz(nz) = force_z(n,m,a2,b2,p,q);

end

% Locate the trapping point
maxforce=z(fz==max(fz));
zeroindex=find(fz<0&z>maxforce,1);

if length(zeroindex)~=0
    % fit to third order polynomial the local points. (only works when
    % dz sufficiently small)
    pz=polyfit(z(max([zeroindex-2,1]):min([zeroindex+2,length(z)])),fz(max([zeroindex↩
        -2,1]):min([zeroindex+2,length(z)])),3);
    root_z=roots(pz); %find roots of 3rd order poly.

    dpz=[3*pz(1),2*pz(2),1*pz(3)]; %derivative of 3rd order poly.

    real_z=root_z(imag(root_z)==0); % finds real roots only.

    rootsofsign=polyval(dpz,real_z); %roots that are stable
    zeq=real_z(rootsofsign<0); %there is at most 1 stable root. critical roots give ↩
        error.
    try
        zeq=zeq(abs(zeq-z(zeroindex))==min(abs(zeq-z(zeroindex))));
    end
else
    zeq=[];
end

if length(zeq)==0
    warning('No axial equilibrium in range!')
    zeq=0;
end
```

```
else
        % Alternatively, we could simply place the particle at the beam centre;
        zeq=0;
end

% Calculate the detection signal %%%%%%%%%%%%%%%%%%%%%%%%%%%%%%%%%%%%%%%%%%

% Define the grid of points used in measurement
theta0=linspace(0,asin(NA_condenser/n_medium),150);% We only need to include points with theta<theta max
N_phi=160;% Make this a divisible by 4, so that each quadrant includes the same number of points.
phi0=pi/N_phi:2*pi/N_phi:2*pi;

[theta,phi]= meshgrid(theta0,phi0);
dA=sin(theta(:))*(theta0(2)-theta0(1))*(phi0(2)-phi0(1)); % The area of each grid point

% Calculate the matrices which transfer from expansion coefficients to
% Electric field amplitudes
[A_p,B_q]=farfield_matrix(n,m,theta(:),phi(:));


% Define the particle displacements for which we calculate the signal, in
% units of the medium wavelength
dx = linspace(-2,2,201);


% Now work out spherical coordinates for the displacements:
if(axis==1)
    [rt,theta_dx,phi_dx]=xyz2rtp(dx,0,zeq); % Displacement along (x,y,z) axis
elseif(axis==2)
    [rt,theta_dx,phi_dx]=xyz2rtp(0,dx,zeq);
elseif(axis==3)
    [rt,theta_dx,phi_dx]=xyz2rtp(0,0,dx);

    if(length(phi_dx)==1) %This seems to be a problem
        phi_dx=phi_dx*ones(size(theta_dx));
    end
else
    warning('axis must be 1, 2, or 3.')
    break
end
% Define these here;
Itot =zeros(size(dx));
QuadX=zeros(size(dx));
QuadY=zeros(size(dx));

for nr = 1:length(dx)

    Rot = z_rotation_matrix(theta_dx(nr),phi_dx(nr)); %calculates an appropriate axis rotation off z.
    D = wigner_rotation_matrix(Nmax,Rot);

    [A,B] = translate_z(Nmax,rt(nr));
    a2 = D'*(  A * D*a +  B * D*b ); % Wigner matricies here are hermitian. Therefore in MATLAB the D' operator is the inverse of D.
    b2 = D'*(  A * D*b +  B * D*a ); % In MATLAB operations on vectors are done first, therefore less calculation is done on the matricies.
```

```
    pq = T * [ a2; b2 ];
    p = pq(1:length(pq)/2);
    q = pq(length(pq)/2+1:end);

    % Now translate the scattered field back into the original reference frame
    [A2,B2] = translate_z(Nmax,-rt(nr));

    p2 = D'*(  A2 * D*p +  B2 * D*q );
    q2 = D'*(  A2 * D*q +  B2 * D*p );

    % Calculate the electric field for these coefficients
    E=reshape(A_p*(a+2*p2)+B_q*(b+2*q2),length(theta(:)),3);


    % This is total current and the two subtraction signals.
    Itot(nr) =sum(sum(abs(E).^2,2).*dA);
    QuadX(nr)=sum(sum(abs(E).^2.*(sign(cos(phi(:)))*ones(1,3)),2).*dA);%/Itot(nr);
    QuadY(nr)=sum(sum(abs(E).^2.*(sign(sin(phi(:)))*ones(1,3)),2).*dA);%/Itot(nr);

end


% Calculate the shot-noise limit %%%%%%%%%%%%%%%%%%%%%%%%%%%%%%%%%%%%%%%%%%

% When finding the smallest resolvable displacement, include only the linear region in dx
Incl=abs(dx)<0.2;
pow=mean(Itot(Incl));

LinfitX=polyfit(dx(Incl),QuadX(Incl)/pow,1);
GX=LinfitX(1);
% LinfitY=polyfit(dx(Incl),QuadY(Incl),1);
% GY=LinfitY(1);
LinfitZ=polyfit(dx(Incl),Itot(Incl)/pow,1);
GZ=LinfitZ(1);

% Minimum resolvable displacement, if a noiseless 100% efficient measurement is performed.
%This is given by 1/(GX*sqrt(n)), with n the measured photon number and GX in units m^-1

N_photflux=Power*wavelength/(6.63e-34*3.00e8);
dx_min=abs(wavelength/(n_medium*GX *sqrt(N_photflux))); % In units of: m Hz^{-1/2}
dz_min=abs(wavelength/(n_medium*GZ *sqrt(N_photflux)));



% Display results %%%%%%%%%%%%%%%%%%%%%%%%%%%%%%%%%%%%%%%%%%%%%%%%%%%%%%%%%



plot(dx*wavelength/n_medium*1e6,[QuadX;QuadY;Itot-mean(Itot)]/pow)
xlim([-1.6,1.6])
xlabel('Displacement (\mum)')
toc
```

A.2 Farfield Calculation

The above program calls on the function "farfield_matrix" to calculate the transmitted field from the expansion coefficients:

```
function [A_p,B_q] = farfield_matrix(Nmax,theta,phi)
% farfield_matrix.m
% Finds matrices which return the far field from VSWF expansion coefficients
%
% usage
% [A_p,B_q] = farfield_matrix(n,m,theta,phi)
%
% then, the electric field is given by
% E=reshape(A_p*(a+2*p2)+B_q*(b+2*q2),length(theta(:)),3);
%
% each row of E is the field (in spherical coordinates) in the
% (theta,phi) direction (assuming a distance scaling factor of kr)
%
% This file is modified from "farfield.m" in the Optical tweezers toolbox 1.2,
% and calls on other functions from that software package.
%
% For details of the Optical tweezers toolbox, see:
% http://www.physics.uq.edu.au/people/nieminen/software.html
%(Copyright 2006-2012 The University of Queensland.)
%
%
% This assumes that n= 1:Nmax, and that for each n, m=-n : n.
% That is, it assumes all modes are input in order.

[theta,phi] = matchsize(theta,phi);

A_p = zeros(length(theta)*3,Nmax^2+2*Nmax);
B_q = zeros(length(theta)*3,Nmax^2+2*Nmax);

for n = 1:Nmax
   [~, Ytheta, Yphi] = spharm(n, -n:n, theta, phi);

   Nn = 1/sqrt(n*(n+1)) ;

   A_p((length(theta)+1):end, n^2:(n^2+2*n)) = Nn * (-1i)^(n+1) * [Yphi;-Ytheta];
   B_q((length(theta)+1):end, n^2:(n^2+2*n)) = Nn * (-1i)^n * [Ytheta;Yphi];

end
return
```

Note that this function has been modified from the version originally published to improve its speed.

Appendix B
Comment on Experimental Study on the Imaging of the Squeezed State Light at 1064 nm

In this thesis, we have claimed that the experiment reported in Chap. 12 demonstrated for the first time that resolution could be enhanced via the application of squeezed light. It is of note that Ref. [1] have also claimed to achieve enhanced resolution via the use of squeezed light. This prior publication, and the follow-up work in Refs. [2, 4], has been disregarded as we consider their claims to be unsubstantiated.

In Ref. [1], an optical parametric amplifier (OPA), consisting of a nonlinear crystal in a Fabry-Perot optical cavity, is used to generate squeezed light. The measured squeezing is first characterized, and then the squeezed light is applied in a simple imaging experiment. In this experiment, a resolution test card with a set of absorbing patterns is imaged onto a CCD camera, and the resolution estimated from the smallest observable features. They claim that the results of this imaging experiment show that squeezed light overcomes the limit of quantum noise, enhances the resolution, and surpasses the diffraction limit.

The diffraction limit arises in absorption imaging experiments such as this because classical diffraction establishes a minimum area to which light can be focused. It is already well known that squeezed light follows classical diffraction, and cannot be used to enhance the resolution of an imaging system which is classically diffraction limited [3]. This is not discussed in Ref. [1], and nor is any mechanism described by which squeezed light could surpass the diffraction limit. Instead, the authors simply assert that an image taken with laser light is diffraction limited (their Fig. 7b), and show that superior resolution could be achieved using their squeezed light source. However, an increase in laser power was shown to improve resolution for both coherent and squeezed light (their Fig. 8), which demonstrates that the image resolution is limited by the low signal-to-noise rather than diffraction. As such, the claimed super-resolution is both unphysical and completely unsubstantiated.

Furthermore, insufficient evidence is provided for the claims of quantum enhanced resolution. Firstly, no reliable evidence is presented that the light is actually squeezed. Although the noise power spectrum was characterized (their Fig. 3), the shot-noise limit was assumed to correspond to the measured laser noise. However, their measured laser noise fluctuates with frequency by over 15 dB, and therefore cannot correspond to shot-noise which is spectrally flat. Without an accurate calibration

M. Taylor, *Quantum Microscopy of Biological Systems*, Springer Theses,
DOI 10.1007/978-3-319-18938-3

of the shot-noise limit, there is no conclusive evidence of squeezing. Additionally, the imaging approach is based on static measurements with a CCD camera. Because the noise was only characterized at frequencies above 500 kHz, there is no evidence whatsoever that squeezing was present at the measurement frequency of the images. Construction of a low frequency squeezed light source is an immensely difficult task [5], and since the authors do not mention of any effort to achieve squeezing in this low frequency regime, the imaging experiments are almost guaranteed to be limited by classical noise. This classical noise was not considered, and the images formed using laser light were simply assumed to be at the classical limit for resolution. However, even if squeezed light were present, no mechanism was described by which it could enhance the resolution. No further support is provided by the follow-up work reported in Refs. [2, 4], which also both fail to provide reliable evidence of squeezing or to describe any mechanism by which the squeezing could improve resolution.

Given this, it is exceedingly unlikely that the improvement in resolution demonstrated in Ref. [1] actually corresponds to a quantum enhancement via squeezed light. It is far more likely that the "squeezed" light provided improved performance due to a reduction in classical noise, while remaining above the shot-noise limit. Alternatively, the improvement may simply result from systematic errors in the imaging apparatus. The authors noted that when using coherent light, peripheral details were unclear compared to those in the center of the image, which was not the case when using squeezed light. Although this was interpreted as evidence for the superior imaging properties of squeezed light, in reality it suggests that the optical focus was changed between the experiments. The achievable resolution is highly sensitive to the focus, and even a small change could produce the observed improvement. The authors did not describe the procedure used to change between the squeezed and coherent light sources, and thus did not rule our any such systematic effects. Overall, Ref. [1] provided no compelling evidence that they achieved quantum enhanced resolution, described no mechanism by which squeezing could enhance the resolution, and left open the possibility that their observed improvement was fully produced by systematic errors.

References

1. L. Chen, S.W. Bi, B.Z. Lu, Experimental study on the imaging of the squeezed state light at 1064 nm. Laser Phys. **21**(7), 1202–1207 (2011)
2. F. Feng, S.W. Bi, B.Z. Lu, M.H. Kang, Long-term stable bright amplitude-squeezed state of light at 1064 nm for quantum imaging. Optik **124**, 1070–1073 (2013)
3. M. Kolobov, C. Fabre, Quantum limits on optical resolution. Phys. Rev. Lett. **85**(18), 3789–3792 (2000)

4. B. Lu, S. Bi, F. Feng, M. Kang, F. Qin, Experimental study on the imaging of the squeezed-state light with a virtual object. Opt. Eng. **51**(11), 119001–119001 (2012)
5. K. McKenzie, N. Grosse, W. Bowen, S. Whitcomb, M. Gray, D. McClelland, P. Lam, Squeezing in the audio gravitational-wave detection band. Phys. Rev. Lett. **93**(16), 161105 (2004)

Curriculum Vitae: Michael Taylor

My primary interest is to develop novel technologies for optical sensing and measurement. I like my experiments to cover new ground and try new strategies, while also holding relevance to practical applications. At the time of this publication, I have 6 years of full-time experimental research experience in the fields of optical trapping, optical microcavities, and quantum measurement. My projects have resulted in 12 published papers, with another 2 under review. Throughout my research to date, I has been a driving force both in terms of creativity and experiments, which is why I am first author on 11 of the 14 papers written.

Qualifications

- PhD in Physics from the University of Queensland, Australia (2014)
- BSc(Hons) first class in Physics from the University of Otago, New Zealand (2008)

Publications

1. **Michael A. Taylor**, Jiri Janousek, Vincent Daria, Joachim Knittel, Boris Hage, Hans-A. Bachor, and Warwick P. Bowen, *Biological measurement beyond the quantum limit*, Nature Photonics **7** 229–233 (2013)
2. **Michael A. Taylor**, Jiri Janousek, Vincent Daria, Joachim Knittel, Boris Hage, Hans-A. Bachor, and Warwick P. Bowen, *Subdiffraction-limited quantum imaging within a living cell*, Physical Review X **4** 011017 (2014)
3. **Michael A. Taylor**, Joachim Knittel, and Warwick P. Bowen, *Fundamental constraints on particle tracking with optical tweezers*, New Journal of Physics **15** 023018 (2013)
4. **Michael A. Taylor**, Joachim Knittel, and Warwick P. Bowen, *Optical lock-in particle tracking in optical tweezers*, Optics Express **21** 8018–8024 (2013)

M. Taylor, *Quantum Microscopy of Biological Systems*, Springer Theses,
DOI 10.1007/978-3-319-18938-3

5. **Michael A. Taylor**, Alex Szorkovszky, Joachim Knittel, Kwan H. Lee, Terry G. McRae, and Warwick P. Bowen, *Cavity optoelectromechanical regenerative amplification*, Optics Express **20** 12742–12751 (2012)
6. **Michael A. Taylor**, Joachim Knittel, Magnus T. L. Hsu, Hans-A. Bachor, and Warwick P. Bowen, *Sagnac interferometer enhanced particle tracking in optical tweezers*, Journal of Optics **13** 044014 (2011)
7. **Michael A. Taylor** and Warwick P. Bowen, *A computational tool for the quadrant detection signal and displacement sensitivity in optical tweezers*, Journal of Optics **15** 085701 (2013)
8. **Michael A. Taylor** and Warwick P. Bowen, *Enhanced sensitivity in dark-field microscopy by optimizing the illumination angle*, Applied Optics **52** 5718–5723 (2013)
9. Jong H. Chow, **Michael A. Taylor**, Timothy T.-Y. Lam, Joachim Knittel, Jye D. Sawtell-Rickson, Daniel A. Shaddock, Malcolm B. Gray, David E. McClelland, and Warwick P. Bowen, *Critical coupling control of a microresonator by laser amplitude modulation*, Optics Express **20** 12622–12630 (2012)
10. Joachim Knittel, Jong H. Chow, Malcolm B. Gray, **Michael A. Taylor**, and Warwick P. Bowen *Ultrasensitive real time measurement of dissipation and dispersion in a whispering-gallery mode microresonator*, Optics Letters **38** 1915–1917 (2013)
11. Jian Wei Tay, **Michael A. Taylor**, and Warwick P. Bowen, *Sagnac-interferometer-based characterization of spatial light modulators*, Applied Optics **48** 2236 (2009)
12. **Michael A. Taylor** and Warwick P. Bowen, *Quantum noise in optical tweezers*, Journal of Physics: Conference Series **467** 012007 (2013)

Articles under review

13. **Michael A. Taylor** and Warwick P. Bowen, *Quantum metrology and its application in biology*, under review; preprint available at ArXiv:1409.0950
14. **Michael A. Taylor**, Muhammad Waleed, Alexander B. Stilgoe, Halina Rubinsztein-Dunlop, and Warwick P. Bowen, *Structured interference force for enhanced optical trapping*, under review;

Research Experience

- *Postdoctoral research*, March 2015 onward, Research Institute of Molecular Pathology, Vienna, Austria. Here I design and construct novel fluorescence microscopes to image neural activity at high speed and at depth.
- *Postdoctoral research*, January 2014 to February 2015, University of Queensland, Brisbane, Australia. A quantum microscope was designed, and the first stage constructed, which should allow sensitivity surpassing the limits of existing state-of-the-art technology. A holographic technique was also developed which can

improve trap stiffness and measurement sensitivity by orders of magnitude for large particles.

- *PhD project*, February 2010 to January 2014, University of Queensland, Brisbane, Australia. I developed techniques to improve sensitivity in microscopic particle tracking, new theoretical tools to characterize such measurements, and then used these to demonstrate quantum enhanced particle tracking microscopy. With this I performed quantum enhanced biological measurements.
- *Research Assistant*, February 2009 to January 2010, University of Otago, Dunedin, New Zealand. Here I built a rig to pole optically nonlinear polymers. This polymer technology aims to replace crystal based modulators for optical fiber based communication.
- *Undergraduate projects*, December 2007 to September 2008, University of Otago, Dunedin, New Zealand. I completed two main projects: (1) lock the frequency of a laser to an atomic absorption line, and (2) characterize the response of a spatial light modulator to computer inputs and reprogram it to provide a linear response.